Doctoral Dissertation
Doctoral Program in Chemical Engineering (33rd Cycle)

Addressing the challenges of the Power-to-Fuel technologies from a catalyst development and techno-economic point of view

Fabio Salomone

* * * * * *

Supervisors
Prof. Samir Bensaid, Supervisor
Prof. Raffaele Pirone, Co-Supervisor

Doctoral Examination Committee:

Massimo Migliori, Professore di II fascia, Università della Calabria, massimo.migliori@unical.it
Carlo Giorgio Visconti, Professore di II fascia, Politecnico di Milano, carlo.visconti@polimi.it
Salvatore Abate, Ricercatore RTDB, Università di Messina, salvatore.abate@unime.it
Debora Fino, Professoressa di I fascia, Politecnico di Torino, debora.fino@polito.it
Marco Piumetti, Professore di II fascia, Politecnico di Torino, marco.piumetti@polito.it

Politecnico di Torino
April 2, 2021

I hereby declare that, the contents and organisation of this dissertation constitute my own original work and does not compromise in any way the rights of third parties, including those relating to the security of personal data.

…………………………………..

Fabio Salomone

Turin, April 2, 2021

Summary

The research focuses on the study of Power-to-Fuel technologies for producing renewable fuels or chemicals (i.e. methane, methanol and dimethyl-ether) from renewable energy sources and CO_2. Renewable energy sources (RES) exhibit an intermittent electric production and the electric energy has to be stored as an energy carrier such as hydrogen that could be produced through water electrolysis. CO_2 could be obtained by using carbon capture technologies in order to favour the closed carbon cycle and produce alternatives to fossil fuels.

Concerning Power-to-Gas technology, research has made significant progress and has been supported by many European projects (e.g. Store&Go and Helmeth). A model of a Power-to-Gas plant for the CO_2 hydrogenation to methane coupled to an intermittent electrical input from renewable energy sources was developed in Matlab® environment. In addition, a technical-economic analysis was carried out on the plant model, considering the possibility of managing the plant with both chemical and electrochemical storage tanks in order to decouple the production from the intermittent electric input. Subsequently, in collaboration with the Energy Department of the Politecnico di Torino and within the European project Store&Go, the coupling of Power-to-Gas plants with the medium voltage network was investigated in order to reduce electrical issues caused by the fluctuations of the electric production of RES. The techno-economic assessment revealed that the process is economically competitive in a future scenario in which the costs of the electrolyser and the electricity price will be lower than current prices. Furthermore, electrochemical storages are too expensive to be implemented, even if they allow the Power-to-Gas plant to be decoupled from the electric grid and to reduce the number of plant shutdowns. Furthermore, small and medium size Power-to-Gas plants allow electrical problems caused by RES fluctuations (i.e. overvoltages, overcurrents and reverse power flow) to be mitigated or solved.

Concerning the Power-to-Methanol technology, three aspects of the topic have been studied. Firstly, mixed copper-ceria catalysts were developed in the context of the Italian project Saturno for understanding in more detail the synergistic effect between the two phases. Secondly, the catalytic reactors for CO_2 hydrogenation to methanol were modelled in Matlab® environment for determining the presence of thermal issues, the best reactor configuration and the start-up time of the plant. Thirdly, a techno-economic and environmental assessment of thermocatalytic and electrocatalytic Power-to-Methanol plants was performed for investigating the feasibility of both processes.

Regarding the development of copper-ceria catalysts, they have been synthesized by means of three different synthesis techniques (i.e. impregnation, solution combustion synthesis and gel-oxalate coprecipitation), characterized by N_2 physisorption, XRD, H_2-TPR, CO_2-TPD, ICP-MS, FE-SEM and EDS analyses. Furthermore, the catalysts were tested in an experimental test bench to evaluate and comparing their performance. These catalysts exhibited a synergistic effect between copper and ceria in CO_2 hydrogenation to methanol. In particular, the oxalate-gel coprecipitation technique favours the formation of small nanoparticles of both phases, the increase of the specific surface area and the interface between copper and ceria; therefore, the methanol productivity is significantly enhanced.

Concerning the reactor modelling, a pseudo-homogeneous one-dimensional model of the reactor was developed and another model that also includes the methanol separation section and the recirculation of unreacted gases. The purpose of the work was to evaluate the internal profiles of the reactor, evaluate the best reactor configuration to obtain the maximum performance of the plant and estimate the plant start-up time. The study has revealed that there are no crucial thermal issues the best reactor configuration is a double refrigerated fixed-bed reactor.

Lastly, the techno-economic and environmental assessments of the feasibility of Power-to-Methanol processes have required to study a scale-up of both processes starting from reliable laboratory data on a ternary catalyst (CuZnAl) for CO_2 hydrogenation to methanol in both reactor configurations. The assessments have revealed that the electrocatalytic technology could be further developed for achieving greater performances and that it could be economically competitive with the thermocatalytic process. Furthermore, the feasibility of even small-sized plants has been demonstrated if the allocation of the product on the market is considered.

Finally, in the field of dimethyl-ether production, the research is focused on the development of CuZnZr ferrierite-based hybrid catalysts for direct CO_2 hydrogenation to dimethyl-ether in a one-step process. The activity and stability of four hybrid catalysts supplied by CNR-ITAE of Messina and obtained by using different synthesis techniques (i.e. co-precipitation, impregnation and physical mixture) were investigated. The tests were carried out varying both the space velocity and the reaction temperature. Moreover, both calcined and aged catalysts were characterized by means of different techniques: N_2 physisorption, H_2-TPR, NH_3 pulse chemisorption, XRD, ICP-MS, FESEM, EDS, XPS and TEM measurements. The coprecipitated CuZnZr-ferrierite hybrid catalysts exhibited the best performances and a higher oxide/zeolite ratio favours the dimethyl-ether yield.

Acknowledgment

I would like to acknowledge European Union's Horizon 2020 research and innovation programme under grant agreement No. 621210 (project HELMETH) and grant agreement No. 691797 (project STORE&GO). The European Union is not liable for any use that may be made of the information contained herein.

Furthermore, I would like to thank the Italian regional project SATURNO in the context of which part of the research was developed.

I would like to acknowledge my supervisor Prof. Samir Bensaid and my co-supervisor Prof. Raffaele Pirone for their priceless contributions to this work.

In addition, I would like to acknowledge Prof. Francesco Frusteri and Dr. Giuseppe Bonura (CNR-ITAE, Messina, Italy) for providing CuZnZr ferrierite-based hybrid catalysts for direct CO_2 hydrogenation to dimethyl-ether, Dr. Marco Fontana and Dr. Angelica Chiodoni (IIT, Turin, Italy) for performing TEM analyses, Dr. Micaela Castellino for carrying out XPS analyses, Prof. Fabio Alessandro Deorsola and Dr. Camilla Galletti for performing ICP-MS analyses and XRD analyses.

I would like to acknowledge Prof. Massimo Santarelli, Dr. Domenico Ferrero, Dr. Andrea Mazza, Dr. Emanuele Giglio, Dr. Eduard Alexandru Morosanu and Dr. Esperanza Batuecas and Dr. Hilmar Guzmán for their contributions and valuable collaboration.

Moreover, I would like to acknowledge my parents and all my family for their great support during these years.

Lastly, I would like to acknowledge my colleagues for their valuable teamwork and my friends for their support and encouragement.

Contents

List of Tables

List of Figures

Introduction

1.1. Greener technologies for fighting climate change

1.1.1. The problem of greenhouse gas emissions

Climate change has become a pivotal aspect in recent decades that must be coped with. Human activities have a fundamental impact on the climate and global warming, obtaining the energy needed to meet society's needs from the combustion of fossil fuels, intensifying deforestation and increasing intensive livestock farming [1–3]. These are some examples of actions that cause the release into the atmosphere of a huge amount of greenhouse gases (GHG) responsible for the increase in the global average temperature compared to the pre-industrial level (1850-1900). The uncontrolled increase in the concentration of greenhouse gases (i.e. CO_2, CH_4, N_2O, etc.) in the atmosphere causes excessive absorption of the infrared radiation emitted by the earth's surface. Consequently, the planet is progressively warming up, putting ecosystems, society and human health in serious danger. The greenhouse gas that is emitted in greater quantities is CO_2 and its concentration has increased dramatically from the beginning of the industrial revolution exceeding 410 ppm in 2019 [4]. CO_2 derives mainly from the combustion of non-renewable fossil fuels (i.e. coal, fuel oil and natural gas): 64% of anthropogenic global warming depends on CO_2 emissions. The energy sector accounts for almost all the CO_2 emissions [1–3]. In fact, the world total primary energy supply roughly has doubled from 71 TWh in 1973 to 159 TWh in 2015 [3]. Furthermore, the amount of CO_2 generated to produce energy accounts for more than half of total greenhouse gas emissions. In 2018, around 90% of CO_2 emissions came from the combustion of coal, fuel oil and natural gas, which accounted for 39%, 31% and 18%, respectively [1–3]. Emissions related to fossil fuels can only be significantly reduced with a massive transition to renewable energy sources, such as hydroelectric, wind, solar and sustainably produced biofuels by adopting carbon capture and utilisation (CCU) technologies. All those aspects have led the most influential nations to sign the Kyoto protocol in 1998 and the Paris Agreement in 2015 for the purpose of reducing CO_2 emissions and pollutants and impacts of global warming [3].

1.1.2. Renewable energy sources

Although in the last decade renewable energy sources (RES) have grown at a faster rate than traditional energy sources, the amount of renewable energy produced in absolute terms is not enough to meet the growth in global demand. CO_2 emissions must be reduced to mitigate future environmental, economic and social impacts that they will entail [1]. Most of the electric energy is produced from non-renewable fossil sources such as coal (39.3 %), natural gas (22.9 %) and oil (4.1 %) [3]; however, a radical change is taking place within the society, leading to its progressive decarbonisation and to a wider penetration of RES. This transformation is one of the crucial aspects of managing energy sources. The most common RES are hydroelectric (16.0 %), photovoltaic, wind power, geothermal and waste (7.1 %) [3]. In accordance with those statistics, the world renewable electric energy production is 23.1 %; however, in Europe, RES produce around 30 % of the electricity [3]. More in detail, photovoltaic and wind power are characterized by a wide periodic variability that causes periods of overproduction and others of lack of electricity. Furthermore, the electricity cannot be stored in the electric grid network because some problems arise (e.g. overvoltages, overpotentials and reverse power flows) [3,5]. There are many electrical storage technologies such as fly wheels, batteries, compressed air energy storage, pumped hydro storage, H_2 and synthetic natural gas (SNG) storage; however, fly wheels and batteries are characterized by a small storage capacity and a short discharge time [6]. Therefore, compressed air energy storage and pumped hydro storage may be suitable to balance the fluctuations and intermittent productions of RES; however, RES production is sensible to seasonal fluctuations if the RES penetration increases significantly [3,5,6]. For these reasons, the storage of electrical energy in the form of chemical energy (e.g. H_2, CH_4, synthetic fuels) seems to be the best solution to face these aspects.

1.1.3. Electrolysis and H_2 production

H_2 could be produced by means of different processes: on the one hand, non-renewable H_2 could be obtained through reforming or pyrolysis of fossil fuels; on the other hand, renewable H_2 could be produced by biological or thermochemical treatments of biomass or by water splitting [7]. More in detail, electrolysis seems to be the most promising process for storing electric energy in an energy carrier such as H_2 [8–11]. Three main technologies of electrolysers are available: proton-exchange membrane electrolysis cells (PEM-EC), alkaline electrolysis cells (AEC) and solid oxide electrolysis cells (SOEC). PEM-EC and AEC technologies are already developed at a commercial stage. Both technologies operate at relatively low temperature (50 – 120 °C) with an efficiency that ranges between 55 % and 70 % (LHV basis) [5]. Firstly, AEC is a mature technology and it is suitable for large scale processes because of its relatively low cost and its long lifetime. The electrolyte is made of an alkaline aqueous solution (e.g. 20 – 30 % KOH or NaOH), but its corrosive action is the main disadvantage increasing maintenance costs [12]. Secondly, PEM-EC is a more recent technology based on a polymeric membrane (e.g. Nafion) and it is characterised by higher power densities, high flexibility suitable for dynamic operations and high H_2 purity; however, the membrane is subjected to fast degradation and, thus, the cell lifetime is relatively short increasing replacement costs [12]. Lastly, SOEC electrolysers are the most recent and still under-development technology. SOEC operate at high temperatures (650 – 1000 °C) because the electrolyte consists of a ceramic material such as yttria-stabilized zirconia (8 %mol Y_2O_3-ZrO_2) for conducting O^{2-} anions [12]. The main advantages of high temperature operation are the reduction of the electric demand because of the lower equilibrium cell voltage and the high electric efficiency that could reach unity (LHV basis) at thermoneutral and even exceeds it in endothermic mode [3,12]. Disadvantages of SOEC technology are related to fast degradation of material due to high operative temperatures, low suitability for intermittent operations and expensive capital costs [12].

Those technologies allows the electric energy to be stored in an energy carrier such as H_2; however, it presents some drawbacks because it is a very reactive gas, flammable and, therefore, it is subjected to legislative limits regarding storage, transport and distribution. For instance, the maximum hydrogen storage pressure in Italy is 200 bar, while in USA it is 700 bar; moreover, the maximum hydrogen concentration in the natural gas distribution grid is 0.5 %vol in Italy and 5.0 %vol in Germany [13]. In fact, hydrogen causes embrittlement of steel in natural gas transport pipelines [8]. Therefore, one of the best solutions may be the production of other energy carriers, synthetic fuels or added-value products (i.e., methane, methanol, dimethyl-ether, hydrocarbons, alcohols, etc.) coupling the electric energy storage and the carbon capture and utilization (CCU) technologies [3].

1.1.4. Carbon capture and utilization technologies

In addition to the introduction of renewable energy sources, climate change can be faced by reducing greenhouse gases (GHG) emissions. Carbon dioxide is the main GHG emitted into the atmosphere, as it derives from all both biological and artificial combustion processes. The production of electricity and heat are the processes that consume the most fossil fuels and emit large amount of CO_2. Hence, the research focused on carbon capture and storage (CCS) and carbon capture and utilization (CCU) technologies [12,14–18]. On the one hand, CCS consists in processes for capturing CO_2 from gaseous streams reducing anthropogenic CO_2 emissions and storing it through underground sequestration or mineral carbonation [15]. However, the feasibility of those technologies requires detailed studies for identifying storage sites, geological, social, economic and environmental impacts [15]. On the other hand, CCU processes are those of greatest interest because they would allow fuelling the closed carbon cycle. The sources of CO_2 can be multiple: capture from combustion fumes (e.g. cement plant, waste incinerators, thermoelectric plants, etc.), biogas or biohydrogen upgrade processes, industrial fermentation processes and air [3,4]. There are many technologies for CO_2 capture and separation such as absorption processes with aqueous solutions of monoethanolamine or ionic liquids, adsorption processes on solid materials (e.g. zeolite, activated carbon, functionalized porous supports), separation processes by means of membranes [3,4,12,14–18].

1.2. Power-to-Fuel technologies

Considering the production of renewable hydrogen by means of electrolysis and the carbon capture processes, the technology that could replace non-renewable fossil sources is Power-to-Fuel (PtF). Therefore, this thesis work is focused on the study of Power-to-Fuel technologies at different levels of detail and development. As shown in Figure 1.1, the goal of a PtF system is the production of synthetic renewable fuels (methane, methanol, dimethyl-ether and light or heavy hydrocarbons) or chemicals (e.g. methanol, dimethyl-ether, light olefins, etc.) [11,12,19–22]. These products are produced from RES and captured CO_2 via CO_2 hydrogenation and they could replace effectively and efficiently non-renewable fossil fuels.

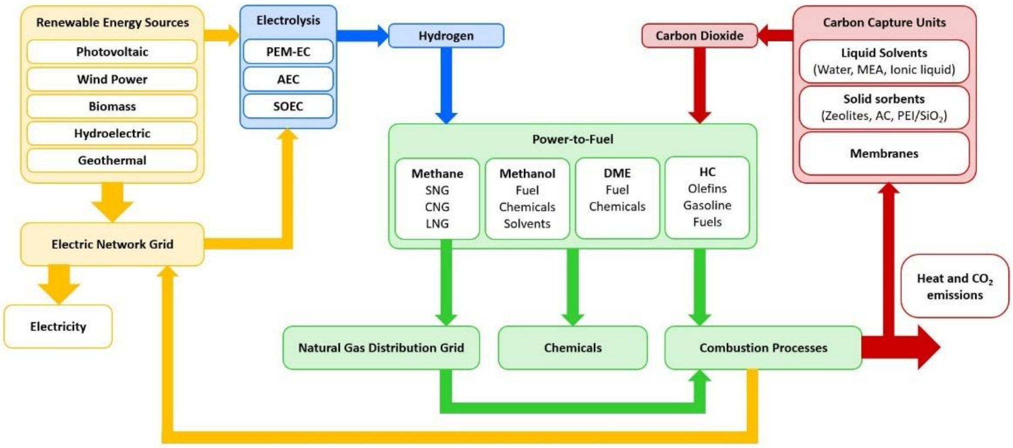

Figure 1.1. Overview of Power-to-Fuel technologies.

1.2.1. Power-to-Gas

The following section contains text previously published in [3] and [5].

Power-to-Gas (PtG) is the first process that is analysed in this thesis work. It consists in the coupling of an electrolyser for H_2 production by using mainly RES-based electricity and a methanation unit for the hydrogenation of CO_2 to methane. The main advantage of methane is that it does not cause problems in the natural gas distribution grid; therefore, it could be injected in the gas grid and distributed to the utilisers if it respects the gas grid specifications [13].

As aforementioned, H_2 could be obtained by means of several electrolysis systems and existing research recognises that technical and economic aspects play a crucial role for implementing this technology at a large scale [3,12,21]. The second important part of the process is the methanation unit, that consists of a series of catalytic reactors that are generally tightly thermally integrated each other. Therefore, the arrangement of the reactors is a key aspect for achieving product specifications, reducing catalytic deactivation and optimising thermal integration [8,12,23–25]. Methanation catalysts consists of an active phase made of a VIII-X group metal (e.g. Fe, Ni, Co or noble metals) supported on a large surface area oxide such as alumina (Al_2O_3), silica (SiO_2) or titania (TiO_2) [12,17,21,24,26–28]. The most common catalyst is Ni/γ-Al_2O_3 that seems to exhibit an excellent compromise between good performances in terms of activity, stability and selectivity and low costs [21], in fact, researchers have been explored performances, operating conditions and deactivation causes [29]. According to the literature, the development of PtG technology is at a very advanced stage (TRL 8) [16,19,20]; therefore, the process has been developed and consolidated, the catalyst (e.g. Ni/γ-Al_2O_3) for CO_2 hydrogenation to methane is already at a commercial stage and its physic-chemical characteristics and its performances are at the state-of-the-art [12,17,21,24,26–28].

The goals of the research in PtG field are mainly two: on the one hand, technical feasibility and economic viability of real case scenarios that make the PtG system competitive must be identified and evaluated; on the other hand, the effects and the management of large PtG plants on the electric grid need to be assessed. Therefore, two chapters of this thesis are dedicated to addressing the two aspects mentioned previously.

Chapter 2 focuses on the behaviour of a PtG system that exploits high-temperature electrolysis tightly thermally integrated with the methanation unit. The case of study is a future scenario with a high RES penetration, in which the intermittency of electric energy production is not negligible. Furthermore, the technical feasibility study is accompanied by an economic viability analysis. In this work a PtG plant coupled to an intermittent RES-based electrical input was modelled. In addition, a technical-economic analysis was carried out on the plant model, considering the possibility of managing the plant with both chemical and electrochemical storages. This part of the work was developed within European Union’s Horizon 2020 research and innovation programme under grant agreement No. 621210 (project HELMETH) that has been already acknowledged. The PhD candidate Fabio Salomone has developed the PtG model on MATLAB® environment, has defined and simulated the cases of study scenarios and has written the original and revised drafts of the article.

Subsequently, Chapter 3 focuses on the effects of the installation of large Power-to-Gas plants based on low-temperature electrolysis coupled to the medium voltage network for managing the intermittent fluctuations of RES production. More in detail, in the literature, there are relatively few studies that combine both PtG and distribution systems. In [30], the authors have investigated the use of an electrolyser as an alternative for network expansion in case of high photovoltaic (PV) penetration. A real network has been modelled and the size of the electrolyser has been obtained by considering the same effect reached by cable substitution. As will be discussed in Chapter 2, the techno-economic analysis has highlighted that the profitability is greatly depending on the local excess of RES [3]. More in detail, RES electric excess has been used for sizing of the PtG plant capacity, reaching an overall PtG plant efficiency of about 77 % (LHV basis) and a utilization factor of about 30 % [3]. These results have been obtained both optimising the thermal integration between the methanation unit and the electrolyser, and analysing the management of each equipment [3]. The use of a low-voltage (LV) electrolyser has been studied by predicting the temporal variation of excess energy occurring in low voltage networks at 2030 and by identifying appropriate electrolyser capacities, while not considering any network topologies but only an equivalent energy balance at a single node [31]. In [32], the mitigation effect of electrolysers on the reverse power flow has been exemplified on a LV grid. The evaluation of the use of power-to-methane chain in case of distribution systems characterised by an excess of wind production has been analysed in [33]. The study has been based on the consumption of gas and electricity of a local area, and the use of combined heat and power (CHP) plants locally installed has been considered as well. In [34], the authors have focused on voltage regulation in active power distribution systems, by presenting a new algorithm for the real time scheduling of PtG and Gas-to-Power (GtP) plants by considering also arbitrage opportunities. In [35], the authors have presented a voltage control strategy by coordinating both the On-Load Tap Changer and an alkaline electrolyser modelled dynamically as in [36]. The same electrolyser model has been used in [37] for studying how the electrolyser can be optimally designed and installed for facing the increase of RES in future active distribution networks. The alleviation of reverse power flow, line congestions and power losses in integrated power and gas network has been studied in [38–40], respectively. In those cases, the authors have presented three different scheduling algorithms to properly deploy power-to-methane and GtP conversion unit for distribution network support.

Hence, the aim of this research work as part of the European Union’s Horizon 2020 research and innovation programme under grant agreement No. 691797 (project STORE&GO) [41] is the development of an integrated model for determining the size, the number and the location of the PtG systems by simulating real scenarios of two electric grids (rural and semi-urban). The objective function of the model consists in the minimization of overvoltages, overpotentials and reverse power flows. In this research work, the PhD candidate Fabio Salomone has adapted the PtG model developed in MATLAB® environment, has defined the hypotheses of the PtG system and has contributed to the writing of the original and revised drafts of the article.

1.2.2. Methanol and dimethyl-ether

The other chapters of the thesis focus on the study of PtF systems; in particular, on the production of methanol and dimethyl-ether. This type of plant is still under development and the TRL is lower than the TRL of PtG technologies [4]. Therefore, the research involves the development of innovative catalysts for the synthesis of methanol and dimethyl-ether via CO_2 hydrogenation, the reactor modelling for the synthesis of these products, the determination of the best reactor configuration and preliminary studies of techno-economic and environmental feasibility. The productions of methanol and dimethyl-ether are linked to each other because dimethyl-ether is produced via methanol dehydration and according to the literature there are both two-steps and one-step processes.

Methanol synthesis

Methanol represents one of the products with the highest versatility and can be used as renewable fuel mixed with gasoline in car engines, as a primary fuel in power generation plants, in the power supply of industrial machinery, as a feed for the production of plastic and as solvent in the chemical industry [42]; or as a precursor of dimethyl-ether (DME), which is obtained through the dehydration of methanol and in recent decades has received increasing attention as an alternative fuel with low environmental impact in diesel engines. The catalytic CO_2 hydrogenation to methanol is described by means of three reactions: CO_2 hydrogenation to methanol (1.1), reverse water gas shift (RWGS) reaction (1.2) and CO hydrogenation to methanol (1.3) [4].

$$CO_2 + 3\ H_2 \leftrightarrow CH_3OH + H_2O \qquad \Delta\widetilde{H}^0 = -48{,}97\ \text{kJ/mol} \tag{1.1}$$

$$CO_2 + H_2 \leftrightarrow CO + H_2O \qquad \Delta\widetilde{H}^0 = +41{,}16\ \text{kJ/mol} \tag{1.2}$$

$$CO + 2\ H_2 \leftrightarrow CH_3OH \qquad \Delta\widetilde{H}^0 = -90{,}14\ \text{kJ/mol} \tag{1.3}$$

CO_2 and CO hydrogenations are exothermic reactions, which are thermodynamically favoured at low temperature, while RWGS is endothermic and, therefore, it is thermodynamically favoured at high temperature.

The most common catalysts in catalytic CO_2 hydrogenation to methanol are metals and their oxides. In particular, the combination of copper and zinc oxide has been widely used for this reaction [42]. Researchers have discovered that zinc oxide manages to maintain a high level of dispersion of copper clusters, reduces the sintering of copper nanoparticles and it promotes the methanol synthesis reaction, without accelerating the parasitic RWGS reaction [42]. This has an important effect on the selectivity of the Cu/ZnO system towards methanol. The surface area of the bimetallic catalyst can be further increased by adding Al_2O_3. Moreover, the introduction of Al_3^+ ions in the material improves stability and it has a beneficial effect on the surface metal area by promoting the copper dispersion [43]. Traditionally methanol is produced by means of CO hydrogenation (i.e. indirect synthesis) [44,45], which is obtained by steam reforming or by the partial oxidation of methane of fossil and non-renewable origin [46]. On the contrary, emerging technologies (e.g. PtF) foresee the production of methanol through the direct hydrogenation of CO_2. The $Cu/ZnO/Al_2O_3$ catalytic system, commercially known as CZA, is generally used in the industrial production of methanol carried out mostly at high pressures (50-100 bar) and high temperatures (220-300 ° C) by feeding syngas at 5% by volume of CO and 5% by volume of CO_2. However, the performance of this system is reduced when a CO_2-H_2 mixture without CO is fed to the reactor due to water poisoning [47].

Recently, Graciani et al. have obtained experimental and theoretical evidence of a superior activity of copper-ceria and copper-ceria-titania catalysts in CO_2 hydrogenation to methanol [48]. According to the literature, copper and ceria appear to have a synergistic effect in the activation of CO_2 and in its hydrogenation to methanol [42,48], however they are little studied as their performances do not seem to be comparable to those of commercial catalysts such as the ternary catalyst CuZnAl [42]. Therefore, Chapter 4 of this thesis is dedicated to the development of copper and cerium-based catalysts for the hydrogenation of CO_2 to methanol and they have been investigated in more detail within the Italian project SATURNO [49]. The catalysts based on Cu and Ce were synthesized with three different synthesis techniques (i.e. wet impregnation, solution combustion synthesis and gel-oxalate coprecipitation) by varying the composition of the material. Subsequently they were characterized with N_2 physisorption, X-ray diffraction (XRD), temperature programmed reduction (H_2-TPR) and desorption (CO_2-TPD), ICP-MS, FE-SEM and EDS analyses. Furthermore, the catalysts were tested in an experimental test bench to determine their catalytic performances.

Another relevant aspect of methanol synthesis via CO_2 hydrogenation concerns the modelling of the reactors. Some researchers have focused their studies on process simulation by using Aspen Plus [46,50]. Kiss et al. [50] have sensitively investigated operative conditions by using a one-dimensional pseudo-homogeneous isothermal tube-bundle fixed-bed reactor. According to the work of Kiss et al. [50], the CO_2 hydrogenation is commonly conducted on a ternary CuZnAl catalyst and the kinetic model that is generally used has been proposed by Graaf et al. [51]. Other researchers have analysed more complex models of the reactors (i.e. bi-dimensional pseudo-homogeneous or heterogeneous reactors) [44,46,52] for the purpose of investigating thermal gradients and hot-spots that could deactivate the catalyst. Hence, Chapter 5 of the thesis concerns the modelling of a methanol synthesis reactor. The research focused on developing a pseudo-homogeneous one-dimensional reactor model and a simplified model of the methanol production section that includes the reactor, the methanol separation section and the recirculation of unreacted gases. The state-of-the-art kinetic model on the $Cu/ZnO/Al_2O_3$ catalyst [42,50,51,53–56] proposed by Graaf et al. [51] was used for the modelling. The purposes of the work are: the evaluation of the internal profiles of the reactor (temperature, CO_2 conversion and methanol yield), the design of the best configuration of the reactor to maximise performances of the plant and the estimation of the start-up time of the plant even at the variation of the operating condition with respect to the nominal design condition.

Power-to-Methanol

The following section contains text previously published in [4].

Regarding PtF processes, as previously mentioned, there are many processes for producing added-value products from CO_2 conversion: neutralization reactions, biochemical, photocatalytic, photoelectrochemical, electrochemical (EC) and thermochemical (TC). Nowadays, the Sabatier and Fisher-Tropsch TC routes are still being investigated to produce fuels or chemicals owing to the fact that it is easy to integrate these processes at an industrial scale [5,29,57–59]. A considerable amount of literature has been published on thermocatalytic CO_2 conversion. Most of these studies have been focused on the MeOH production. MeOH provides an excellent means to store energy, it is a vital intermediate for several bulk chemicals and it can be used as a convenient fuel since it has a high-octane rating (almost half of the kWh/L relative to gasoline or diesel) [60]. Since 2009, MeOH installed production capacity is rising around 10% annually [61]. Around of 2 million tons of methanol are produced annually utilizing CO_2 as feedstock [62]. Nonetheless, the results are not yet satisfactory because the traditional TC processes has some weaknesses, such as poor stability of support in the presence of steam, it is less thermodynamically favourable than the existing syngas route, and it requires a high energy demand [63]. On the other hand, the hydrogen required by the process is still mainly produced from steam methane reforming (SMR), which is not a cost-effective and sustainable process [64]. In terms of maturity, in 2016, Pérez-Fortes et al.[65] cited a TRL of 6–7 for methanol synthesis from CO_2, which implies that this technology has been demonstrated at prototypal scale in an operational environment. Hence, this TRL suggests that the thermochemical conversion of CO_2 to produce methanol may be early industrialized [66].

On the other hand, the EC conversion of CO_2 to methanol have advantages with respect to current TC processes, such as (i) the direct use of renewable energy source, (ii) the use of water for the in-situ protons (H^+) generation and (iii) mild reaction conditions to convert the CO_2 into fuels or chemicals, which are conventionally derived from petroleum. However, large overpotentials are required to electrochemically reduce CO_2 (> 3.0 V) and to get reasonable amounts of fuels. Other issues of the EC CO_2 reduction to methanol (or other liquid fuels) are the low productivity and the low selectivity of state-of-the-art EC processes [67–75]. Moreover, the practical application of this technology is delayed not only by fundamental developments (i.e. of new catalysts materials) but also by the few efforts focused on process engineering optimization and scale-up [76]. Nonetheless, the future for electrosynthesis processes is promising. Compared with 10 years ago, there is now a growing awareness of EC routes and the practical targets that might be achieved by electrochemical processes. Also, with the increasing availability of a great diversity of EC cells and an increasing experience of integrating electrolytic cells for H_2 production into complete industrial processes [64,76–79], there are now lower obstacles to their scale-up. The EC CO_2 reduction technology has been demonstrated at a broad range of TRLs from 3 to 6 [80–82]. The lower TRL of this technology with respect to the TC one demonstrates the lower level of current progress for its commercialisation. It is still required additional engineering work on both novel electrocatalyst integrating smart catalyst and EC reactors, properly optimized to avoid mass transfer, selectivity and kinetics limitations. However, despite its relative immaturity, the current and continuous investments for the development of this technology may allow it to progress to higher TRLs, so that their positive attributes, such as CO_2 utilisation with renewable energy, may be exploited sooner [66].

Chemical industry is on track to achieve the emissions reductions required by 2050 (as defined during the Paris Agreement). The International Energy Agency recommends research in chemistry and engineering projects that will lower the energy use and the GHG footprint [61]. In this regard, some research has been carried out about different catalytic routes for the conversion of CO_2 into MeOH [59,75,83]. However, there is still very little scientific understanding of their environmental challenges [84]. Other than the efficiency of the process, it is also of main importance to evaluate its sustainability (in the overall life cycle analysis of exploited materials and energy sources). Perez-Fortes et al. [77] carried out an exhaustive work about the MeOH synthesis by TC processes using captured CO_2. They assessed the techno-economic aspects and the environmental issues by means of CO_2 metrics, however they did not conduct a Life Cycle Assessment (LCA) but pointed out that a complete LCA study should be done in the future. Furthermore, CO_2 hydrogenation is highly dependent on an efficient catalyst [85,86]. Consequently, research [87] recognises the necessity of exploring the environmental impact of the catalyst in the CO_2 conversion technologies as well as of integrated water electrolysis systems [88].

In Chapter 6, the potential of both TC and EC-based PtF processes for the production of methanol is faced. Therefore, a TC PtF process for the synthesis of methanol was designed and a techno-economic assessment was performed to evaluate its feasibility. Nonetheless, TC PtF plants are not the unique technology available for methanol synthesis. In fact, the electrolyser and the reactor can be thought of as a single electrocatalytic equipment, in which the CO_2 hydrogenation occurs on the surface of one of the two electrodes of the electrocatalytic cell, while the electrolysis reaction takes place on the surface of the other electrode [4]. Then a ternary CuZnAl catalyst was synthesized by coprecipitation, deposited on the electrode and tested in the experimental electrochemical test bench to obtain the experimental data for scaling up of the electrocatalytic system. In fact, the electrocatalytic system is at a low stage of development [4]. Starting from the laboratory data, a scale-up of the electrocatalytic system was carried out, developing different scenarios compatible with future developments that can be derived from literature studies that simulate the development of the technology over time until the performance of the thermocatalytic system is reached. Finally, a techno-economic assessment and an environmental comparison was made between thermocatalytic and electrocatalytic PtF plants. With respect to this work, the PhD candidate Fabio Salomone has tested the thermocatalytic performances of the CuZnAl ternary oxide catalyst that was synthetised by Hilmar Guzmán, has modelled the scale-up of both TC and EC processes, has performed the techno-economic assessment, has provided TC data of the Life Cycle Inventory (LCI) that were used by Esperanza Batuecas for performing the Life Cycle Assessment (LCA) and has participated to the writing of the original and revised drafts of the article.

Dimethyl-ether synthesis

The synthesis of dimethyl-ether (DME) through CO_2 hydrogenation seems to be one of the most promising processes to obtain a useful, valuable and environmentally friendly product. DME is indeed an added-value product with a high cetane rating and low pollutant emissions during the combustion; thus, it could be used as a substitute of diesel fuel. Moreover, DME is a key intermediate for producing chemicals or petrochemicals [53,89–94].

Industrially, DME is generally produced from syngas though the most mature pathway which involves a two-step process: the hydrogenation of CO to methanol (MeOH) on a Cu-based catalyst, which is economically cheaper than noble metals, and a subsequent dehydration of MeOH to DME on an acidic catalyst [53,90,93,95]. This process is strongly limited by thermodynamics due to the exothermicity of the methanol synthesis reaction; in addition, MeOH is a favoured product at high pressures (the operating condition ranges between 260-280 °C and 5-10 MPa) [52,53,95,96]. As previously mentioned, researchers have recently shown a growth of interest in CO_2 hydrogenation; thus, novel hybrid catalysts have been developed for the purpose of directly producing DME in a single-step process [53,93]. The net reaction of DME synthesis is reported in equation (1.4); however, the overall process consists of four main reactions: the CO_2 hydrogenation to MeOH (1.5), the reverse water gas shift (RWGS) reaction (1.6), the CO hydrogenation to MeOH (1.7) and the MeOH dehydration to DME (1.8). In the single-step process thermodynamic limitations of the MeOH synthesis could be overcome thanks to its dehydration to DME; hence, the CO_2 per pass conversion could be increased even at low temperatures [42,53,95].

$$CO_{2(g)} + 6 \cdot H_{2(g)} \rightleftarrows CH_3OCH_{3(g)} + 3 \cdot H_2O_{(g)} \qquad \Delta\tilde{H}^0_{298.15} = -122.2 \text{ kJ/mol} \tag{1.4}$$

$$CO_{2(g)} + 3 \cdot H_{2(g)} \rightleftarrows CH_3OH_{(g)} + H_2O_{(g)} \qquad \Delta\tilde{H}^0_{298.15} = -49.4 \text{ kJ/mol} \tag{1.5}$$

$$CO_{2(g)} + H_{2(g)} \rightleftarrows CO_{(g)} + H_2O_{(g)} \qquad \Delta\tilde{H}^0_{298.15} = +41.2 \text{ kJ/mol} \tag{1.6}$$

$$CO_{(g)} + 2 \cdot H_{2(g)} \rightleftarrows CH_3OH_{(g)} \qquad \Delta\tilde{H}^0_{298.15} = -90.4 \text{ kJ/mol} \tag{1.7}$$

$$2 \cdot CH_3OH_{(g)} \rightleftarrows CH_3OCH_{3(g)} + H_2O_{(g)} \qquad \Delta\tilde{H}^0_{298.15} = -23.4 \text{ kJ/mol} \tag{1.8}$$

The most common Cu/ZnO-based catalysts are typically supported on a ceramic material, for instance alumina (Al_2O_3), zirconia (ZrO_2) or silica (SiO_2) in order to increase the surface area and to prevent sintering of Cu particles [42,53–56]. These catalysts are remarkably selective towards methanol, which is not the thermodynamically favoured product of the reaction; while, the main by-product is CO due to the endothermic RWGS reaction [42,95]. Existing research has demonstrated that CO_2 hydrogenation is favoured over Cu/ZnO-based catalysts, which reduce the activation energy of the reaction; whereas, the activation energy of CO hydrogenation over Cu/ZnO-based catalysts is greater than over a Cu-based catalyst [97–99].

Concerning the acidic catalyst, performances of many materials have been explored in the open literature. Zeolites (for instance H-ZSM5, Theta-1, mordenite and ferrierite) and γ-alumina are the most investigated catalysts for dehydrating MeOH to DME [42,100–102]. Bonura et al. have recently revealed that ferrierite is one of the most promising acidic catalyst for this purpose, compared to mordenite and H-ZSM5 [100]. The number, the distribution and the strength of the acidic sites are the most important features of these catalysts [101,103]. Generally, an increase in acidic sites uniformly distributed on the surface of the material causes an increase in DME yield. Furthermore, some authors have shown that weak and medium strong acid sites are active in methanol dehydration; however, some correlation between the increase in DME yield and the higher concentration of strong acidic sites have been reported [90,93,100,101,103].

In the open literature, many synthesis techniques have been explored in order to obtain hybrid catalysts for direct CO_2 hydrogenation to DME. The most common techniques are physical mixtures, coprecipitation and wet impregnation [42,90,100]. Each technique has many issues that must be considered, for instance, the control of synthesis conditions and their repeatability, the composition and the distribution of the metallic load on the surface of the acidic catalyst, the dimensions of the particles and their homogeneity. Some authors have reported that metals could be greatly dispersed, obtaining a high Cu metallic surface area; however, few studies have investigated the deactivation phenomena that involve the catalysts during on-stream operating conditions [56,91,102,104].

Concerning DME production, Chapter 7 is dedicated to the development of innovative hybrid catalysts for direct CO_2 hydrogenation to dimethyl-ether in a one-step process. Prof. Francesco Frusteri and Dr. Giuseppe Bonura from CNR-ITAE of Messina have provided us with hybrid catalysts based on copper, zinc, zirconia and ferrierite obtained with different synthesis techniques (co-precipitation, impregnation and mechanical mixing). These catalysts were characterized and experimentally tested. The tests were performed by varying both the space velocity and the reaction temperature. In addition, calcined and aged catalysts were characterized with different techniques: N_2 physisorption, temperature programmed reduction (H_2-TPR), NH_3 pulse chemisorption, X-ray diffraction (XRD), ICP-MS, FESEM, EDS, X-ray photoelectron spectroscopy (XPS) and TEM measurements.

1.2.3. Hydrocarbons

For the sake of completeness, there are other PtF technologies for producing light and heavy hydrocarbons through the CO_2 hydrogenation. On the one hand, for instance, the Fischer-Tropsch (FT) process has been investigated to produce hydrocarbons. More in detail, the two-steps process that involves a RWGS reactor for producing syngas and a conventional FT reactor for obtaining hydrocarbons has been examined [105–107]. However, researchers are developing catalysts for directly converting CO_2 and H_2 to hydrocarbons in a one-step FT reactor [108–110]. The direct conversion seems to be a promising process that still requires efforts to be optimised and implemented [111]. On the other hand, other technologies are based on the methanol synthesis such as Methanol-to-Olefins (MtO) or Methanol-to-Gasoline (MtG) [112–114]. The study of these technologies is out of the scope of this thesis work; however, they are processes that complete the overview of PtF technologies on which researchers are carrying out in-depth studies to reduce CO_2 emissions, use RES for replacing fossil energy sources and fuel the closed carbon cycle.

Chapter 2

Techno-economic modelling of a Power-to-Gas system based on SOEC electrolysis and CO_2 methanation in a RES-based electric grid

The techno-economic analysis presented in this chapter was published as [3]:

Salomone, F.; Giglio, E.; Ferrero, D.; Santarelli, M.; Pirone, R.; Bensaid, S. Techno-economic modelling of a Power-to-Gas system based on SOEC electrolysis and CO_2 methanation in a RES-based electric grid. *Chem. Eng. J.* **2019**, *377*, 120233, doi: 10.1016/j.cej.2018.10.170.

2.1. Introduction

As explained in Section 1.1, the awareness of climate change and the need to develop alternative energy sources have led to a significant growth of the RES. In Europe, they have reached about 30 % in 2017 [2]. As an example, Germany is the world's second and third largest producer of solar and wind power, respectively; and it is also the seventh largest producer of electricity in the world [1]. Furthermore, RES exhibited a rapid growth in recent years, which could not be ignored in terms of the energy balance of the electric grid.

One of the greatest challenges is the power grid management, caused by the greater penetration of the RES, often presenting an intermittent and unpredictable profile of their electric productivity. For this reason, there are periods of high renewable electric production followed by periods which are characterized by the lack of renewable electric production. For the purpose of avoiding either power supply overloads or blackouts, the electric energy has to be stored in a stable and efficient way. It could be subsequently used either to repower the electric network or also for many other applications depending on the type of storage.

Currently, great importance has been given to the study of the PtG systems coupled to the intermittent RES-based electric production, which is also the topic on which this chapter focuses. As described in Subsection 1.2.1, a PtG system consists of two coupled sections: the electrolysis and the methanation unit. The first one produces hydrogen (H_2) through the electrolysis of water (H_2O) and it is powered by electricity. While the second one is a catalytic reactor system that converts a mixture of hydrogen and carbon dioxide (CO_2) into synthetic natural gas (SNG), mainly composed by methane [115].

Existing research recognises the critical role played by several technical and economic aspects of both the PtG technology and process. In fact, many researchers and companies are currently working on a large number of PtG projects [16,19,20]. Several researchers have investigated the coupling of PtG technology with RES-based power grids in some European countries [116,117]. For example, Danish [118], German [18,119–121], Irish [122], Italian [123], Portuguese [124], Romanian [125] and Spanish [126,127] current and future scenarios have been examined: on the one hand, different energy profiles have been considered, depending on the prevalence of the wind or photovoltaic power production; on the other hand, the integration of the PtG technology with electric and transport sectors and its feasibility have been analysed in the literature dealing with the decarbonization of the society.

This work is focused on the behaviour of a PtG plant based on solid oxide electrolysis cells (SOEC) operating with an electric residual profile (ERP) of a future scenario based only on RES (case study Germany 2050 [117]). The selection of SOEC as core technology for the electrolyser stems from the higher electrolysis efficiency of this technology as compared to alternative ones [8–11], coupled to the extremely convenient heat integration between steam generation for electrolysis and methanation heat rejection, that leads to extremely high PtG overall efficiencies (as will be later described). In addition, the optimal arrangement of a PtG plant in the presence of both chemical (hydrogen tank and steam drum) and electrochemical (accumulators) storage facilities, is also considered. Accordingly, techno-economic assessments on the behaviour of the PtG plant arrangement coupled with the case study scenario are discussed for the purpose of highlighting the most critical aspects of the system.

2.2. Methodology

2.2.1. PtG plant description

The HTE-based PtG plant consists of two main sections: a high-temperature electrolyser (HTE), made by several SOEC modules, and a methanation unit, which is a tightly thermally integrated system of catalytic reactors [8,14,18,25,119,126,128]. Furthermore, the PtG plant could also include both chemical and electrochemical storage. Figure 2.1 illustrates a simplified scheme of the PtG plant. The water evaporates within the methanation unit recovering the heat of reaction and then it is fed to the SOEC electrolyser which is powered by electricity. H_2 and CO_2 are fed to the methanation unit for producing SNG that has to be purified to achieve NG grid specifications. As schematized in Figure 2.2 [25], the integrated PtG plant is moderately complicated and it will be presented and explained in detail in the further paragraphs.

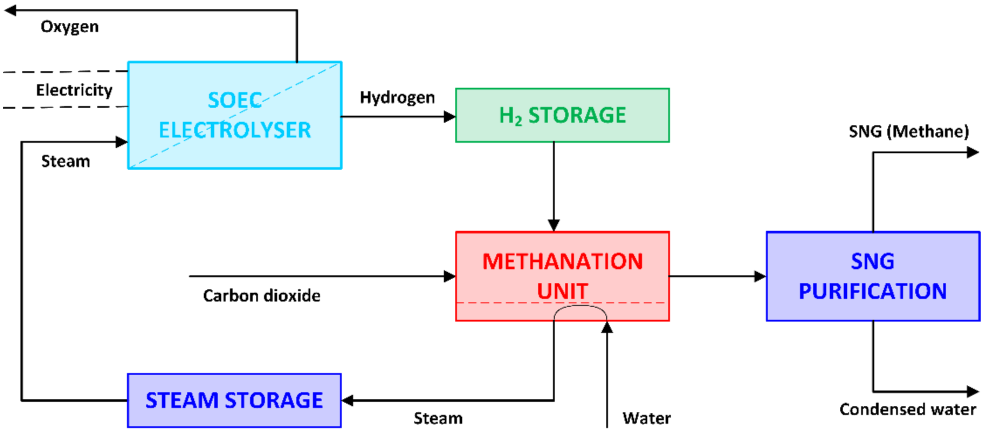

Figure 2.1. Simplified scheme of the integrated SOEC-based Power-to-Gas plant.

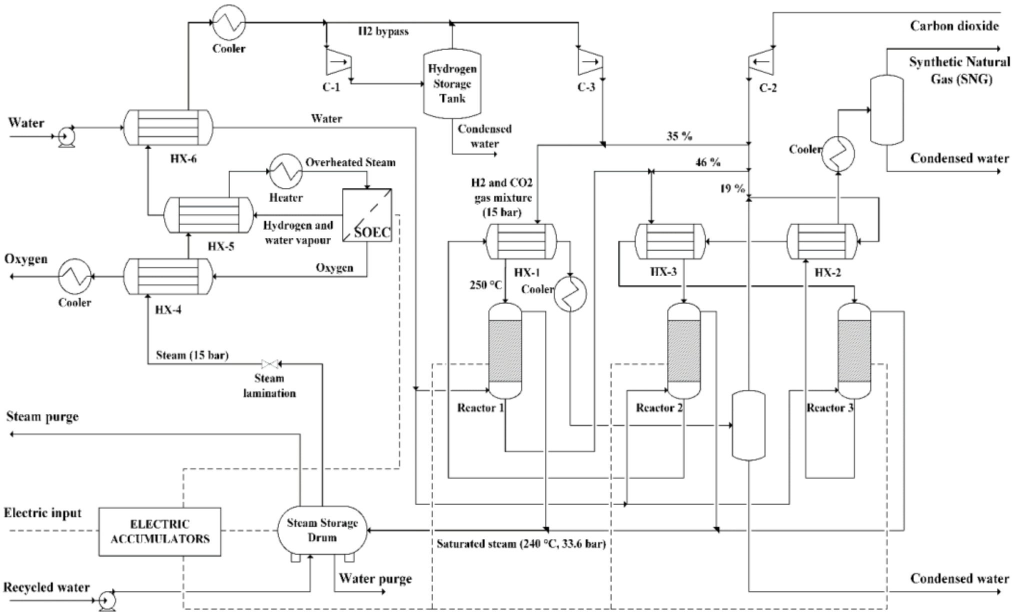

Figure 2.2. Overview of the integrated SOEC-based Power-to-Gas plant scheme.

SOEC electrolysers and methanation

The first section of the PtG plant involves an electrolyser, which consists of high-temperature solid oxide electrolysis cells (SOEC). The SOEC technology is suitable for large stationary systems, in accordance with [12]. A single SOEC cell consists of a cathode and an anode, which are separated by an electrolyte [129–131]. The electrolyte is a ceramic material whose characteristics are thermal stability and resistance and notable efficiency in oxygen anions conduction (O^{2-}) at high temperatures [10,12]. The SOEC equipment could operate between 700 °C and 1000 °C and it could be pressurized [12]. Indeed, the superheated steam is fed to the cathode at 800 °C and 15 bar [25]. The greatest advantage of the SOEC technology is related to a high theoretical power-to-hydrogen efficiency (considered as the ratio between the produced H_2 chemical power on LHV basis and the DC electric input to the electrolyser, without including the steam generation), which can be even 100%, if the equipment works at the thermoneutral point [8,12]. The SOEC is one of the best available technologies for water electrolysis, but it is not yet a mature technology [12]. The overall water electrolysis reaction involved in the SOEC is presented in equation (2.1) [8,12].

$$2\ H_2O_{(g)} \rightleftarrows 2\ H_{2(g)} + O_{2(g)} \qquad \Delta\widetilde{H}^0_{298.15} = +285.8\ \text{kJ/mol} \qquad (2.1)$$

The second main section of the PtG plant involves the methanator, in which the methanation reaction occurs on a catalyst, for instance Ni/Al_2O_3 [24,26–28,132], in a temperature range of 250 °C to 700 °C. The reactors are conceived as tube-bundles vertically arranged [25]. The refrigerating medium is evaporating water at 240 °C and 33.6 bar [25]. In this work, temperature profiles and catalyst deactivation phenomena were not considered. The CO_2 is mixed with the H_2-rich process gas streams in three different steps in order to control the reaction temperature profile, reduce the amount of catalyst and optimize the CO_2 conversion, as evidenced in a previous research [25]. In addition, the gas streams are cleverly thermally integrated to recover the heat in the outlet streams of the reactors, preheat the inlet ones and condensate the water moisture between the second and the third reactor [25]. Moreover, all the high-temperature equipment (e.g. SOEC-based electrolyser, reactors and steam drum) is thermally insulated in order to minimize heat losses, and it could be maintained in hot standby conditions by means of electric power to balance the estimated heat dissipations. Besides, the length of the third reactor is designed to reach a SNG quality of at least 95 % of methane on dry molar basis, thus the overall CO_2 conversion is at least 98.9 % [25,122].

Within the reactors many different reactions may occur due to the reactant species that are formed [12]. The major reaction is the hydrogenation of carbon dioxide (CO_2) (2.2) [12], which is the desired reaction for methane production; in fact, the reactants are fed into stoichiometric ratio H_2/CO_2 equal to 4.

$$CO_{2(g)} + 4\ H_{2(g)} \rightleftarrows CH_{4(g)} + 2\ H_2O_{(g)} \qquad \Delta\widetilde{H}^0_{298.15} = -165.1\ \text{kJ/mol} \qquad (2.2)$$

Carbon dioxide sources

One of the two main chemical reactants of the PtG process is carbon dioxide (CO_2), which must be a continuous source, even if the PtG plant may operate in intermittent conditions. The CO_2 source has to be very pure in order to avoid unexpected deactivation of the catalyst [21] and ensure the SNG quality. CO_2 could be captured from various sources, as the exhaust gases of large industries (ammonia and cement plants), biogas-to-biomethane upgrading plants, alcoholic fermentation plants (breweries, wineries and distilleries) or ambient air [14,17]. The choice of the CO_2 source is based on two aspects: the first is the cost of the CCS process, while the second is linked to the location of the PtG plant. In fact, the biogas-to-biomethane upgrading plants are probably the best choice for coupling with the P2G system, because they provide a very pure continuous stream of CO_2 and are located near both the electric grid and the gas distribution network. Instead the use of exhausted gases requires more expensive CCS treatments and purification, but they have huge flow rates. Finally, the CCS from the ambient air releases the P2G plant from the location and the size; however, the costs are extremely high. In Germany, each biomethane plant produces from 0.38 kt/y to 37.4 kt/y of CO_2 depending on the plant size; hence, the PtG plant capacity coupled with them can vary between 0.28 MW and 27.6 MW [14,25,133]. Nevertheless, the Energie Park in Güstrow is the largest biogas-to-biomethane upgrading plant in Germany, emitting about 53.6 kt/y of CO_2: it might be thus coupled with a 39.6 MW P2G plant [133,134].

Hydrogen stream and electrochemical storage

The PtG system could have an intermittent operation linked to the electric grid fluctuations. For this reason, intermediate chemical storage may be necessary. A hydrogen storage tank may be needed to dissociate the electrolyser from the methanator. It is positioned between these two sections and should be filled primarily to guarantee enough H_2 to the reactors, even when the SOEC is kept in standby mode during electrical deficits. Furthermore, the H_2 tank could reduce flow and pressure fluctuations by acting as a buffer. Both the SOEC and the methanator operate at 15 bar [25], whereas the H_2 storage could be carried out at higher pressures to reduce the storage volume. Thus, two compressors may be necessary: the first is placed before the H_2 tank to fill it; while the second is placed downstream the H_2 tank to ensure complete emptying.

The catalytic reactors are cooled with evaporating water at 240 ° C and 33.6 bar, which was chosen to refrigerate the reactors and to not condensate water vapour through the throttling valve [25]. Subsequently, the saturated vapor is overheated with an electric heater and, eventually, it is injected into the electrolyser. In this configuration, the strongly exothermic reaction releases a great amount of heat, which is used for the vaporization of water; this step requires a large quantity of energy. Thus, a steam drum could be useful as a water vapour reserve when the electrolyser is operating at higher loads than the methanator. However, the steam could condense during long periods of deficit due to thermal dissipations. Furthermore, in this case, compressors are not provided because the vaporizing pressure (33.6 bar) is higher than the SOEC working pressure (15 bar). Therefore, a heating system of the steam drum is needed to compensate the heat dissipations when the internal pressure drops below the minimum pressure (15 bar). Moreover, it is also useful in order to produce additional steam, when the steam production is lower than the SOEC steam demand.

All the items of equipment could be maintained in hot standby mode when a deficit period occurs. Therefore, an electrochemical storage should be taken into account in order to compensate all heat losses. The energy has to be recovered when intense spikes occur, for the purpose of absorbing also the excess of surplus energy, which could not be exploited by the electrolyser. Furthermore, a specific electrochemical technology was not selected because this research field is currently undergoing strong development. There are many possible technologies that could be applied to support PtG systems (e.g., lithium ion, vanadium redox flow or lithium polysulfide batteries) [135,136].

2.2.2. Model assumptions

This work aims to study the behaviour of a PtG system coupled with an intermittent RES-based electric residual profile (ERP). As will be detailed in Section 2.2.4, the ERP is the difference between the electric production profile and the electric consumption profile. The difference between production and consumption is normally near zero for balancing the electric grid. However, the balance of the electric grid could not to be verified increasing the RES penetration; therefore, surplus and deficit periods must be compensated for avoiding electric issues. Furthermore, the reduction of greenhouse gas emissions and a switch to RES-based electric supply system seem to be important goals for Germany in the next years [117]. Moreover, the distribution of the different RES technologies in Germany is extremely wide and, in the reference works, the forecast of future scenarios is carefully detailed [117]. In 2016, the average RES production in the European Union is 17.4 %, while in Germany is approximately 14.8 % and it has been increasing following the targets [137]. For the purpose of performing the best technical, economical and managemental plant assessment, an algorithm of the PtG system model was developed in MATLAB environment. The only input of the model is the ERP on the network for a certain period of time. In this study, an ERP for the whole year in Germany in 2050 based on meteorological data in 2016 was considered [117,138]. Concerning the simulation, the EPR profile has to be regularly discretized, for instance in 15-minute intervals, since the data were obtained from the ENTSO-E databank [138]. Furthermore, the algorithm could require some additional parameters, which describe the PtG plant arrangement and its operating conditions. These parameters will be analysed and optimized by means of some sensitivities. The following part of this chapter moves on to present and explain in detail all the assumptions of the model.

SOEC electrolyser

A SOEC could work in thermoneutral conditions, which means that the net heat flux is zero at the thermoneutral voltage, as was adequately discussed in a previous work [8]. For this reason, all the electrical energy, that is absorbed by the SOEC, is converted into chemical energy, which is contained into H_2 molecules. Thus, the thermoneutral operating condition of the electrolyser was assumed in order to reach a 100 % electrolysis efficiency (η_{SOEC}) [8]. However, the SOEC requires a AC/DC rectifier, which efficiency ($\eta_{AC/DC}$) was assumed to be 98 % [8]. The power-to-H_2 yield (η_{el_H2}) was related to the absorbed power from the electric grid (P_{el}, MW) and to the produced H_2 molar flow ($\dot{n}_{H2}$, kmol/s) by means of equation (2.3); where MW_{H2} is the H_2 molar weight (kg/kmol), LHV_{H2} is the hydrogen lower heating value (MJ/kg) and P_{SOEC} is the useful power of the SOEC (MW).

$$\eta_{\mathrm{el\_H2}} = \eta_{\mathrm{SOEC}} \cdot \eta_{\mathrm{AC/DC}} = \frac{\dot{n}_{\mathrm{H2}} \cdot MW_{\mathrm{H2}} \cdot LHV_{\mathrm{H2}}}{P_{\mathrm{SOEC}}} \cdot \frac{P_{\mathrm{SOEC}}}{P_{\mathrm{el}}} \tag{2.3}$$

The electrolyser section consists of a certain number of SOEC modules (n_M), which is determined according to the nominal power of the PtG plant. The considered geometry of a single SOEC module consists of 6 SOEC stacks (n_S), each one consisting of 8 SOEC blocks (n_B); this configuration is similar to other existing SOEC modules [139]. In this work, cells with an active area of 260 cm^2 (A_{act}) have been considered: this is an intermediate value among those available in the literature [140,141]. A power density of 400 mW/cm^2 (σ_P) is assumed [141]. Moreover, a minimum partial load of a single module ($f_{M,min}$) of 50 % was assumed [9,142], thus the arrangement of a single module is a relevant feature in order to ensure a good compromise between rangeability and heat losses of the SOEC equipment. For these reasons, the number of cells (n_C) stacked in a SOEC block depends on the nominal power of the SOEC module. The power of a single SOEC module (P_M, MW) is evaluated by means of equation (2.4); the depth (L_1, cm), the height (L_2, cm) and the width (L_3, cm) of the module are calculated by using equations(2.5), (2.6) and (2.7), respectively. In this work, a 0.3 cm cell thickness (e_C), a 5 cm stack endplate thickness (e_{ep}), a 2.6 cm inactive cell space (e_{inact}), a 2 cm stack space for manifolds (e_{stack}) and a 30 cm insulation thickness (e_{ins}) are assumed [140]. Finally, the total external surface area of all the modules (A_{ext}, m^2) is evaluated by means of equation (2.8); where the number of modules (n_M) is calculated as the ratio between the P2G plant capacity and the SOEC module power and it is approximated by excess.

$$P_{\mathrm{M}} = n_{\mathrm{C}} \cdot n_{\mathrm{B}} \cdot n_{\mathrm{S}} \cdot A_{\mathrm{act}} \cdot (\sigma_{\mathrm{P}} \cdot 10^{-9}) \tag{2.4}$$

$$L_1 = n_{\mathrm{C}} \cdot e_{\mathrm{C}} + 2 \cdot e_{\mathrm{ep}} + 2 \cdot e_{\mathrm{ins}} \tag{2.5}$$

$$L_2 = n_{\mathrm{B}} \cdot \left(\sqrt{A_{\mathrm{act}}} + 2 \cdot e_{\mathrm{inact}} + 2 \cdot e_{\mathrm{stack}}\right) + 2 \cdot e_{\mathrm{ins}} \tag{2.6}$$

$$L_3 = n_{\mathrm{S}} \cdot \left(\sqrt{A_{\mathrm{act}}} + 2 \cdot e_{\mathrm{inact}} + 2 \cdot e_{\mathrm{stack}}\right) + 2 \cdot e_{\mathrm{ins}} \tag{2.7}$$

$$A_{\mathrm{ext}} = 2 \cdot n_{\mathrm{M}} \cdot (L_1 \cdot L_2 + L_2 \cdot L_3 + L_1 \cdot L_3) \cdot 10^4 \tag{2.8}$$

The cells number within a SOEC block was selected in order to have 5 SOEC modules. This choice was made taking into account that the methanation unit consists of catalytic reactors, which are generally not modular; thus, their rangeability is more limited than that of the electrolyser [25]. On the one hand, a greater number of modules implies a wider rangeability; on the other hand, it causes higher thermal losses. Furthermore, the electrolyser and the methanator should be faultlessly coupled together, and their minimum partial load should be able to be the same. Therefore, a minimum partial load of about 10 % seemed to be a good compromise to ensure the coupling between the two items of equipment, also considering a broader rangeability of multitube reactors [25].

As far as the steam is concerned, it is superheated at 800 °C and is fed to the cathode side of the electrolyser [25]; then the electrolysis reaction occurs and hydrogen (H_2) is produced at the cathode side, while oxygen (O_2) is produced at the anode side. The steam conversion (*SC*) within the electrolyser was assumed to be 85 %; in the literature, steam conversion up to 90 % is reported [143], which should be taken as the technical limit of the equipment. Indeed, the overpotential dramatically increase, if the steam conversion is too high. The cause should be related to a low steam concentration in the final section of the electrolyser; thus, the mass transfer phenomena are slow due to the small amount of reactant. Saturated steam is sent to the electrolyser, which operates at 15 bar, but it is produced at higher pressure in the reactors (33.6 bar). Therefore, it has to be expanded through an adiabatic throttling valve. This process is isoenthalpic with a positive Joule-Thompson coefficient [25], thus, the temperature decreases as the pressure drops. More in detail, saturated steam does not condense through the throttling process between the two conditions [25].

Thermal insulation

All high-temperature devices are thermally insulated; heat losses ($\dot{Q}$, MW) could be evaluated by means of equation (2.9), in which the thermal conductivity (k, $Wm^{-1}K^{-1}$) refers to a microporous insulation material [140,144], resisting at high temperatures.

$$\dot{Q} = \frac{k \cdot 10^{-4}}{e_{\mathrm{ins}}} \cdot A \cdot (T_{AIR} - T_{IN}) \tag{2.9}$$

In equation (2.9), A is the heat exchange area (m^2), T_{AIR} is the external air temperature (20 °C for each equipment) and T_{IN} is the temperature of the internal surface (800 °C for the SOEC electrolyser, and 240 °C for the reactors and the steam drum). In this work, external temperature profiles, due to convection and diffusion, and geometrical curvatures were not considered. In addition, the thermal conductivity is temperature dependent, for that reason an average value of the panel temperature is assumed. The thermal conductivity (k, $Wm^{-1}K^{-1}$) of the material is evaluated by means of the equation (2.10) [140,144], where T (K) is the absolute temperature of the material.

$$k = 1.875 \cdot 10^{-8} \cdot T^2 - 7.488 \cdot 10^{-6} \cdot T + 0.0224 \tag{2.10}$$

Methanation section

The CO_2 hydrogenation is a strongly exothermal reaction; hence, only a fraction of the H_2 chemical energy is converted into CH_4 chemical energy. Thus, a methanation efficiency ($\eta_{\mathrm{H2\_SNG}}$) can be defined according to equation (2.11); where $\dot{n}_{\mathrm{H2,in}}$ is the H_2 molar flow (kmol/s) at the inlet of the first reactor, $\dot{n}_{\mathrm{H2,out}}$ and $\dot{n}_{\mathrm{CH4,out}}$ are the H_2 and the CH_4 molar flow (kmol/s) at the outlet of the last reactor, respectively. In addition, MW_{CH4} is the methane molar weight (kg/kmol), LHV_{CH4}

is the methane lower heating value (MJ/kg), ν_{H2} and ν_{CH4} are the H_2 and CH_4 stoichiometric parameters, respectively.

$$\eta_{\mathrm{H2\_SNG}} = \frac{\dot{n}_{\mathrm{CH4,out}} \cdot MW_{\mathrm{CH4}} \cdot LHV_{\mathrm{CH4}} + \dot{n}_{\mathrm{H2,out}} \cdot MW_{\mathrm{H2}} \cdot LHV_{\mathrm{H2}}}{\dot{n}_{\mathrm{H2,in}} \cdot MW_{\mathrm{H2}} \cdot LHV_{\mathrm{H2}}} \tag{2.11}$$

More specifically, about 83 % of the H_2 energy is converted into CH_4 energy, while about 17 % is released as reaction heat. The calculation was made according to equation (2.12), which was derived from equation (2.11); besides, ζ_{CO2} is the overall CO_2 conversion within the methanation section of the PtG plant. In this work, it was assumed to be at least 98.9 % for the purpose of achieving the SNG quality [25], as earlier mentioned. Furthermore, H_2 and CO_2 were fed in stoichiometric ratio, which is equal to 4.

$$\eta_{\mathrm{H2\_SNG}} = (1 - \zeta_{\mathrm{CO2}}) + \frac{\nu_{\mathrm{CH4}} \cdot \zeta_{\mathrm{CO2}} \cdot MW_{\mathrm{CH4}} \cdot LHV_{\mathrm{CH4}}}{\nu_{\mathrm{H2}} \cdot MW_{\mathrm{H2}} \cdot LHV_{\mathrm{H2}}} \tag{2.12}$$

The methanation section of the PtG plant consists of three multi-tube fixed bed reactors. According to a previous work [25], the geometrical parameters of the reactors can be estimated. Only the number of tubes should change by varying the P2G plant capacity, if all the other conditions would not change, because only the reactant gas mixture flow rate was varied [25]. According to equation (2.9), the external surface of each reactor is a key parameter to estimate the heat losses, External surface depends on the diameter and length of the reactors; also, in this case, a 30 cm thickness of insulating material was assumed.

PtG process efficiencies

In the PtG system, a nominal efficiency of the process (η_N) is defined according to equation (2.13); the numerator represents the SNG chemical energy obtained through the PtG process, whereas the denominator represents the total amount of energy, which is needed to run the PtG plant in a base case arrangement. In more detail, this PtG plant consists of a SOEC electrolyser, a methanator, a CO_2 compressor, a water pump and an electric heater; thus, no storage is considered.

$$\eta_N = \frac{\sum_{\mathrm{i=1}}^{\mathrm{N}} \left(\dot{n}_{\mathrm{CH4,out,i}} \cdot MW_{\mathrm{CH4}} \cdot LHV_{\mathrm{CH4}} + \dot{n}_{\mathrm{H2,out,i}} \cdot MW_{\mathrm{H2}} \cdot LHV_{\mathrm{H2}} \right) \cdot t_{\mathrm{i}}}{E_{\mathrm{SOEC}} + E_{\mathrm{heater}} + E_{\mathrm{compr}} + E_{\mathrm{steam}}} \tag{2.13}$$

E_{SOEC} is the total energy absorbed by the electrolyser (MJ), E_{heater} is the energy absorbed by the electric heater to overheat the steam (MJ), E_{compr} represents the energy spent for the compression (MJ) and E_{steam} is the energy which is required to produce saturated steam when the methanator does not provide all the steam required by the electrolyser. Moreover, N is the number of steps in which the year was divided and t_i is the time duration of each step (s).

The PtG plant could not operate continuously, if it is coupled with an intermittent RES-based electric residual profile (ERP). For this reason, the amount of energy spent during standby periods had to be considered, because all high temperature devices were maintained in hot standby condition. In addition, the presence of chemical and electrochemical storage was taken into account. The overall efficiency of the PtG process (η_{OV}) was defined according to equation (2.14).

$$\eta_{\mathrm{OV}} = \frac{\sum_{\mathrm{i=1}}^{\mathrm{N}} \left(\dot{n}_{\mathrm{CH4,out,i}} \cdot MW_{\mathrm{CH4}} \cdot LHV_{\mathrm{CH4}} + \dot{n}_{\mathrm{H2,out,i}} \cdot MW_{\mathrm{H2}} \cdot LHV_{\mathrm{H2}} \right) \cdot t_{\mathrm{i}}}{E_{\mathrm{SOEC}} + E_{\mathrm{heater}} + E_{\mathrm{compr}} + E_{\mathrm{h,SOEC}} + E_{\mathrm{h,MET}} + E_{\mathrm{drum}} - E_{\mathrm{H2,tank}} - E_{\mathrm{batteries}}} \tag{2.14}$$

The total amount of energy absorbed both by the electrolyser ($E_{\mathrm{h,SOEC}}$, MJ) and by the catalytic reactors ($E_{\mathrm{h,MET}}$, MJ), when the pieces of equipment are maintained in hot standby configuration, was estimated according to equation (2.9). Moreover, E_{drum} represents the total amount of energy (MJ) absorbed by the steam drum to both compensate heat losses and vaporize water. This consumption was required in order to avoid the depressurization of the steam drum (no steam compression was considered). $E_{\mathrm{H2,tank}}$ represents the H_2 chemical energy (MJ) contained between the initial and final state of the H_2 storage tank (LHV basis). Similarly, $E_{\mathrm{batteries}}$ represents the energy (MJ) accumulated in the batteries between the initial and final state of the simulation.

Methane could be used to repower the electric grid, for instance in a thermoelectric power plant. The repowering efficiency of a Gas-to-Power plant ($\eta_{\mathrm{SNG\_el}}$) is assumed to be 45 %, even considering further improvement of the existing technologies [145].

Finally, another important parameter of the PtG plant is the plant utilization factor (*PUF*), which represents the exploitation of the PtG plant coupled with the ERP during the entire year. This parameter is evaluated according to equation (2.15), in which E_{SNG} is the total amount of energy produced as SNG during the year ($\mathrm{MWh_{SNG}}$, LHV basis) and P_{P2G} is the P2G plant capacity (MW).

$$PUF = \frac{E_{SNG}}{8760 \cdot P_{\mathrm{P2G}}} \tag{2.15}$$

Compression and pumping power consumption

CO_2 stream is compressed from 1 bar to 15 bar; whereas hydrogen was compressed from 15 bar to the maximum storage pressure (for instance 60 bar might be assumed), when the H_2 tank was filling. When the H_2 tank was emptying (i.e., the pressure is below 15 bar), the stored H_2 is compressed up to 15 bar. Therefore, for gas mixtures, the compression energy (E_{compr}, MJ) was calculated according to equation (2.16) [146].

$$E_{\mathrm{compr}} = \sum_{j=1}^{N_C} \sum_{\mathrm{i=1}}^{\mathrm{N}} Z_j \cdot R \cdot T_{\mathrm{1,i,j}} \cdot \frac{\gamma_j \cdot \eta_{\mathrm{compr,j}}}{\gamma_j - 1} \cdot \left[\left(\frac{p_{\mathrm{2,i,j}}}{p_{\mathrm{1,i,j}}} \right)^{\frac{\gamma_j - 1}{\gamma_j \cdot \eta_{\mathrm{compr,j}}}} - 1 \right] \cdot \dot{n}_{\mathrm{in,i,j}} \tag{2.16}$$

In this correlation, Z is the compressibility factor, R is the molar ideal gas constant ($0.008314\ \mathrm{MJ \cdot kmol^{-1} \cdot K^{-1}}$), γ is the heat capacity ratio and η_{compr} is the compression efficiency, which was set at 70 % (considered constant for all centrifugal compressors) [146]. $T_{\mathrm{1,i,j}}$ (K) and $p_{\mathrm{1,i,j}}$ (bar) are the temperature and the pressure at the inlet of the j-th compressor at the i-th time step, respectively; and lastly, $p_{2,i,j}$ (bar) is the pressure at the outlet of the equipment. Moreover, N_C is the number of compressors, and lastly, $\dot{n}_{in,i,j}$ is the molar flow of the gas mixture at the inlet of the j-th compressor at the i-th time step. For liquid water the pumping energy was neglected due to the extremely low specific power [146].

Electrochemical and chemical storage sizing

The electrochemical storage capacity depends on both the required power during the deficit periods and their duration. The size of the accumulators was evaluated by creating a profile of both charges and discharges of the batteries during all the simulation. Then, the electrochemical storage capacity corresponds to the difference between the maximum and the minimum values of that profile. Moreover, a 90 % total efficiency of the accumulators was assumed [147].

During deficit periods, the methanator could operate at the minimum power load. Thus, stored H_2 can be used to feed the reactors. Hence, the H_2 storage tank was sized in order to feed the methanation unit for a certain number of hours (H_2 storage time, t_{H2}, h) at minimum load. Hydrogen storage capacity (V_{H2}, kmol) was evaluated according to equation (2.17), which was obtained using previous equations(2.3), (2.4), (2.11) and (2.12).

$$V_{H2} = \frac{\nu_{H2} \cdot \eta_{el\_H2} \cdot \left(\eta_{H2\_SNG} + \zeta_{CO2} - 1\right)}{\nu_{CH4} \cdot \eta_{AC/DC} \cdot \zeta_{CO2} \cdot MW_{CH4} \cdot \ LHV_{CH4}} \cdot f_{M,min} \cdot P_M \cdot t_{H2} \cdot 3600 \qquad (2.17)$$

Furthermore, the steam storage capacity (V_{H2O}, m^3) was calculated by means of equation (2.18), taking into account that the stored steam has to completely fill the H_2 tank. In addition, it could work between two conditions, because no steam compressors are considered. When the steam storage is full, the temperature is 240 °C ($T_{VAP,max}$, 513.2 K) and the pressure is 33.6 bar ($p_{VAP,max}$, 3.36 MPa); whereas, when the steam storage is considered empty, the temperature is 198.4 °C ($T_{VAP,min}$, 471.6 K) and the pressure is 15 bar ($p_{VAP,min}$, 1.5 MPa). Equation (2.18) was obtained with the ideal gas approximation; however, the phase equilibrium was implemented in the model with the Van der Waals equation.

$$V_{H2O} = \frac{V_{H2} \cdot R \cdot T_{VAP,max} \cdot T_{VAP,min}}{SC \cdot \left(p_{VAP,max} \cdot T_{VAP,min} - p_{VAP,min} \cdot T_{VAP,max}\right)} \qquad (2.18)$$

Saturated steam (produced through the methanation cooling) can be partly stored in the steam tank and partly sent to the electrolyser. The steam tank should have a relatively large volume, so the thermal dissipations should not be neglected. Thus, heat losses could be estimated by means of equation (2.9); the amount of condensed water can be thus evaluated via the enthalpy balance [148]. Moreover, the vapour-liquid equilibrium of water was estimated by means of the Van der Waals equation and the modified Riedel equation [148].

2.2.3. Economic analysis

An economic evaluation is extremely useful to compare different configurations of the PtG plant coupled with the same ERP, because the price of the product clearly explains the economic competitiveness of the process. Therefore, both the capital and the operating costs of the PtG plant were estimated, as will be described in the following paragraphs.

Levelized cost of product

The economic analysis allows a cost of product (*COP*, €/$\mathrm{MWh_{SNG}}$) to be calculated; similarly, a levelized cost of product (*LCOP*, €/$\mathrm{MWh_{SNG}}$) can be evaluated in order to express the price of the SNG. These two quantities could vary considerably at the variation of some relevant feature of the P2G process. Equation (2.19) shows the relationship between the two variables, where *IR* is the inflation rate, which was reasonably assumed to be 2 %, and *TH* is the time horizon of the economic assessment, which was prudently defined as 20 years [8,149].

$$LCOP = \frac{COP}{TH} \cdot \sum_{t=1}^{TH} (1 + IR)^t \tag{2.19}$$

The main assumption to evaluate the *LCOP* is that the net present value (*NPV*, €) is zero at the end of the time horizon. The *NPV* could be expressed as the difference between the total plant investment (*TPI*, €) and the sum of the discounted cash flows over the time horizon. Hence, the *NPV* is defined according to equation (2.20), where *DR* represents the discount rate, which was assumed to be 10 %, and CF_t (€/y) is the cash flow in the t-th year [8,146,150].

$$NPV = -TPI + \sum_{t=1}^{TH} \frac{CF_t}{(1 + DR)^t} \tag{2.20}$$

The cash flow could be evaluated as the difference between the revenues and the costs as shown in equation (2.21); where E_{el} ($\mathrm{MWh_{el}}$) is the amount of electric energy absorbed by the whole P2G plant during the whole t-th year, *LCOE* is the levelized cost of electricity (€/$\mathrm{MWh_{el}}$) and *O&M* represents the operating and maintenance cost (€/y) over the whole t-th year [8].

$$CF_t = E_{SNG} \cdot LCOP - O\&M - E_{el} \cdot LCOE \tag{2.21}$$

Operating and maintenance (O&M) cost

O&M cost represents the sum of costs related to maintenance (C_M, €/y), operating labour (C_{OL}, €/y), replacement (C_R, €/y), raw materials (H_2O and CO_2) (C_{RM}, €/y) and waste treatment/disposal (C_{WT}, €/y), according to equation (2.22) [8,150].

$$O\&M = C_M + C_{OL} + C_R + C_{RM} + C_{WT} \tag{2.22}$$

Maintenance and insurance costs were estimated to be as 3 % of the total plant investment [8]; these costs are linked to equipment repairs, inspections, authorisations, local taxes and other overhead costs. Operating labour cost is low due to highly automatization of the P2G plant, thus a single specialized operator was considered [8]. The methanation catalyst is stable at low temperatures, but its degradation might be quite fast at high temperatures [28], which could be reached in the reactors due to the strong exothermic reaction [25]. Therefore, an yearly catalyst replacement was supposed [8]. In addition, the SOEC cells are also affected by degradation [8], thus a replacement of the SOEC stacks was considered over the time horizon. This replacement was estimated as the 60 % of the total module cost of the SOEC electrolyser because only stacks and enclosures were substituted [8]. The waste disposal is linked to the catalyst replacement and the liquid treatment of condensed water, which may contain dissolved gases and catalytic particles [8]. Lastly, the carbon dioxide price strongly depends on the purity and distance of the CO_2 source [8,18]. The operating and maintenance assumptions are summarized in Table 2.1 [8,18]; in this work, an average exchange rate (E_R, €/$) equal to 0.8459 €/$ was assumed, which corresponds to the mean value between January 1999 and May 2018 [151].

Table 2.1. Data of the operative and maintenance costs.

Maintenance and insurance cost	% TPI	3.0
Operator labour cost	€/operator/y	63443
Catalyst replacement rate	Times/y	1
Catalyst price	€/m^3	29.88
SOEC stacks replacement rate	Times/20y	1
SOEC stacks replacement cost	€	60 % TMC_{SOEC}
Carbon dioxide price	€/t	3.38 – 50.75
Demineralized water price	€/t	0.85
Waste treatment and disposal	€/t	13.73
Surplus electric energy price	€/MWh_{el}	4.05 – 10.77
Deficit electric energy price	€/MWh_{el}	46.69 – 62.00

Electricity cost

The estimation of the levelized cost of electricity (*LCOE*, €/MWh_{el}) could be very difficult because projections of its future price are not straightforward. Moreover, a RES-based electric input is characterized by both surplus and deficit periods, thus the electricity price is influenced by these events. Therefore, the levelized cost of electricity was estimated starting from the unitary spot price of electricity data of the Energinet between 2014 and 2017 [152]. The price of electricity was based on percentiles of the spot price profile, which were defined as the ratio between the number of events that have a value below the threshold and the number of total events. Therefore, a percentage range from 3 % to 7 % was considered, for the cost of surplus electricity; while the band from 93 % to 97 % was assumed for the cost of electricity in deficit periods. The results of the calculation are reported in Table 2.1.

Total plant investment

The total plant investment (*TPI*, €) represents the sum of the total module costs of each item of equipment (*TMC*, €), which are installed into the P2G plant [146,150,153]. The total module cost (TMC_j, €) in a generic j-th year depends on the purchase module cost (PMC_i, \$) of a piece of equipment in a reference i-th year and on many economic and technical factors: material, labour, specific characteristics, indirect costs, contingency, fee and economic indexes [8,146,150,153]. In the literature, there are many correlations in order to evaluate the cost of existing and mature technologies, for instance compressors, vessels, pumps, heat exchangers and reactors. Whereas, the cost of innovative and laboratory scale technologies is very difficult to estimate: in this work learning curves were thus used.

Cost estimation of mature technologies

The total module cost (TMC_j) of existing and mature pieces of equipment could be estimated by means of equation (2.23) according to the literature [8,146,150,153].

$$TMC_j = E_R \cdot \frac{I_j}{I_i} \cdot PMC_i \cdot F_{BM} \cdot (1 + \alpha_C + \alpha_F) \tag{2.23}$$

I_j and I_i represent the economical indexes (CEPCI, Chemical Engineering Plant Cost Index), which consider the inflation rate between the i-th and the j-th years, F_{BM} is the bare module factor, which is evaluated according to equation (2.24) [8,150], α_C and α_F are the contingency and fee factors, respectively. Moreover, the exchange rate (E_R, €/\$) between euro and dollar was considered.

$$F_{BM} = B_1 + B_2 \cdot F_P \cdot F_M \tag{2.24}$$

B_1 and B_2 are bare module constants for a specific equipment, F_M is the material factor and F_P is the pressure factor. On the one hand, the material factor only depends on the construction material and data are available in the literature [150]. On the other hand, the pressure factor depends on both the operating conditions and the item of equipment. Therefore, equation (2.25) [8,150] was used to calculate the pressure factor of heat exchangers, heaters and compressors; where z_1, z_2 and z_3 are pressure factor parameters, which are different for each piece of equipment, and p is the operative pressure (barg) of the system.

$$log_{10}(F_P) = z_1 + z_2 \cdot log_{10}(p) + z_3 \cdot [log_{10}(p)]^2 \tag{2.25}$$

Instead, the correlation (2.26) [8,150] for estimating the pressure factor in case of vessels is completely different due to the geometry of the equipment.

$$F_P = \frac{\frac{(p+1) \cdot D}{2 \cdot w \cdot \sigma + 1.2 \cdot p} + c_A}{s_{min}} \tag{2.26}$$

D represents the diameter of the vessel (m), w is the weld efficiency, σ is the maximum allowable stress of the material (bar), c_A is the corrosion allowance (m) and s_{min} is the minimum wall thickness (m).

In addition, the purchase module cost of an item of equipment was estimated by means of equation (2.27) [150]; in which k_1, k_2 and k_3 are purchase module cost constants, while S represents the size of the piece of equipment.

$$log_{10}(PMC) = k_1 + k_2 \cdot log_{10}(S) + k_3 \cdot [log_{10}(S)]^2 \tag{2.27}$$

Finally, according to the literature [150], the correlations for the cost estimation of mature technologies depends on cost indexes and factors. The chemical engineering plant cost index (CEPCI) was 397 in 2001 (reference year), while it was 573 in December 2017 [154]. Finally, both contingency and fee factors were supposed equal to 0.20. In conclusion, all the values of the parameters, that were assumed, are summarized in Table 2.2.

Table 2.2. Economic data for all items of equipment.

Equipment	Unit	Equipment factors			Pressure factors and parameters			Bare factors		Material factors (F_M)			
	S	k_1	k_2	k_3	z_1	z_2	z_3	B_1	B_2	CS/CS	CS/SS	SS/SS	Ni/Ni
Heat exchanger	m^2	4.8306	-0.8509	0.3187	-0.00164	-0.00627	0.0123	1.63	1.66	1.00	-	2.70	3.70
Reactor	m^2	4.8306	-0.8509	0.3187	-0.00164	-0.00627	0.0123	1.63	1.66	-	1.80	-	-
Compressor	kW	5.0355	-1.8002	0.8253	0	0	0	0	1.00	2.40	-	-	-
	S	k_1	k_2	k_3	σ	w	c_A	B_1	B_2	CS/CS	CS/SS	SS/SS	Ni/Ni
Horizontal vessel	m^3	3.5565	0.3776	0.0905	850	0.7	0.00315	1.49	1.52	-	-	3.10	-
Vertical vessel	m^3	3.4974	0.4485	0.1074	850	0.7	0.00315	2.25	1.82	1.00	-	-	-
	Unit	Exponent		Reference price		Reference market		Future market			Experience rate		Experience rate error
	S	a		C_k		G_k		G_j			r_e		e_e
Electrolyser	MW	0.907		5700000		1		181			0.28		0.16
Batteries	MWh	0.95		347000		2.5		367.5			0.16		0.08

Cost estimation of a SOEC electrolyser

The SOEC technology is strongly under development and it seems to be very promising in future applications such as in PtG systems. SOEC is not yet a commercial technology, thus, its cost estimation is a very difficult and relevant issue, because SOEC is an extremely expensive system. However, according to Schmidt et al. [9], the cost estimation of solid oxide electrolytic cells could be made by means of a learning curve, which is based on the growth of the market. Thus, further technical research and commercialization play a key role in determining the price of the SOEC technology. The SOEC specific price (C_j, €/MW) in the j-th was estimated according to equation (2.28), which considers a production scale-up in the future [9]. The SOEC specific price was about $5.7 \cdot 10^6$ €/MW in 2015 (C_k) [9]; moreover, G_j and G_k represent the total cumulative production (GW) of SOEC modules in the j-th year and in the k-th reference year, respectively. The cost projection made by Schmidt et al. [9] stopped in 2030, but in this work, a cost projection in 2050 is needed. Thus, a 5 GW/y SOEC yearly production was assumed between 2030 and 2040, then a 10 GW/y yearly production was hypothesized until 2050. Moreover, in agreement with these authors [9], a 28 % experience rate (r_e) and a 16 % experience rate error (e_e) were considered.

$$C_j = C_k \cdot \left(\frac{G_j}{G_k}\right)^{-(r_e \pm e_e)} \tag{2.28}$$

The total module cost of an electrolyser can be then estimated by means of equation (2.29); where a represents a size exponential parameter, estimated by elaborating data of Schmidt et al. [9], and set equal to 0.907. S is the SOEC electrolyser power capacity (MW). These economic assumptions are indicated in Table 2.2.

$$TMC_j = C_j \cdot S^a \tag{2.29}$$

Cost estimation of accumulators

Accumulators are a mature technology for small dimensions, but research and development in this sector is constantly advancing. Some interesting types of batteries are lithium ion batteries, vanadium oxide flow batteries and lithium polysulfide batteries [135]. In this work, a specific technology of accumulators was not selected; but according to Seungbum and Gallagher [135], a future state of the accumulators cost could be estimated. Therefore, a learning curve was assessed in order to predict the future price of electrochemical systems, which might be used for grid storage [135]. Similarly to the SOEC price evaluation, the estimation of the price of accumulators was made by means of equation (2.28); in which the specific price of the accumulators in 2014 (reference year) was assumed equal to $0.347 \cdot 10^6$ €/MWh [135]. In addition, a production scale-up was hypothesized; more in detail, a 2.5 GWh/y was assumed between 2014 and 2020, then a 5 GWh/y was considered for the next ten years, after that an annual production of 10 GWh/y was taken onto account between 2030 and 2040, and eventually, a 20 GWh/y yearly production was assumed until 2050. Furthermore, a 16 % experience rate and a 8 % experience rate error were hypothesized for a conservative evaluation and according to future cost projections, which are present in the literature [135,136,155]. Finally, the total module cost of accumulators was calculated by means of equation (2.29), where C_j is the price of accumulators in the j-th year (€/MWh), S is the size of the batteries (MWh) and a represents the size exponential factor, which was conservatively hypothesized equal to 0.95. All the economic data are presented in Table 2.2.

2.2.4. Case study scenario: Germany 2050

The renewable energy sources have been grown in many countries recently, but Germany is one of the most relevant European countries in which a great increase in RES installations is expected in the next years [117]. According to the German Federal Environment Agency [117], a future scenario in Germany 2050 was chosen. The scenario consists of a projection of the national energy balance in Germany 2050, and it was based on the German meteorological data in 2016 [117,138]. Moreover, the scenario was exclusively based on RES, which are geothermal, hydroelectric, biomass, wind and photovoltaic. The PtG plant has to be coupled with an ERP; thus, both electric production and electric consumption profiles had to be forecasted taking into account both the RES installed capacity and the meteorological data.

Electric residual profile

An ERP could be predicted in 2050 by means of both recent electric production and load profile. Indeed, these profiles are available in the ENTSO-E database [138] for 2016, which was arbitrary assumed as the reference meteorological year of the scenario. The PtG plant has to be coupled with an ERP, which could be forecasted by means of the electric grid data and forecasts of the German Federal Environment Agency [117,138]. Therefore, the production power profile in 2050 was evaluated proportionally to the installed power capacity of each RES, according to equation (2.30).

$$P_{\mathrm{P,2050,i}} = P_{\mathrm{P,2016,i}} \cdot \frac{P_{\mathrm{I,2050}}}{P_{\mathrm{I,2016}}} \tag{2.30}$$

$P_{\mathrm{P,2050,i}}$ and $P_{\mathrm{P,2016,i}}$ represent the produced power (MW) of a single RES in 2050 and in 2016 (reference year) at a specific i-th time of the year, respectively. Whereas, $P_{\mathrm{I,2050}}$ and $P_{\mathrm{I,2016}}$ are the installed power capacity (MW) of that RES in 2050 and in 2016, respectively.

According to the German Federal Environment Agency [117], the electric load on the grid should not change considerably between 2016 and 2050, because the consumes should be reduced by the energy optimizations, while they should be increased by the growth in electric vehicles and industrial activities [117]. Hence, the electric load profile ($P_{\mathrm{L,2050}}$, MW) in 2050 was assumed to be the same as that in 2016.

Therefore, the national ERP ($P_{\mathrm{R,2050}}$, MW) in Germany 2050 was evaluated as the difference between the electric generation profile in 2050 and the electric load profile in 2050. Finally, a local ERP was estimated, considering that the largest CO_2 source from biogas plants in Germany is the Energie Park in Güstrow, which emits 53.6 kt/y of CO_2 [134]; this site could be coupled with a 39.6 MW P2G plant, as earlier discussed. For this reason, a 0.04 % scaling factor of the profile was calculated, taking into account that the most intense spike of the local profile has a maximum value of 40 MW; instead, the highest peak of the national profile has a value of about 100 GW. For instance, this means that the projected national ERP may be equally distributed among 2500 P2G plants; however, a real local ERP depends on both the geographic position and the electric grid limitations, which were neglected in the case study scenario.

2.2.5. Algorithm of the PtG model

One of the aims of this work is the development of a model to simulate the behaviour of a PtG plant coupled with a RES-based intermittent ERP. Subsequently, technical and economic assessments of the results were performed in order to highlight advantages and disadvantages of the analysed configurations. The algorithm was developed in MATLAB environment and steady-state conditions were considered for each time step of the electric input; thus, no transient behaviours of the single equipment were explored.

SOEC electrolyser and electrochemical storage management

The local ERP was the input of the PtG algorithm and the SOEC electrolyser can operate only between the minimum and the maximum power (from about 10 % to 100 %). Hence, three management configurations were considered: the first condition is a high electric power availability; the second one is an electric power availability comparable to the electrolyser power; and the last one is extremely low or no electric power availability.

In the first case, the electrolyser can work at its maximum power because all the other electric supplies, both auxiliary consumptions and heat losses, were compensated by the electric surpluses. Furthermore, the accumulators could be recharged recovering more available electricity, if the batteries were not completely charged. In the second case, the electrolyser can operate at partial load because the available electricity is used to power both the electrolyser and the auxiliaries and to compensate thermal dissipations. Moreover, the accumulators were neither recharged nor discharged because all the available surpluses were exploited by the PtG plant. In the third case, the electrolyser was maintained in hot standby configuration due to the lack of electric energy. During deficit periods, heat losses were compensated by means of accumulators or using deficit energy, which was assumed as existing. However, the electrolyser could operate for a certain amount of time (SOEC deficit coverage period) during the initial part of deficit periods, if the accumulators could power it. Finally, the accumulators could be partially recharged, if a very low amount of surplus energy, below the minimum partial load, was available. As far as this part of the PtG model is concerned, the algorithm is outlined in Figure 2.3.

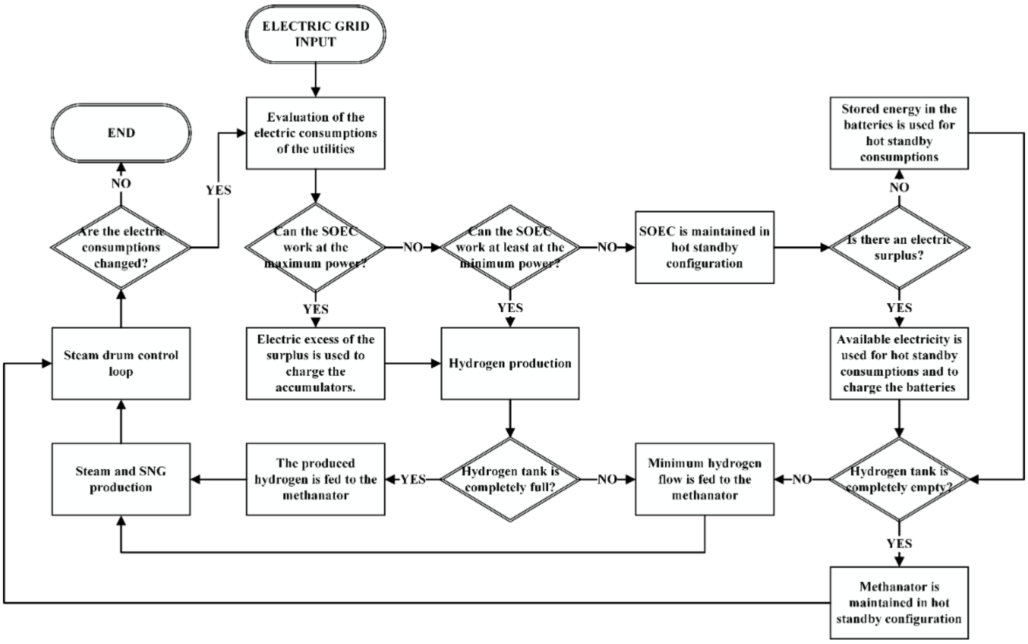

Figure 2.3. Flowchart of the PtG plant model.

Methanation unit and hydrogen storage management

The electrolyser produces hydrogen, which could be used in different ways depending on both the hydrogen storage filling fraction and the electrolyser load. The methanation section is always operating when the electrolyser is producing H_2, thus at least the minimum H_2 flow is sent to the reactors to allow them to work at least at the minimum partial load. Furthermore, the priority H_2 tank filling condition was assumed; it means that the methanator works at the minimum partial load until the H_2 tank is completely filled. This configuration was chosen to ensure that the H_2 tank was almost certainly completely full at the beginning of a deficit period. Hydrogen could be sent directly to the H_2 storage either through a bypass until the pressure within the H_2 tank is equal to the SOEC operative pressure (15 bar), or through a compressor, if the H_2 tank pressure is higher.

On the contrary, hydrogen could be continuously fed to the methanator until the H_2 tank is completely empty (atmospheric pressure inside the tank), even if the electrolyser is maintained in hot standby configuration. The minimum H_2 flow could be sent directly to the methanator though a bypass until the H_2 tank pressure is equal to the methanator operative pressure (15 bar); otherwise, it has to be compressed, if the pressure within the H_2 storage is lower. Eventually, hydrogen was mixed with the CO_2 compressed stream in order to produce SNG within the reactors. This second part of the PtG model is also illustrated in Figure 2.3.

Steam storage management

The three reactors are cooled by means of evaporating water. The saturated steam can be directly fed to the electrolyser, if no steam storage is considered in the PtG plant arrangement. On the other side, the water vapour could be sent in the steam tank. Some steam condenses within the H_2O storage because of heat losses;

thus, an electric heater may be needed in two different conditions. In the first case, some additional steam had to be produced, when the SOEC partial load was strongly higher than the methanator partial load, and the pressure within the tank was at the minimum value (15 bar). However, in the second case, the H_2O drum pressure was decreasing due to condensation until the lowest pressure (15 bar), when a deficit period occurred; then, the H_2O storage was maintained in hot standby equilibrium at 15 bar and 198.4 °C.

2.2.6. Sensitivity analyses

In order to elucidate the effects of the coupling between the ERP and the PtG plant, some sensitivity analyses were performed. Both technical and economic aspects were investigated at the variation of the PtG plant capacity between 1 MW and 20 MW, considering the absence of all the storage. Then the effects of the presence of an electrochemical storage were evaluated by varying the SOEC deficit coverage period from 0 h to 24 h. This range was made due to the duration of the night, in which photovoltaic cannot generate power because of the absence of sun radiation. Finally, to decouple the electrolyser and the methanation unit, chemical storage was considered with a variation of the H_2 storage time ranging from 0 h to 12 h.

2.3. Results and Discussion

2.3.1. RES-based local electric residual profile

According to both the German Federal Environment Agency [117] and the ENTSO-E [138], the RES installed power should increase significantly in the future years. Only the hydroelectric production may not change because hydroelectric exploitation may be already completely developed. Table 2.3 shows the substitution of RES-based power production for fossil energy sources between 2016 and 2050; moreover, the national energy balance is also provided. According to Table 2.3, RES produce about 35 % of the annual energy in 2016, but daily peaks can currently reach higher productions due to photovoltaic. Besides, the electric load should not rise in the future because of two different trends: electric consumption optimization and electric vehicle penetration [117].

Table 2.3. Installed power and energy balance in Germany both in 2016 and 2050.

	Installed power in 2016 (GW) [138]	Installed power in 2050 (GW) [117]	Energy balance in 2016 (TWh) [138]	Energy balance in 2050 (TWh)
Biomass	6.61	23.3	35.5	125.1
Geothermal	0.05	6.4	0.05	6.4
Hydroelectric	12.93	13.0	22.6	22.7
Photovoltaic	38.99	120.0	33.8	104.0
Wind off-shore	3.26	45.0	11.7	161.5
Wind on-shore	39.94	60.0	62.7	94.2
Traditional	97.3	-	309.7	0.0
Total energy production	-	-	476.05	514

Total load on the electric grid	-	-	476.05	476
RES production	-	-	166.35	514
RES energy fraction (%)	-	-	34.9	100

The local ERP in Germany 2050 was the input of the PtG plant model, and the shape of the ERP caused some relevant effects on the results; thus, the main crucial aspects must be described. Firstly, Germany is divided in two main parts: photovoltaic generation is prevailing in the south of the state; while, wind power is predominant in the north. As illustrated in Figure 2.4, the local ERP is characterized by a high frequency of oscillation (363 oscillations during the entire year), and the surplus spikes are sometimes very intense. These features are mainly caused by the photovoltaic generation, which is concentrated during the day; more in detail, the most intense production is around 1:00 p.m. whereas, no photovoltaic generation is present during the night. Furthermore, the electric load profile has a weekly periodicity, but it has not a wide range of oscillation [33,126,138]. For these reasons, the ERP has a daily frequency of oscillation. Nevertheless, a more uniform power generation and a lower oscillation frequency distinguish wind power production [118,125,138]. In addition, the ERP shows a seasonal trend, in fact, photovoltaic has strong intense spikes during summer (between April and September); while, wind power is prevailing during winter (from October to March). Thus, the summer oscillation frequency is higher than the winter one due to weather conditions during different seasons.

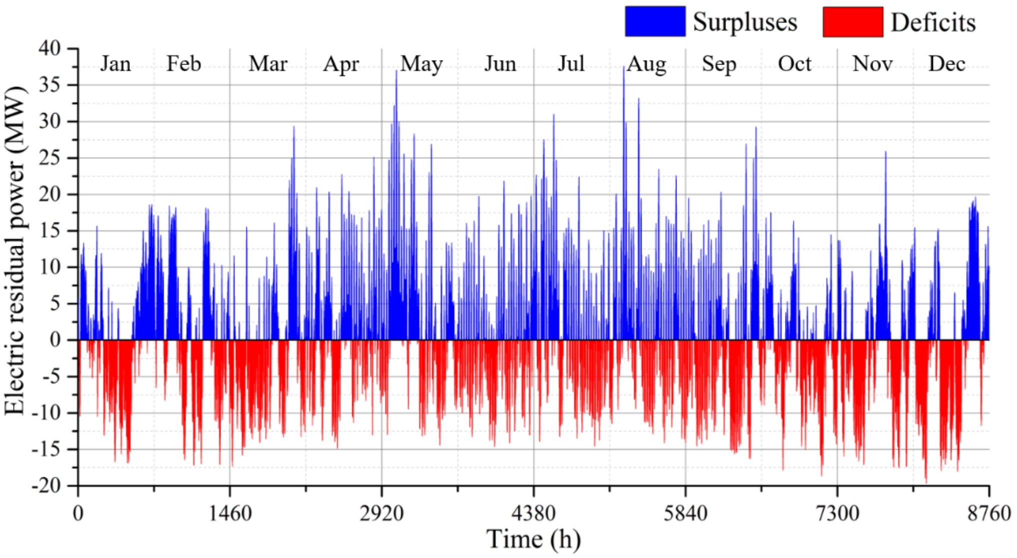

Figure 2.4. Local electric residual profile in Germany 2050.

The local ERP is a mixed RES-based intermittent input, in which photovoltaic and wind power are the main sources of electric generation. The ERP features certainly should have consequences on the coupling between the PtG plant and the ERP. More specifically, the intensity and the duration of the surplus spikes could determine the PtG plant capacity and the SNG productivity. Moreover, they should have effects on both the efficiency and the exploitation of the PtG plant.

Furthermore, the oscillation frequency should have relevant effects on both the electrolyser and the methanator management. Finally, the total amount of surplus energy is 34.2 GWh, which is greater than the amount of deficit energy (about 29.8 GWh); while, the number of oscillations between surplus and deficit is 363.

2.3.2. PtG plant model

As illustrated in both Figure 2.5a and Figure 2.5b, the results of a simulation have to be discussed for the purpose of better clarifying and understanding all the aspects of the PtG system coupled with the local ERP. A case study depicted in Figure 2.5a and Figure 2.5b, exemplifies the behaviour of the PtG plant, which was coupled with the local ERP. In detail, a 7 MW PtG plant capacity was considered, both a SOEC deficit coverage and a hydrogen storage time of 6 h were assumed and a 36.57 MWh size of the accumulators was considered (they ensure no electricity requirement from the grid during deficits). Subsequently, the main power profiles should be described in different conditions of the ERP, as Figure 2.5a shows between the end of March and the beginning of April. This time interval highlights the differences between extended periods of surplus residual energy and short intermittent ones. On the one side, an intense wind power generation results in long surplus periods, in which the PtG plant could operate continuously. Therefore, the electrolyser and the methanator work perfectly coupled together at the same partial load; recovering a large amount of energy and exploiting both the PtG plant and the ERP to the best possible. On the other side, short periodic intermittent spikes are a consequence of the daily photovoltaic power production; thus, in this case, storage plays an important role. In fact, an electrochemical storage could be used to recover a large amount of surplus energy, and to operate for a certain period at the minimum partial load during the deficit periods, which was defined as SOEC deficit coverage period.

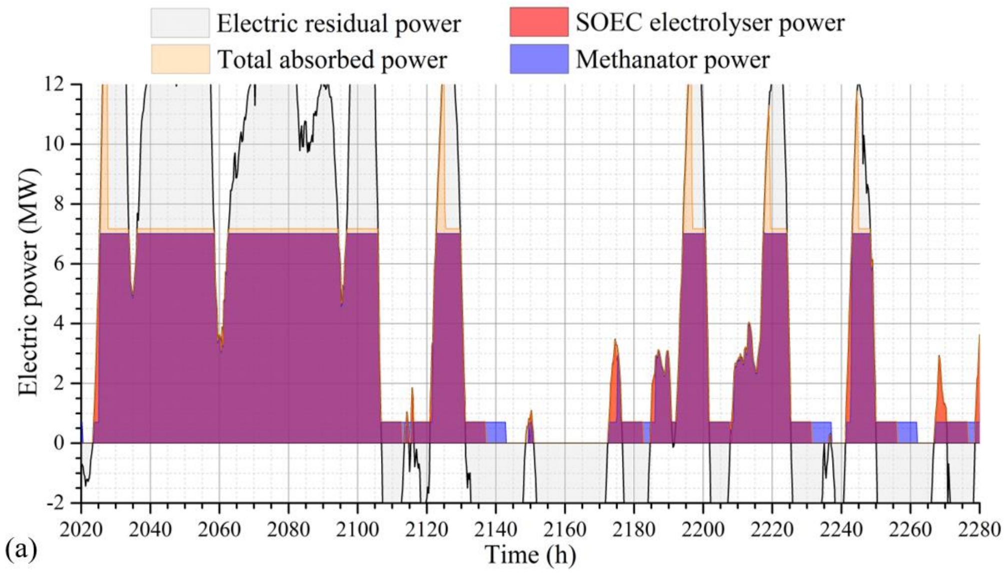

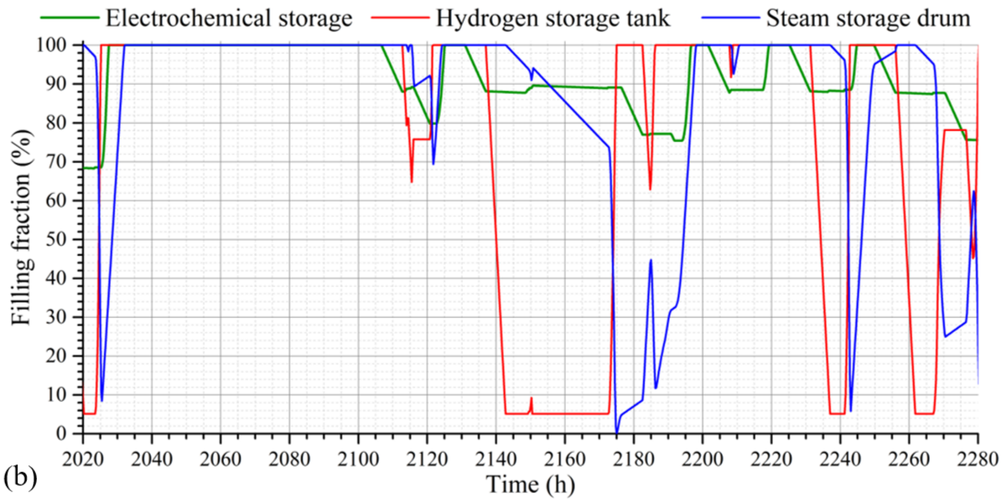

Figure 2.5. Results of a PtG plant simulation between the end of March 2050 and the beginning of April 2050. A 7 MW PtG plant capacity, both a SOEC deficit coverage period and a H_2 storage time of 6 h and a 36.57 MWh electrochemical storage size were considered. (a) Electric power profiles of the local EPR, of both the SOEC electrolyser and the methanator load and of the total absorbed power; (b) charge and discharge profiles of both electrochemical and chemical storage.

More in detail, the electrolyser starts to operate immediately when a surplus spike occurs, if it can work at least at the minimum power load. Similarly, the methanation unit operates at the minimum load during the H_2 tank filling. Then, when the H_2 tank is completely full, the methanator works at the same partial load of the electrolyser until a deficit occurs. After that, the SOEC operates at the minimum load, if the accumulators can power it. During the SOEC deficit coverage period the two main pieces of equipment run at the same minimum power load until that period is over. Afterwards, the electrolyser is maintained in hot standby configuration, while the methanation unit continues to operate powered by the H_2 stored in the tank until it is empty. Eventually, the methanator is switched in hot standby mode when the stored H_2 is finished. This PtG management implies that the PtG plant is maintained in hot standby mode only if the two periods of time are over. Therefore, the number of shutdowns of the equipment would markedly drop, if both the SOEC coverage period and the H_2 storage time increased. Finally, the total absorbed power is greater than the SOEC absorbed power due to all auxiliary consumptions of the PtG plant, such as electric heater, compressors and thermal losses.

As far as the accumulators are concerned, they are rapidly discharged during the SOEC deficit coverage period (minimum load about 10 %); whereas, they are slowly discharged during the hot standby periods (e.g. heat losses are around 15 kW in this case study). However, the electrochemical storage is recharged in two different situations: on the one hand, they are quickly recharged when an intense surplus spike occurs; on the other hand, they are partially recharged when a very small peak of surplus appears. This arrangement allows the PtG plant to recover a greater amount of energy and increase both the SNG productivity and the plant utilization factor.

In a real case, the electric residual profile might be predicted thanks to weather forecast and electric load anticipations. However, these aspects could not be quantified; thus, they were not considered. For this reason, the PtG model was constructed to work step by step without considering any type of anticipations. Therefore, in this case study, the electrochemical storage is not completely discharged among a deficit period because a 6 h SOEC deficit coverage was selected. But the accumulators could be completely discharged, if there are many deficit periods alternating with slightly intense surplus spikes. Due to the low intensity of the surpluses, the batteries are not recharged; but they are progressively discharged when a deficit occurs, as illustrated in Figure 2.5b.

Finally, with respect to the chemical storage, the most interesting aspects of Figure 2.5b are the profile of charge and discharge of both the H_2 tank and the steam drum. In fact, they seem to be coupled together. More clearly, what stands out in the profile is that often a filling of the H_2 tank corresponds to an emptying of the steam drum and vice versa. The steam drum is emptied when the electrolyser is turned on; moreover, the methanation unit operates at the minimum load, thus the H_2 tank is filled until it is full. Then the items of equipment work perfectly coupled and all the excess of steam is accumulated in the steam storage. At the end of the SOEC deficit coverage period, the electrolyser is turned off, while the methanation unit continues to work using the stored H_2 until the buffer is empty. Afterwards, the methanation section is switched off and the PtG plant is maintained in hot standby configuration. Meanwhile, the pressure within the steam drum starts to diminish due to condensation.

These results provide important insights into both the behaviour of the PtG plant and the interactions between all the pieces of equipment. Furthermore, the coupling of different PtG plant with the ERP was not discussed yet. Indeed, this was a qualitative assessment of the PtG plant behaviour, but a quantitative evaluation will be needed to understand clearly the coupling of a RES-based electric input with a PtG plant. In the next chapters, a technical and economic evaluation will be performed to achieve these objectives.

2.3.3. PtG plant sizing

An important aim was to determine the best PtG plant capacity, which had to be coupled with the local ERP in Germany 2050. In this first analysis, a PtG plant without both electrochemical and chemical storage was considered. Figure 2.6 compares the efficiencies of the PtG system at the variation of the PtG plant capacity. As can be seen, the overall LHV-based efficiency increases slightly from 76.4 % to 77.0 % as the PtG plant capacity rises, and it is close to the nominal value of 77.4 % [28]. This should be probably related to the greater SNG productivity and a lower growth of the heat losses (from 6 kW at 2 MW to 15 kW at 20 MW installed PtG plant). Accordingly, the increase in SNG productivity prevails over the greater amount of energy required by the hot standby periods. More in detail, this operative configuration is needed to start immediately all the PtG items of equipment when a surplus spike occurs. This hypothesis is adequate because the main devices work at high temperature; thus, a cold start-up would require a long period of time due to the thermal inertia. Instead, a hot start-up of the plant is much quicker. However, the PtG plant dissipates heat, which must be compensated with auxiliary energy.

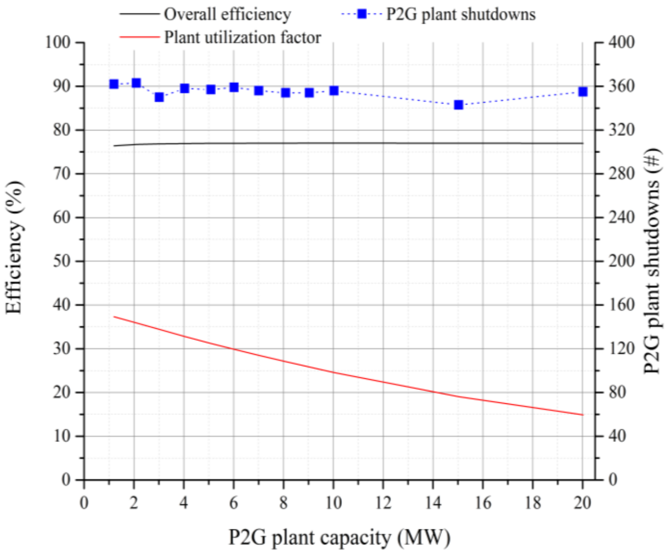

Figure 2.6. Efficiencies and number of shutdowns of PtG plants without any storage at the variation of the PtG plant capacity.

On the contrary, the PtG plant utilization factor decreases significantly from 37 % to 15 % if the PtG plant capacity expands from 1 MW to 20 MW, as can be seen from Figure 2.6. Small PtG plants are appropriately exploited because the minimum load of the electrolyser is low. Nonetheless, the ERP is certainly not suitably exploited, if the PtG plant capacity is too small. The best compromise is thus a larger PtG plant capacity, which allow many surplus spikes to be adequately recovered, increasing the SNG productivity.

Finally, the SOEC electrolyser and the methanator are faultlessly coupled together; thus, the number of shutdowns (corresponds to the number of times in which the equipment is maintained in hot standby mode) is equal for both the equipment. The number of shutdowns is around 360, corresponding to an average of once a day. This feature is strongly linked to the local ERP and to the intermittent photovoltaic power generation, as previously mentioned.

The criterion for choosing the optimal PtG plant capacity was the minimum value of the average levelized cost of product (LCOP), which was calculated using the estimated specific costs in 2050. This economic assessment is crucial because the SNG productivity has a monotonous rising trend at the variation of the PtG plant capacity, as depicted in Figure 2.7, whereas the average LCOP (the LCOP band represents the uncertainty on capital and operating costs) shows a minimum, resulting from two opposite effects.

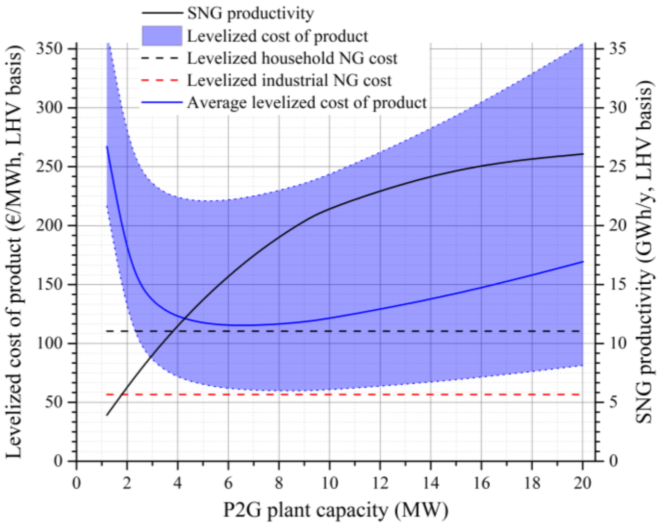

Figure 2.7. SNG productivity (LHV basis) and levelized cost of product (LCOP) based on specific costs in 2050 (average specific costs are 1330 €/kW for SOEC, 27.07 €/t for CO_2, 8.71 €/MWh_{el} for surplus electric energy and 50.92 €/MWh_{el} for deficit electricity).

On the one hand, both the capital and operative costs of the PtG plant increase as the PtG plant capacity rises, due to the larger size of all the items of equipment. On the other hand, the SNG productivity rapidly increases as the PtG plant capacity rises. However, the SNG productivity reaches a maximum threshold because very intense spikes are rare, and most of the surplus energy is already recovered by the PtG plant. In addition, the minimum intensity of the recovered spikes is greater if the PtG plant capacity increases, due to the SOEC rangeability. For all these reasons, the LCOP is high at low PtG plant capacity due to the small SNG productivity; while at high PtG plant capacity, the LCOP increases because the SNG productivity is roughly constant. Therefore, in this case study scenario, the optimal PtG plant capacity, which should be coupled with the local ERP, is 7 MW, with a SNG productivity of about 1289 t/y (17.5 GWh/y, LHV basis). The LCOP varies between 0.81 €/kg (60.2 €/MWh, LHV basis) and 3.03 €/kg (224.9 €/MWh, LHV basis). This price range of the SNG is partially compatible with the current prices of industrial (0.77 €/kg; 56.70 €/MWh, LHV basis) and household (1.50 €/kg; 110.36 €/MWh, LHV basis) fossil natural gas (NG) [23]. Consequently, the PtG process could be economically competitive, if the SOEC technology, which is the most expensive equipment of the PtG plant (between 61.3 % and 89.3 % of the TPI), will be improved.

Currently, SOEC is one the best available technology for power-to-H_2 process due to its high efficiency at the thermoneutral point [20]. Nevertheless, it is a small-scale technology, thus its cost is still very high [24]. In addition, as illustrated in Figure 2.8, the SOEC market projections (2180 €/kW, 1665 €/kW and 1330 €/kW in 2030, 2040 and 2050, respectively) are uncertain in the future [24], and this fact results in a wide range of costs (e.g. between 579 €/kW and 3055 €/kW in 2050).

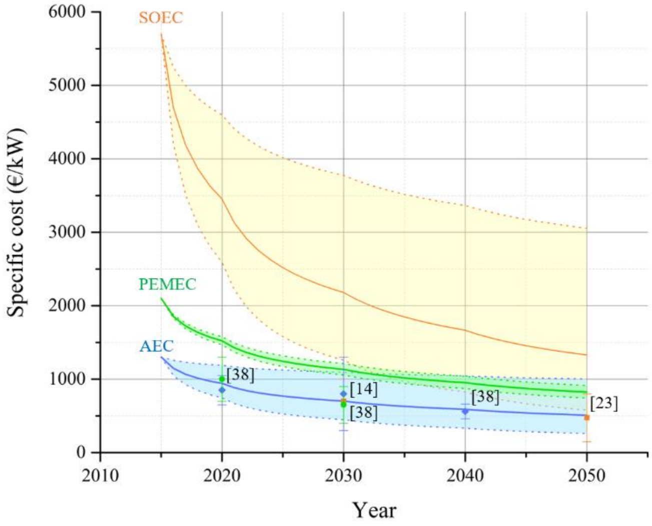

Figure 2.8. Comparison of the specific costs of SOEC-based, AEC-based and PEMEC-based electrolysers between 2015 and 2050 using a production scale-up in annual market projection (1 GW/y until 2020, 2.5 GW/y until 2030, 5 GW/y until 2040 and 10 GW/y until 2050). According to Schmidt et al. [9], experience rates are 28 ± 16 % for SOEC, 18 ± 13 % for AEC and 18 ± 2 % for PEMEC.

The HT-based PtG plant is completely different from LT-based systems, which operate at about 80 °C [24], due to thermal integration, high heat requirement and high costs of the SOEC technology. For this reason, it could be useful compare the LCOP of SNG obtained from HT-based PtG plants with SNG synthetized in LT-based processes to assess the economic competitiveness. Therefore, a power-to-hydrogen efficiency of 65 % (LHV basis) for both AEC and PEMEC electrolysers was assumed [24], [38], [71]; the scheme of the methanation unit was maintained to ensure a CO_2 conversion of at least 98.9 %, but without the equipment related to the heat integration.

As far as projected costs are concerned, the specific costs of both AEC and PEMEC electrolysers for the future (2015-2050) were evaluated similarly to the SOEC one. The results of these projections are illustrated in Figure 2.8, which were obtained according to Schmidt et al. [24]. A sensitivity analysis on the installed power capacity ranges from 1 MW to 20 MW of a simplified and not optimized LT-based PtG system model has been highlighted that the SNG productivity varies between 2.6 GWh/y and 17.4 GWh/y (LHV basis), as depicted in Figure 2.9. This fact is caused by the lower power-to-hydrogen efficiency, in fact, the overall efficiency of these systems is around 52 %. In addition, the number of shutdowns is around 360 for all the three systems because they were coupled to the same local ERP in Germany 2050.

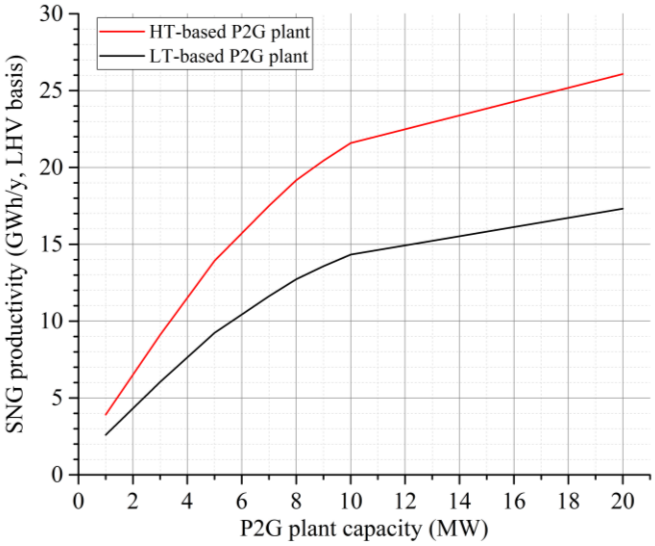

Figure 2.9. Comparison of the SNG productivity between HT-based and LT-based PtG plants (the simplest configuration of SOEC-based, AEC-based and PEMEC-based PtG plants coupled to the local ERP in Germany 2050 was considered).

As depicted in Figure 2.10, the average LCOP of SNG obtained from LT-based PtG plant shows a minimum around 8 MW (between 104.3 €/MWh and 142.3 €/MWh) for the PEMEC and around 9 MW (between 58.6 €/MWh and 152.2 €/MWh) for the AEC because of the different projected specific cost of the electrolysers in 2050, which are related to the maturity of the technology. This analysis pointed out that the AEC-based systems may be the most competitive (average LCOP lower than 110.36 €/MWh); while, if specific costs decreased considerably SOEC-based technology would be economically competitive. Conversely, the PEMEC-based electrolyser is a commercial technology; thus, the process may be not profitable (compared to household NG cost: 110.36 €/MWh) due to higher and quite constant specific costs with respect to the AEC ones, and low SNG productivity due to the electrolysis efficiency. Moreover, these economic results seem to be coherent with the data reported in the literature. For instance, the LCOP of SNG obtained from LT-based processes decreases from about 165 €/MWh in 2020 to about 105 €/MWh in 2050 for a 10 MW PTG plant [14], [38], [71]. Furthermore, the LCOP of SNG obtained from HT-based systems reduces from about 160 €/MWh in 2030 [71] to about 120 €/MWh in 2050 [23], [71] for a 10 MW installed capacity.

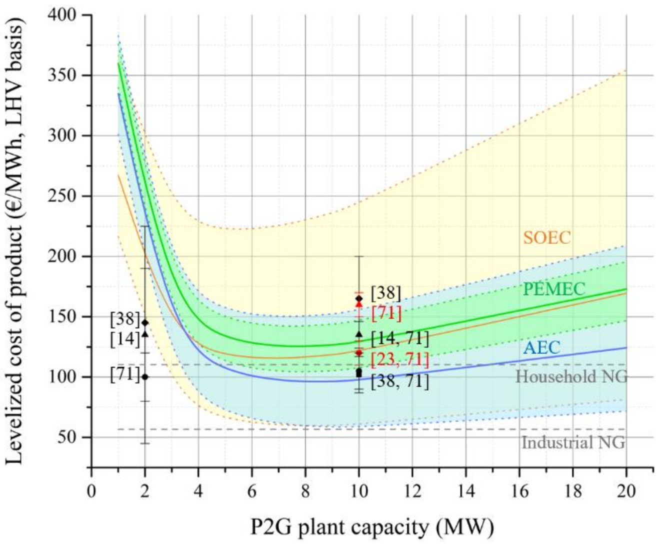

Figure 2.10. Comparison of the levelized cost of product (the simplest configuration of SOEC-based, AEC-based and PEMEC-based PtG plants coupled to the local ERP in Germany 2050 was considered) with LCOP data of the literature, which refers to HT-based PtG plants (red) and LT-based PtG plants (black) in different future scenarios (♦ 2020, ▲2030, ■ 2040 and ● 2050).

After this comparison between HT-based and LT-based systems, the study will focus only on the analysis of the behaviour of the SOEC-based PtG plant coupled to the local ERP, which is the goal of the work.

2.3.4. PtG plant arrangement and management

PtG plant shutdowns

The previous study on the optimization of the PtG plant capacity gave rise to a problem that could create complications for the PtG plant management: the high frequency of switching off the system. In fact, the hot start up may not guarantee the SNG quality during the initial transient; although this aspect was not taken into account in the PtG model. Moreover, the PtG management should require an extremely high level of automatization because of intermittent operations. For the purpose of reducing the number of shutdowns of the PtG plant, a SOEC deficit coverage period could be introduced. It consists in a time interval during which the electrolyser operates at the minimum power load. Therefore, the PtG plant has not to be immediately turned off after a surplus period, but it could continuously operate at the minimum power load. Hence, the number of shutdowns would decrease, if the duration of the deficit period was less than or equal to the SOEC deficit coverage period. Besides, both the SNG productivity and the PUF should increase slightly from 28.5 % to 32 %; while the overall efficiency remained around 77 %. As clearly depicted in Figure 2.11a, the SNG productivity would increase from 17.5 GWh/y to 19.6 GWh/y (LHV basis), if the SOEC deficit coverage reached 24 h. At the same time, the number of shutdowns would drop down drastically from 360 to 40, if the deficit coverage rose up to 24 h. In Figure 2.11b two steps appear in the profile of yearly shutdowns.

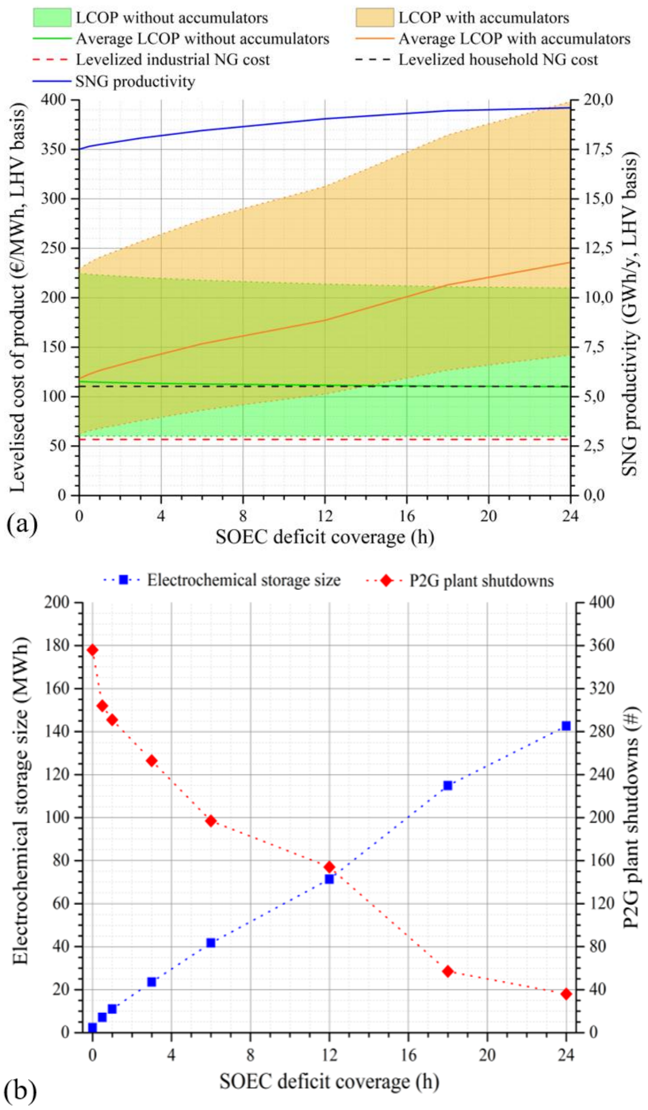

Figure 2.11. Simulation results of two case study at the variation of the SOEC deficit coverage: the first without any storage; the second with accumulators. (a) SNG productivity (LHV basis) and levelized cost of product based on specific costs in 2050 (average specific cost for accumulators is 156 €/kWh); (b) accumulators size and number of shutdowns of the PtG plant.

The first one is located between 0 h and 3 h of deficit coverage, this should be related to fast changes in weather conditions (e.g., they might be linked to photovoltaic power oscillations). The other one appears between 12 h and 18 h of SOEC deficit coverage; in this second case, the cause should be completely different. In fact, the SOEC deficit coverage period is sufficiently large and allows the electrolyser to work continuously even over the whole night, which lasts about 16 h. During the night photovoltaic parks do not produce electricity; hence, the rate of shutdowns would decrease significantly from 160 to 40, if the coverage had a long duration. Furthermore, the number of remaining shutdowns is caused by very long periods that are not directly related to precise weather events, but they are often unpredictable. This analysis had demonstrated that the shutdown frequency of the PtG plant would fall from once a day to once a week, if the SOEC deficit coverage period increased from 0 h to 18 h. Lastly, as earlier mentioned, Figure 2.11a illustrates that the SNG productivity rises gradually from 17.5 GWh/y to 19.6 GWh/y (LHV basis) if the coverage increases from 0 h to 24 h due to the SNG production over deficit periods. This growth in SNG production may cause a slight decline in the LCOP of about 4 % for high values of the SOEC deficit coverage period (e.g. 24 h). For this reason, the PtG system remains always economically competitive, regardless of the SOEC deficit coverage duration, but the load on the electric grid increases due to the PtG plant consumptions.

Electrochemical storage

The electrolyser requires a certain amount of electricity to ensure the minimum partial load during deficit periods. Nevertheless, a completely RES-based scenario was chosen [117]; thus, there is not enough electricity on the electric grid to balance the electric load of the users, even though the hot standby consumption must be guaranteed. Gas-to-power plants could be employed to balance all the amount of deficit energy; for instance, exploiting the SNG stored in the natural gas distribution grid, which was formerly produced in the PtG plants. All these aspects concerning the balance of both the electric grid and the natural gas distribution network are not straightforward and are out of the scope of this work.

An electrochemical storage within the PtG plant was considered. The main purpose of the batteries is to accumulate a part of the excess of surplus energy, which could not be exploited by the electrolyser due to its nominal power. Then, the accumulators power the PtG plant during the deficit periods, thus no electricity is required from the electric grid. However, two further problems arise: the first is linked to the electrochemical storage capacity; the second is related to the cost of the accumulators. As shown in Figure 2.11b, the electrochemical storage capacity to balance all the hot standby consumptions is fairly small (about 2.34 MWh). Despite this fact, the size of the batteries increases sharply from 2.34 MWh to 142.6 MWh if the SOEC deficit coverage rises from 0 h to 24 h. It is associated with the large amount of energy required to maintain the electrolyser at the minimum partial load during the deficit coverage. The main consequence of the large electrochemical storage size is the dramatic increase of the average LCOP from 118.1 €/MWh to 235.9 €/MWh (LHV basis), as depicted in Figure 2.11a; in fact, the estimated decrease of the average specific cost of the accumulator in future years is limited (205 €/kWh in 2030, 177 €/kWh in 2040 and 156 €/kWh in 2050) and uncertain (e.g. between 105 €/kWh and 233 €/kWh in 2050). Furthermore, if the accumulator size is too large, the PtG plant configuration with batteries is not economically competitive. In the best market condition such configuration would be competitive if the SOEC deficit coverage was lower than 14 h; otherwise, the LCOP would be higher than the current household natural gas price [8], which was considered as a reference.

Chemical storage

In order to decouple the electrolyser and the methanation unit, a H_2 tank could be introduced in the PtG plant. Moreover, also a steam storage was considered, to reduce the amount of steam which would be externally produced, if no steam storage was considered. In this configuration, the PtG plant operates as previously described. Figure 2.12a and Figure 2.12b present simulation results of PtG plants with both chemical and electrochemical storage, considering both the variation of the SOEC deficit coverage period and the H_2 storage time.

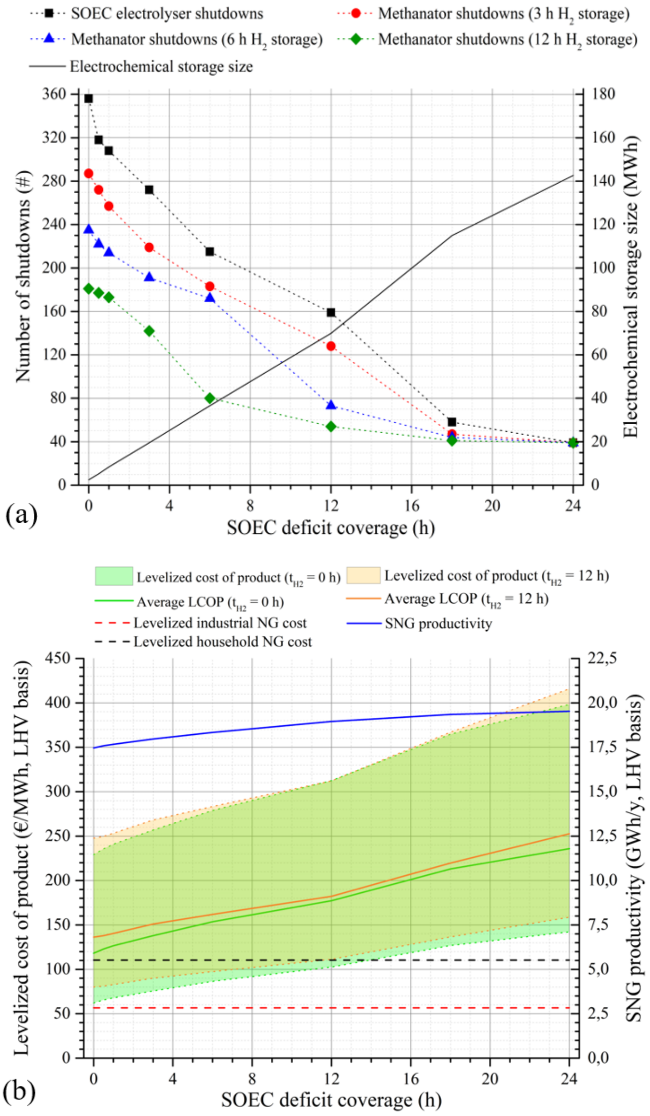

Figure 2.12. Simulation results of PtG plants with electrochemical and chemical storage at the variation of both the SOEC deficit period and the H_2 storage time: (a) electrochemical storage capacity and number of shutdowns of both the electrolyser and the methanation unit; (b) SNG productivity (LHV basis) and levelized cost of product based on specific costs in 2050.

What stands out in Figure 2.12a is that the electrochemical storage capacity required to power the SOEC among all the deficit and the SOEC deficit coverage periods, did not change by varying the H_2 storage time. The estimated heat losses were very small (between 9 kW and 20 kW), thus their capacity depends predominantly on the SOEC deficit coverage.

Interestingly, the number of shutdowns of the electrolyser remained unchanged at the variation of the H_2 storage time. The evidence of this fact is that the SOEC electrolyser produces H_2, but it is powered by electricity. Therefore, its number of shutdowns only depends on the duration of the SOEC deficit coverage period and obviously not on the presence of the H_2 storage tank.

On the contrary, the number of shutdowns of the methanation unit depends both on the SOEC deficit coverage period and the H_2 storage time. A likely explanation is that it could be considered depending on the sum of these two contributions. On the one hand, the number of shutdowns of the reactors decreased as the SOEC deficit period increase, as earlier discussed. On the other hand, it diminishes even more because the equipment operates continuously, even if the electrolyser is already maintained in hot standby mode, thanks to the stored H_2. As can be seen in Figure 2.12a, the methanator shutdowns fall down when a 12 h H_2 storage time and a 6 h SOEC deficit coverage period were considered. This happens because the methanator could work uninterruptedly during the night, covering the gap between two surplus spikes caused by the lack of photovoltaic power generation.

The presence of chemical storage does not imply an increase of the SNG productivity, as depicted in Figure 2.12b, because the H_2 tank is filled at the beginning of a surplus spike; but the methanator works at the minimum load. Indeed, the amount of recovered surplus does not change at the variation of the chemical storage capacity. Moreover, the overall LHV-based efficiency decreases slightly from 77 % to 76 % due to the higher thermal dissipation and additional energy, which were required to manage the steam condensation within the steam drum. In addition, the LCOP increases as the chemical storage capacity rises due to the greater capital cost investment (the LCOP increases by about 10 €/MWh considering a H_2 buffer time of 12 h); thus, the PtG process could be not economically competitive in the current gas market, as Figure 2.12b shows. For the sake of clarity, as illustrated in Figure 2.13, the different contributions to the LCOP were examined for a single case study considering all the equipment. The LCOP is mainly affected by the capital costs (65 %) due to both the high cost of the SOEC electrolyser (40.7 %) and the presence of the accumulators (39 %); but the heat integration is a non-negligible term (5.7 %). Furthermore, maintenance (47.7 %), replacement (19.5 %) and surplus electricity (17.5 %) are the most important contributions to the operating costs.

The presence of these storage tanks could have some benefits. In fact, the continuous operation of the plant implies an easier PtG system management; thus, the operative and maintenance costs might be partially reduced. Moreover, a small number of start-ups and shut-downs reduces the risk of out-of-specification product, even if the SNG quality must be guarantee before the injection in the natural gas distribution grid.

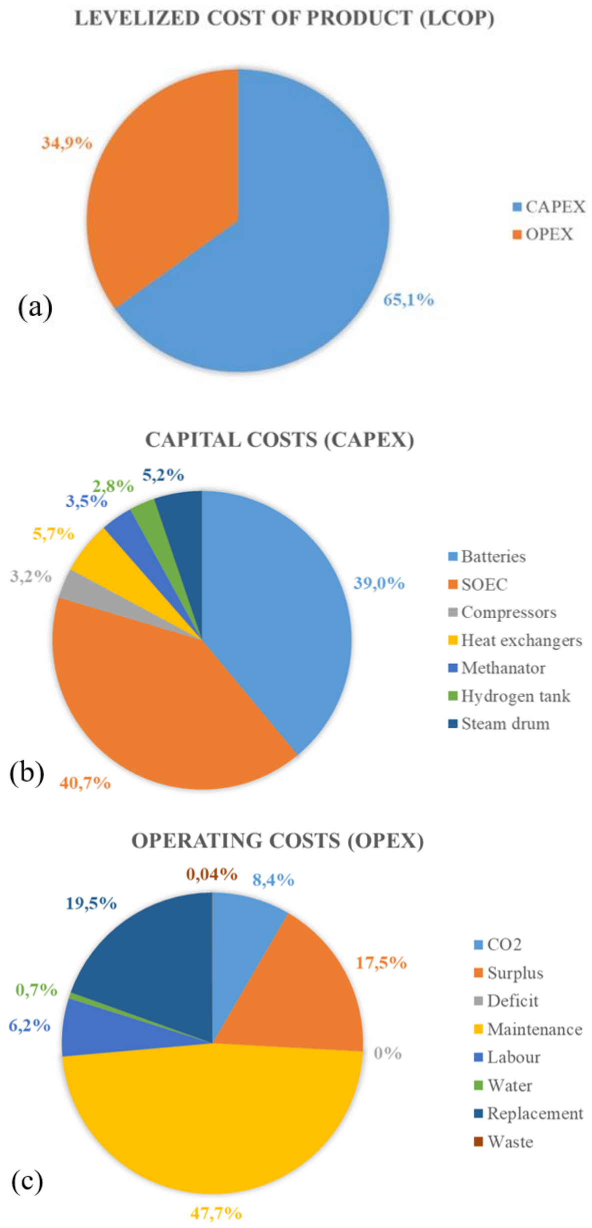

Figure 2.13. Economic contributions to the (a) levelized cost of product (LCOP) in 2050: (b) capital costs and (c) operating costs; considering a 7 MW SOEC-based PtG plant, 12 h of hydrogen buffer time, 12 h of SOEC deficit coverage, 59 MWh of accumulators size and average prices in 2050.

2.3.5. Long-term and seasonal storage

Thus far, this study has been focused on the PtG plant sizing and arrangement, analysing all the aspects that are linked to the management of the plant and the electric residual profile; but another relevant facet of the PtG systems is the compensation of the electric deficits. The PtG plants are connected to the electric grid to absorb and recover the electric energy surplus converting it into SNG. Then, the gas could be injected in the natural gas distribution network to store and transport it to the users. During the deficit periods, the RES-based power generation is lower than the electric load, which corresponds to the consumption of the users. Besides, in this case study scenario, fossil energy sources were not considered.

Hence, the compensation of the deficits is a problem that should be addressed. Therefore, a study on both the long-term and seasonal storage of the SNG will be performed in this paragraph.

Due to the lack of traditional energy sources, the deficits may be compensated by means of the SNG, using it to repower the electric grid. Thus, the repowering efficiency of the gas was assumed equal to 45 %. The SNG was produced by the PtG plant and then stored in the gas network, which has a huge volume. Generally, during deficit periods, it could be used into gas-to-power plants, such as thermoelectric plants, for the purpose of balancing the electric grid. Figure 2.14 illustrates the SNG production profile of the same PtG plant that was analysed in Subsection 2.3.2; the yearly SNG production corresponds to about 1411 t/y (18.4 GWh/y, LHV basis). Moreover, the profile of the SNG storage in the gas network was evaluated, considering the SNG injection into the gas grid and its consumption to compensate the deficits. Finally, fossil NG was considered to balance the electric grid when there was no more SNG to perform the balancing. In fact, Figure 2.14 shows traditional NG spikes linked to its consumption in gas-to-power plants.

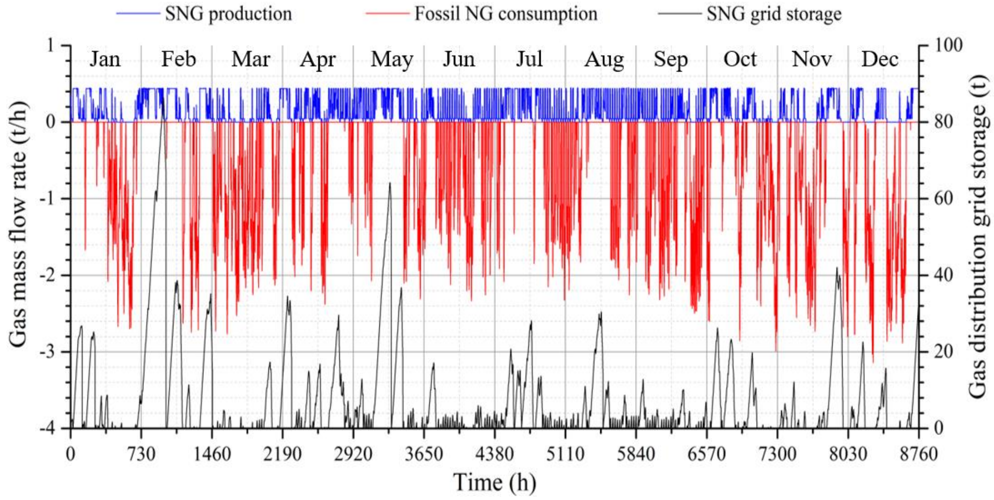

Figure 2.14. SNG productivity and storage in the gas distribution network and fossil NG consumption to balance all the deficits. In this case study, a 7 MW PtG plant capacity, both a SOEC deficit coverage period and a H_2 storage time of 6 h and a 36.57 MWh electrochemical storage size were considered.

The yearly consumption of methane to balance completely the deficits is around 4768 t/y (29.8 GWh/y, LHV basis). Therefore, the SNG produced by the PtG plant could compensate around 29.6 % of the deficits; the remaining part might be balanced using around 3357 t/y of fossil gas. The SNG balance a quite low amount of deficit energy because of the low repowering efficiency; but it could ideally compensate at most 61.7 % of the all deficits. However, considering all the PtG plants that could be coupled with the national ERP, which should be 2500 in this case study, CO_2 emissions may be reduced of about 9.7 Mt/y because carbon was captured from exhausted streams and stored as CH_4; than CH_4 could be burned to produce electricity and heat. More specifically, the corresponding amount of fossil gas or other fuels was not exploited in gas-to-power; thus, the CO_2 emissions related to this scenario decreased from 32.7 Mt/y to 23.0 Mt/y.

As far as the SNG seasonal storage is concerned, this type of management of the gas distribution network seems not to be performed due to the strong intensity of the deficit spikes. Indeed, the gas storage accumulates slowly SNG because the flow rate depends both on the surplus spikes and on the PtG plant capacity. Nevertheless, it is rapidly consumed to repower the electric grid, as can be seen in Figure 2.14. Therefore, the amount of SNG is not enough to balance all the deficits of the season neither in winter nor in summer. Wind power prevails in winter; thus, sometimes the gas storage accumulates a large amount of SNG for a relatively long period (long-term storage). However, it was exploited in a very short period. On the contrary, photovoltaic power generation is prevalent in summer; hence, the surplus spikes are intermittent. Therefore, the SNG is produced during the day, but it is often consumed during the night (short-term storage).

2.4. Conclusion

The main purpose of the present study was to assess both qualitatively and quantitatively the technical, managemental and economic aspects of the coupling between a PtG plant and a totally RES-based intermittent residual profile in a future scenario.

First of all, the RES-based electric residual profile in Germany 2050 was analysed. The most obvious findings to emerge from this study are that wind power generation prevails during winter periods, while photovoltaic power production is prevalent in summer due to weather conditions. These facts are highlighted by the high frequency of oscillation of the electric residuals, which corresponds to a mean value of 363. Moreover, the intermittency of the electric input implies that the PtG plant is characterized by a complicated management.

Subsequently, this study has provided a comprehensive assessment of the coupling between the PtG plant and the ERP, in which a PtG plant with both electrochemical and chemical storage was examined. The results of this research have supported the idea that the PtG plant could possibly work continuously thanks to the presence of the storage. In fact, the accumulators allow the electrolyser to operate also during period of lack of residual electricity, if they provide enough electric energy. Furthermore, the PtG plant exploitation increases, if the batteries store a certain amount of the excess of the surplus spike, which could not be exploited by the SOEC. Moreover, the electrolyser and the methanation unit can be decoupled by means of the H_2 storage tank, which allows the reactors to work continuously even if the SOEC electrolyser is turned off in hot standby configuration. Hence, the number of shutdowns of the PtG plant could be reduced to improve and ease the PtG plant management.

To better investigate the implications of these assessments, many sensitivity analyses were performed by varying the PtG plant capacity, the SOEC deficit coverage period and the H_2 storage time. On the question of the PtG plant capacity, the study was performed increasing it to clearly understand the variations in the

SNG productivity and its LCOP. The evidence from the study has revealed that the SNG yearly productivity has increased, and then it has approached to a maximum threshold. This fact has been reflected on the LCOP, which has shown a minimum around 7 MW of PtG plant capacity. For this case, the LCOP has varied between 60.2 €/MWh and 224.9 €/MWh (LHV basis), which means that the PtG process could be economically competitive if it is compared to the current levelized NG cost range. Moreover, the overall LHV-based efficiency is around 77 %, and the number of shutdowns of the PtG plant is extremely high and equal to 356.

For the purpose of reducing the number of shutdowns of the PtG plant, a sensitivity analysis at the variation of the SOEC deficit coverage period was performed. This investigation has shown that the number of shutdowns decreases rapidly as the SOEC deficit period rises. The presence of accumulators was also considered; but the LCOP raises as the capacity of the electrochemical storage increases. Thus, the break-even battery capacity is around 75 MWh, which corresponds to a SOEC deficit coverage period of 14 h.

Finally, the investigation of long-term storage of the SNG has revealed that the produced gas could be stored in the natural gas distribution network and used to repower the electric grid. However, the amount of SNG could not compensate all the deficits due to the low repowering efficiency. In fact, the overall power-to-power efficiency corresponds to about 34.6 %. As described in Subsection 2.3.2, the yearly amount of surplus energy was about 34.2 GWh, while the yearly amount of deficit energy was 29.8 GWh and the total SNG production was around 18.4 GWh/y. This means that the PtG plant has recovered about 69.9 % (23.9 GWh) of the available surplus energy. Consequently, other energy sources, such as fossil NG are needed to balance completely all the lack of energy during deficit periods. In conclusion, the usage of SNG for repowering the electric grid results in a reduction of CO_2 emissions of around 29.6 % due to a lower consumption of fossil energy sources and to the capture of CO_2, which was one of the two reactants in the methanation process.

The generalisability of these results is subject to certain limitations. For instance, the major one is the electric residual profile, which is a projection based on data from the past. However, the analysis performed over a year should be little subject to occasional weather events. Furthermore, another source of weakness in this study, which could have affected mainly the economic analyses, was the uncertainty of the costs of both the electrolyser and the accumulators, which are the most expensive items of equipment in the PtG plant. In addition, in this work, oxygen and taxation were not valued economically in order to better highlight the aspect strictly related to the PtG plant arrangement.

A natural progression of this work will be the assessment of transient effects of both the SOEC electrolyser and the reactors, considering also the deactivation of materials and out-of-specification products. Moreover, a greater focus on the implementation of the PtG model within electric grid models will produce interesting findings that account more for the further improvement and application of the PtG technology.

Chapter 3

Impact of Power-to-Gas on distribution systems with large renewable energy penetration

The study presented in this chapter was published as [5]:

Mazza, A.; Salomone, F.; Bensaid, S.; Bompard, E.; Chicco, G.; Arrigo, F.; Impact of Power-to-Gas on distribution systems with large renewable energy penetration *Energy Convers. Manag. X* **2020**, *7*, 100053, doi:10.1016/j.ecmx.2020.100053.

3.1. Introduction

As introduced in Chapter 1, the increase of Renewable Energy Sources (RES) has changed the paradigm of the distribution system operation, by imposing a shift from the traditional case of a completely passive network to a more and more active network hosting an increasing share of local generation. The local generation is variable during time and can create different issues, such as i) reverse power flow (occurring when the distribution system injects power into the transmission system), and ii) operational constraint violations (in terms of voltage and current limits). For solving these problems without the RES production curtailment, the excess of local generation should be converted and stored in appropriate forms.

Power-to-Gas (PtG) seems to be a promising solution for exploiting the electric excess of the local generation system to produce and store gas, then using the stored gas at a later time for different purposes. These characteristics make PtG adapt to be integrated into multi-energy systems [156,157] and to participate in the energy system operation in a flexible way [115]. As carefully discussed in Chapter 1, many research works have modelled the PtG units as "black boxes" without considering the physical connections existing among the different plant parts, and thus also auxiliary services (such as compression systems) have been missed by the modelling aspects. Thanks to the multi-disciplinary team composing the project STORE&GO [41], the complete model of a PtG plant has been created and then included in a power flow calculation. For representing the effect on different seasons, four daily irradiation profiles have been considered with reference to the installation sites of the demonstration plants of the project. Furthermore, for understanding the effect on different network topologies, two realistic network models have been introduced to show the effect on both rural and semi-urban grids. Typical load profiles have been included to represent the variability of the loads in time. Great attention has been devoted to the case study creation, by considering different possible positions of the PV plants in the grid.

Regarding the electrical point of view, the PtG plant is a particular type of load, and as such it has to be properly modelled in a power flow calculation tool. The PtG plant modelling is an open research issue, especially because of the need of providing a sound validation of the model on the basis of real case applications. On the basis of the previous considerations, this paper presents a number of specific contributions to the modelling and exploitation of PtG in distribution systems, namely:

- The PtG plant modelling is addressed in order to formulate a steady-state model of PtG to be incorporated in the power flow equation solvers. The validation of the model is carried out on the basis of measurements collected from a real PtG plant.
- The impact of PtG on the distribution system operation is then studied through simulations in steady-state conditions. Different loading and RES penetration are considered for reproducing different network issues that may be alleviated by using PtG plants. Dedicated cases are created with different RES penetration, by locating the RES sources at network nodes that correspond to critical conditions for the amount of reverse power flows, as well as for the presence of overcurrent and overvoltage issues in the distribution network.

3.2. PtG plant model

The PtG plant consists of a low temperature-based electrolyser (LTE), a buffer and a methanation unit. A simplified scheme of the PtG process is illustrated in Figure 3.1. The LTE converts liquid water into gaseous oxygen at the anode and gaseous hydrogen at the cathode through electrolysis [3,8,19,158]. According to the literature, the efficiency of the electrolysis ranges between 55 % to 70 % (LHV basis) [3,12,122]. The hydrogen produced within the LTE could be stored in a tank or sent to the methanation unit. The hydrogen is mixed in stoichiometric ratio with carbon dioxide (H_2/CO_2 molar ratio equal to 4) in order to supply the methanation unit that produces synthetic natural gas (SNG) [3,8].

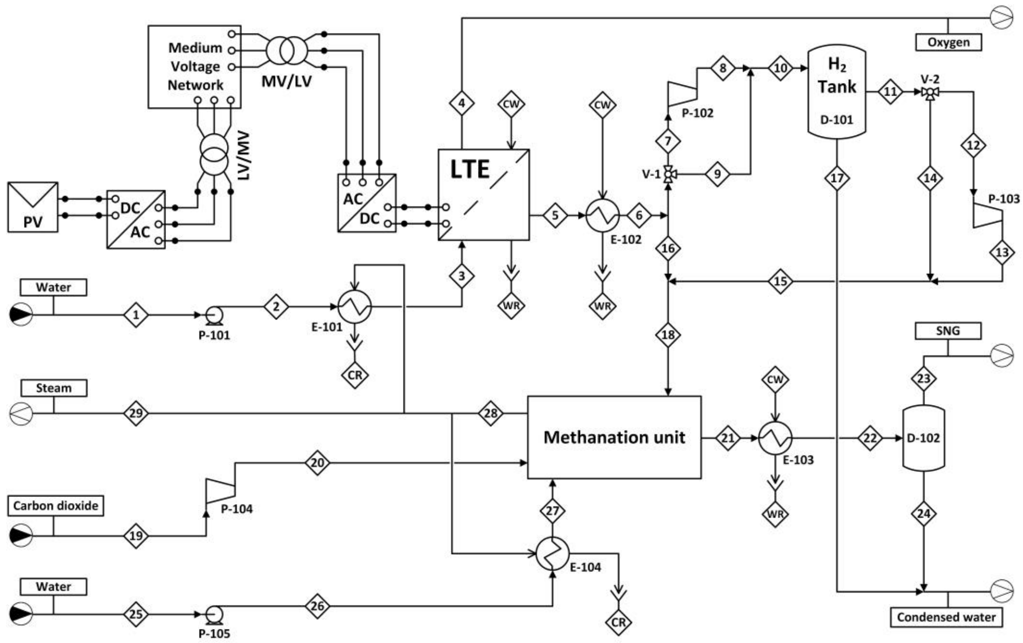

Figure 3.1. Simplified low temperature-based Power-to-Gas process scheme considering H_2 storage.

In addition, the main characteristics of the PtG are summarized in Table 3.1.

Table 3.1. Installed power and energy balance in Germany both in 2016 and 2050.

Parameter	Value	Parameter	Value
LTE operating temperature	80 °C	CO_2 conversion in the reactors	98.5 %
LTE and methanation unit pressure	15 bar	In – out T of the cooling water	28 – 32 °C
H_2 tank maximum pressure	60 bar	Coolant T in the methanation unit	250 °C
Compression efficiency	75 %	Power-to-H_2 efficiency (LHV basis)	57.6 %

3.2.1. Characteristics of the electrolyser

A low temperature-based electrolyser is characterised by a power-to-hydrogen efficiency, whereas the methanation unit is characterised by a certain value of the CO_2 conversion efficiency (i.e., 98.5 % [3,8,25]).

The PtG model has been built considering the dynamics (start-ups, shutdowns and partial loads) of a real plant installed in the demonstration site of Falkenhagen (Germany), whose process is based on Alkaline Electrolysis (AEC). This plant consists of a 2 MW AEC-electrolyser, which is composed of 6 AEC modules (330 kW each one). The electrolysis technology considered has minimum load P_{MIN} =20% [12] and power-to-hydrogen efficiency $\eta_{H2} = 57.6\%$ (real data, LHV basis)).

The characteristics of minimum load and efficiency of the AEC technology has been directly provided by the Falkenhagen plant managers, based on their long-time experience in the plant operation. It is worth noting that the AEC efficiency is in line with the related literature [9,122]. Regarding the minimum load of the electrolyser (i.e., the power to be provided for producing the minimum amount of H_2), the values existing in the literature are even lower than 20 % but they may lead to problems (see for example [12,159]). The modularity of these technologies simplifies the management of the electrolyser, moreover each module could be maintained in hot stand-by if there is not enough electrical energy for supplying the PtG plant.

On the one hand, the electrolyser has a wide rangeability thanks to its modularity. On the contrary, the methanation reactors have a narrow rangeability due to the kinetics of the methanation reaction [25,29]. More specifically, according to the literature [25], the reactors are conceived as tube-bundles refrigerated by evaporating water at 250 °C. The methanation reaction is extremely exothermic [24,29]; hence, the tube diameter must be small for avoiding too high radial thermal profiles. Obviously, the design of a methanation reactor is made for the nominal productivity; however, the residence time increases (and the gas hourly space velocity decreases) reducing the productivity. Consequently, the heat generation profile along the axis of the reactor becomes narrower and more intense; in addition, the overall heat exchange coefficient decreases [8,25]. Therefore, it could cause problems of thermal management, hot spots and local deactivation of the Ni/γ-Al_2O_3 catalyst (i.e. sintering) [3,24,29,160]. Hence, each reactor could be parallelized in 3 or 4 bundle in order to increase the rangeability of the PtG plant, for instance, from about 60-110 % (i.e., only one bundle for each reactor) to about 20-110 % (i.e., three bundles in parallel for each reactor). For all these reasons, the best option is to maintain the methanation unit at least at the minimum operative load.

The model developed in this work, as additional feature, considers also all the auxiliary consumptions, which can be easily adjusted according to the actual PtG plant layout. More in detail, the energy consumption of a compressor (E_{compr}, W) was calculated according to equation (3.1) [146], where Z is the compressibility factor that was assumed unitary, R (8.314 J mol^{-1} K^{-1}) is the ideal gas constant, T_{in} (K) is the inlet temperature, $\dot{n}_{\mathrm{in}}$ (mol s^{-1}) is the inlet molar flow rate, γ is the heat capacity ratio, η_{compr} is the compression efficiency, which was set equal to 70 % and p_{in} and p_{out} represent the inlet and outlet pressure, respectively. In addition, multistage compression was considered if the compression ratio (p_{out}/p_{in}) was greater than 4.

$$E_{\mathrm{compr}} = Z \cdot R \cdot T_{\mathrm{in}} \cdot \frac{\gamma \cdot \eta_{\mathrm{compr}}}{\gamma - 1} \cdot \left[\left(\frac{p_{\mathrm{out}}}{p_{\mathrm{in}}} \right)^{\frac{\gamma - 1}{\gamma \cdot \eta_{\mathrm{compr}}}} - 1 \right] \cdot \dot{n}_{\mathrm{in}} \qquad (3.1)$$

Moreover, the methanation unit and the electrolyser require an additional electric consumption due to heat dissipations caused by natural convection [3], if they are maintained in hot stand-by.

3.2.2. The electrolyser model

The dynamic behaviour of the AEC-electrolyser has been obtained from the analysis of a test carried out at the Falkenhagen plant (shown in Figure 3.2).

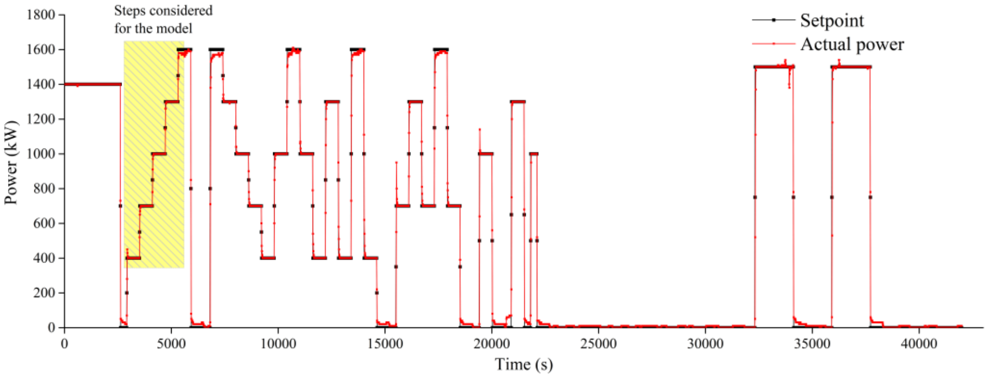

Figure 3.2. Falkenhagen test on an AEC-based electrolyser.

The test had a duration of about 11.5 h, and it highlighted that the AEC-based electrolyser had a fast response when the setpoint changed. Therefore, its response could be modelled for the purpose of forecasting the behaviour of the AEC-based electrolyser when it is coupled with an intermittent RES-based electrical profile. It is worth mentioning that during the test, the set point of the electrolyser was periodically changed with steps of different amplitude to explore a large number of operating conditions.

The easiest model to describe the AEC-based electrolyser behaviour is a first order system with delay, which is characterised by three parameters; the mathematical model of its response to a step is described by means of equation (3.2) [148,161,162]:

$$\begin{cases} y(t) = 0 & \text{If } t < \alpha \\ y(t) = A \cdot K \cdot \left[1 - \exp\left(-\frac{t-\alpha}{\tau}\right)\right] & \text{If } t \geq \alpha \end{cases} \tag{3.2}$$

In this equation, $y(t)$ is the actual power of the AEC-based electrolyser (MW) at the time step t (s), A is the step amplitude of the set point (MW), K is the gain of the system, α is the time delay of the response (s), τ is the time constant of the system (s). The gain K can be evaluated by means of equation (3.3), where $y(\infty)$ is the actual power of the electrolyser after a large period of time (stationary condition):

$$K = \frac{y(\infty)}{A} \tag{3.3}$$

The two time parameters (α and τ) have been estimated by means of the Sundaresan and Krishnaswamy's method [163], according to equations (3.4) and (3.5), respectively. The two parameters were calculated using two characteristic points of the response curve: t_1 represents the time in which the response reaches 35.3% of the stationary value $y(\infty)$, while t_2 is estimated as the time in which the response reaches 85.3% of the final value $y(\infty)$:

$$\alpha = 1.3 \cdot t_1 - 0.29 \cdot t_2 \tag{3.4}$$

$$\tau = 0.67 \cdot (t_2 - t_1) \tag{3.5}$$

For the purpose of evaluating these three parameters, four steps with the same amplitude (i.e., 0.3 MW) have been considered, by obtaining the parameters shown in Table 3.2. These steps are highlighted in Figure 3.2 between 40 min and 100 min of the test.

Table 3.2. Characteristics of the low temperature-based electrolyser.

Parameter	Value
K	1
α , s	14.62
τ , s	11.73

The fit between the model output and the real data is shown in Figure 3.3.

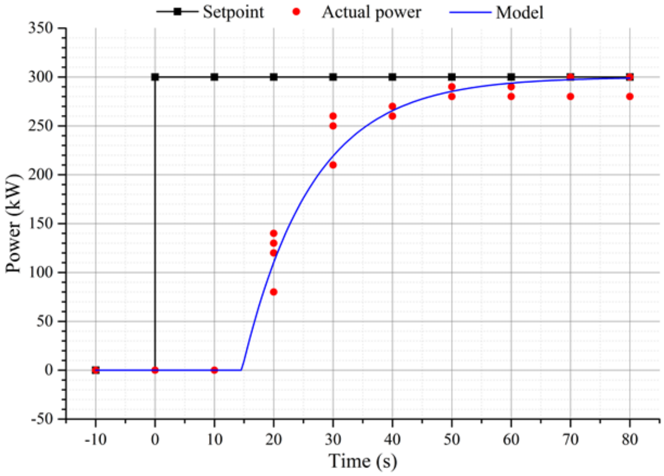

Figure 3.3. AEC-based electrolyser response model estimated using Falkenhagen test data (first order system with delay). It is worth noting that the experimental data (red spots) are referred to the four steps considered for the modelling, as mentioned in the text. For comparing the behaviour of the response, the starting values of the real steps were shifted to zero (baseline), and thus some data are overlapping.

3.2.3. Simulation algorithm of the PtG plant model

The flowchart of the simulation algorithm (called in the follow *function_PtG*) is shown in Figure 3.4.

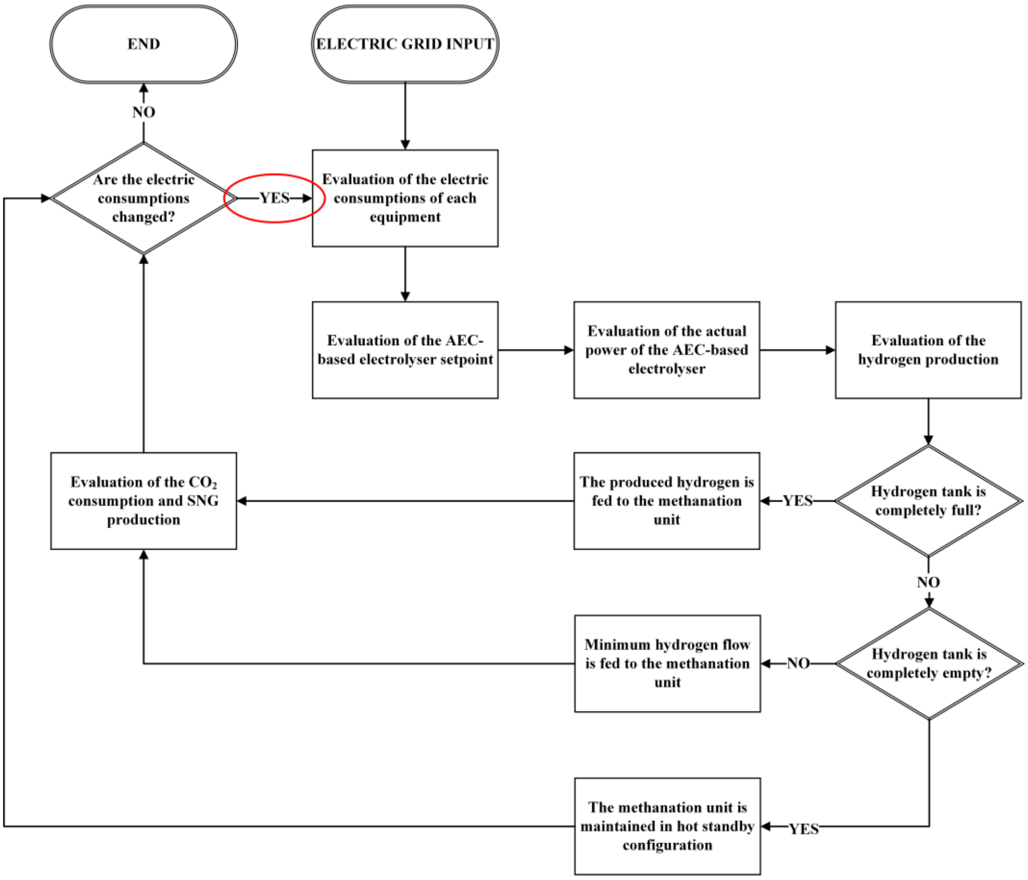

Figure 3.4. Flowchart of the algorithm (function_PtG).

The simulation algorithm consists of the following main instructions:

- *Setpoint*: the setpoint is defined as the theoretical maximum operative power at which the electrolyser may work. This maximum can correspond to either the power provided by the grid (when it is lower than the nominal power of the electrolyser) or the nominal power of the electrolyser (in the case it exceeds the nominal power of the electrolyser).
- *Actual power*: it represents the actual electric consumption that could be calculated using the dynamic model of the AEC-based electrolyser (Section 3.2.2).
- *Hydrogen production*: the hydrogen flow could be evaluated taking into account the efficiency of the electrolyser.
- *Hydrogen tank management*: if the electrolyser is operative, a minimum hydrogen flow feeds the methanation unit. Beyond this, certain amount of hydrogen is sent to a hydrogen tank until the tank is completely full (the priority is filling the tank). This operation allows to decouple the methanation unit from the electrolyser. When the electrolyser is not operative, the stored hydrogen is fed to the methanation unit, for producing continuously SNG. In this case, the methanation unit works at the minimum power load; when the hydrogen tank is completely empty, it could be turned off and remain in hot standby conditions. More in detail, H_2 produced in the

LTE could be split into two streams. During the filling of the H_2 tank three configurations have to be considered:

  - If the H_2 tank is empty, its pressure is lower than the operative pressure of both the LTE and the methanation unit. Therefore, the compressor (P-102) is useless and the H_2 tank could be partially filled using stream 9 until the storage pressure is equal to the operative pressure of the LTE.
  - If the H_2 tank is partially filled, its pressure ranges between the operative pressure of the LTE and the maximum storage pressure. Therefore, the compressor (P-102) is used for filling the tank until it is completely full.
  - If the H_2 tank is completely full, the produced H_2 is directly fed to the methanation unit using stream 16.

  If the LTE does not produce H_2, the methanation unit could be fed using the stored H_2. In this case, three configurations could be possible:

  - If the tank pressure is higher than the operative pressure of the methanation unit, H_2 could be fed to the methanation unit through stream 14.
  - If the tank is emptying, H_2 could be fed to the methanation unit using the compressor P-103 until the tank is completely empty.
  - If the H_2 tank is empty and no electricity is available for producing H_2, the methanation unit must be turned off (shutdown of the PtG plant).

- *Auxiliary consumptions*: all the consumptions of the auxiliary items of equipment are related to the amount of produced hydrogen. Firstly, the hydrogen could be compressed; secondly, the carbon dioxide has to be compressed; thirdly, the water has to be pumped and lastly it must be heated up to the temperature of the electrolyser.
- *Control of the setpoint*: the setpoint power of the electrolyser must be recalculated considering the new auxiliary consumptions, because the available electricity is comparable with the power absorbed by the electrolyser. This affects the power withdrawn from the power grid.
- *Methanation unit*: the amount of SNG could be calculated using the CO_2 conversion, or alternatively, the hydrogen-to-SNG efficiency.

3.3. Creation of the case studies

As widely shown in literature (for example in [164]), the installation of large share of RES can create the following issues:

- *Reverse power flow (RPF)*: on the one hand, a reverse power flow affects the transmission system because the point of connection between transmission and distribution system becomes equivalent to a non-controllable active node. On the other hand, the presence of reverse power flow can create issues also at the distribution system, for example in terms of not proper protection schemes. Usually, these problems are nowadays solved by cutting the excess of production or using some pilot battery-based storage [165].
- *Overcurrent (OC)*: the large share of RES can create overcurrents along the feeders. These overcurrents can affect only a portion of the network (e.g., the last portion) or the entire network, depending on the level of load and distributed generation, together with the geographical position of the PV plants.
- *Overvoltages (OV)*: this problem is characteristic especially of rural networks, composed of long feeders (also up to 10 km), and characterized by a high R/X ratio, which leads to have to voltage levels changes strictly linked with the active power flowing in the grid branches.

It is worth noting that the presence of reverse power flow leads the network to operate in an alert condition, whereas the presence of overcurrent and overvoltage are symptoms of an emergency condition (because directly affecting the operational constraints of the network) [166] and the distribution system operators needs to solve these problems as soon as possible, by making use of different approaches which can even result in lower quality of service (e.g. load disconnections). So, the simulations carried out starting from conditions in which the network constraints are not satisfied (even though these conditions do not correspond to real situations) have the goal to show, in very extreme cases, how the potential use of PtG can alleviate also these problems.

The creation of the case studies needs the proper placement of the PV plants. In this study, the placement of the PV plants has been carried out by using two different approaches:

- *Topological approach*: the PV plants have been installed according to the length of the network lines
- *Losses Allocation Factors-based approach*: in this case, the approach shown in [167] and based on [168] has been adopted. A detailed analysis on the implication of the use of the loss allocation for distribution system analysis can be found in [169].

3.3.1. The network samples

This work considers two network samples:

- *Semi-urban network*, adapted from the one shown in [170], by adding time-varying loads with different profiles. For this network only the topological PV placement has been applied [171].
- *Rural network*, developed in the project *Atlantide* [172]. For this network, both PV placement methods have been used.

The two network samples aim to represent different network topologies and allow to emulate the distribution systems in the areas where the demo sites of the project are installed. The two demo sites are in installed in Solothurn (Switzerland) and in Troia (Italy). In particular, the network semi-urban refers to Solothurn area, whereas the rural network refers to Troia area.

Few samples referring to daily PV profiles in different months used for the two networks are shown in Figure 3.5, whereas the load profiles used are shown in Figure 3.6. It is worth noting that the PV profiles are different for the two network samples because referring to two different geographic and have been obtained from the Bright Solar Resource Model.

Moreover, during the night time the PtG plant is supplied by the main grid to guarantee the continuous operation of the plant in compliance with its minimum power specified in Section 3 (i.e., P_{MIN}=20%).

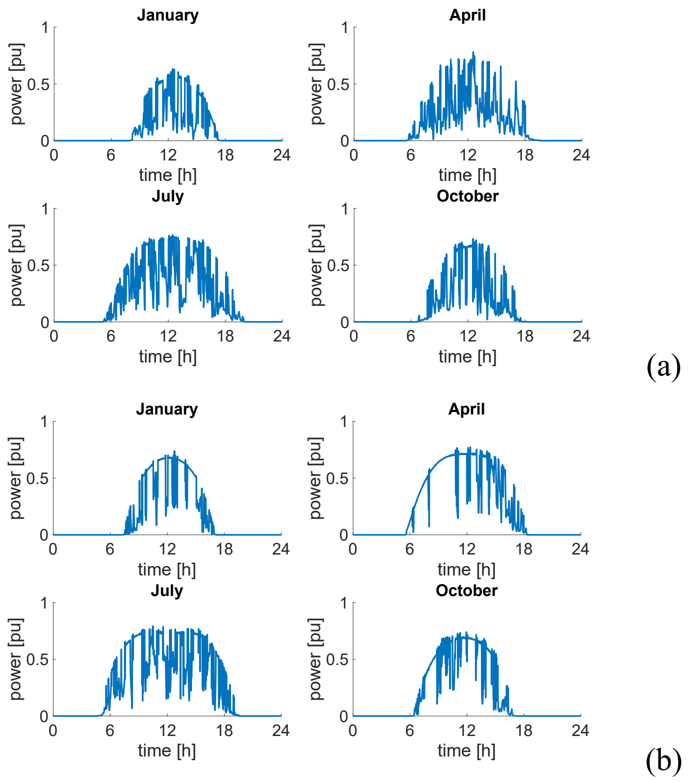

Figure 3.5. PV profiles considered for building the case studies. Four months have been considered (January, April, July and October): (a) semi-urban network and (b) rural network.

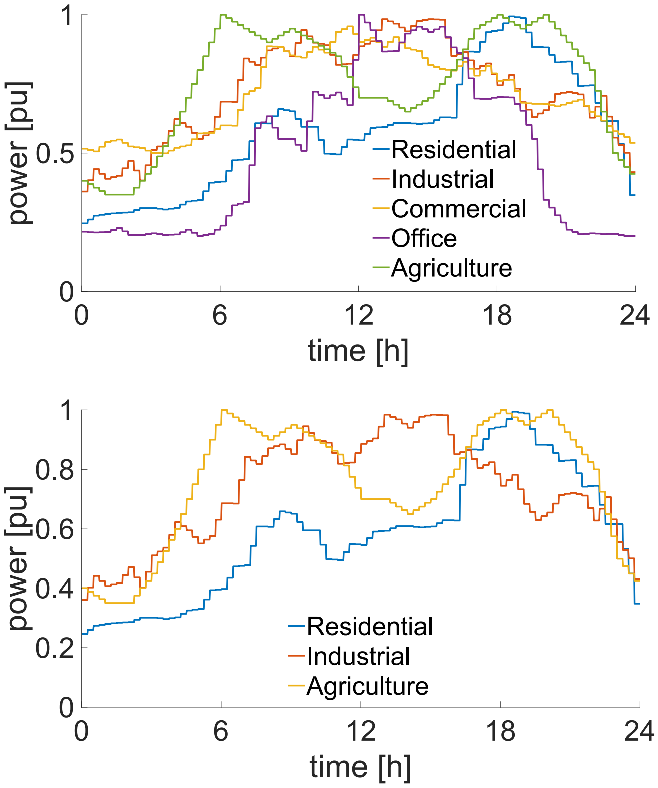

(a)

(b)

Figure 3.6. Load profiles used in (a) semi-urban network and (b) rural network [172].

3.3.2. Introduction of the PtG plant model into the calculation loop of the network operation

The model of the PtG explained in Section 3.2 needs to be integrated in the network solver, which is based on the Backward Forward Sweep (BFS) method [173]. The response of the PtG unit is modelled as a first order system and solved through the Matlab®-embedded solver ode45. The calculation loop is shown in Figure 3.7. The variables used in the calculation loop are presented in Table 3.3.

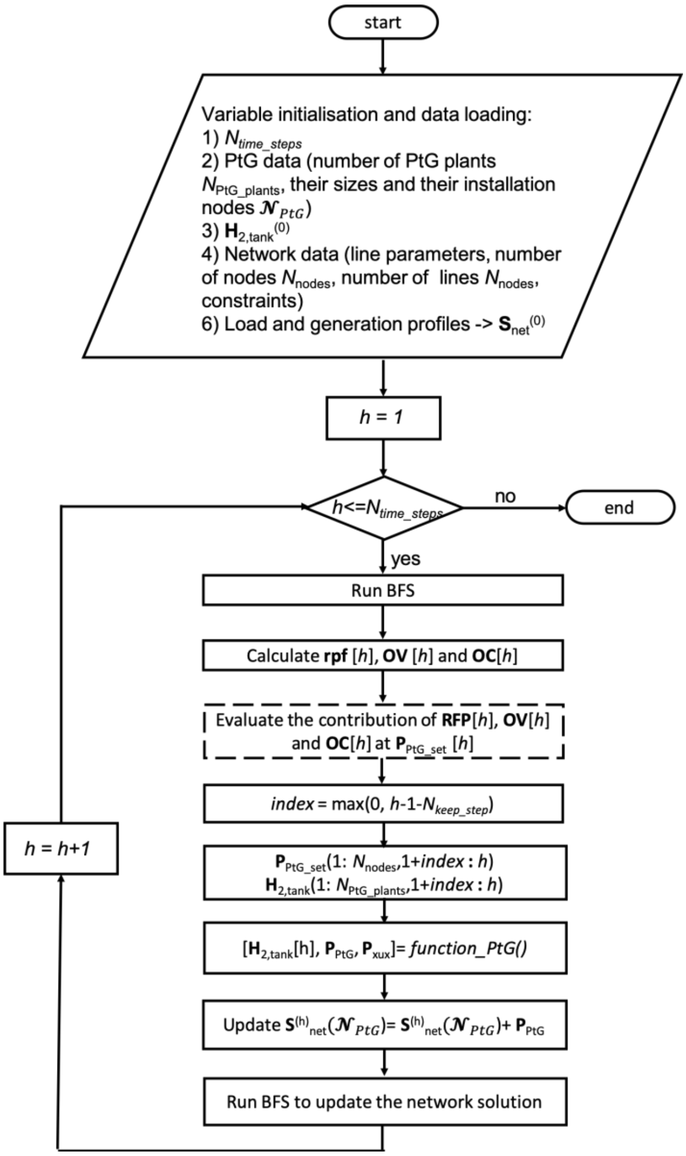

Figure 3.7. The main calculation loop of the distribution system. The function called *function_PtG* represents the PtG complete model.

Table 3.3. Input parameters of the main calculation loop.

Inputs	**Description**
N_{time_steps}	Number of time steps of the analysis
PtG data	Number of the PtG plants N_{PtG_plants}, their positions (indicated by the nodes contained in the set $\mathcal{N}_{PtG}$) and their sizes
$\mathbf{H}_{2,\ tank}^{(0)}$	Initial value of the matrix of dimensions $\{N_{PtG\_plants}, N_{time\_steps}\}$ representing the volume of H_2 in the tank in time
N_{keep_steps}	Number of points for running PtG model
Network data	Number of nodes N_{nodes}, number of branches $N_{branches}$, line parameters, incidence matrix, rate nodal power, lines thermal limits
Load and generation profiles	Load and generation profiles for evaluating the initial value of the matrix $\mathbf{S}_{net}^{(0)}$, i.e., the net nodal power (dimensions $\{N_{nodes}, N_{time\_steps}\}$)
RPF	Matrix of dimensions $\{N_{branches}, N_{time\_steps}\}$ containing the value of reverse power flow at every time step
OC	Matrix of dimensions $\{N_{branches}, N_{time\_steps}\}$ containing the value of overcurrent for every branch during the time span of simulation

OV	Matrix of dimensions $\{N_{branches}, N_{time\_steps}\}$ containing the value of overvoltages for every node during the time span of simulation
$\mathbf{P}_{PtG\_set}$	Matrix of dimensions $\{N_{PtG\_plants}, N_{time\_steps}\}$ containing the set points of the PtG plants
$\mathbf{P}_{PtG}$	Matrix of dimensions $\{N_{PtG\_plants}, N_{time\_steps}\}$ containing the actual power that the PtG plants are able to accept (linked to their sizes)

After having loaded the inputs, the algorithm runs the BFS for the first time: this is requested for defining the network conditions (i.e., nodal voltages and branch currents). On the basis of this, the h-th column of the matrix **RPF** (containing the value of RPF at every branch the interaction h) is updated. At the same time, the h-th columns of both matrices **OV** and **OC** are updated with the values of overvoltage and overcurrent, respectively. On the basis of the above values, a *compound set point* $\mathbf{P}_{PtG\_set}[h]$ is produced, and is referred to the *RPF* and overcurrent value of the branch upstream with respect to the node of the PtG plant, while the contribution regarding the overvoltage is linked to the overvoltage value of the node where the PtG plant has been installed as presented in equation (3.6), i.e.,

$$\mathbf{P}_{PtG\_set}[h] = f(\mathbf{RPF}[h], \mathbf{OV}[h], \mathbf{OC}[h]) \tag{3.6}$$

In particular, the different set point components are set as follows:

- *Component referring to the RPF*: this component is equal to value of power needed for eliminating the reverse power flow in the upstream branch with respect to the node where the PtG plant is installed.
- *Component referring to the OC*: this component is equal to the value of power that, absorbed from the PtG plant, would help to reduce (at 80% of the thermal limit) the current flowing in the upstream branch with respect to the node where the PtG plant is installed.
- *Component referring to the OV*: this component is equal to the value of power that, absorbed from the PtG plant, would help to reduce (at 1.05 pu) the voltage of the node where the PtG plant is installed.

3.3.3. Installation and sizing of the PtG plants

The study of the impact of the PtG plants on the distribution system requires to i) choose the node where the plants are installed and ii) their sizes. These two elements are requested by the calculation loop shown in Figure 3.7, and in this work have been solved by applying the Simulated Annealing (SA) method [174]. It is worth noting that the main goal of this paper is not introducing a new algorithm for the siting and sizing of the PtG plants; but creating meaningful case studies to get insights regarding the *impact of the PtG plants* on distribution system operation. However, the step regarding the siting and sizing is requested as preliminary task, for emulating the process that, in the future, could bring to rationally install a defined number of MW-scale PtG plants. Few notes regarding the use of the SA in this work are reported in Section 3.3.4.

The objective functions used in the algorithm have as main variables the value of reverse power flow, overcurrent and overvoltage of the network. In particular, the network with the installed PtG plants (denoted as **X**) can be affected by:

- Only reverse power flow
- Reverse power flow and overcurrent
- Reverse power flow and overvoltage
- The combination of the last two cases

All the cases make use of a penalised objective function where the constraints of the problem are integrated within the objective function through penalisation factors indicated with the Greek letter ρ. This approach allows to drive the optimisation towards solution with no (or only slight) constraints violations. In particular, the operational constraints are the voltages V_j of the network nodes and the currents I_b flowing in the network branches, which have to respect the following ranges:

- $V_j^{(min)} \leq V_j \leq V_j^{(max)}$, with $j \in \mathbf{J}$, where $\mathbf{J}$ denotes the set of nodes. The node voltage is usually expressed in per unit (pu) with respect to the nominal voltage. (i.e., V_j=1 means that the voltage value of the node j is equal to the nominal voltage of the system). Usual values of the extremes of the range are $V_j^{(min)} = 0.9$ pu and $V_j^{(max)} = 1.1$ pu.
- $I_b \leq I_b^{(th,max)}$, with $b \in \mathbf{B}$, where $\mathbf{B}$ denotes the set of branches. The value of $I_b^{(th,max)}$ is strictly depending on the conductors installed.

The objective function at the iteration k of the method in case of existence of the sole reverse power flow is shown in equation (3.7):

$$f_k(\mathbf{X}) = \frac{RPF_k}{RPF_0} \cdot \left(1 + \sum_{j \in \mathbf{J}} \rho_V \left(\frac{V_j^{(max)} - V_j^{(worst)}}{V_j^{(max)}} \right)^2 + \sum_{j \in \mathbf{J}} \rho_V \left(\frac{V_j^{(min)} - V_j^{(worst)}}{V_j^{(min)}} \right)^2 + \sum_{b \in \mathbf{B}} \rho_I \left(\frac{I_b^{(th,max)} - I_b^{(worst)}}{I_b^{(max)}} \right)^2 \right) \tag{3.7}$$

The penalised objective function at the iteration k is expressed in pu with respect to the value of the reverse power flow in the initial configuration. The reverse power flow is evaluated here through the number of minutes in which it is present during the entire period of analysis. The formulation penalises (through the factors ρ_V and ρ_I) all the configurations that do not respect the operational constraints (i.e., maximum and minimum voltage, and thermal limits) of the network. Thus, the constraints of the objective function (3.7) are the operational constraints of the network $V_j^{(max)}$, $V_j^{(min)}$ and $I_b^{(th,max)}$, for node j and branch b, respectively. For every node/branch the *worst* condition (e.g., the maximum value of current $I_b^{(worst)}$ during the day) is chosen as representative value to force the worst condition respects the imposed constraint.

When both overcurrent and reverse power flow exist in the initial configuration, the objective function is modified as reported in equation (3.8):

$$f_k(\mathbf{X}) = \left(\frac{RPF_k}{RPF_0} + \frac{OC_k}{OC_0}\right) \cdot \left(1 + \sum_{j\in\mathbf{J}} \rho_V \left(\frac{V_j^{(max)} - V_j^{(worst)}}{V_j^{(max)}}\right)^2 + \sum_{j\in\mathbf{J}} \rho_V \left(\frac{V_j^{(min)} - V_j^{(worst)}}{V_j^{(min)}}\right)^2\right) \tag{3.8}$$

In this case, the objective function is still expressed in pu with respect to the initial configuration. The normalised sum of the minute of overcurrent and the minute of reverse power flow during the entire day are modified according to the product of the penalty factors and the value of the constraint violation. In this case, the constraints of are the maximum and the minimum voltage vale, indicates as $V_j^{(max)}$ and $V_j^{(min)}$, respectively.

The objective function in case both overvoltage and reverse power flow exist is shown in equation (3.9) and differs with respect to equation (3.8) only for the constraints considered, i.e., related to the branch thermal limits $I_b^{(th,max)}$ and the minimum nodal voltages $V_j^{(min)}$:

$$f_k(\mathbf{X}) = \left(\frac{RPF_k}{RPF_0} + \frac{OV_k}{OV_0}\right) \cdot \left(1 + \sum_{j\in\mathbf{J}} \rho_V \left(\frac{V_j^{(min)} - V_j^{(worst)}}{V_j^{(min)}}\right)^2 + \sum_{b\in\mathbf{B}} \rho_I \left(\frac{I_b^{(th,max)} - I_b^{(worst)}}{I_b^{(max)}}\right)^2\right) \tag{3.9}$$

When all the issues listed above (i.e., reverse power flow, overvoltages and overcurrents) affect the grid, then the objective function is changed to solve them, as shown in equation (3.10):

$$f_k(\mathbf{X}) = \left(\frac{RPF_k}{RPF_0} + \frac{OV_k}{OV_0} + \frac{OC_k}{OC_0}\right) \cdot \left(1 + \sum_{j\in\mathbf{J}} \rho_V \left(\frac{V_j^{(min)} - V_j^{(worst)}}{V_j^{(min)}}\right)^2\right) \tag{3.10}$$

It is worth noting that in equation (3.9) the constraint related to the minimum voltage value is still considered as part of the penalized objective function, to avoid that the worst value reached by the voltages in the period under analysis $V_j^{(worst)}$ are below the minimum allowed value $V_j^{(min)}$.

As final comment, the above objective functions are chosen *a priori* according to the network issues affecting the distribution system under analysis.

3.3.4. Simulated Annealing algorithm

The Simulated Annealing (SA) algorithm is composed of an external loop, as shown in Figure 3.8.

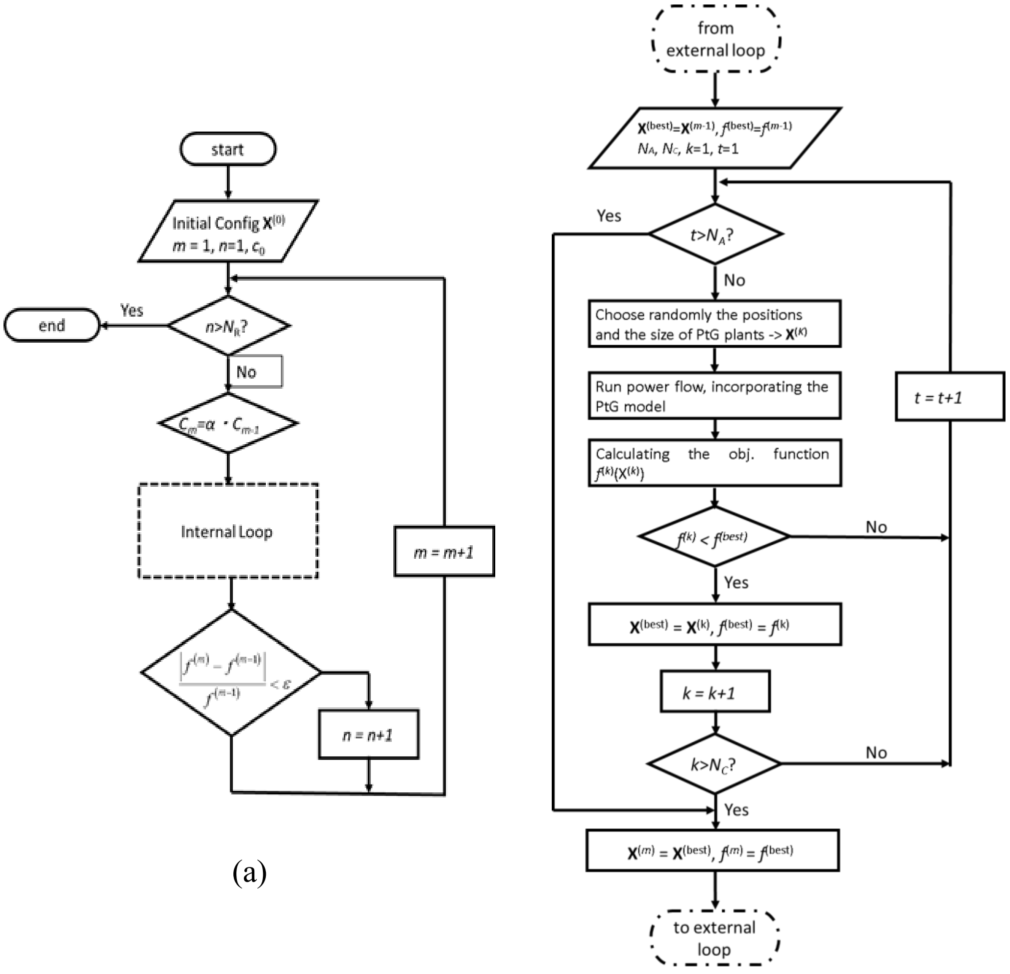

(a)

(b)

Figure 3.8. The external loop (a) and the internal loop (b) of the SA used for siting and sizing.

The external cycle depends on a control parameter called C, whose initial value is named C_0. For every iteration $m > 0$ of the external cycle, the control parameter is updated with a certain velocity described by the cooling rate, i.e.:

$$C_m = \alpha \cdot C_{m-1} \tag{3.11}$$

The stop criterion of the external cycle is based on the persistence of the solution found so far: once the solution found persists (or the changes are below a certain threshold) for at least N_R successive iterations, the external cycle stops.

At each iteration of the external cycle, the internal cycle is run. For every iteration m of the external cycle, the inputs of the internal cycle are:

- *Initial configuration* $\mathbf{X}^{(best)}$ and its objective function $f^{(best)}$: it refers to the best configuration found so far (the solution provided as output at the iteration m-1)
- *Value of the control parameter* C_m
- *Number of solutions to be analysed* N_A
- *Number* of solutions to be accepted N_C

The last two inputs are necessary for the stopping criterion of the internal cycle, which is composed as follows: the internal cycle stops when either N_C or N_A are reached. The first condition is usually reached with high C_m (i.e., when many new solutions are accepted), whereas the second condition is usually reached with low C_m (i.e., when the number of accepted solutions decreases, up to the final internal cycles before stopping, in which there is no acceptance of new solutions).

3.4. Results and discussion

3.4.1. Yearly simulation

Network performance indexes

Different PV penetrations have been assumed for the creation of the case studies. The penetration has been calculated in terms of *percentage the energy* provided by the PV plants with respect to the system passive load considering the PV production in July. In the case with 40% of PV penetration, the production in July covers 40% of the passive load. According to this, the PV penetration in other months varies following the different PV profiles.

The considered case studies and the existing problems in the different cases are shown in Table 3.4 and Table 3.5, for the semi-urban network and the rural network, respectively. The tables show entries different from zeros when that kind of problem exists, and the entry indicates the magnitude of the problem. The label "Pre" in the table indicates the magnitude of the problem without PtG installed, whereas the label "Post" refers to the condition when PtG plants have been installed. The RPF has been indicated in MWh, whereas the OC and OV are expressed in minutes.

The values refer to yearly simulations. The two tables show the number of plants installed and, only for the rural network, the size of the plants as well. Due to the large number of plants installed in the case of semi-urban network, the sizes of the plants are summarised in Figure 3.9.

Table 3.4. Case studies for the semi-urban network.

Case number	Length [km][*]	PV penetration	RPF [MWh]		OC [min]		OV [min]		Number of PtG plants
			Pre	Post	Pre	Post	Pre	post	
1	$0<L\leq 0.45$	40 %	11298	9.37	-		-	-	7
2		80 %	151920	33654	90616	35	-	-	20
3	$0.5\leq L\leq 3$	40 %	10213	31.4	430087	6978	3356	0	12
4		60 %	71272	7165	2388634	25156	900407	0	17

[*] The length refers to the branches of the MV semi-urban network

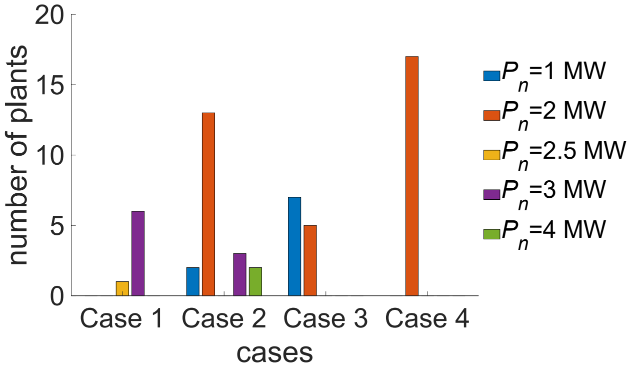

Figure 3.9. Number and sizes of the PtG plants installed in the semi-urban network.

Table 3.5. Case studies for the rural network.

Case	Method PV placement	Length* [km]	PV penetration	RPF [MWh]		OC [min]		OV [min]		Number of PtG plants	Size [MW]
				pre	post	pre	post	pre	post		
5	Topological	$0<L\leq0.9$	40%	266.27	0	-	-	-	-	1	2.5
6			80 %	19861	1633.9	165047	0	504	-	4	2 (all)
7		$2\leq L\leq3$	40 %	248.99	0.10	-	-	-	-	1	2
8			80 %	19206	3337.4	-	-	276329	0	4	2 (three plants) 1.5 (one plant)
9	Loss allocation	-	40 %	167.9	0	-	-	-	-	2	2 (all)
10			80 %	20991	1868.4	-	-	-	-	4	2 (all)

*The length refers to the branches of the MV network

First of all, it is evident that, while in the rural network is possible to obtain cases with problems of overvoltages and reverse power flow, in the semi-urban network is difficult to decouple overvoltage and overcurrent. This is linked with the nature of the lines composing the networks, which are highly resistive for the rural network because mostly composed of long overhead lines.

It is worth noting that, as demonstrated through the rural network, the reverse power flow issue is not strictly linked to overvoltage problems, but these two aspects can be decoupled through a suitable installation of PV generation (as the one guaranteed by the procedure shown in [167]).

From the two tables it is evident that the deployment of PtG has a positive impact on alleviating the grid issues.

For the *semi-urban network*, in the cases in which the PV is installed at the end of lines with length L lying in the range $0<L\leq0.45$, the impact of PtG is really powerful because both cases reveals how the reverse power flow can be strongly reduced: in fact, in case of PV penetration equal to 40% the reduction is over 99.9% (passing from almost 11.3 GWh to 9.37 MWh), whereas with PV penetration equal to 80% the reduction is almost 78% (passing from almost 152 GWh to 34 GWh). In the cases with PV plants installed at the end of lines with length L lying in the range $0.5\leq L\leq3$, the reduction of reverse power flow is stronger for lower PV penetration (more than 99.6% with PV penetration equal to 40%), but is anyway high also with PV penetration equal to 60% (the reverse power flow reduction

reached almost 90%). Residual problems of overcurrents appear in all the cases except the case number 1.

By analysing the worst case (i.e., the one with PV penetration equal to 60%), these issues affect in total thirteen branches, and the number of minutes in which the lines are overloaded lies between 4 to 5456 minutes, whereas the maximum overload conditions at which they operate lies in the range between 2.24% and 13.39%, as shown in Table 3.6. The system operator has to act for establishing again the proper network conditions, because the alleviation effect of the PtG deployment cannot solve completely the overcurrent issues.

Table 3.6. Analysis of the overloaded lines in of semi-urban network, with 60% of PV penetration.

Lines overloaded	Cumulative overload period [min]	Maximum overloading [%]
6	284	11.47
32	13	9.02
152	79	13.39
155	5032	9.05
156	4747	8.86
157	5456	10.10
159	2717	6.12
161	910	17.33
165	1395	2.43
169	4382	7.62
170	123	13.10
185	4	2.24
196	14	4.78

For the rural network, in the cases in which the PV is installed at the end of lines with length L lying in the range $0<L \leq 0.45$, the impact of PtG is really powerful because in one case (i.e., PV penetration equal to 40%) the reverse power flow is completely solved, whereas in the case with 80% of PV penetration the reverse power flow is strongly reduced, passing from 19.861 GWh to 1633.9 MWh (reduction of almost 92%). In the cases with PV plants installed at the end of lines with length L lying in the range $2 \leq L \leq 3$, the reduction of reverse power flow is stronger in case of lower PV penetration (almost 100% with PV penetration equal to 40%), but is anyway high also with PV penetration equal to 80% (the reverse power flow reduction reached almost 83%).

Finally, the case created with the rural network by using the loss allocation shows that the reverse power flow problem can be solved in case of 40% of PV penetration, whereas a residual reverse power flow remains for the case 80% (but even in this case the reduction is more than 90%).

Capacity factors

The successful use of PtG plants needs a justification in terms of plant use, i.e., a *capacity factor* high enough.

The capacity factor $C_f^{(i)}$ referred to the i-th PtG unit is the ratio between the energy $E_{PtG}^{(i)}$ consumed by the i-th PtG unit during the simulation period Δt and the theoretical energy that the plant would be able to absorb during the same time period if it had consumed its nominal power; it was calculated according to equation (3.12):

$$C_f^{(i)} = \frac{E_{PtG}^{(i)}}{P_{n,PtG}^{(i)} \cdot \Delta t} \tag{3.12}$$

where $E_{PtG}^{(i)}$ is the consumed energy during the simulate time horizon Δt by the i-th PtG plant and $P_{n,PtG}^{(i)}$ is the nominal power of the i-th PtG plant.

Figure 3.10 shows the capacity factors for the semi-urban network. It shows that in the Case 1 the plants result underused, and thus the number of plants chosen is too high. A reduction of the number of plants installed could lead to a more fruitful use of the plants. In Case 2, only one plant results underused (i.e., having capacity factor equal to 23%), whereas the other plants are quite well exploited.

Case 3 presents 12 plants having a capacity factor lying in the range 40%-50%, whereas the remaining has a capacity factor between 50 and 60%.

Finally, Case 4 presents three plants with capacity factor lower than 40% (i.e., from 28% to 37%), whereas all the other plants are well exploited (minimum about 51%).

From the results it is evident that the number of plants installed has a great impact and need to be carefully considered. The analysis carried out, in any case, neglects the presence of suitable gas network points: in the reality, the presence of real infrastructures will limit the potential nodes where PtG can be installed to a smaller number than the one considered here.

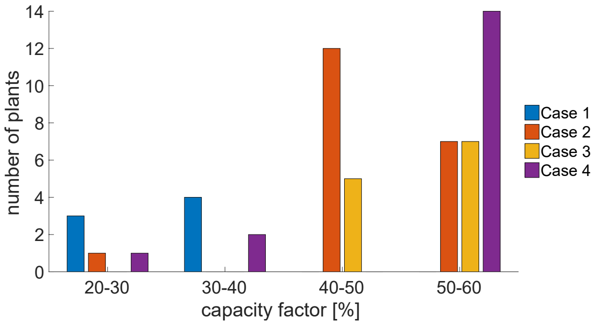

Figure 3.10. Capacity factors for the different cases of semi-urban network.

In the case of the rural network, the results are summarised in Table 3.7. With respect the previous case, the minimum capacity factor results higher than 60% in all the cases and reaches almost 90% in one case. The results in the table indicate also for this case that PtG can handle very well the issues created from PV generation installed at the end of relatively long lines, by maintaining a sufficiently high capacity factor.

Table 3.7. Yearly capacity factors for the rural network.

Case	PV penetration	Min capacity load [%]	Max capacity load [%]
5	40%	47.55	-
6	80 %	43.47	54.96
7	40 %	47.10[4]	-
8	80 %	48.50	56.0
9	40 %	43.07	49.26
10	80 %	45.68	50.88

A good performance index of the network is the value of the power losses, which are summarized in Table 3.8.

The value of the losses (in MWh and in percentage) reduce in all the cases. This reduction is obtained thanks the installation of the plants that help to improve the network operation.

Table 3.8. Network losses for both the semi-urban network and the rural network.

Case	Power Losses [MWh]		Power Losses [%]		Case	Power Losses [MWh]		Power Losses [%]	
	pre	post	pre	post		pre	post	pre	post
1	2122.5	2314.9	0.95	0.20	5	1,149.8	1,128.9	2.22	1.82
2	3445.1	2902.4	7.36	0.69	6	2040.0	1,363.1	9.34	2.38
3	3779.0	3278.7	1.71	0.28	7	1142.5	1042. 1	2.21	1.74
4	6517.5	4082.1	4.86	0.50	8	2,683.5	1,972.0	12.29	3.82
					9	1263.9	1,205.9	2.42	1.77
					10	20,991	1358.0	7.68	2.51

Another performance indicator is the maximum and minimum voltage magnitude, whose values for both semi-urban and rural networks are shown in Table 3.9. It is evident the effect of PtG to reduce the voltage at levels that are lying within the admissible ranges.

Table 3.9. Minimum and maximum voltage magnitude for both semi-urban and rural networks.

Case	Minimum voltage [pu]		Maximum voltage [pu]		Case	Minimum voltage [pu]		Maximum voltage [pu]	
	pre	post	pre	post		pre	post	pre	post
1	1.00	1.00	1.04	1.03	5	0.93	0.93	1.05	1.04
2	1.00	1.00	1.06	1.05	6	0.93	0.93	1.11	1.06
3	1.00	1.00	1.11	1.09	7	0.93	0.93	1.07	1.03
4	1.00	0.93	1.15	1.04	8	0.93	0.93	1.14	1.09
					9	0.93	0.92	1.05	1.01
					10	0.93	0.93	1.06	1.05

3.4.2. Network effect

This section aims to highlight the role of the network infrastructure in the proper evaluation of the effect of the PtG deployment.

In fact, some approaches existing in literature (e.g., [3]) do not consider the existence of the electrical infrastructure, but only the potential unbalance between local generation and loads. However, this approach could not be proper for solving completely the issue caused by the excess of RES.

Taking as example a particular day of Case 5 (the day considered has as PV profile the one shown in Figure 3.5b, Month July), the difference between generation and loads, without taking into account the network is shown in Figure 3.11. The same figure also reports the actual reverse power flow existing in the network. The two curves are quite similar, but the first one overestimates the actual reverse power flow value.

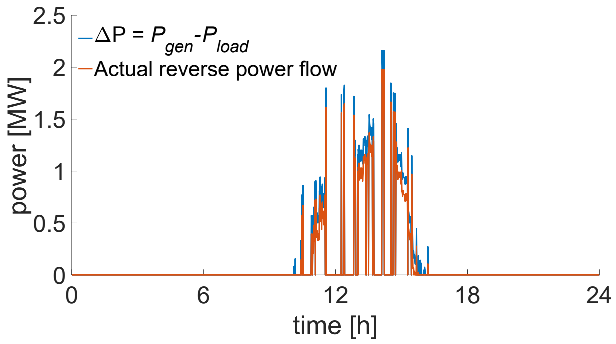

Figure 3.11. Comparison between the actual reverse power flow (with and without the network).

For the sake of clarity, the rural network schematic is shown in Figure 3.12.

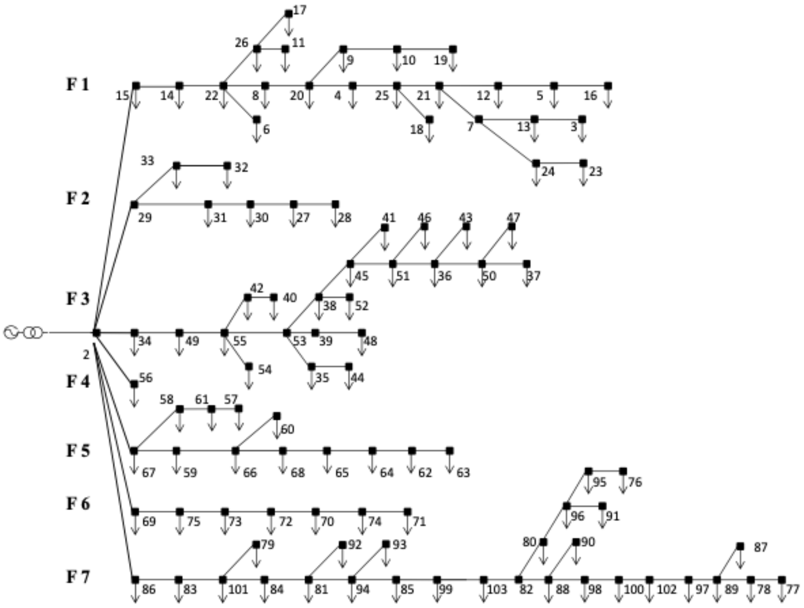

Figure 3.12. Rural network.

The installation of plants characterised by different size at node 2 (connected to the network slack node) instead of node 83 (as in Case 5) leads to the results shown in Table 3.10. The solutions show that the reverse power flow issue can be almost completely solved by using a plant with smaller size than the one referring at Case 5. This may lead to think that the solution of Case 5 could be not be optimal, because of the size. However, the capacity factor highlights that the installation of the plant at the node connected to the slack bus does not guarantee a good utilisation of the potential of the plant and thus the installation node should be carefully chosen. Furthermore, the use of the plant with the position and size of Case 5 allows improving the network conditions, in terms of power losses and reverse power flow. This simple example aims to be an effective way to show the importance of the network information to capture all the aspects regarding the new operation of the electrical system when new devices are installed.

Table 3.10. Comparison between the network performance without PtG, with PtG installed without optimisation process and with optimisation process (Case 5).

Size [MW]	Reverse power flow [MWh]	Reverse power flow [min]	Power Losses [MWh]	Power Losses [%]	Capacity factor [%]
0 (no PtG)	2.16	151	3.08	2.29	-
0.5	1.026	143	3.09	2.24	50.81
1	0.284	139	3.096	2.20	44.21
1.5	0.062	135	3.102	2.17	36.02
2	0.025	120	3.108	2.14	30.44
2.5	0.022	110	3.114	2.11	27.03
2.5 (Case 5, Table 3.4)	0	0	3.00	1.85	69.22

3.4.3. Response of the PtG model

The PtG model provides in output the following quantities:

- Power profile sent by the control system to the electrolyser $P_{elec,sp}$;
- Power profile of the electrolyser P_{elec};
- Power profile of the auxiliary services P_{aux}, referring to i) the CO_2 compression system, ii) the circulation of H_2O, iii) the compression of the H_2, and iv) the water heating;
- The hydrogen flow rate sent to the tank $\varphi_{H2,tank}$ (kmol/s);
- The hydrogen sent to the methanation unit directly from the electrolyser $\varphi_{H2,dir}$ (kmol/s);
- The hydrogen sent to the methanation unit from the tank after compression $\varphi_{H2,tank,meth}$ (kmol/s);
- The level of the hydrogen tank (%);
- The SNG produced seen as power profile (MW) or energy profile (MWh).

With reference to the same day considered in Section 3.4.2 of Case 5, $P_{elec,sp}$, P_{elec} and P_{aux}, are shown in Figure 3.13. In Figure 3.13a, it is evident the saturation imposed by the nominal power of the plant. Furthermore, the minimum power required by the AEC is different from zero and has to be provided by the main network. Figure 3.13b, instead, shows the power related to the auxiliary services. Three zones with different auxiliary service power exist, and each of them is characterised by different contributions as highlighted in Figure 3.14. More specifically, during the night no excess of electrical power is available for the PtG plant; therefore, it operates at the minimum power load corresponding to 20 % of the nominal installed power. As illustrated in Figure 3.14a auxiliary consumptions are principally due to the CO_2 compression, while water pumping and H_2 compression are marginal contributions. Subsequently, in the first part of the day (between 6 h and 11 h) the electrical availability increases, and the electrolyser could work in its whole operative range (from 20 % to 100 %); thus, it produces a large amount of H_2, which is mainly stored in the tank until it is completely full. Hence, H_2 compression represents 96% of all auxiliary consumptions, as shown in Figure 3.14b. At the same time, the methanation unit operates at the minimum power load for allowing the tank to be filled, in fact, the CO_2 compression represents 3% of the auxiliary consumptions even though it is the minimum power consumption for compressing CO_2. Lastly, in the second part of the day (between 11 h and 18 h), both the electrolyser and the methanation unit work in their whole operational range and the H_2 tank is entirely full. More in detail, as depicted in Figure 3.14c, H_2 has not to be compressed and the CO_2 compression cost increases as the CO_2 flow rises (H_2 and CO_2 are fed in stoichiometric ratio to the methanation unit). Furthermore, all these aspects of the process are clearly illustrated in Figure 3.15. As shown in Figure 3.15a and Figure 3.15b, the H_2 tank is filled during the first hours of the day, when there is a large excess of electrical energy availability. Subsequently, both the electrolyser and the methanation unit operate for producing SNG, as depicted in Figure 3.15b and Figure 3.15c. In this case study (Case 5), the alkaline electrolyser absorbs 28 MWh of electricity, which is converted into 237.4 kmol of H_2 (15.8 MWh, LHV basis). Initially, the produced H_2 is partially stored in the tank (50.9 kmol) until it is completely full; subsequently, the H_2 flow is sent to the methanation unit for producing SNG (10.4 MWh, LHV basis). In this case study, the auxiliaries require 0.21 MWh of electrical energy during the whole day. It is worth noting that the tank is not discharged because the minimum operative power set for the electrolyser was assumed to be 20% (as specified in Section 3.2), which is equal to the minimum flow required by the methanation unit. However, the model includes also the storage system, which can intervene if a different control is applied.

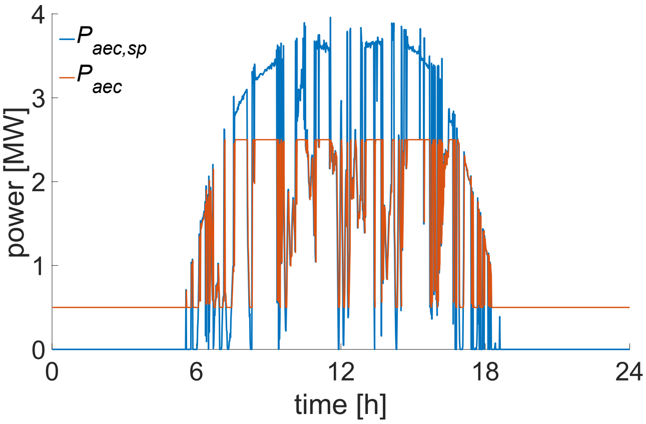

(a)

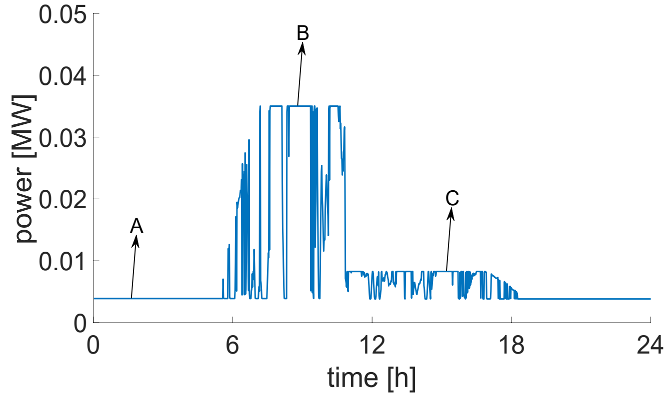

(b)

Figure 3.13. Electrical quantities provided by the PtG model: (a) input power profiles and (b) power profile of the auxiliary services.

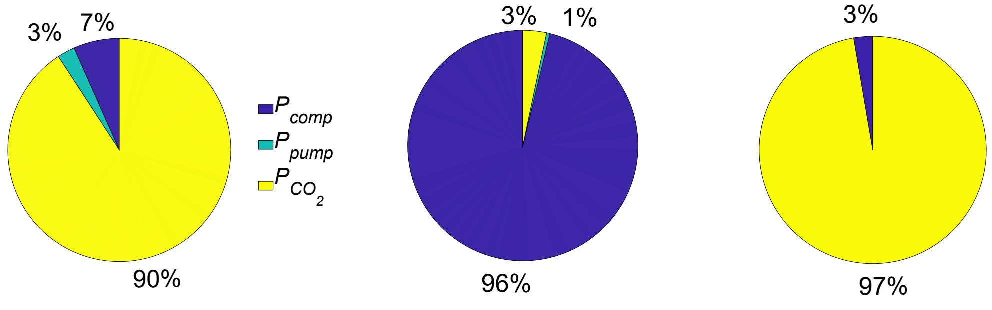

(a) (b) (c)

Figure 3.14. Comparison of the auxiliary services in the different periods of the day.

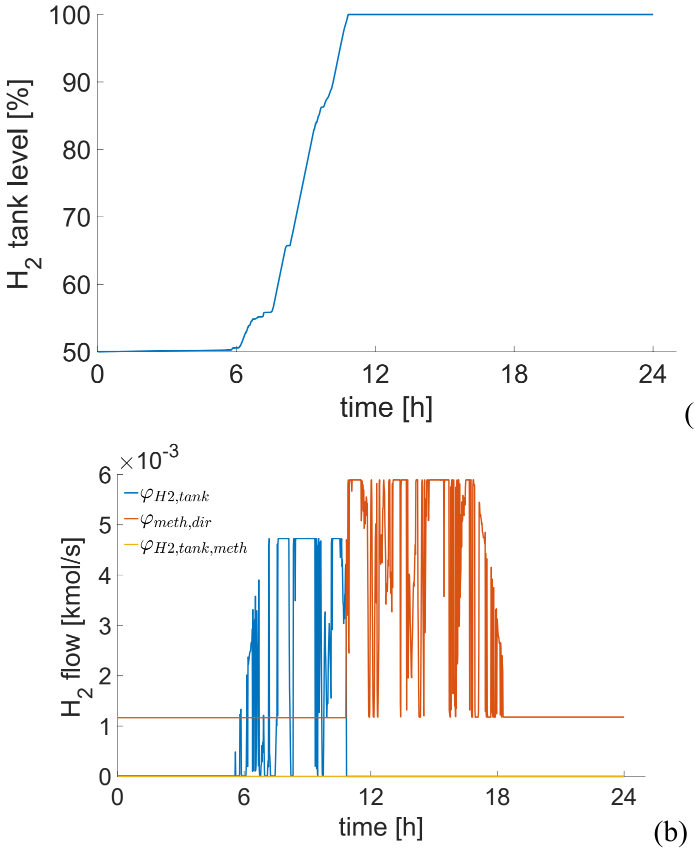

(a)

(b)

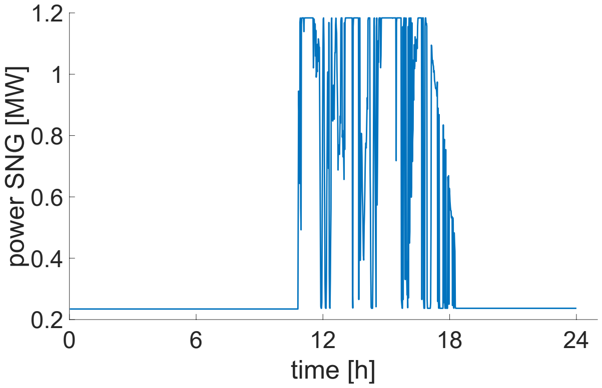

Figure 3.15. (a) H_2 tank filling, (b) H_2 molar flow rates and (c) SNG productivity of the PtG plant.

3.5. Conclusions

This chapter presented a detailed study regarding the impact of PtG technology on the electrical distribution system. The study takes into account both electrical aspects and information related to the process chain leading to the SNG production.

Thanks to the physical model of the PtG plant, the evaluation of the values of its internal variables (e.g., hydrogen flows) can be checked, and this allows acting on the downstream portion of the plant, i.e., methanation plant and hydrogen buffer.

Furthermore, the request of energy to supply the auxiliary services can be successfully evaluated. It is worth noting that the plant layout can be changed, both in terms of control and in terms of components adopted.

From the electrical point of view, this chapter shows that the evaluation of the impact of PtG plants on the distribution system has to be considered the local network conditions, because different network samples lead to different problem to be solved. The knowledge of the type of network where the plants will be installed is, thus, fundamental and has been presented here by considering two network samples.

Furthermore, the level of RES penetration is another important aspect to be considered, due to the different network issues introduced. From the paper results it was evident the difference between alert and emergency network operation, which linked to different variables (reverse power flow and network constraints, respectively).

For the semi-urban network, the number and the sizes of the PtG plants are higher than the ones used for the rural network, due to the higher number of nodes and higher load. The results obtained are beneficial, with a reduction of the reverse power flow energy falling in the range 78-100%, with better performances for lower PV penetration. Furthermore, in all the cases the installation of PtG plants has reduced the network losses of the network and no problems of undervoltages have been found in the during the year, even with scares solar radiation (i.e., in winter months).

By considering the rural network the case $0 < L \leq 0.9$ km sees a reduction of the reverse power flow energy falling in the range 92-100%, whereas in the case $2 \leq L$

≤ 3 km the reduction lies in the range 83-100%. In all cases, the installation of PtG is also able to alleviate the problems due to violations of constraints if PtG is absent, by reaching the complete elimination of these violations for the lower PV penetrations.

The load factor of the plants provides information on how much a PtG plant is used: these values strongly depend on the network conditions (correlated to the PV penetration value), as well as on the positioning of the PtG and on the size. The values of capacity factors is higher for rural network than for semi-urban network: in fact, the minimum capacity factor values for the rural network is around 50% whereas for the rural network can fall up to 21%.This suggests that the installation of PtG plants at the level of distribution system has to be made by considering the local characteristics of the network.

All the performances of the plants have been obtained by considering the network effect and has been shown with an effective evidence that neglecting its presence can lead to wrong results (e.g., lower capacity factor or slight over-estimation of the reverse power flow).

In conclusion, it can be said that the addition of PtG systems in a distribution network can stabilise the network even for very high (even extreme) RES penetrations, thus increasing the ability of a network to host higher penetration of intermittent generation. The deployment of the plants in the real network needs to be considered the presence of a proper gas network, to be fed with the renewable synthetic gas that, having the same characteristics of the natural gas, open new perspectives to decarbonise the entire energy system.

Chapter 4

Copper-ceria catalysts for CO_2 hydrogenation to methanol

4.1. Introduction

As previously introduced in Chapter 1, climate change is a problem that must be addressed to reduce global warming, and negative impacts on the ecosystem, society and human health. On the one hand, a strategy to improve the management of the exploitation of RES-based power sources is the storage of energy in an energy carrier such as H_2. On the other hand, the scientific community has begun to consider CO_2 as a resource to obtain fuels or chemicals by closing the carbon cycle and reducing the consumption of non-renewable energy from fossil sources. Among the CO_2 hydrogenation products, methanol seems to be one of the most promising and versatile molecules that can be used as a renewable fuel or as a solvent in the chemical industry. More specifically, this chapter of the thesis focuses on the study of catalysts for CO_2 hydrogenation to methanol.

In the context of the CO_2 hydrogenation to methanol, the bimetallic copper-ceria system has been little studied in the literature due to its apparent low catalytic performances and no structural effects of ceria nanoparticles [42]. However, Graciani et al. [48] has studied copper-ceria and copper-ceria-titania systems for CO_2 hydrogenation to methanol obtaining particularly active catalytic systems with catalytic performances better than Cu/ZnO bimetallic systems. More specifically, Graciani et al. [48] have reported theoretical and experimental evidence that CO_2 efficiently converts to methanol at the interface of copper and ceria. Furthermore, they have proved that the conversion of CO_2 to methanol occurs in two steps: the first is the formation of CO and subsequently CO is hydrogenated to methanol.

This chapter is dedicated to the development of Cu and Ce-based catalysts for the hydrogenation of CO_2 to methanol. According to the literature, Cu and Ce seem to have a synergistic effect in the activation of CO_2 and in its hydrogenation to methanol [42,48]. As mentioned, some authors have obtained promising results [48], so mixed Cu-Ce catalysts have been investigated in more detail within the Italian project SATURNO [49]. The catalysts based on Cu and Ce were synthesized with three different synthesis techniques (wet impregnation, solution combustion synthesis and gel-oxalate coprecipitation) by varying the composition of the material. Subsequently they were characterized with N_2 physisorption, X-ray diffraction (XRD), temperature programmed reduction (H_2-TPR) and desorption

(CO_2-TPD), ICP-MS, FE-SEM and EDS analyses. Furthermore, the catalysts were tested in an experimental test bench to determine their catalytic performance.

4.2. Methodology

4.2.1. Preparation of the catalysts

The catalysts presented in this chapter were prepared by using three different synthesis techniques: solution combustion synthesis (SCS), wet impregnation (WI) and gel-oxalate co-precipitation (OX).

Solution combustion synthesis

An aqueous solution at 0.15 M of metal precursors (i.e. copper and cerium nitrates) and fuel (urea) was prepared. The fuel-to-oxidizer molar ratio (φ) between urea and nitrates was optimized and it is described in further paragraphs. The aqueous solution was stirred at room temperature for 30 min in order to completely dissolve the solids. Subsequently, it was poured into a ceramic crucible and placed in a muffle to perform the synthesis [175,176]. The oven temperature was heated up from room temperature to 400 ° C (+5 °C/min) and kept at 400 °C for 30 min. Lastly, the catalyst was cooled down and grounded to obtain the powder. The reactions involved during the synthesis are described in equations (4.1), (4.2) and (4.3).

$$2\,Cu(NO_3)_2 \longrightarrow 2\,CuO + 2\,N_2 + 5\,O_2 \tag{4.1}$$

$$2\,Ce(NO_3)_3 \longrightarrow 2\,CeO_2 + 3\,N_2 + 7\,O_2 \tag{4.2}$$

$$2\,CO(NH_2)_2 + 3\,O_2 \longrightarrow 4\,H_2O + 2\,CO_2 + 2\,N_2 \tag{4.3}$$

Regarding the fuel-to-oxidizer molar ratio, three different catalysts with the same composition (40 %at Cu and 60 %at Ce) were prepared at three different fuel-to-oxidizer ratios (i.e. sub-stoichiometric, stoichiometric and over-stoichiometric):

- $Cu_{40}Ce_{60}$-SCS_{50}: φ is sub-stoichiometric an equal to 0.5;
- $Cu_{40}Ce_{60}$-SCS_{100}: φ is stoichiometric an equal to 1.0;
- $Cu_{40}Ce_{60}$-SCS_{200}: φ is over-stoichiometric an equal to 2.0.

As described in further sections, the stoichiometric fuel-to-oxidizer ratio was considered as the optimal condition. Therefore, five catalysts were prepared varying their composition and keeping constant the fuel-to-oxidizer ratio (φ equal to 1):

- Cu_{100}-SCS_{100}: pure copper oxide (100 %at Cu) was prepared as reference;
- $Cu_{40}Ce_{60}$-SCS_{100}: the catalyst nominal composition is 40 %at Cu and 60 %at Ce;
- $Cu_{60}Ce_{40}$-SCS_{100}: the catalyst nominal composition is 60 %at Cu and 40 %at Ce;

- $Cu_{80}Ce_{20}$-SCS_{100}: the catalyst nominal composition is 80 %at Cu and 20 %at Ce;
- Ce_{100}-SCS_{100}: pure ceria (100 %at Ce) was prepared as reference and it was used as the support in the wet impregnation.

Wet impregnation

A porous support (i.e. Ce_{100}-SCS_{100}) was suspended in an aqueous solution of the precursor (i.e. copper nitrate) of the active phase; subsequently, the solvent was evaporated at 90°C keeping the solution stirred until it was completely dry. The impregnated powder was then calcined at 400 ° C (+5 °C/min) for 30 min. As aforementioned, the support is constituted by pure ceria (CeO_2) obtained by means of the SCS method described above and by using a stoichiometric ratio. Four catalysts were synthesised by using this technique:

- $Cu_{13}Ce_{87}$-WI: the nominal composition of the catalyst is 5 %wt Cu of the calcined catalyst, which corresponds to an atomic composition of 12.6 %at Cu and 87.4 %at Ce;
- $Cu_{40}Ce_{60}$-WI: the nominal composition of the catalyst is 18.8 %wt Cu of the calcined catalyst, which corresponds to an atomic composition of 40 %at Cu and 60 %at Ce;
- $Cu_{60}Ce_{40}$-WI: the nominal composition of the catalyst is 32.7 %wt Cu of the calcined catalyst, which corresponds to an atomic composition of 60 %at Cu and 40 %at Ce;
- $Cu_{80}Ce_{20}$-WI: the nominal composition of the catalyst is 51.8 %wt Cu of the calcined catalyst, which corresponds to an atomic composition of 80 %at Cu and 20 %at Ce.

Gel-oxalate co-precipitation

A 0.1 M solution of metal precursors (i.e. copper and cerium nitrates) in ethanol and a 1 M solution of oxalic acid in ethanol. Subsequently, the oxalic acid solution was quickly poured (~1 ml/s) into the nitrate solution (as reported in the literature, an excess of 20% oxalic acid solution was used [177]), which was kept under vigorous stirring at room temperature. The precipitate was aged for 2 h keeping the solution stirred. The gel (precipitate) was separated from the solvent (supernatant) by centrifugation and then it was dried at 60 ° C overnight. Lastly, as reported in the literature, the solid was calcined at 360 ° C for 4 h and then ground in a mortar for obtaining the powder [90,177,178]. Five catalysts were synthesised by means of this technique:

- Cu_{100}-OX: pure copper oxide (100 %at Cu) was prepared as reference;
- $Cu_{40}Ce_{60}$-OX: the catalyst nominal composition is 40 %at Cu and 60 %at Ce;

- $Cu_{60}Ce_{40}$-OX: the catalyst nominal composition is 60 %at Cu and 40 %at Ce;
- $Cu_{80}Ce_{20}$-OX: the catalyst nominal composition is 80 %at Cu and 20 %at Ce;
- Ce_{100}-OX: pure ceria (100 %at Ce) was prepared as reference and it was used as the support in the wet impregnation.

4.2.2. Characterization techniques

Catalysts were characterised by using different techniques: N_2 physisorption, X-ray diffraction (XRD), FE-SEM microscopy, temperature programmed reduction (H_2-TPR), temperature programmed desorption of CO_2 (CO_2-TPD) and ICP-MS. More specifically, calcined, fresh reduced and aged catalysts were characterised to relate their catalytic performances to their characteristics.

Total surface area and porosimetry measurements

Textural properties of both calcined and aged catalysts were determined by N_2 physisorption at -196 °C using a Micromeritics Tristar II ASAP 3020 analyser. The samples (~80 mg) were previously outgassed at 200 °C in inert (N_2) gas for 2 h using a Micromeritics Flow-Prep 060, in order to remove water and other atmospheric contaminants from the surface. The total surface area was calculated by means of equation (4.4) according to the Brunauer-Emmett-Teller theory. BET adsorption model is reported in equation (4.5) [179].

$$S_{BET} = \frac{10^{-6} \cdot q_m \cdot N_A \cdot \sigma_{N_2}}{\tilde{v}} \tag{4.4}$$

$$\frac{\frac{p}{p^s}}{q \cdot \left(1 - \frac{p}{p^s}\right)} = \frac{1}{c \cdot q_m} + \frac{c-1}{c \cdot q_m} \cdot \frac{p}{p^s} \tag{4.5}$$

In equations (4.4) and (4.5), S_{BET} (m^2/g_{cat}) represents the specific surface area, N_A ($6.022 \cdot 10^{23}$ mol^{-1}) is the Avogadro's number, σ_{N_2} ($1.62 \cdot 10^{-19}$ m^2) is the N_2 molecular cross-sectional area, $\tilde{v}$ ($2.2414 \cdot 10^{-2}$ Nm^3/mol) is the molar volume of an ideal gas at normal conditions (i.e. 273.15 K and 101325 Pa), p/p^s represents the relative pressure of N_2, q (cm^3_{STP}/g_{cat}) is the amount of N_2 adsorbed, q_m (cm^3_{STP}/g_{cat}) is the amount of N_2 adsorbed in a monolayer and c is the BET constant.

The micropore surface area and volume were evaluated via the t-plot method by using the Harkins and Jura equation (4.6) for the estimation of the statistical thickness (t, Å) [180–182]; p/p^s represents the relative pressure.

$$t = \sqrt{\frac{13.99}{0.034 - \log_{10}\left(\frac{p}{p^s}\right)}} \tag{4.6}$$

The porosimetry analysis was performed by applying the Barrett-Joyner-Halenda (BJH) algorithm to the desorption branch of the isotherm [183,184].

X-ray diffraction (XRD) measurements

Powders of both fresh and aged catalysts were investigated in a Philips X'Pert PW3040 diffractometer operating at 40 kV and 40 mA, using a Ni β-filtered Cu-Kα radiation characterized by a wavelength (λ) equal to $1.5406 \cdot 10^{-10}$ m. X-ray diffraction (XRD) patterns were collected at room temperature over the 2θ angle range of 5°–90°, with a scan step size of 0.013° 2θ and a time per step equal to 0.3 s. The average crystallite size (d_c, nm) was estimated according to Scherrer's equation (4.7) [185], where F_s is a shape factor equal to 0.9, θ (rad) is the Bragg's angle, β (rad) and β_0 (rad) represent respectively the full-width at half maximum (FWHM) of the most intense peak of the phase and the nearest peak of the lanthanum hexaboride (LaB_6) standard.

$$d_c = \frac{F_s \cdot \lambda}{(\beta - \beta_0) \cdot \cos\theta} \tag{4.7}$$

Chemical and morphological analyses

Both calcined and aged catalysts were observed with a field emission scanning electron microscope (FE-SEM) Zeiss Merlin equipped with a Gemini-II column, for the purpose of analysing their morphology. Moreover, energy dispersive X-ray spectroscopy (EDS) was employed to determine the elemental composition of portions of the catalysts. For the sake of clarity, in order to investigate and observe the microstructure of the oxides, the samples were coated with a thin and conductive layer of metal (i.e. Pt) for avoiding charge accumulation phenomena.

Furthermore, for determining the real elemental composition of the catalysts, an inductively coupled plasma mass spectrometer (iCAP Q ICP-MS, Thermo Fisher Scientific) was employed. Each calcined catalyst (~100 mg) was digested in 30 ml of an acid aqueous solution (0.25 M L-ascorbic acid and 3.0 M HNO_3) at room temperature overnight [186]. Each solution was diluted by using deionised water in order to have 100 ml of concentrated solution. After that, each concentrated solution was diluted using deionised water to achieve the concentration of each element within the calibration range (i.e. 100 – 2000 ppb), then these samples were analysed by using ICP-MS.

Temperature programmed reduction (H_2-TPR) measurements

Temperature-programmed analyses were performed in a Thermoquest TPD/R/O 1100 analyser, equipped with a thermal conductivity detector (TCD). For performing temperature-programmed reduction (H_2-TPR) experiments, each calcined catalyst (~20 mg) was placed in a quartz tube reactor between two layers of quartz wool. Each sample was pre-treated in pure O_2 flow (40 ml/min) to ensure the complete oxidation of metals, heating the oven from room temperature to 350

°C [90] with a constant heating rate of 10 °C/min and holding it for 30 min. Subsequently the sample was cleaned in He flow (40 ml/min) at 350 °C for 30 min and then it was cooled to 50 °C. The H_2-TPR was carried out under a constant flow (20 ml/min) of 5.000 %vol H_2/Ar, heating the sample from 50 °C to 900 °C with a heating rate of 10 °C/min.

Temperature programmed desorption (CO_2-TPD) measurements

Temperature-programmed desorption (TPD) analyses were performed in the same equipment described previously (i.e. Thermoquest TPD/R/O 1100 analyser). Similar to the H_2-TPR measurements, each calcined catalyst (~80 mg) was placed in a quartz tube reactor between two layers of quartz wool. Each sample was pre-treated in 5 %vol H_2/Ar flow (40 ml/min) at 350 °C for 1 h for obtaining the fresh reduced catalyst. Subsequently the sample was cooled down to 50 °C in He flow (40 ml/min), saturated with pure CO_2 (40 ml/min) for 30 min at 50 °C and then cleaned in He flow (40 ml/min) for 1 h at 50 °C. The CO_2-TPD was performed by using a constant He flow (20 ml/min) heating the sample from 50 °C to 900 °C with a heating rate of 10 °C/min.

4.2.3. Catalytic tests

The catalytic activity of each sample (catalyst load: 1.0 g) was investigated in a fixed-bed stainless steel reactor. The catalytic bed had an annular section (i.d. 3 mm, o.d. 8 mm) due to the presence of an innertube, in which was inserted a thermocouple for the measurement of the reaction temperature within the catalytic bed. In order to compare the results, all the catalytic tests were carried out keeping constant the weight hourly space velocity (WHSV, $Nl \cdot g_{cat}^{-1} \cdot h^{-1}$). For the sake of clarity, normal conditions were defined at 0 °C (273.15 K) and 101325 Pa.

Concerning the catalytic tests, each sample was pre-treated in situ at 350 °C for 1 h by using 10 %vol H_2/N_2 (30 Nl/h) at 0.2 MPa prior to undertaking the experimental campaign. Subsequently, each sample was tested continuatively (stability test) for 20 h at 275 °C, 2.5 MPa and 20 $Nl \cdot g_{cat}^{-1} \cdot h^{-1}$ (inlet composition: 60 %vol H_2, 20 %vol CO_2 and 20 %vol N_2). After the stabilization, activity tests were performed on each catalyst at 2.5 MPa, 20 $Nl \cdot g_{cat}^{-1} \cdot h^{-1}$ (inlet composition: 60 %vol H_2, 20 %vol CO_2 and 20 %vol N_2) varying the reaction temperature between 200 °C and 300 °C. At the end of the catalytic tests, the catalyst was removed from the reactor, sieved to remove quartz wool fibers and collected to characterise it. For the sake of clarity, catalysts after the catalytic tests were named: aged catalyst. They were analysed because the catalytic material changed during the catalytic tests; therefore, performances are linked to the characteristics of the aged catalyst and not only those of the calcined catalysts.

The gases at the outlet of the reactor were split in two streams. On the one side, a portion of the gases was directly analysed using a gas chromatograph (7890B GC System, Agilent Technologies) equipped with a heated transfer line (120 °C, atmospheric pressure), a two-columns separation system (HP-PLOT/Q and HP-

PLOT Molesieve) connected to a thermal conductivity detector (TCD) and a flame ionization detector (FID). On the other side, water and methanol were condensed in a small tank (room temperature and 2.5 MPa), then the gaseous stream was completely dehydrated using a silica gel trap (room temperature and atmospheric pressure), and it was eventually analysed with an in-line X-STREAM EMERSON gas analyser equipped with two nondispersive infrared (NDIR) sensors and a thermal conductivity detector (TCD) for monitoring CO, CO_2 and H_2 concentrations, respectively.

4.3. Results and Discussion

4.3.1. Surface area and porosimetry

First of all, the specific surface area and the porosimetry of all calcined and aged catalysts were analysed for investigating their textural properties and their variations.

Wet impregnated (WI) catalysts

Considering wet impregnated CuCe samples, Figure 4.1 highlights the relationship between the specific pore volume and the specific surface area of both calcined and aged catalysts; furthermore, it shows their variation with the catalyst composition. It is worth noting that both the specific surface area and the specific pore volume decrease linearly as the Cu loading increases. This trend was ascribed to a progressive occlusion of the porosity of the support (i.e. ceria) caused by the extremely low specific surface area and porosity of CuO [187]. Large size of CuO crystallites and non-porous structure of CuO nanoparticles was confirmed by further characterizations (i.e. XRD, FE-SEM). The change of the slope for low Cu content could be attributed to the distortion of the crystalline structure caused by the formation of a solid solution of Cu atoms in ceria structure during calcination. The maximum value of Cu solubility in CeO_2 is approximately 5%wt; therefore, the correlation is linear at high Cu loadings because the reduction of textural properties is linked to physical causes [188,189].

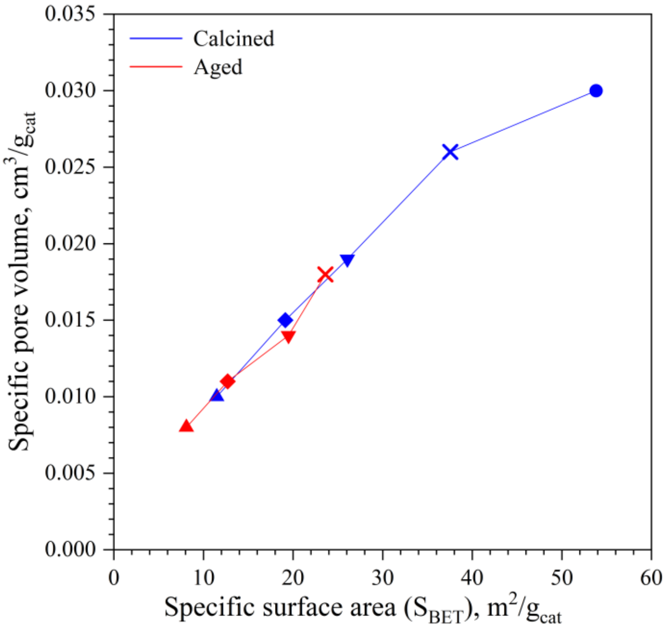

Figure 4.1. Relationship between BET specific surface area and total specific pore volume of both calcined and aged Cu_xCe_{1-x}-WI catalysts. For the sake of clarity, symbols refer to different compositions: ● Ce_{100}-SCS_{100} (bare support); × $Cu_{13}Ce_{87}$-WI; ▼ $Cu_{40}Ce_{60}$-WI; ♦ $Cu_{60}Ce_{40}$-WI and ▲ $Cu_{80}Ce_{20}$-WI.

Solution combustion synthesis (SCS) catalysts

Regarding the solution combustion synthesis, two kind of investigations could be carried out: the effect of the fuel-to-oxidizer ratio and the effect of the composition. Firstly, the fuel-to-oxidizer ratio was varied from 0.5 to 2; as illustrated in Figure 4.2, $Cu_{40}Ce_{60}$ SCS samples exhibited a maximum of specific surface area and pore volume for a stoichiometric φ (i.e. $Cu_{40}Ce_{60}$-SCS_{100}). This behaviour of textural properties was ascribed to two different effect of the increase in φ. On the one hand, the temperature of the material during the synthesis increases as φ rises due to a greater amount of heat released by the combustion of urea. Sintering phenomena prevail at higher temperature; hence, textural properties of $Cu_{40}Ce_{60}$-SCS_{200} diminished dramatically. On the other hand, the quantity of gases (i.e. CO_2, N_2 and O_2) released during the combustion increases as φ rises; therefore, it favours the porosity of the catalyst. In conclusion, the amount of gases produced in sub-stoichiometric conditions is not enough to obtain a high porosity; whereas, in over-stoichiometric conditions the structure collapsed due to sintering phenomena [190]. Hence, according to the volcano plots that are illustrated in Figure 4.2, the stoichiometric fuel-to-oxidizer ratio (i.e. φ equal to 1) was assumed as the best synthesis condition for obtaining good textural properties.

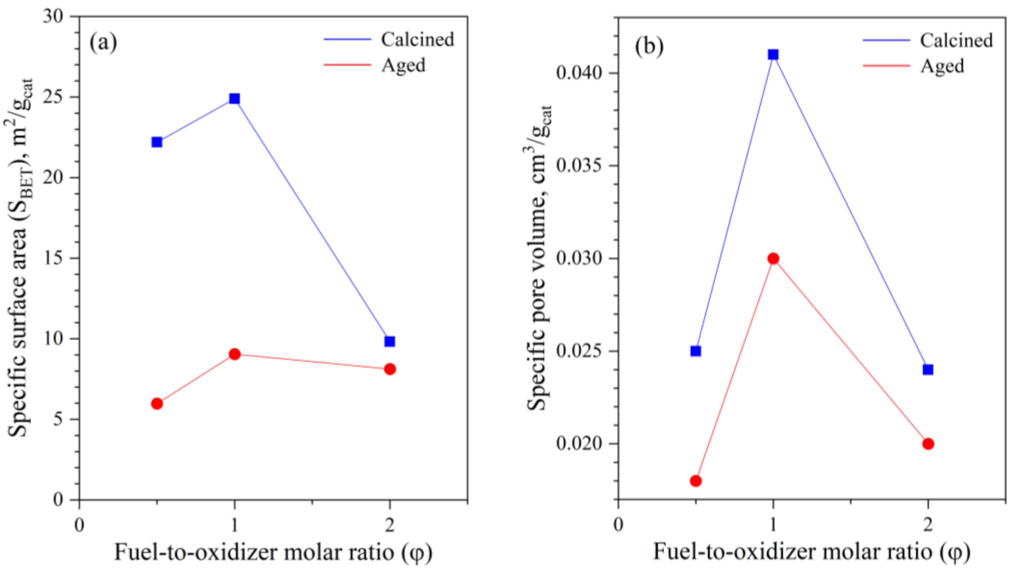

Figure 4.2. (a) BET specific surface area and (b) total specific pore volume at the variation of the fuel-to-oxidizer molar ratio (φ) of both calcined and aged $Cu_{40}Ce_{60}$ SCS catalysts.

Considering Cu_xCe_{1-x}-SCS_{100} catalysts, as shown in Figure 4.3, the specific surface area does not change sensibly varying the composition. However, $Cu_{60}Ce_{40}$-SCS_{100} catalyst exhibited a maximum value of surface area, that was emphasised after the experimental campaign (i.e. aged catalysts). More in detail, the specific surface area of calcined Cu_xCe_{1-x}-SCS_{100} catalysts is ~25 m^2/g; whereas, pure ceria exhibits a porous structure (~54 m^2/g) and copper oxide shows a non-porous structure (i.e. ~3 m^2/g). On the contrary, the specific pore volume of Cu_xCe_{1-x}-SCS_{100} catalysts decreases as the Cu content rises. The behaviour of Cu_xCe_{1-x}-SCS_{100} samples was ascribed to a decrease in meso- and macro-porosity counterbalanced by a slightly increase in microporosity as the Cu content rises. Regarding aged catalysts, their textural properties decrease during the tests because their structure sintered during the pre-treatment and the stability test.

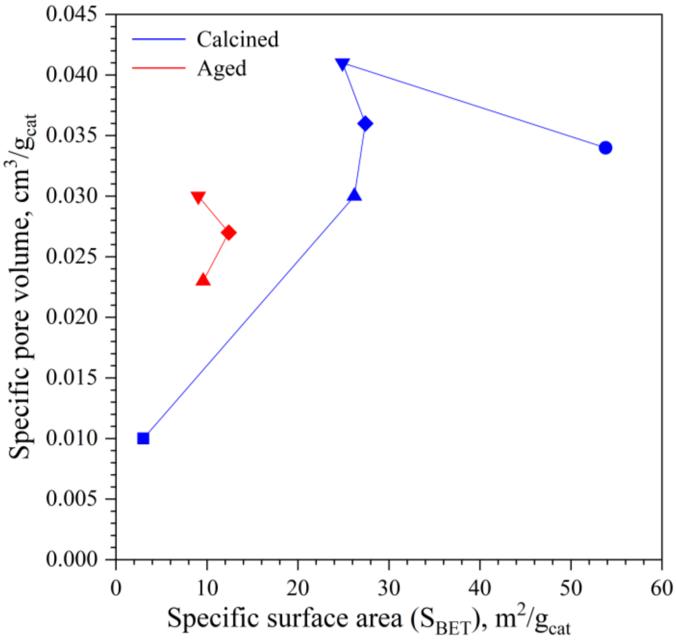

Figure 4.3. BET specific surface area and total specific pore volume of both calcined and aged Cu_xCe_{1-x}-SCS catalysts obtained with stoichiometric fuel-to-oxidizer molar ratio (i.e. φ equal to 1). For the sake of clarity, symbols refer to different compositions: ● Ce_{100}-SCS_{100}; ▼ $Cu_{40}Ce_{60}$-SCS_{100}; ♦ $Cu_{60}Ce_{40}$-SCS_{100}; ▲ $Cu_{80}Ce_{20}$-SCS_{100} and ■ Cu_{100}-SCS_{100}.

Gel-oxalate coprecipitation (OX) catalysts

The coprecipitated Cu_xCe_{1-x}-OX catalysts exhibited a completely different behaviour with respect to the aforementioned synthesis techniques; in fact, both the specific pore volumes and the specific surface areas are at least tripled. What stands out in Figure 4.4 is that the specific pore volume increases highly rising the Cu content; pure ceria has a monomodal distribution of mesopores centred at 4 nm; whereas, a bimodal distribution appears when Cu atoms are inserted in the structure forming larger mesopores centred at ~10 nm. Calcined Cu_xCe_{1-x}-OX catalysts exhibit a higher specific surface area with respect to the pure coprecipitated ceria and a maximum value was achieved by the $Cu_{60}Ce_{40}$-OX catalyst (i.e. ~94 m^2/g). Similar to the SCS method, coprecipitated copper oxide showed a non-porous structure. Lastly, the structure of mixed catalysts collapsed during the experimental tests due to the CuO reduction to metallic Cu and the low stability of this highly porous structure that could easily sinter.

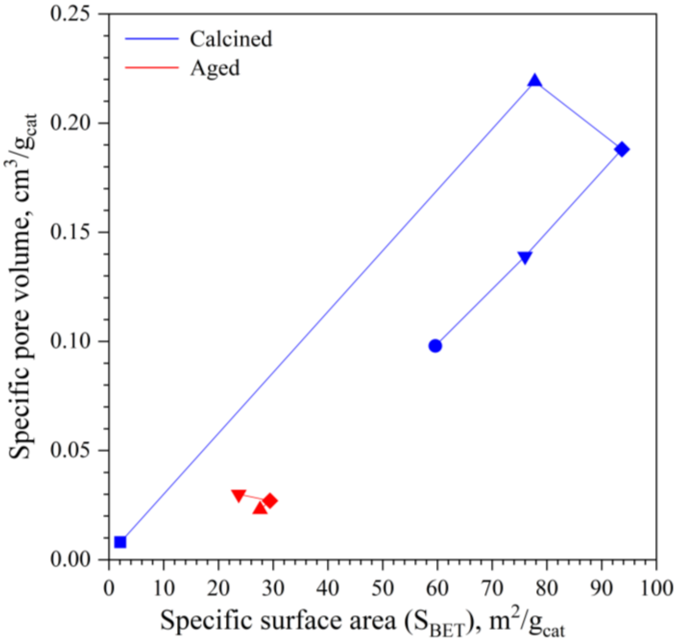

Figure 4.4. BET specific surface area and total specific pore volume of both calcined and aged Cu_xCe_{1-x}-OX catalysts. For the sake of clarity, symbols refer to different compositions: ● Ce_{100}-OX; ▼ $Cu_{40}Ce_{60}$-OX; ♦ $Cu_{60}Ce_{40}$-OX; ▲ $Cu_{80}Ce_{20}$-OX and ■ Cu_{100}-OX.

4.3.2. X-ray diffraction (XRD)

Wet impregnated (WI) catalysts

Figure 4.5 illustrates X-ray diffractograms of both calcined and aged wet impregnated catalysts. The support is constituted by pure ceria (PDF 01-075-0076, face-centred cubic cell), whose main diffraction peaks are located at 28.7°, 33.2°, 47.7°, and 56.6°. What stands out in Figure 4.5 is that no characteristic peaks of CuO or Cu were detected in the $Cu_{13}Ce_{87}$-WI sample; hence, it confirmed that Cu atoms were solubilized in the crystalline structure of the support. The other samples exhibited three narrow and intense peaks at 35.5°, 38.7° and 48.8°, which are associated at the monoclinic structure of CuO (PDF 01-080-0076). Their intensity increase as the Cu content rises. Moreover, as shown in Table 4.1, the average size of CuO crystallites is higher than the average crystallite size of CeO_2. Regarding aged catalysts, the CuO was completely reduced to metallic Cu; in fact, three narrow and intense peaks were detected at 43.3°, 50.4° and 74.0°, that are related to the cubic structure of metallic Cu (PDF 01-085-1326). In addition, Cu crystallites sintered because their average size increased sensibly; whereas, ceria had a more stable structure because the size of its crystallites increased slightly. This behaviour was ascribed to different Hüttig and Tammann temperatures of the two phases because the fusion temperature of ceria is roughly two times the fusion temperature of copper.

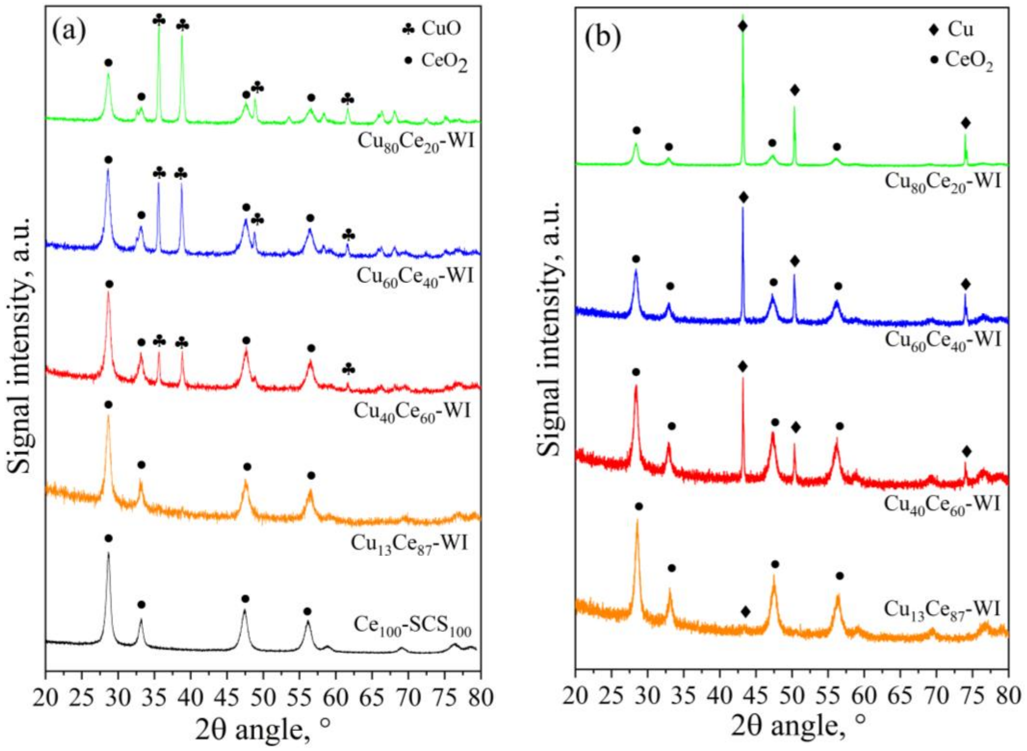

Figure 4.5. XRD patterns of (a) calcined and (b) aged WI catalysts.

Table 4.1. Crystallite size of CuO, Cu and CeO_2 of both calcined and aged WI catalysts.

	Calcined samples		Aged samples	
	d_{111} CuO, nm	d_{111} CeO_2, nm	d_{111} Cu, nm	d_{111} CeO_2, nm
$Cu_{13}Ce_{87}$-WI	-	11.9	-	12.6
$Cu_{40}Ce_{60}$-WI	44.1	12.8	176	14.8
$Cu_{60}Ce_{40}$-WI	52.2	12.4	143	13.9
$Cu_{80}Ce_{20}$-WI	49.3	11.4	321	13.5

Solution combustion synthesis (SCS) catalysts

Considering SCS catalysts, the diffraction peaks that were detected were the same of the previous samples. However, as shown in Figure 4.6, the calcined $Cu_{40}Ce_{60}$-SCS_{200} sample exhibited incomplete oxidation of copper. The cubic structure of Cu_2O (PDF 01-078-2076) was indeed detected at 36.4° and 42.3°; furthermore, metallic Cu was detected in the same catalyst at 43.3°. Their weight fractions equal to ~8 %wt of Cu_2O and ~5 %wt of metallic Cu were estimated by using the reference intensity ratio (RIR) of all phases [191]. This fact was ascribed to the high fuel-to-oxidizer ratio because the combustion of the excess of urea consumed a large amount of oxygen; hence, Cu could not be completely oxidised during the copper nitrate decomposition. Furthermore, as shown in Table 4.2, the CuO crystallite size decreases as the fuel-to-oxidizer ratio rises due to the higher reaction rate and the greater amount of gases produced during the syntheses. However, the average crystallite size of ceria increases as the fuel-to-oxidizer ratio rises because of the higher reaction temperature that prevails on the effect of gas production.

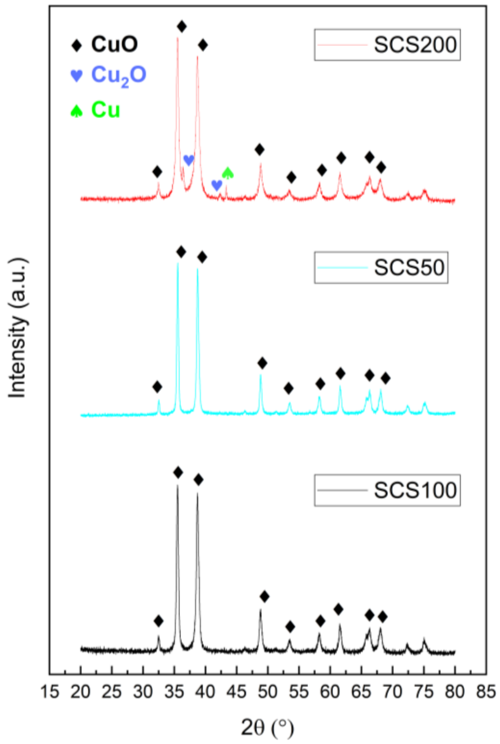

Figure 4.6. XRD patterns of calcined $Cu_{40}Ce_{60}$ SCS catalysts at the variation of the fuel-to-oxidizer ratio.

Table 4.2. Crystallite size of CuO, Cu and CeO_2 of both calcined and aged $Cu_{40}Ce_{60}$ catalysts at the variation of the fuel-to-oxidizer ratio.

	Calcined samples		Aged samples	
	d_{111} CuO, nm	d_{111} CeO_2, nm	d_{111} Cu, nm	d_{111} CeO_2, nm
$Cu_{40}Ce_{60}$-SCS_{50}	27.4	6.9	27.4	6.9
$Cu_{40}Ce_{60}$-SCS_{100}	17.9	8.0	50.0	10.2
$Cu_{40}Ce_{60}$-SCS_{200}	17.6	23.3	31.1	29.9

As far as Cu_xCe_{1-x}-SCS_{100} catalysts are concerned, CuO and CeO_2 were the two phases that were detected in calcined samples; whereas, as expected, Cu_2O and Cu were not present in the calcined catalysts. Moreover, CuO was completely reduced to metallic Cu during the experimental tests. As shown in Table 4.3, the average crystallite size of CuO increases and the average crystallite size of CeO_2 decreases as the Cu content rises. However, the crystallite size of both CuO and CeO_2 are lower than the size in WI samples.

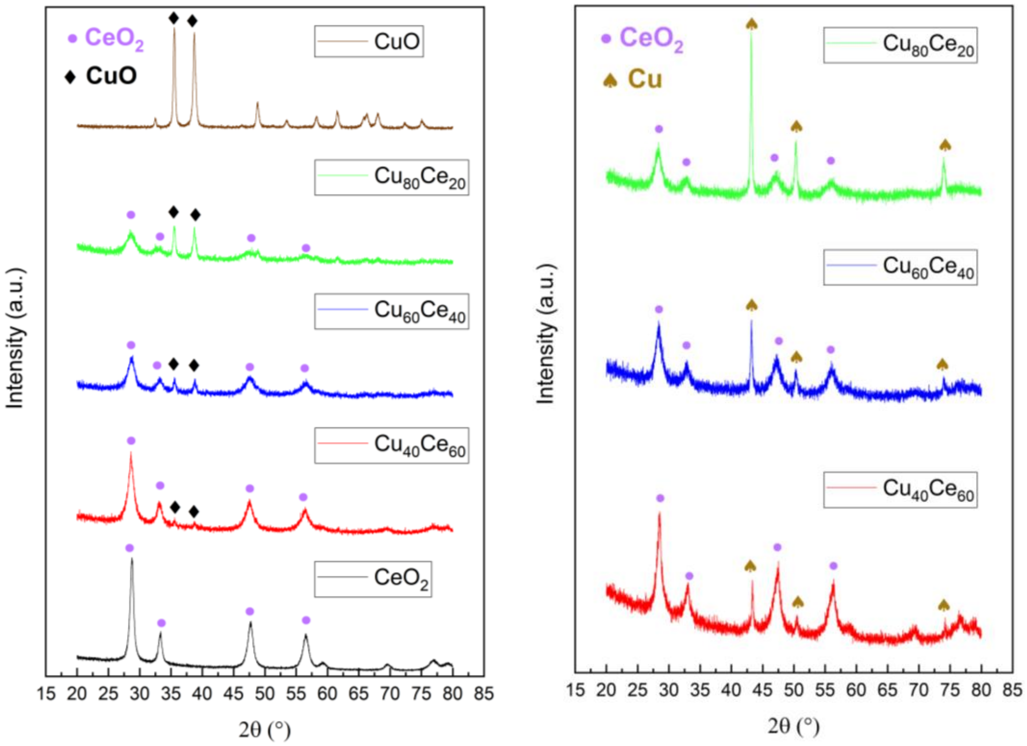

Figure 4.7. XRD patterns of (a) calcined and (b) aged Cu_xCe_{1-x} SCS catalysts obtained with a stoichiometric fuel-to-oxidizer ratio ($\varphi = 1$).

Table 4.3. Crystallite size of CuO, Cu and CeO_2 of both calcined and aged SCS catalysts obtained with a stoichiometric fuel-to-oxidizer ratio.

	Calcined samples		Aged samples	
	d_{111} CuO, nm	d_{111} CeO_2, nm	d_{111} Cu, nm	d_{111} CeO_2, nm
Ce_{100}-SCS_{100}	-	12.8	-	-
$Cu_{40}Ce_{60}$-SCS_{100}	17.9	8.0	50.0	9.8
$Cu_{60}Ce_{40}$-SCS_{100}	25.6	7.4	42.5	10.2

$Cu_{80}Ce_{20}$-SCS_{100}	26.8	6.6	45.9	10.6
Cu_{100}-SCS_{100}	32.8	-	-	-

Gel-oxalate coprecipitation (OX) catalysts

Considering coprecipitated catalysts, as illustrated in Figure 4.8, their diffraction peaks are broadened due to the smaller crystallite size of both phases, as shown in Table 4.4. Cu_2O diffraction peaks were detected in the calcined Cu_{100}-OX sample; this fact was ascribed to the decomposition of the oxalate and the non-porous structure of the material that prevented the combustion of the oxalate with gaseous O_2. The weight fractions of Cu_2O and Cu in calcined Cu_{100}-OX sample are ~8 %wt and ~1 %wt, respectively. Regarding aged catalysts, the samples were not completely reduced during experimental tests; in fact, a small peak at ~36° was detected increasing the Cu content.

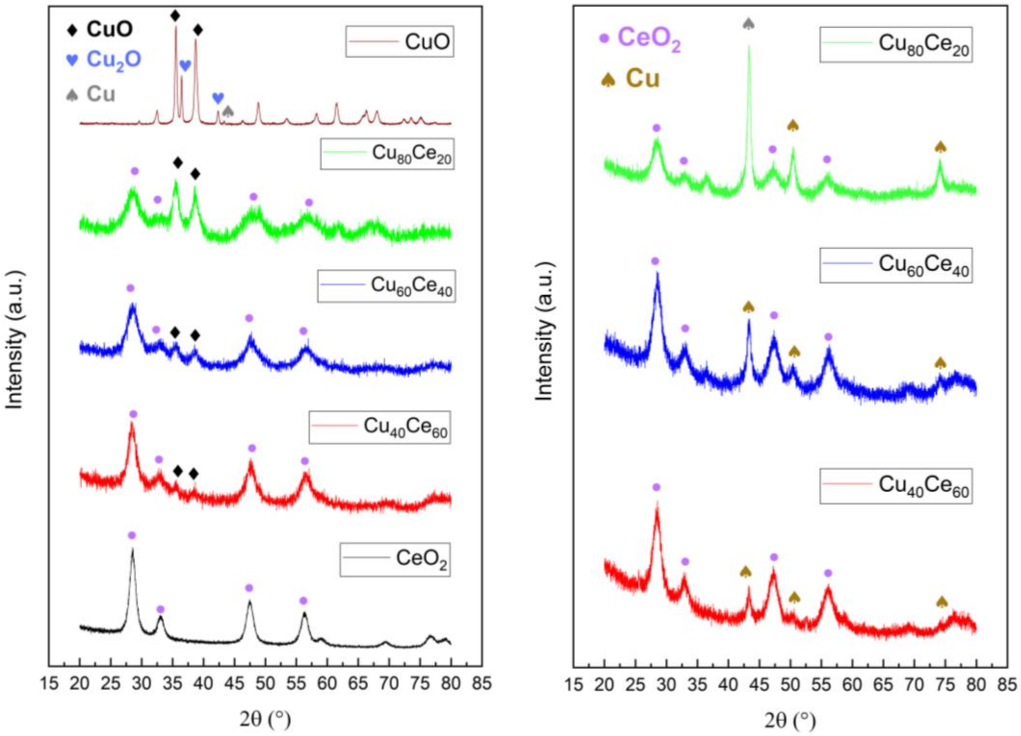

Figure 4.8. XRD patterns of (a) calcined and (b) aged OX catalysts.

Table 4.4. Crystallite size of CuO, Cu and CeO_2 of both calcined and aged WI catalysts.

	Calcined samples		Aged samples	
	d_{111} CuO, nm	d_{111} CeO_2, nm	d_{111} Cu, nm	d_{111} CeO_2, nm
Ce_{100}-OX	-	8.1	-	-
$Cu_{40}Ce_{60}$-OX	9.0	5.8	17.5	5.5
$Cu_{60}Ce_{40}$-OX	9.9	4.8	13.6	5.5
$Cu_{80}Ce_{20}$-OX	10.9	4.0	16.0	5.5
Cu_{100}-OX	33.3	-	-	-

4.3.3. FE-SEM images

Considering the wet impregnated samples, the copper precursor was impregnated on the surface of ceria. As illustrated in Figure 4.9, ceria nanoparticles have a size of ~800 nm and they are porous agglomerates of small crystallites. Whereas, copper nanoparticles have a smaller size; however, during the catalytic tests they sintered forming larger crystallites as observed in XRD analyses. It is worth noting that the surface of CuO nanoparticles is smoother and more compact that ceria nanoparticles confirming its extremely low porosity. For the sake of clarity, the composition of nanoparticles was determined by means of EDS measurements.

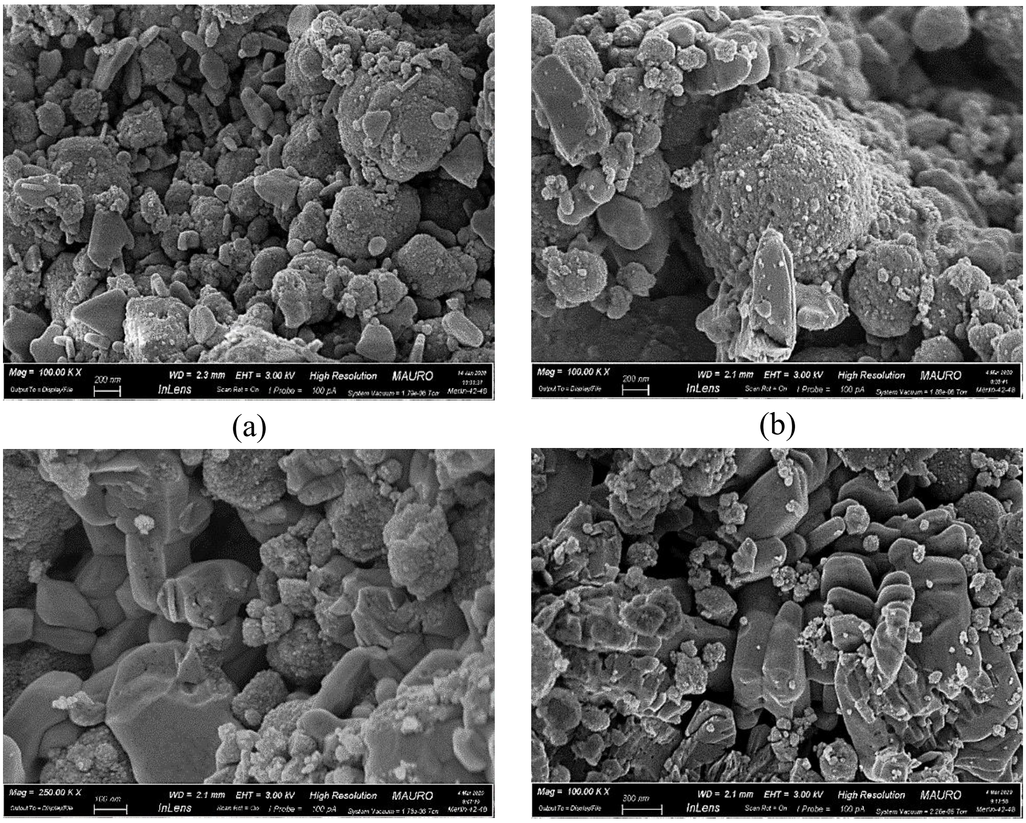

(a) (b)

(c) (d)

Figure 4.9. FE-SEM images of calcined WI samples: (a) $Cu_{13}Ce_{87}$-WI; (b) $Cu_{40}Ce_{60}$-WI; (c) $Cu_{60}Ce_{40}$-WI and (d) $Cu_{80}Ce_{20}$-WI.

Concerning SCS catalysts, the morphological difference between agglomerates of ceria and copper oxide is evident in Figure 4.10. On the one hand, pure CuO formed smooth and non-porous clusters of ~200 nm of embedded crystallites. On the other hand, pure ceria nanoparticles showed a broadened nanoparticle size distribution and their corrugated surface highlighted the presence of micropores, as observed in the pore size distribution. Binary oxides (i.e. Cu_xCe_{1-x}-SCS_{100}) formed smaller clusters with a more uniform size distribution; this result is consistent with the literature [192].

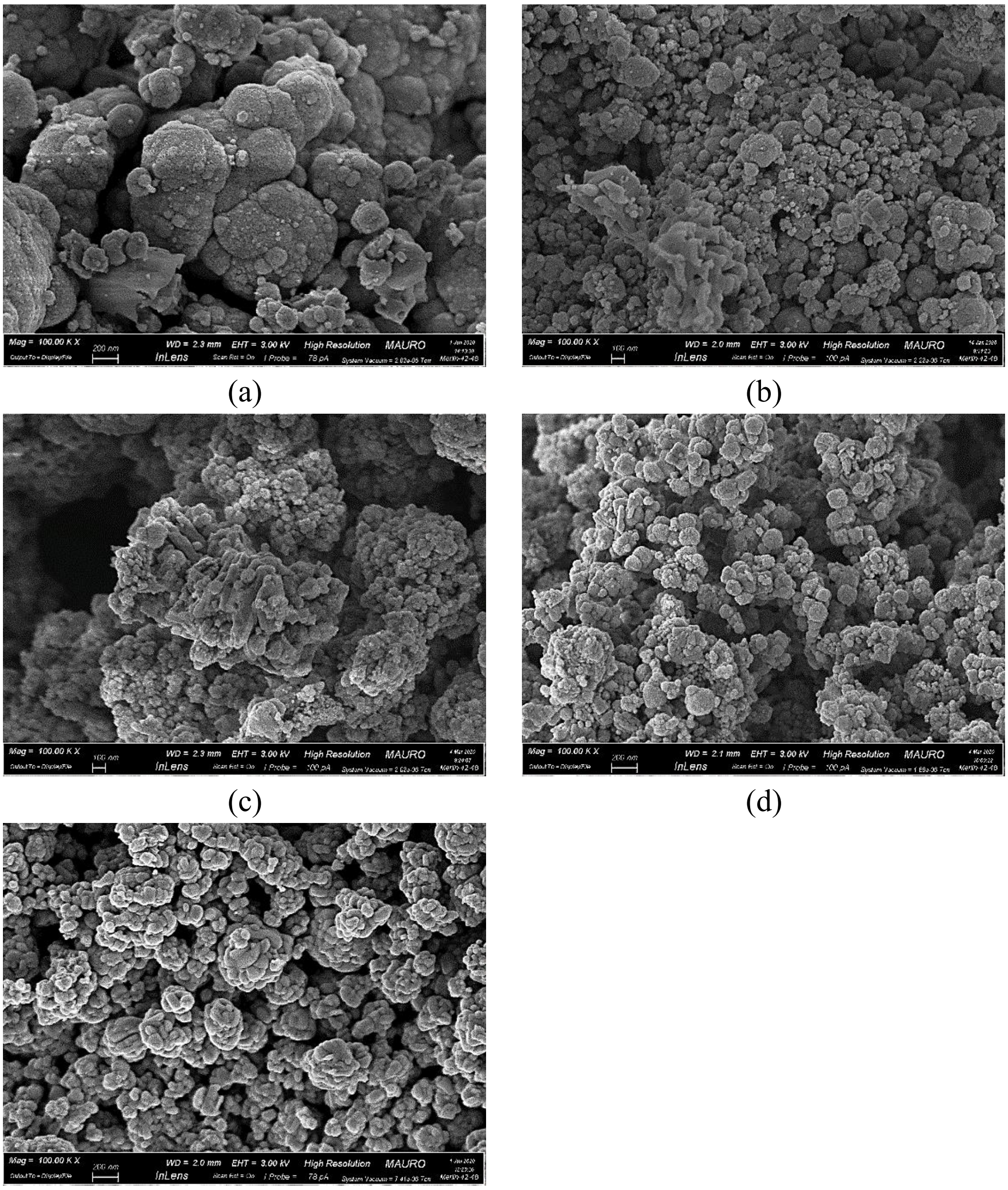

(a)

(b)

(c)

(d)

(e)

Figure 4.10. FE-SEM images of calcined SCS samples obtained with a stoichiometric fuel-to-oxidizer ratio: (a) Ce_{100}-SCS_{100}; (b) $Cu_{40}Ce_{60}$-SCS_{100}; (c) $Cu_{60}Ce_{40}$-SCS_{100}; (d) $Cu_{80}Ce_{20}$-SCS_{100} and Cu_{100}-SCS_{100}.

As illustrated in Figure 4.11, the morphological structure of coprecipitated aged catalyst is constituted by extremely small spherical nanoparticles (<50 nm); therefore, these samples have a sponge-like structure that evidence the presence of both micropores and mesopores. For the sake of clarity, large, flat and cracked surfaces are the result of the pelletizing of the powder.

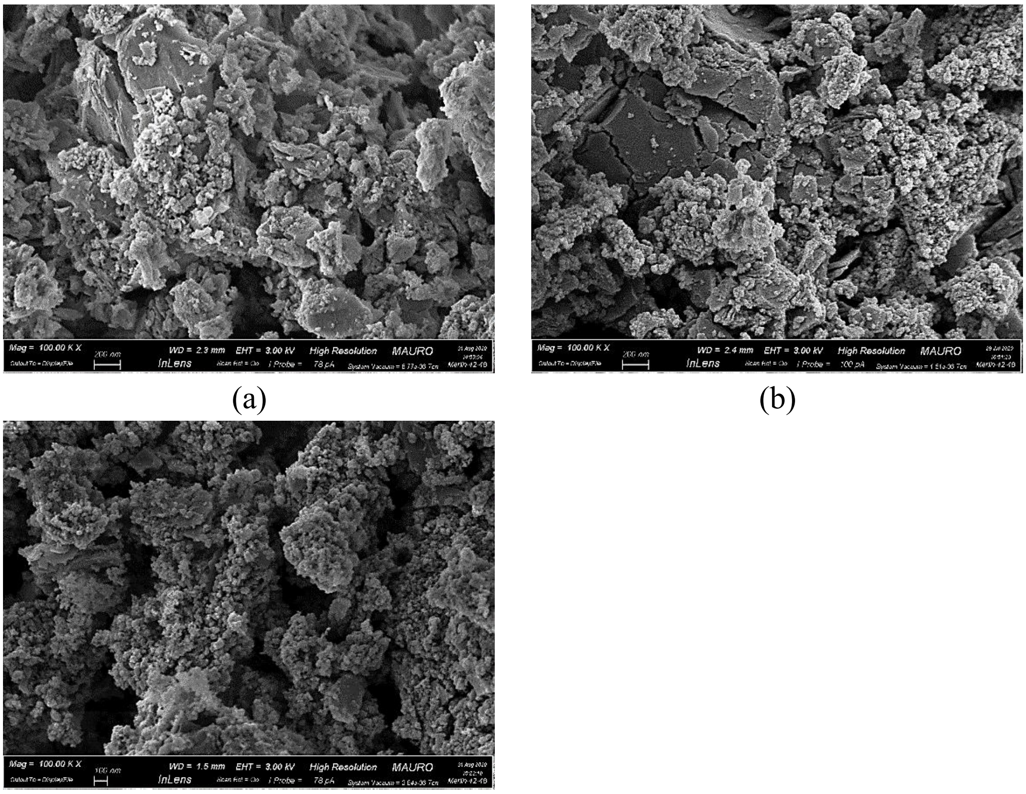

(a) (b)

(c)

Figure 4.11. FE-SEM images of aged OX samples: (a) $Cu_{40}Ce_{60}$-OX; (b) $Cu_{60}Ce_{40}$-OX and (c) $Cu_{80}Ce_{20}$-OX.

4.3.4. H_2-TPR analyses

The H_2-TPR profiles of the WI catalysts are illustrated in Figure 4.12. It is worth noting that the reduction profile of the pure ceria is completely different from the other profiles. In fact, superficial CeO_2 reduces to Ce_2O_3 at ~500°C; while bulk ceria reduces at ~900°C. Accordingly to the literature, the presence of Cu atoms in the structure of ceria distorts the crystalline structure and enhance the reducibility of ceria. A reduction peak appears between 200°C and 300°C for the binary WI catalysts. The temperature of reduction increases as the Cu content rises, because CuO formed isolated clusters that reduces at higher temperature. As summarised in Table 4.5, the H_2/Cu molar ratio at low temperature (<350°C) decreases as the Cu loading increases because a small amount of Cu atoms could solubilise in ceria structure enhancing its reducibility; this fact is clearly evident for the $Cu_{13}Ce_{87}$-WI sample.

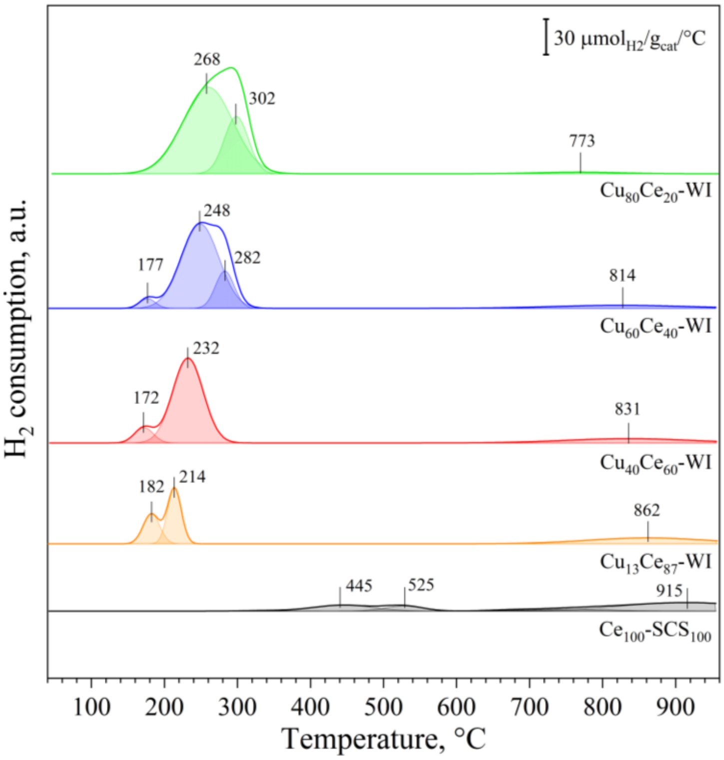

Figure 4.12. H_2-TPR profiles of WI catalysts.

Considering SCS catalysts, the oxides were reduced at low temperature (200°C – 300°C). However, in this case the effect of the Cu loading is less important, because the precursors were solubilised in water before the synthesis. Hence, Cu atoms could easily include within the crystalline structure of the ceria. As reported in Table 4.5, the H_2/Cu molar ratio of SCS samples is similar to the one of the WI catalysts. Therefore, a very small amount of Cu atoms allows ceria reducibility to be extremely enhanced.

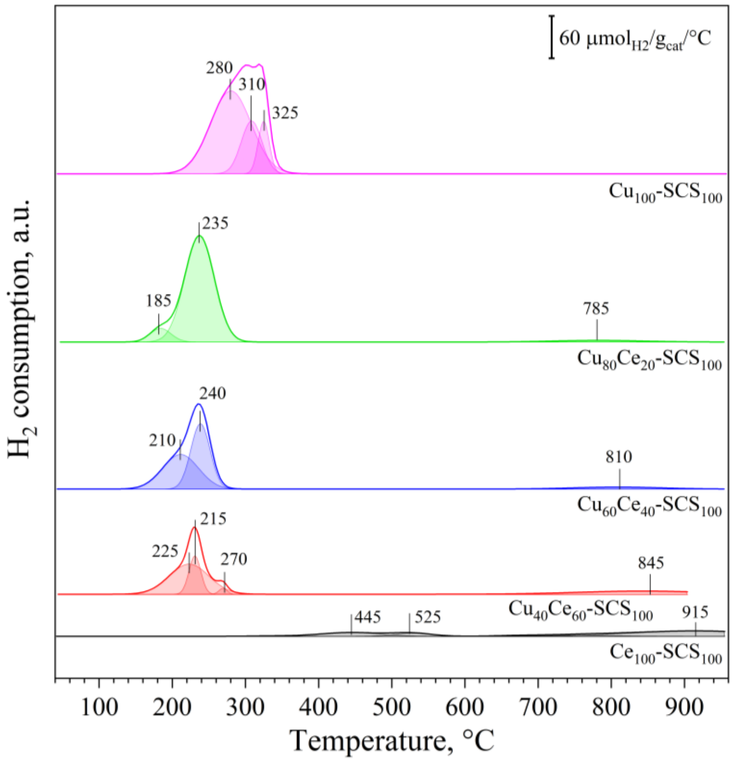

Figure 4.13. H_2-TPR profiles of SCS$_{100}$ catalysts.

Regarding coprecipitated catalysts, the reduction peak of the oxides is located at low temperature similar to the aforementioned samples. More in detail, the reduction peaks of OX catalysts are broadened, and the reduction is completed at ~400°C. This fact confirms the incomplete reduction of CuO that was detected in the XRD diffractograms of aged OX samples. According to the literature [193], the activation energy of the reduction of Cu_2O is higher than the one of the CuO reduction. Hence, the reduction peak of Cu$_{100}$-OX is broadened and asymmetric ranging from ~300°C and ~500°C due to the presence of Cu_2O that was detected by using XRD.

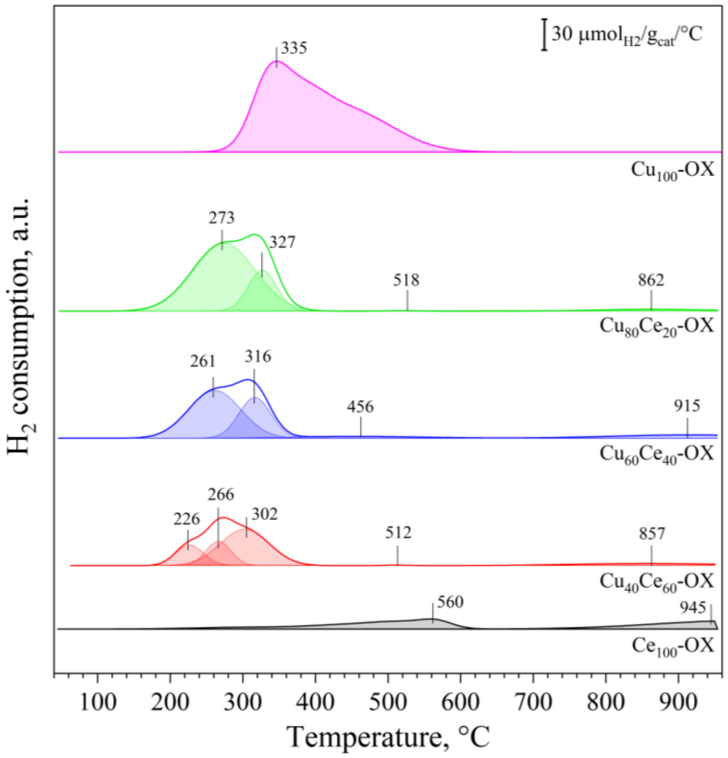

Figure 4.14. H_2-TPR profiles of OX catalysts.

Table 4.5. Quantitative analyses of H_2-TPR measurements.

	WI		SCS_{100}		OX	
	H_2 uptake	H_2/Cu	H_2 uptake	H_2/Cu	H_2 uptake	H_2/Cu
	mmol/g	-	mmol/g	-	mmol/g	-
Ce_{100}	-	-	0.85	-	1.25	-
$Cu_{13}Ce_{87}$	1.98	2.55	-	-	-	-
$Cu_{40}Ce_{60}$	4.42	1.49	4.20	1.42	4.81	1.62
$Cu_{60}Ce_{40}$	6.19	1.20	6.20	1.20	6.22	1.21
$Cu_{80}Ce_{20}$	8.83	1.08	8.48	1.04	8.81	1.08
Cu_{100}	-	-	12.6	1.00	12.6	1.00

4.3.5. CO_2-TPD analyses

Considering the desorption of CO_2 from the catalytic samples, the desorption profiles exhibited three broad halos. The first one is located at low temperature (100°C-250°C) ad it was ascribed to weak basic sites such as hydroxyls groups and metal-oxygen pairs, which correspond to the formation of bicarbonate or carbonate bidentate, respectively. The second halo is located at extremely high temperature (600°C-800°C) for pure ceria; whereas, the third one appears in binary samples and it is located at intermediate temperatures (300°C-600°C). These high temperature halos were ascribed to strong basic sites such as low-coordination oxygen atoms or oxygen vacancies of the crystalline lattice of ceria and copper-ceria nanoparticles, which lead to the formation of carbonate unidentate [194–196]. As summarised in Table 4.6, the total amount of CO_2 desorbed by the samples decreases as the Cu content rises. However, the strength of the bonds decreases because the desorption temperatures are lower.

Table 4.6. Quantitative analyses of CO_2-TPD measurements on aged catalysts.

	CO_2 uptake, mmol/g		
	WI	SCS_{100}	OX
Ce_{100} (fresh reduced)	-	3.39	3.87
$Cu_{13}Ce_{87}$	3.18	-	-
$Cu_{40}Ce_{60}$	2.04	1.89	2.41
$Cu_{60}Ce_{40}$	1.04	1.75	0.90
$Cu_{80}Ce_{20}$	1.30	3.36	0.79

4.3.6. ICP-MS measurements

Table 4.7 summarises the results of the ICP-MS measurements. The composition of the catalysts is consistent with the nominal values.

Table 4.7. Quantitative analyses of ICP-MS measurements.

	Nominal value		WI		SCS_{100}		OX	
	Cu, %at	Ce, %at	Cu, %at	Ce, %at	Cu, %at	Ce, %at	Cu, %at	Ce, %at
Ce_{100}	0	100	-	-	0	100	0	100
$Cu_{13}Ce_{87}$	12.6	87.4	12.2	87.8	-	-	-	-
$Cu_{40}Ce_{60}$	40.0	60.0	41.0	59.0	39.1	60.9	39.6	60.4
$Cu_{60}Ce_{40}$	60.0	40.0	61.8	38.2	57.1	42.9	60.4	39.6
$Cu_{80}Ce_{20}$	80.0	20.0	81.9	18.1	77.0	23.0	80.7	19.3
Cu_{100}	100	0	-	-	100	0	100	0

4.3.7. Stability tests

All the catalysts were pre-treated in 10% H_2/N_2 at 350 °C for 1 h; after that the samples were tested for a relatively long period of time (stability test, 20 h) at 275 °C, 25 bar, 20 Nl/g/h and $H_2/CO_2/N_2$ molar ratio equal to 3:1:1. During these stabilisations catalysts exhibited a loss in activity (i.e. CO_2 conversion) probably due to sintering phenomena. After the stabilisation, activity tests could be performed on the catalysts at the variation of the temperature and the results are comparable. In fact, the initial loss in activity during the stability test is extremely fast (i.e. 2-3 h) and intense (i.e. around -20% of CO_2 conversion).

Considering the WI catalysts, as showed in Figure 4.15, their activity at 275°C exhibited a maximum at the variation of the Cu content (i.e. $Cu_{40}Ce_{60}$-WI catalyst). Then, the activity of the catalysts containing a higher amount of Cu is lower because of the loss in specific surface area that was not counterbalanced by the increase in active sites. The low textural properties of WI samples limit the CO_2 conversion. Furthermore, the loss in activity during the stability test ranges from -17% of the $Cu_{60}Ce_{40}$-WI to -48% of the $Cu_{13}Ce_{87}$-WI.

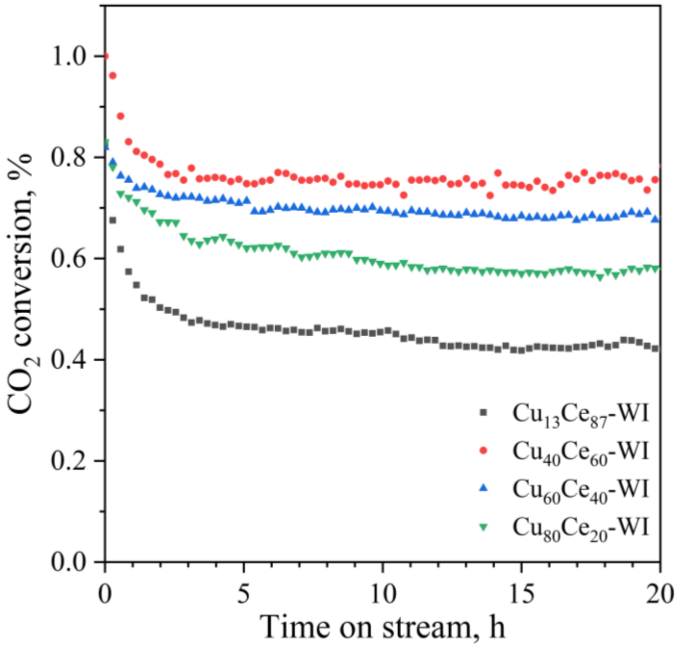

Figure 4.15. Stability tests of WI catalysts. For the sake of clarity, reaction conditions are: 275 °C, 25 bar, 20 Nl/g/h and $H_2/CO_2/N_2$ molar ratio equal to 3:1:1.

Considering SCS catalysts obtained at the variation of the fuel-to-oxidizer ratio, as observed during the characterization, textural properties of the catalyst obtained with a stoichiometric fuel-to-oxidizer ratio exhibited the best performances, as illustrated in Figure 4.16. The loss in activity is less important (-20 % of activity) with respect to the WI catalysts.

As illustrated in Figure 4.17, $Cu_{80}Ce_{20}$-SCS_{100} exhibited the best performances because textural properties of this binary sample are greater than the ones of the WI catalyst. The CO_2 conversion at the end of the stability test achieve ~5%, and it has exhibited a loss in activity of about -23%.

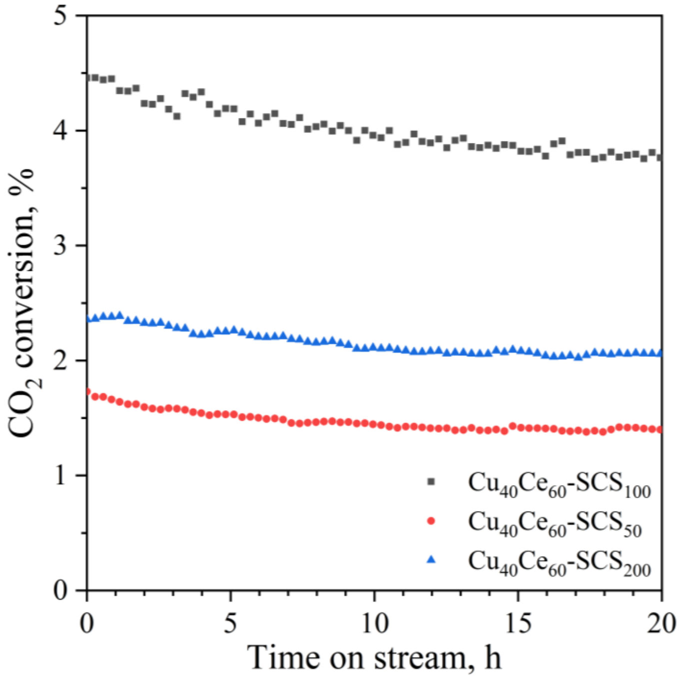

Figure 4.16. Stability tests of SCS catalysts at the variation of the fuel-to-oxidizer ratio. For the sake of clarity, reaction conditions are: 275 °C, 25 bar, 20 Nl/g/h and $H_2/CO_2/N_2$ molar ratio equal to 3:1:1.

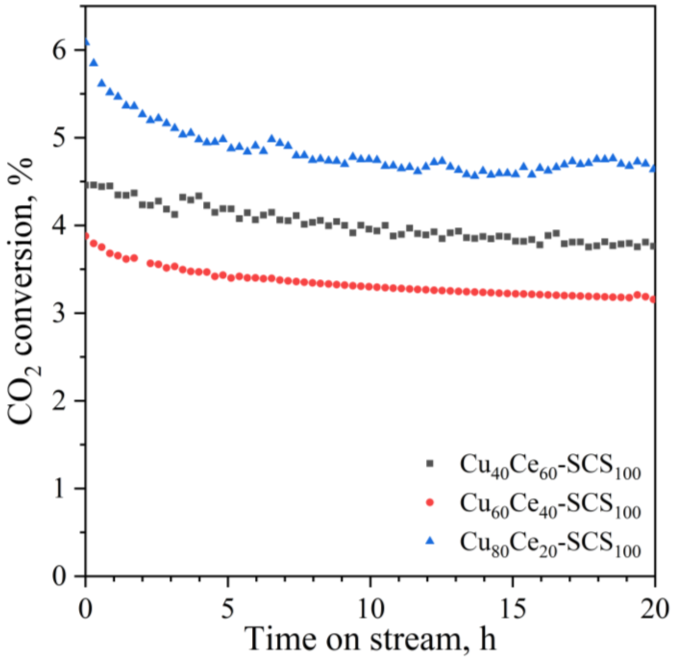

Figure 4.17. Stability tests of SCS catalysts obtained with a stoichiometric fuel-to-oxidizer ratio. For the sake of clarity, reaction conditions are: 275 °C, 25 bar, 20 Nl/g/h and $H_2/CO_2/N_2$ molar ratio equal to 3:1:1.

Lastly, considering coprecipitated catalysts, their activity increases increasing the Cu content; however, during the stability tests the activity progressively decreases because the nanoparticles sinter and the extremely porous structure shrunk. Therefore, the loss in activity of these samples ranges between -30% and -40%.

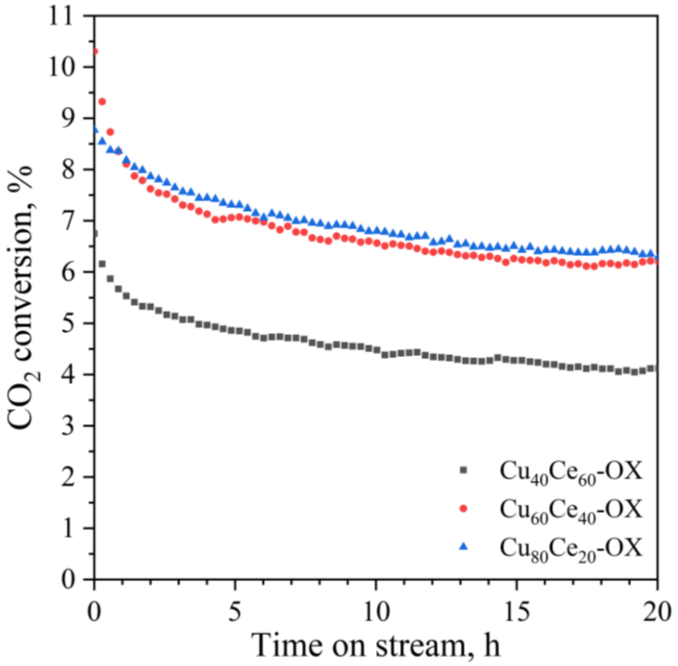

Figure 4.18. Stability tests of OX catalysts. For the sake of clarity, reaction conditions are: 275 °C, 25 bar, 20 Nl/g/h and $H_2/CO_2/N_2$ molar ratio equal to 3:1:1.

4.3.8. Activity tests

Considering activity tests, the performances of each catalyst was confirmed at all temperatures. More specifically, as shown in Figure 4.19, WI catalysts exhibited the lowest activity and the methanol selectivity decreases dramatically increasing the reaction temperature. Hence, there is not a synergistic effect between ceria and copper; this fact was ascribed to the synthesis technique, in which the copper covers the surface of the support. SCS and OX samples exhibited enhanced performances and higher activity as the reaction temperature rises. However, the methanol selectivity decreases rapidly at low temperature and then it stabilised at higher temperatures due to the approach to the thermodynamic equilibrium. The increase in activity rapidly rises at temperature greater than 250 °C due to the increase of the CO hydrogenation reaction rate, as will be discussed in the next chapter.

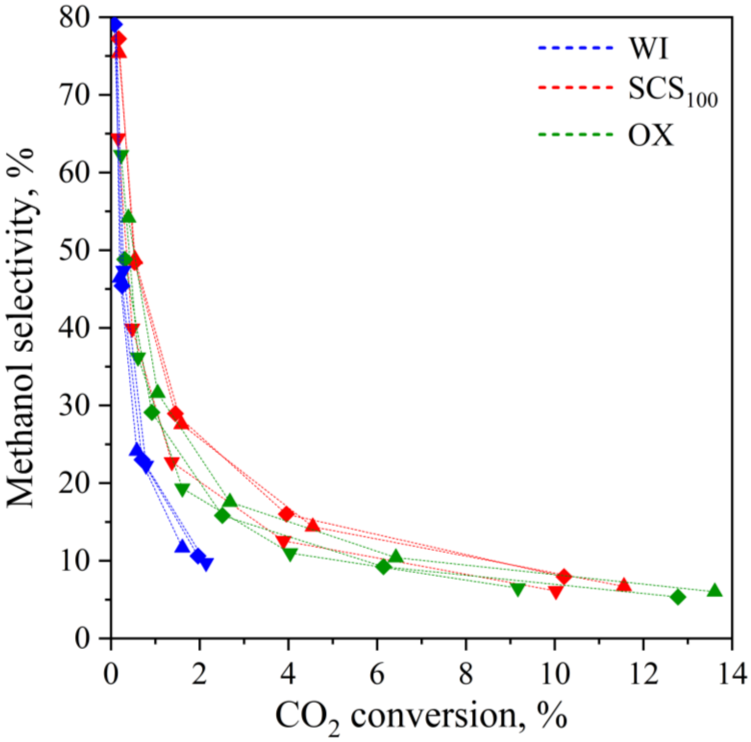

Figure 4.19. Conversion-selectivity map of the activity tests of all catalysts. For the sake of clarity, reaction conditions are: 25 bar, 20 Nl/g/h and $H_2/CO_2/N_2$ molar ratio equal to 3:1:1. In addition, symbols refer to different compositions: ▼ $Cu_{40}Ce_{60}$; ♦ $Cu_{60}Ce_{40}$ and ▲ $Cu_{80}Ce_{20}$. Lastly, each sample was tested between 200°C and 300°C with temperature steps of 25°C.

From the catalytic activity tests at 250 ° C reported in Figure 4.20, it is worth noting that the coprecipitated catalysts are the most active, thanks to a greater specific surface area and a more intimate contact between copper and ceria; while, the wet impregnated catalysts showed the least activity, despite having an intermediate surface area. Aged SCS catalysts have a surface area comparable to aged WI samples, but their activity is higher. In conclusion, there is a synergy effect between Cu and Ce and the interaction of Cu and CeO_2 nanoparticles favours the hydrogenation of CO_2 to methanol and CO. These catalysts showed lower activity than the commercial CuZnAl catalyst, which is based on the synergistic effect between Cu and ZnO. Therefore, it might be useful investigating CuZnCe ternary catalysts, which exploit both the interaction between Cu and CeO_2 and that between Cu and ZnO.

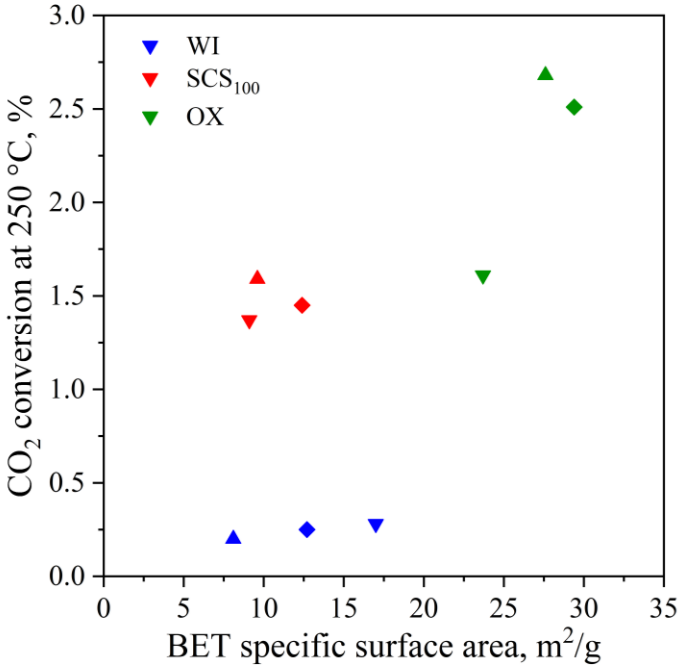

Figure 4.20. CO_2 conversion at the variation of the BET specific surface area of the aged catalysts. For the sake of clarity, reaction conditions are: 275 °C, 25 bar, 20 Nl/g/h and $H_2/CO_2/N_2$ molar ratio equal to 3:1:1. In addition, symbols refer to different compositions: ▼ $Cu_{40}Ce_{60}$; ♦ $Cu_{60}Ce_{40}$ and ▲ $Cu_{80}Ce_{20}$.

4.4. Conclusion

This chapter dealt with the study of CuCe mixed catalysts for CO_2 hydrogenation to methanol. More specifically, catalysts with different atomic compositions were synthesized with three different synthesis techniques (i.e. WI, SCS and OX). Subsequently, the samples were experimentally tested to compare their catalytic performance and both calcined and aged samples were characterized. It is worth noting that WI catalysts have significantly lower performance than SCS and OX catalysts. More in detail, the Cu crystallites are coarser in the WI samples than in the SCS and OX samples. In addition, the activity (at 250 °C) of the catalysts decreases linearly as the crystallite size rises because of the lower dispersion of the active phase. The SCS and OX techniques produced much smaller crystallites, the interface areas increase creating a more intimate contact between the phases and a more marked synergistic effect which translates into an enhanced methanol yield [48]. Among SCS and OX samples $Cu_{40}Ce_{60}$ samples exhibited the lowest methanol yield due to large Cu crystallite size and a lower intimate contact between Cu and

CeO_2. Finally, the synergistic effect between Cu and CeO_2 enhance the catalytic performances of mixed CuCe catalysts; however, the performances of commercial CuZnAl catalyst are extremely higher at lower temperature. Therefore, the synergistic effect between Cu and Zn is extremely important. Hence, ternary catalysts such as CuZnCe might be investigated.

Chapter 5

Modelling of reactors for Methanol production via CO_2 hydrogenation

5.1. Introduction

The CO_2 hydrogenation to methanol has been widely studied in the literature in the context of PtF processes because, as aforementioned in Chapter 1, methanol is a very useful molecule in the world economy. In Chapter 4, CuCe-based catalyst were presented; however, their performances did not reached those of the common CuZnAl ternary oxide catalyst for methanol synthesis. Therefore, in the present Chapter, the study was developed considering the CuZnAl catalyst that is already at the state-of-the-art and its kinetic model was proposed be Graaf et al. [51]. This ternary oxide catalyst was used for comparing electrocatalysis and thermocatalysis in the next Chapter of this thesis.

The present chapter focuses on the study of the reaction section of a PtF plant, which is composed of four parts: reactor, head-tail heat exchanger, two-phase gas-liquid separator and gas recirculation. As aforementioned, the work concerns the study of the kinetics of CO_2 hydrogenation on a ternary CuZnAl catalyst. The research focused on developing a pseudo-homogeneous one-dimensional reactor model and a simplified model of the methanol production section that includes the reactor, the methanol separation section and the recirculation of unreacted gases. The purposes of the work are: the evaluation of the internal profiles of the reactor (temperature, CO_2 conversion and methanol yield), the design of the best configuration of the reactor to maximise performances of the plant and the estimation of the start-up time of the plant even at the variation of the operating condition with respect to the nominal design condition.

5.2. Methodology

5.2.1. Methanol synthesis reaction kinetics

As presented in Chapter 1, the CO_2 hydrogenation to methanol is described by means of three reactions:

In the literature, the effective reaction mechanism is not definitely clarified. In fact, researchers have reported kinetic models that consider the formation of methanol via CO hydrogenation [50,51]; on the contrary, other researchers have considered CO_2 hydrogenation to methanol as the main reaction [99]; lastly, others have assumed that the formation of methanol occurs starting from both CO and CO_2 [50,51].

The kinetic model used in the following work has been proposed by Kiss et al. [50], and it has been based on the study of Graaf et al.[51], which have started from the assumption that methanol could be formed from both CO_2 and CO. The kinetics are described by a Langmuir-Hinshelwood-Hougen-Watson (LHHW) equation, obtained with a $Cu/ZnO/Al_2O_3$-based catalyst, which is commonly known as a commercial catalyst for methanol synthesis.

It is worth pointing out that, in this kinetic model, the pre-exponential factor of the kinetic factor of the CO_2 hydrogenation is several orders of magnitude lower than the pre-exponential factor of the kinetic factor of the CO hydrogenation, as stands out in Table 5.1; hence, CO hydrogenation reaction rate prevails over the CO_2 hydrogenation reaction rate.

The reaction rate of the i-th reaction (r_i, $mol \cdot s^{-1} \cdot kg_{cat}^{-1}$) was calculated according to equation (5.1); where k_i represents the kinetic factor of the i-th reaction, DF_i is the driving force of the i-th reaction, AG is the adsorption group and m is the exponent of the adsorption group [50].

$$r_i = \frac{k_i \cdot DF_i}{AG^m} \tag{5.1}$$

The kinetic factor of the generic i-th reaction was evaluated according to the Arrhenius equation (5.2); where $k_{\infty,i}$ is the pre-exponential factor of the i-th reaction, $E_{A,i}$ ($J \cdot mol^{-1}$) is the activation energy of the i-th reaction, R (8.314 $J \cdot mol^{-1} \cdot K^{-1}$) is the ideal gas constant and T (K) represents the reaction temperature.

$$k_i = k_{\infty,i} \cdot \exp\left(\frac{-E_{A,i}}{R \cdot T}\right) \tag{5.2}$$

The parameters of the kinetic factors are reported in Table 5.1.

Table 5.1. Parameters of the kinetic factors of the three reactions.

Reaction	$k_{\infty,i}$	$E_{A,i}$
(1)	$1.5188 \cdot 10^{-30}$ $mol \cdot s^{-1} \cdot kg_{cat}^{-1} \cdot Pa^{-1}$	266010 $J \cdot mol^{-1}$
(2)	$9.0421 \cdot 10^{11}$ $mol \cdot s^{-1} \cdot kg_{cat}^{-1} \cdot Pa^{-0.5}$	112860 $J \cdot mol^{-1}$
(3)	$4.0638 \cdot 10^{-3}$ $mol \cdot s^{-1} \cdot kg_{cat}^{-1} \cdot Pa^{-1}$	11700 $J \cdot mol^{-1}$

Driving forces have been expressed by using fugacities in the studies of Graaf et at. [51] and Kiss et al. [50]; however, in this work, the model was simplified and fugacities were approximated by using partial pressures. This approximation is consistent with the literature in the range of operative conditions [197]. Driving forces of the three reactions were estimated by means of equations (5.3), (5.4) and (5.5).

$$DF_1 = K_{CO_2} \cdot p_{CO_2} \cdot p_{H_2}^{3/2} - \frac{K_{CO_2}}{K_{eq,1}} \cdot p_{H_2O} \cdot p_{CH_3OH} \cdot p_{H_2}^{-3/2} \tag{5.3}$$

$$DF_2 = K_{CO_2} \cdot p_{CO_2} \cdot p_{H_2} - \frac{K_{CO_2}}{K_{eq,2}} \cdot p_{H_2O} \cdot p_{CO} \tag{5.4}$$

$$DF_3 = K_{CO} \cdot p_{CO} \cdot p_{H_2}^{3/2} - \frac{K_{CO}}{K_{eq,3}} \cdot p_{CH_3OH} \cdot p_{H_2}^{-1/2} \tag{5.5}$$

Where p_j represents the partial pressure of the j-th chemical species, $K_{eq,i}$ represents the equilibrium constant of the i-th reaction and K_j represents a constant of the j-th chemical species. These constants were evaluate according to equations (5.6), (5.7), (5.8), (5.9) and (5.10).

$$K_{CO_2} = 1.7214 \cdot 10^{-10} \cdot \exp\left(\frac{81287}{RT}\right) \qquad \text{Pa}^{-1} \tag{5.6}$$

$$K_{CO} = 8.3965 \cdot 10^{-11} \cdot \exp\left(\frac{118270}{RT}\right) \qquad \text{Pa}^{-1} \tag{5.7}$$

$$\frac{K_{CO_2}}{K_{eq,1}} = 2.5813 \cdot 10^{10} \cdot \exp\left(\frac{26788}{RT}\right) \qquad \text{Pa} \tag{5.8}$$

$$\frac{K_{CO_2}}{K_{eq,2}} = 6.1221 \cdot 10^{-13} \cdot \exp\left(\frac{125226}{RT}\right) \qquad \text{Pa}^{-1} \tag{5.9}$$

$$\frac{K_{CO}}{K_{eq,3}} = 3.5408 \cdot 10^{12} \cdot \exp\left(\frac{19832}{RT}\right) \qquad \text{Pa} \tag{5.10}$$

The adsorption group was calculated according to equation (5.11) and the adsorption constants of the j-th chemical species were estimated according to equations (5.12), (5.13) and (5.14). The *m* exponent of the adsorption group is unitary.

$$\begin{aligned} AG^m = \sqrt{p_{H_2}} + \frac{K_{H_2O}}{\sqrt{K_H}} \cdot p_{H_2O} + K_{CO} \cdot p_{CO} \cdot \sqrt{p_{H_2}} + K_{CO} \cdot \frac{K_{H_2O}}{\sqrt{K_H}} \cdot p_{CO} \cdot p_{H_2O} \\ + K_{CO_2} \cdot p_{CO_2} \cdot \sqrt{p_{H_2}} + K_{CO_2} \cdot \frac{K_{H_2O}}{\sqrt{K_H}} \cdot p_{CO_2} \cdot p_{H_2O} \end{aligned} \tag{5.11}$$

$$\frac{K_{H_2O}}{\sqrt{K_H}} = 4.3676 \cdot 10^{-12} \cdot \exp\left(\frac{115080}{RT}\right) \qquad \text{Pa}^{-0.5} \tag{5.12}$$

$$K_{CO} \cdot \frac{K_{H_2O}}{\sqrt{K_H}} = 3.6673 \cdot 10^{-22} \cdot \exp\left(\frac{233350}{RT}\right) \qquad \text{Pa}^{-1.5} \tag{5.13}$$

$$K_{CO_2} \cdot \frac{K_{H_2O}}{\sqrt{K_H}} = 7{,}5184 \cdot 10^{-22} \cdot \exp\left(\frac{197270}{RT}\right) \qquad \text{Pa}^{-1.5} \tag{5.14}$$

5.2.2. Reactor modelling

The modelling of the reactor is described in this Section. Three types of fixed bed reactor were considered: isothermal reactor, adiabatic reactor and refrigerated reactor. The main assumptions of the model are the following:

- explicit pseudo-homogeneous mono-dimensional first order model;
- ideal gas model;
- the intrinsic kinetics was approximated to the extrinsic kinetics by using an effectiveness equal to 1 because CZA catalyst is on the surface of the particles (i.e. egg-shell catalyst particles);
- both radial and axial diffusion were neglected;
- the production of by-products (e.g. CH_4) was neglected;
- 7 chemical species were considered: 5 reactants (i.e. CO_2, H_2, CO, CH_3OH and H_2O) and 2 inert species (i.e. N_2 and CH_4).

Isothermal reactor model

The simplest reactor model is the isothermal reactor, which involves the mass balance equations and the momentum balance equation. The mass balance equation of a generic j-th chemical species is described in equation (5.15). Where v ($m \cdot s^{-1}$) is the superficial velocity, C_j ($mol \cdot m^{-3}$) represents the molar concentration of the j-th species, z (m) is the axial coordinate, ρ_b ($kg_{cat} \cdot m_{bed}^{-3}$), $\nu_{j,i}$ and $\nu_{k,i}$ are the stoichiometric coefficient of the j-th species and of the key (k-th) component of the i-th reaction, respectively, $r_{k,i}$ ($mol \cdot s^{-1} \cdot kg_{cat}^{-1}$) is the reaction rate of the i-th reaction referred to the key component and M is the total number of reaction (i.e. 3). For the sake of clarity, the generation term for inert species is null (i.e. $\nu_{j,i} = 0$).

$$\frac{d(v \cdot C_j)}{dz} = \rho_b \cdot \sum_{i=1}^{M} \frac{\nu_{j,i}}{\nu_{k,i}} \cdot r_{k,i} \qquad j = CO_2, H_2, CO, CH_3OH, H_2O, N_2, CH_4 \tag{5.15}$$

The momentum balance is evaluated according to Ergun's equation (5.16) in order to estimate pressure drops (dp/dz, $Pa \cdot m^{-1}$) along the fixed bed reactor. In the equation, ρ ($kg \cdot m^{-3}$) represents the density of the gaseous mixture, d_p (m) is the particle diameter, ε_b is the bed void fraction and μ (Pa·s) is the viscosity of the gaseous mixture.

$$\frac{dp}{dz} = -\left(\frac{\rho \cdot v}{\rho \cdot d_p}\right) \cdot \left(\frac{1-\varepsilon_b}{\varepsilon_b^3}\right) \cdot \left[\frac{150 \cdot (1-\varepsilon_b) \cdot \mu}{d_p} + 1.75 \cdot \rho \cdot v\right] \tag{5.16}$$

Table 5.2 summarises the parameters of the of the catalytic bed. Furthermore, the reactor model developed in Matlab® environment was validated by using Aspen Plus and adopting Soave-Redlich-Kwong as thermodynamic method according to Kiss et al. [7].

Table 5.2. Parameters of the catalytic bed [7][17].

Parameter	Symbol	Value
Bed void fraction	ε_b	0.4
Catalyst void fraction	ε_{cat}	0.98
Catalyst density	ρ_{cat}	1775 kg·m^{-3}
Particle diameter	d_p	0.0055 m

Adiabatic reactor model

Regarding the adiabatic reactor model, the energy balance must be solved in order to calculate the reaction temperature. More in detail, the energy balance for the adiabatic reactor is reported in equation (5.17). Where C_t (mol·m^{-3}) represent the total molar concentration of the gaseous species, $\tilde{c}_p$ (J·mol^{-1}·K^{-1}) is the molar specific heat of the gaseous mixture and $\Delta_r\widetilde{H}_i$ (J·mol^{-1}).

$$v \cdot C_t \cdot \tilde{c}_p \cdot \frac{dT}{dz} = \rho_b \cdot \sum_{i=1}^{M} -\Delta_r\widetilde{H}_{i,k} \cdot \frac{r_{k,i}}{v_{k,i}} \tag{5.17}$$

Refrigerated reactor model

Concerning the refrigerated reactor model, the energy balance takes into account heat losses, which were approximated according to Leva's correlation [2]. The energy balance is described by using equation (5.18). Where d_t (m) is the tube diameter, U (W·m^{-2}·K^{-1}) is the overall heat transfer coefficient and T_c (K) is the cooling medium temperature.

$$v \cdot C_t \cdot \tilde{c}_p \cdot \frac{dT}{dz} = \rho_b \cdot \sum_{i=1}^{M} \left(-\Delta_r\widetilde{H}_{i,k} \cdot \frac{r_{k,i}}{v_{k,i}}\right) - \left(\frac{4}{d_t}\right) \cdot U \cdot (T - T_c) \tag{5.18}$$

The overall heat exchange coefficient was evaluated by using equation (5.19); where h_i (W·m^{-2}·K^{-1}) and h_e (W·m^{-2}·K^{-1}) are the internal and external heat transfer coefficient, respectively, A_i (m^2) and A_e (m^2) are the internal and external area of heat exchange, respectively. Whereas, h_i was estimated according to equation (5.20), in which k (W·m^{-1}·K^{-1}) is the thermal conductivity of the gaseous mixture.

$$\frac{1}{U} = \frac{1}{h_i} + \frac{1}{h_e} \cdot \frac{A_i}{A_e} \tag{5.19}$$

$$h_i = \frac{k}{d_t} \cdot \left[3.5 \cdot \left(\frac{d_p \cdot \rho \cdot v}{\mu}\right)^{0,7}\right] \cdot e^{\frac{-4.6 \cdot d_p}{d_t}} \tag{5.20}$$

5.2.3. Plant model with gas recycle

Model with one reactor

The reactor model with gas recycle was designed to overcome the computational difficulties of a transient calculation model, with the aim of studying the pseudo-temporal evolution of the system with gas recycle and to estimate the start-up time of the plant.

First of all, the evolution of the system is defined as "pseudo-temporal" because the "time" variable is expressed as the sum of the residence times of the process stream in the reactor, and therefore matches with a cumulative residence time within the reactor. Secondly, the residence time in the recirculation pipeline that in the heat exchangers could be added to the residence time into the reactor for estimating the start-up duration. Figure 5.1 illustrates the scheme of the plant model with gas recycle, in which the fresh feed is mixed with the recirculated unreacted gaseous stream. The inlet gas mixture is pre-heated in a head-tail heat exchanger (E-102) and then heated up to the operative temperature by means of a heater (E-101). The gaseous mixture at the outlet of the reactor (R-101) is cooled down to the operative temperature of the biphasic vessel (T-101) producing a liquid mixture of water and methanol that could be distilled and a gaseous stream that is partially purged to avoid inert accumulation. The recycle is compressed to compensate pressure drops.

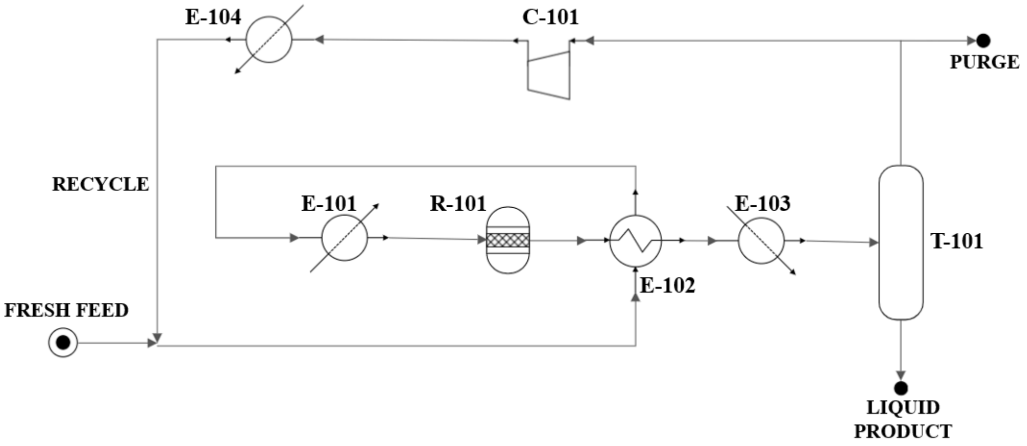

Figure 5.1. Conceptual scheme of the plant with recycle and one reactor.

The compression power required to compensate pressure drops was calculated according to equation (5.21); where Z is the compressibility factor (equal to 1 for ideal gases), T_1 (K) is the temperature at the inlet of the compressor, γ is the compressibility factor, η_c is the compressor efficiency, that was assumed equal to 70 %, $\dot{n}_R$ (mol·s^{-1}) is the molar flow rate of the recycled stream, p_1 (Pa) and p_2 (Pa) are the pressure at the inlet and at the outlet of the compressor, respectively.

$$P_c = Z \cdot R \cdot T_1 \cdot \left(\frac{\gamma \cdot \eta_c}{\gamma - 1}\right) \cdot \left[\left(\frac{p_2}{p_1}\right)^{\frac{\gamma-1}{\gamma \cdot \eta_c}} - 1\right] \cdot \dot{n}_R \tag{5.21}$$

The liquid-vapor separation within the vessel (T-101) was estimated by using the Rachford-Rice equation (5.22) in the case of an isothermal flash, which was solved by using the Newton's method. In the equation, φ is the vapour fraction, z_j is the inlet molar fraction of each j-th component and K_j is the equilibrium constant of the j-th component. K_j could be calculated as the ratio between the vapour pressure of the j-th component (p_j^s, Pa) and the total pressure (p, Pa). Lastly, the vapour pressure could be estimated by using the Antoine's equation (5.23); where A_j, B_j and C_j are the Antoine's parameters and T (°C) is the temperature.

$$\sum_{j=1}^{N} \frac{(1-K_j)\cdot z_j}{1+(K_j-1)\cdot\varphi} = 0 \tag{5.22}$$

$$Log_{10}(p_j^s) = A_j - \frac{B_j}{C_j + T} \tag{5.23}$$

Table 5.3 summarises the parameters of the Antoine's equation.

Table 5.3. Parameters of the Antoine's equation [148].

Component	A_j	B_j	C_j
CO_2	6.81228	1301.679	-3.494
H_2	2.93954	66.79540	275.65
CO	3.81912	291.7430	267.996
H_2O	5.11564	1687.537	230.17
CH_3OH	5.20277	1580.080	239.500
CH_4	3.76870	395.7440	266.681
N_2	3.61947	255.68	266.55

The assumptions for the operative conditions are as follows:

- The fresh feed molar composition is: 24.75 % CO_2, 74.25 % H_2 and 1.00 % N_2. The H_2/CO_2 molar ratio is stoichiometric.
- The fresh feed stream is already at 220 °C and 5 MPa.
- The heat exchanger E-101 heats the stream at the operative temperature (i.e. 220 °C).
- The cooler E-103 cools down the stream at 30 °C.
- The operative temperature and pressure of the vessel T-101 are 30 °C and 4.5 MPa, respectively.
- The purge fraction of the gaseous stream is 1.5 %; whereas, the 98.5 % of the stream is compressed up to 5 MPa in C-101, recycled and mixed with the fresh feed stream.
- The methanol productivity in the liquid product stream was assumed equal to 500 t/d.

- The spatial velocity within the reactor ranges between 5000 and 10000 $Nm^3 \cdot h^{-1} \cdot m_{bed}^{-3}$.

Model with two reactors

Another configuration of the methanol plant was modelled and investigated. In more detail, the second plant configuration consists of two reactors with a split of the inlet stream and, consequently, a quench between the two reactors, as illustrated in Figure 5.2.

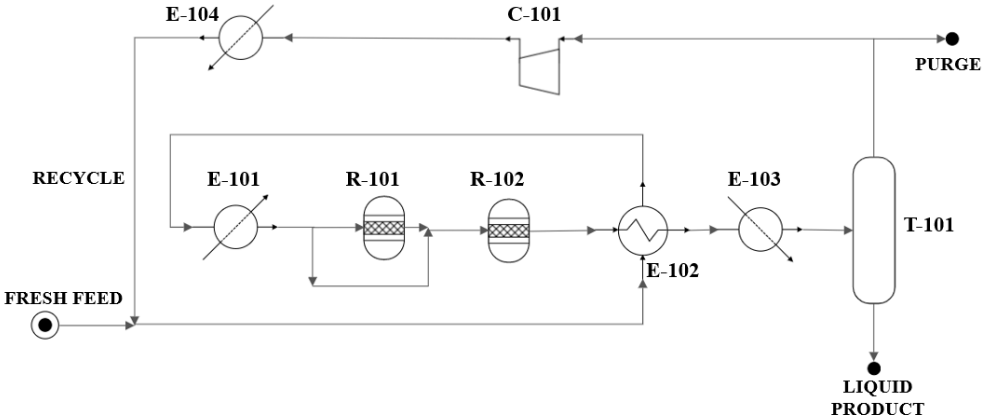

Figure 5.2. Conceptual scheme of the plant with recycle and two reactors.

Five configurations were analysed in this work; more in detail, they were namely:

- **C1**: plant configuration with a single refrigerated multi-tube fixed-bed reactor (i.e. base case of study);
- **C2**: plant configuration with two adiabatic single-tube fixed-bed reactors;
- **C3**: plant configuration with one adiabatic single-tube fixed-bed reactor;
- **C4**: plant configuration with an adiabatic single-tube fixed-bed reactor (i.e. first reactor, R-101) followed by a refrigerated multi-tube fixed bed reactor (i.e. second reactor, R-102);
- **C5**: plant configuration with two refrigerated multi-tube fixed-bed reactors.

Lastly, for the evaluation of the best performances of the plant configuration some boundaries were considered:

- The maximum temperature of the catalytic bed was set to 280 °C because of deactivation phenomena of the catalyst [50];
- The maximum pressure drops were set to 0.5 MPa [50];
- The methanol productivity was assumed equal to 500 t/d;

Table 5.4 summarises the main parameters of the five configurations.

Table 5.4. Characteristics of the 5 configurations.

Configuration	Reactor	Length, m	Tube diameter, m	Number of tubes
C1	refrigerated	12.0	0.06	2000
C2	adiabatic	6.0	2.40	1
	adiabatic	7.5	3.00	1
C3	adiabatic	13.5	2.70	1
C4	adiabatic	6.0	2.40	1
	refrigerated	4.2	0.06	4433
C5	refrigerated	1.5	0.10	2304
	refrigerated	6.0	0.15	491

5.3. Results and Discussion

5.3.1. Analysis of the methanol kinetics

First of all, the kinetics of the reactions were sensitively analysed by varying operating conditions to understand how the CO_2 is hydrogenated to CO and methanol. Temperature, pressure and composition of the gaseous mixture were varied to perform the sensitivity analysis. Firstly, the temperature of reaction was varied between 200 °C and 300 °C. What stands out in Figure 5.3 is that the reaction rate of the CO_2 hydrogenation is roughly null at each temperature; therefore, CO_2 is firstly hydrogenated to CO and then it forms methanol. The reaction rate of the CO hydrogenation exhibited a maximum at ~255°C and a fast reduction at higher temperatures. Whereas, the reaction rate of the endothermic RWGS reaction increases exponentially as the temperature rises. As a result, this analysis demonstrates that at low temperatures ($T < 230$°C) the CO_2 hydrogenation and the RWGS reaction are kinetically limited; while at higher temperatures ($T > 280$°C) the methanol formation is thermodynamically limited favouring CO production.

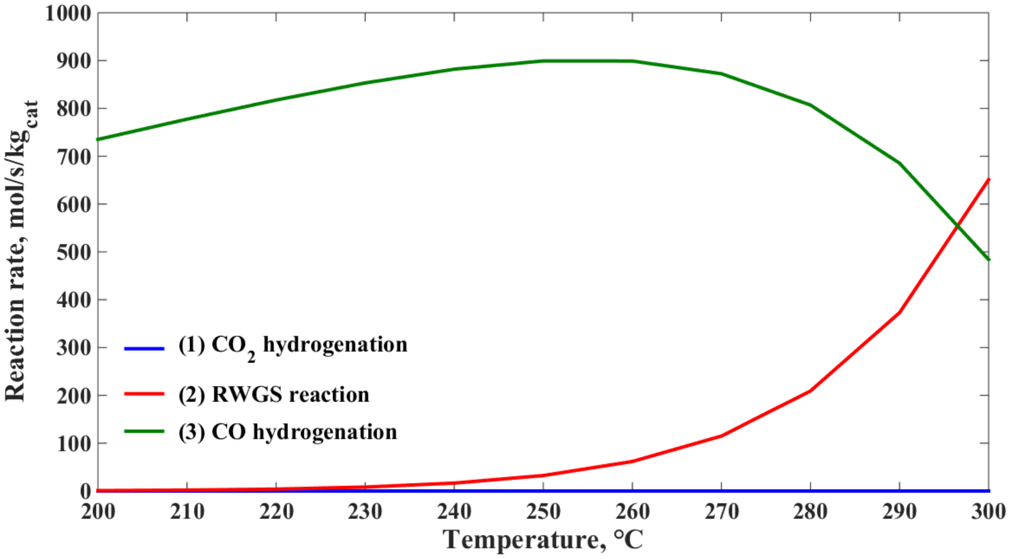

Figure 5.3. Sensitivity analysis of the reaction rate at the variation of the temperature (Conditions: 25.14 %mol CO_2, 71.39 %mol H_2, 2.96 %mol CO, 0.51 %mol CH_3OH, 5 MPa [50]).

Furthermore, the reaction rates change as the operating pressure varies. More specifically, the most sensible reaction is the CO hydrogenation because of the reduction of the moles (i.e. $\Delta\nu<0$). In addition, the reaction rates increase slightly rising the H_2/CO_2 molar ratio. Whereas, the reaction rates decrease slightly increasing the inert content of the gaseous mixture because of the reduction in partial pressure of the reactants.

5.3.2. Simulation of single reactors

The results of the behaviour of single reactors are presented and compared. In addition, the model developed in Matlab® environment is verified with the data reported in the literature. More specifically, as reported in Table 5.5, a simulation of a multi-tube isothermal reactor was carried out and compared with the results obtained by Kiss et al. [50]. The model that was developed and the assumptions are validated because the percentage error between the model and the reference data is lower than 5%.

Table 5.5. Comparison between the results obtained by Kiss et al [50] and the model developed in Matlab® environment for an isothermal multi-tube reactor (reaction temperature 250 °C, operative pressure 5 MPa, reactor length 12 m, number of tubes 810, tube diameter 0.06 m). For the sake of clarity, the percentage error was evaluated with respect to the molar flow rate of each component.

	Reactor inlet	Reactor outlet (Ref. [50])	Reactor outlet (Simulated)	Error, %
Flow rate, mol·s^{-1}	2511.4	2294.2	2288.9	
CO_2, %mol	25.14	22.78	22.62	0.93
H_2, %mol	71.39	63.95	63.65	0.70
CO, %mol	2.96	3.24	3.35	3.16
H_2O, %mol	0.0	4.74	4.96	4.40
CH_3OH, %mol	0.51	5.29	5.42	2.22

Figure 5.4 illustrates the axial CO_2 conversion profiles along the three types of reactors (i.e. isothermal, adiabatic and refrigerated). What stands out from these profiles is that the CO_2 conversion increases rapidly at the inlet of the reactors achieving ~18 % in the case of isothermal and adiabatic reactors. Whereas, in the refrigerated reactor the CO_2 conversion is lower and rises slightly along the reactor. This behaviours are caused by the three different temperature profiles, as shown in Figure 5.5; in fact, the isothermal reactor is at 250 °C, whereas, the temperature in the adiabatic reactor reaches ~276°C and decreases to ~274°C due to the endothermal RWGS reaction. Lastly, the refrigerated reactor exhibited an adiabatic behaviour at the inlet of the reactor, but then the temperature decreases to the

cooling medium temperature (i.e. 234°C) favouring thermodynamically the CO_2 conversion and the methanol selectivity. However, the low temperature inhibits the reaction rate of the RWGS reaction and, thus, also the CO hydrogenation to methanol.

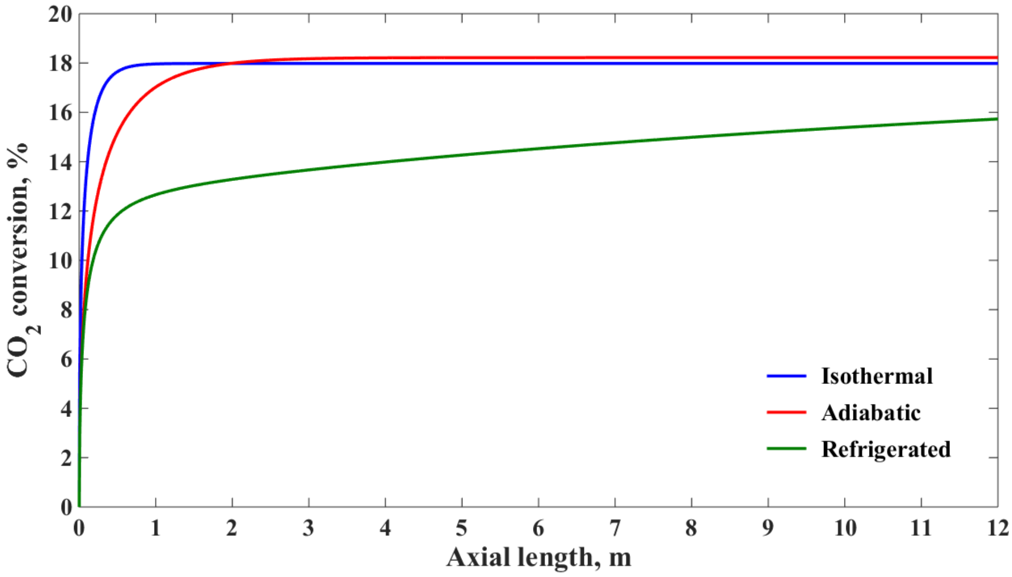

Figure 5.4. Axial CO_2 conversion profiles along the three different types of reactors (Conditions: 25.14 %mol CO_2, 71.39 %mol H_2, 2.96 %mol CO, 0.51 %mol CH_3OH, 5 MPa, inlet temperature 250 °C, cooling medium temperature 234 °C [50]).

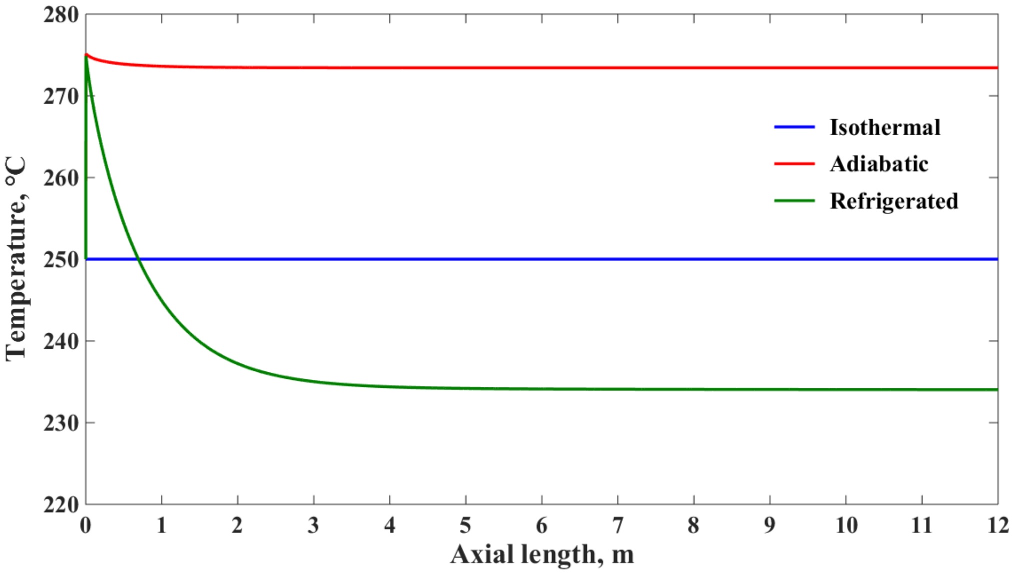

Figure 5.5. Axial temperature profiles along the three different types of reactors (Conditions: 25.14 %mol CO_2, 71.39 %mol H_2, 2.96 %mol CO, 0.51 %mol CH_3OH, 5 MPa, inlet temperature 250 °C, cooling medium temperature 234 °C [50]).

In conclusion, the methanol yield profiles highlight the overall efficiency of each reactor. More in detail, as illustrated in Figure 5.6, the adiabatic reactor achieves the lowest methanol yield (~11%); the isothermal reactor rapidly reaches ~17% but the 90% of the reactor length is inoperative. Lastly, the methanol yield in the refrigerated reactor increases slowly and achieves the highest value (~21%)

because the low reaction temperature strongly favours the selectivity towards methanol. Therefore, the refrigerated reactor exhibited the greatest performances.

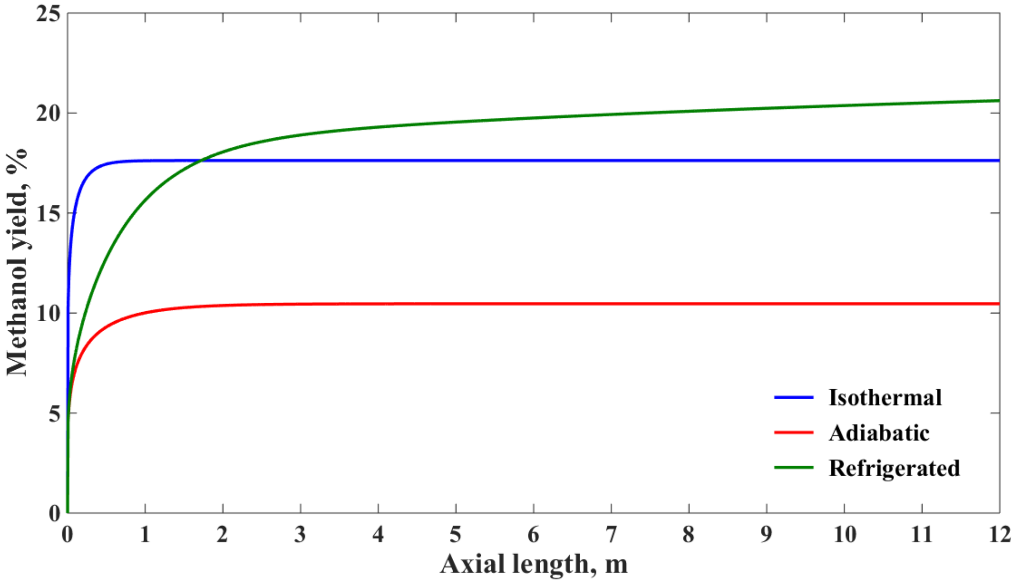

Figure 5.6. Axial methanol yield profiles along the three different types of reactors (Conditions: 25.14 %mol CO_2, 71.39 %mol H_2, 2.96 %mol CO, 0.51 %mol CH_3OH, 5 MPa, inlet temperature 250 °C, cooling medium temperature 234 °C [50]).

5.3.3. Simulations of the plant configurations

Regarding the 5 plant configurations described in Section 5.2.3, some key performance indicators were evaluated for comparing the results of each configuration. More in detail, the scale factor indicates the efficiency in methanol production; in fact, configurations C4 and C5 require a lower quantity of reactants in order to produce 500 t/d of methanol in the liquid product. Whereas, configurations C2 and C3 exhibited a lower efficiency with respect to the base configuration (i.e. C1) because the scale factor is greater than 1. These results are confirmed by other parameters; in fact, configurations C4 and C5 exhibited a higher methanol yield, lower pressure drops and fraction of purged H_2 than the other configuration.

Table 5.6. Comparison between the 5 different plant configurations.

	C1	C2	C3	C4	C5
Scale factor	1.000	1.029	1.033	0.994	0.994
Methanol yield per unit of reactor volume, %/m^3	0.30	0.21	0.21	0.26	0.27
Methanol yield per unit of reactor length, %/m	1.72	1.25	1.21	2.05	2.81
Pressure drops, bar	2.47	2.83	5.71	0.48	0.50

Methanol yield in the liquid product, %	89.03	85.95	85.60	89.04	89.06
Methanol molar fraction at the outlet of the reactors, %mol	4.42	3.30	3.19	4.50	4.52
Fraction of purged H_2, %	6.8	9.1	9.4	6.9	6.6

5.3.4. Configuration of the plant with two refrigerated reactors

As mentioned before, configuration C5 exhibited the best performances; hence, it was analysed in more detail in order to estimate a start-up duration, the sensitivity to the split fraction between the two reactors and the behaviour at the variation of the operative condition.

Figure 5.7 illustrates the stationary CO_2 conversion profile along the two refrigerated reactors with respect to the reaction temperature. What stands out from the figure is that the adiabatic behaviour at the inlet of the reactor is caused by the CO hydrogenation to methanol; in fact, CO is present in the recycled gas mixture. The temperature rapidly rises and then RWGS reaction occurs converting CO_2 to CO, which is subsequently hydrogenated to methanol according to the analysis of the kinetics. In the first reactor, the CO_2 conversion achieves ~11% and the gaseous stream is quenched by at the outlet of the reactor. Similarly, within the second reactor, CO is firstly hydrogenated to methanol and, subsequently, CO_2 starts to be converted into CO and methanol, reaching a CO_2 conversion of ~21%.

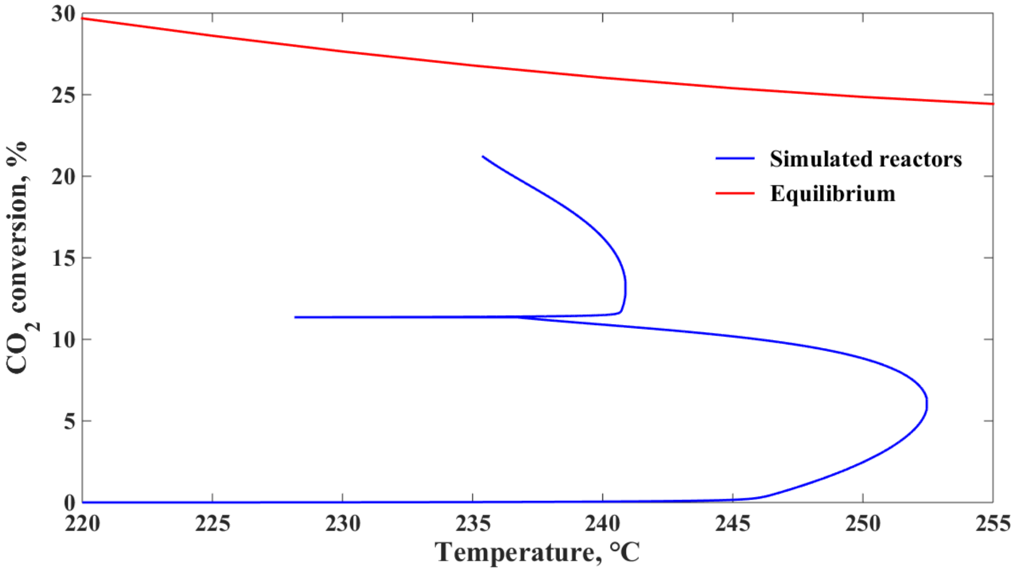

Figure 5.7. Equilibrium CO_2 conversion (red line) and stationary conversion-temperature map within the two refrigerated reactors in configuration C5 (blue line). Fresh feed: 24.75 %mol CO_2, 74.25 %mol H_2, 1.00 %mol N_2, 220 °C, 5 MPa; cooling medium temperature 234 °C; liquid-vapour separation at 30 °C and 4.5 MPa; split faction 0.5.

Regarding the estimation of the start-up time, the following assumption were done before the simulations:

- The length of the pipelines (including the vessel) were practically assumed equal to 5 times the total length of the two reactors;
- At stationary condition the gas velocity in the pipeline was assumed equal to 20 m/s; moreover, at stationary condition the volumetric flow rate is ~112 Nm^3/s.

Figure 5.8 illustrates the pseudo-temporal CO_2 conversion profile at the outlet of the two reactors. The stationary condition is achieved after ~6000 s (i.e. ~1.7 h) as confirmed by the power consumption of the compressor in Figure 5.9. Furthermore, the pseudo-temporal CO_2 conversion exhibited a minimum at the outlet of the reactors after ~900 s because the pseudo-temporal temperature profile exhibited an increase in the peak temperature; therefore, all the temperature profile along the reactor shifts at slightly higher temperatures. Whereas, the power consumption of the compressor is a monotonous because it depends on the molar flow rate of the recycled gas mixture.

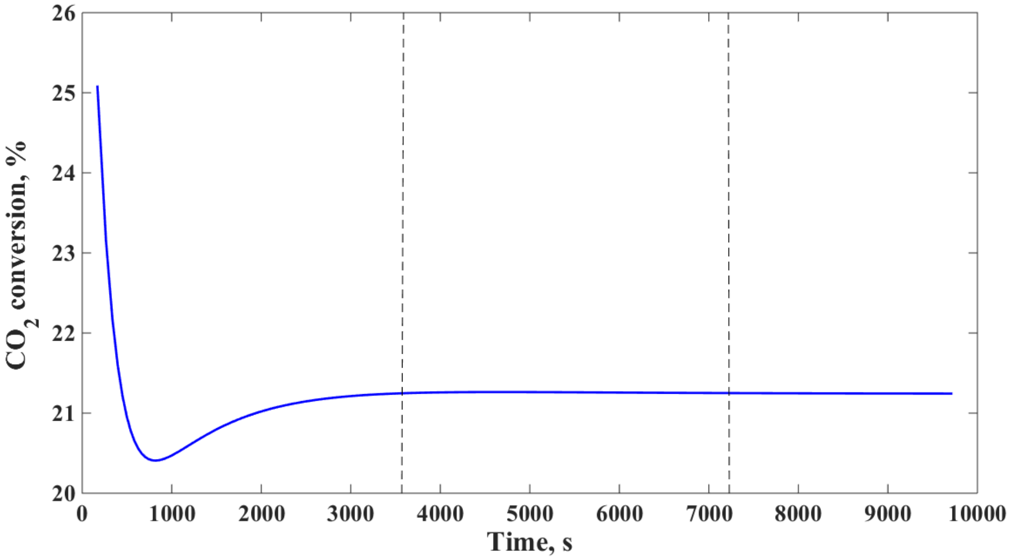

Figure 5.8. Pseudo-temporal CO_2 conversion profile at the outlet of the second reactor in configuration C5. Fresh feed: 24.75 %mol CO_2, 74.25 %mol H_2, 1.00 %mol N_2, 220 °C, 5 MPa; cooling medium temperature 234 °C; liquid-vapour separation at 30 °C and 4.5 MPa, split fraction 0.5.

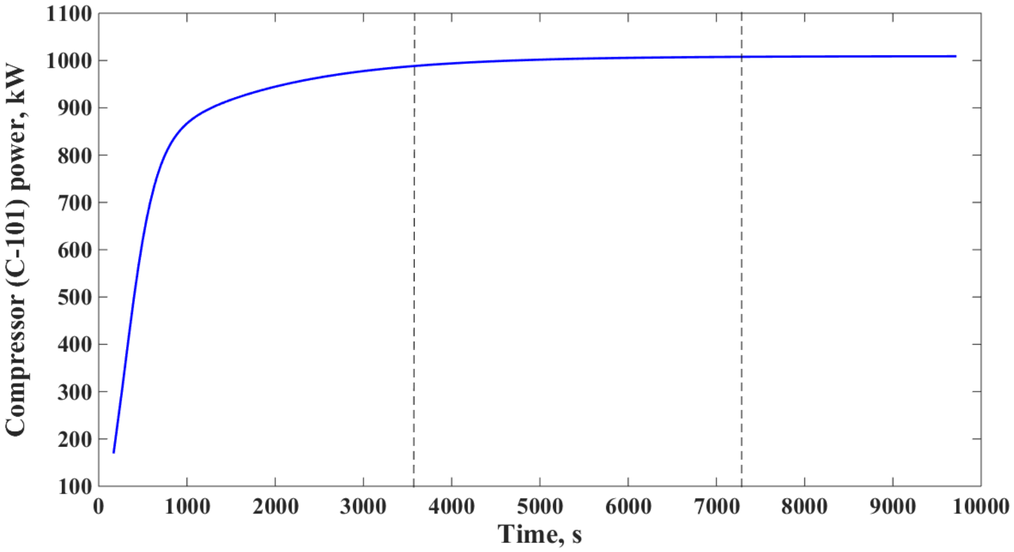

Figure 5.9. Pseudo-temporal compression power consumption profile in configuration C5. Fresh feed: 24.75 %mol CO_2, 74.25 %mol H_2, 1.00 %mol N_2, 220 °C, 5 MPa; cooling medium temperature 234 °C; liquid-vapour separation at 30 °C and 4.5 MPa, split fraction 0.5.

A sensitivity analysis on the fraction of split between the two reactors was carried out in order to evaluate the best value of the parameter. The split fraction (SF) was defined as the ratio between the flow rate at the inlet of the first reactor and the total flow rate at the inlet of the reactors. Therefore, as shown in Figure 5.10, the pseudo-temporal profile of the maximum temperature within the two reactors shifts at lower temperatures increasing the split fraction. However, the first reactor is not as sensible as the second reactor to this variation. In fact, in the first reactor the shift of the temperature is ~1.5°C; whereas, in the second reactor it achieves ~5.7°C because if the gas mixture is mainly fed to R-101, the reaction will occur in R-101 but the residence time decreases. Moreover, a lower amount of CO_2 will be converted in R-102 while the spatial velocity is roughly constant. Lastly, the methanol productivity does not vary changing the split fraction between the two reactors; hence a split fraction equal to 0.5 seems to be a good compromise.

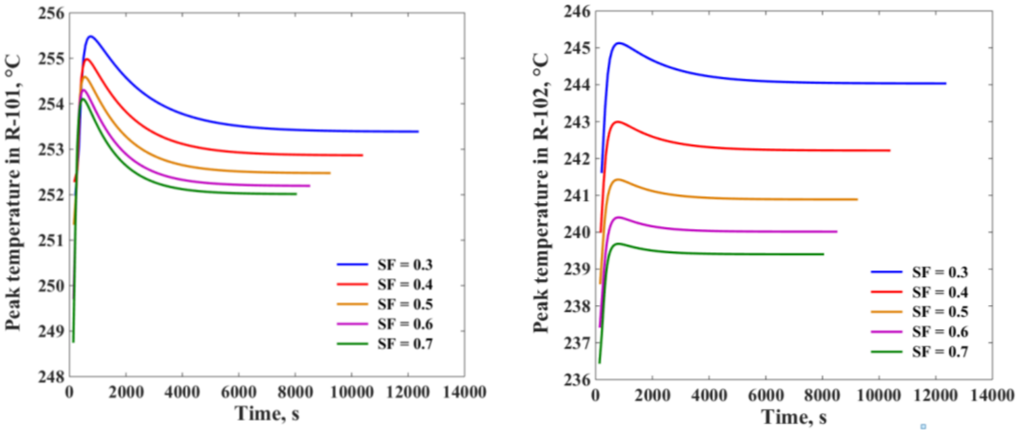

(a) (b)

Figure 5.10. Pseudo-temporal peak temperature profile (a) in the first reactor (R-101) and (b) in the second reactor (R-102) at the variation of the split fraction of the inlet stream between R-101 and R-102. Fresh feed: 24.75 %mol CO_2, 74.25 %mol H_2, 1.00

%mol N_2, 220 °C, 5 MPa; cooling medium temperature 234 °C; liquid-vapour separation at 30 °C and 4.5 MPa.

Regarding the operating condition of the plant configuration C5, it was sensitively analysed ranging the operating condition between 25% and 100 % of the nominal productivity. For the sake of clarity, the size of all pieces of equipment was not changed with respect to the nominal plant productivity (i.e. 500 t/d). Two main parameters changed reducing the operative load of the plant: the peak temperature profile and the start-up time of the plant. On the one hand, the maximum temperature within both reactors increases reducing the operating load because overall flow rate diminishes. This reduction in flow rates results in an increase of the residence time in the reactors and a lower heat transfer coefficient; hence the temperature profile shifts at higher values. As shown in Figure 5.11, the temperature increases of ~2.6°C reducing the operating load from 100% to 25% of the nominal value. On the other hand, the reduction in flow rates increases the residence time in all the equipment and, therefore, as shown in Figure 5.11, the start-up time increases proportionally as the operating load decreases; in fact, it reaches ~8h if the operating load is 25% of the nominal value.

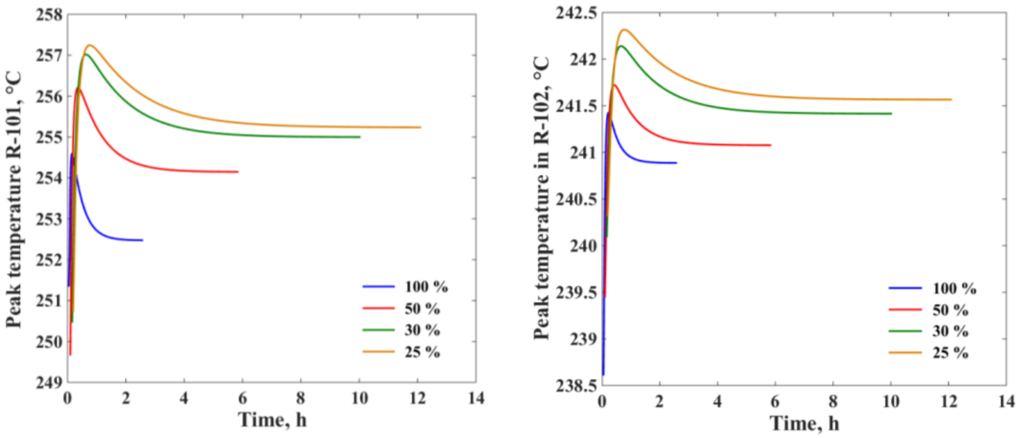

(a) (b)

Figure 5.11. Pseudo-temporal peak temperature profile (a) in the first reactor (R-101) and (b) in the second reactor (R-102) at the variation of the operative load of the plant. Fresh feed: 24.75 %mol CO_2, 74.25 %mol H_2, 1.00 %mol N_2, 220 °C, 5 MPa; cooling medium temperature 234 °C; liquid-vapour separation at 30 °C and 4.5 MPa, split fraction 0.5.

5.4. Conclusion

This section summarises the results and conclusions to which this work has led. The first part of the work focuses on the modelling of an isothermal, an adiabatic and a refrigerated reactor for the synthesis of methanol. The model of the isothermal reactor was verified with those obtained in the literature [50]; whereas, the validation of the adiabatic and refrigerated reactors was done by using the Aspen Plus process simulator.

The second part of the work illustrates the development of a simplified process model, which includes the reactor, the separation section and the gas recycle. The simulation of the scheme was carried out for estimating the start-up time of the plant. Furthermore, this simulation allowed the pseudo-temporal evolution of variables to be studied. The thermal management of the reactor for the synthesis of methanol is crucial to preserve the activity of the catalyst.

Five different plant configurations were compared by defining key performance indicators. The configuration that exhibited the best performances consists of two refrigerated reactors in series, achieving a high overall methanol yield. The reactor developed in this work has been sized to produce 500 ton/day of methanol in the liquefied stream downstream of the biphasic separator, a current which must then be sent to a further separation section in which the methanol is separated from the water and the non-condensable gases until the required purity is reached.

A sensitivity analysis was performed varying the operating condition of the plant between 25% and 100% of the nominal productivity. The configuration with two refrigerated reactors did not show any critical issues in this regard. However, this fact was ascribed to the nature of the pseudo-homogeneous model that was developed in this work. A natural progression of this work should be oriented towards the development of a heterogeneous model, that is more suitable for identifying hotspots within the reactor. Similarly, the development of a two-dimensional model (pseudo-homogeneous and heterogeneous) would also be useful.

Finally, the dependence on the split fraction between the two reactors of the maximum temperature in the two catalytic beds at each passage of the process stream and of the methanol productivity was investigated. The pseudo-temporal evolution of the temperature peaks in the two reactors showed a slightly dependence on the split fraction; however, it did not highlight any critical issues. Moreover, the methanol productivity is substantially independent of this variable.

Chapter 6

How to make sustainable CO_2 conversion to Methanol: thermo-catalytic versus electro-catalytic technology

The study presented in this chapter was published as [4]:

Guzmán, H.; Salomone, F.; Batuecas, E.; Tommasi, T.; Russo, N.; Bensaid, S.; Hernández, S.; How to make sustainable CO_2 conversion to Methanol: thermocatalytic versus electrocatalytic technology *Chem. Eng. J.* **2020**, 127973, doi:10.1016/j.cej.2020.127973.

6.1. Introduction

As introduced in Chapter 1, there are different technologies for producing methanol via CO_2 hydrogenation. More in detail, the present Chapter focuses on the comparison between the thermocatalytic (TC) and the electrocatalytic (EC) routes. On the one hand, the TC route consists of an electrolyser, a CCU unit, a reaction section and a separation and purification section. The reaction occurs in a heterogeneous catalytic bed at high temperature and pressure. However, other processes seem to be promising at a laboratory scale. In fact, on the other hand, the EC conversion of CO_2 to methanol consists in the direct electroreduction of CO_2 on the surface of the electrocatalyst by using electricity and water for the in-situ production of protons in mild conditions. The most challenging aspects of the EC process are the reduction of overpotentials, the scalability of the EC reactor and the optimization of the electrocatalyst.

The aim of this work is to analyse the potential of scaling-up the TC and EC CO_2-to-methanol conversion processes. Therefore, the catalytic CO_2-to-methanol conversion was firstly evaluated at laboratory-scale by means of the electrocatalytic and thermocatalytic pathways, whose performance was compared. A low-cost catalyst composed of three oxides: copper oxide (CuO), zinc oxide (ZnO) and aluminium oxide (Al_2O_3), with a state-of-the-art performance for the TC process, was synthesised by the co-precipitation method and tested for this purpose. Herein, this kind of catalyst was tested for the first time in an EC CO_2 reduction process and its ability to produce methanol by this low temperature process is demonstrated.

In this way, the performances of these two CO_2-to methanol conversion processes were simulated in a scaled-up configuration. To this purpose, considering the different lab-scale productivities of the two processes, certain assumptions have been made based on literature and our experimental data, to find feasible target in operative conditions that can bring to their practical implementation. Another standpoint of this work is to consider the entire process, including downstream separation and purification steps to obtain a commercial product (99.9 $\%mol_{methanol}$). For the TC case, both the lab-scale reactor performance and a scaled-up process able to reach an industrial methanol productivity of 3 kg/h were analyzed. Instead, a step by step and more detailed study was performed for the scale-up of the EC CO_2 reduction process, because it has poorly been studied in literature. Stating from the lab-scale case, another six EC cases were analysed to subsequently consider the influence of: recycling of unreacted CO_2; increase of the electrode area up to 100 cm^2; increase of the inlet gas flow rate; increase of the current density up to 100 mA/cm^2 and increase of the Faradaic efficiency up to ~90%, in order to reach the same final productivity of the scaled-up TC process, for comparison purposes. A complete analyses of energy requirements of all these process conditions was made. Moreover, the economic assessment (comprising a estimation of operative and capital costs) and climate impacts (determined by a full LCA) of the most promising cases of study are also presented, focusing then into the strategies to be implemented to attain techno-economic and environmental benefits from these two TC and EC technologies with respect to an industrial fossil-fuel-based process for methanol production.

6.2. Methodology

6.2.1. Process description of laboratory scale processes

A ternary $CuO/ZnO/Al_2O_3$ (CZA) catalyst was prepared via the coprecipitation route according to a method modified from literature [198]. The detailed description of the CZA catalyst preparation, and the experimental description of the thermocatalytic and electrocatalytic CO_2 reduction laboratory tests are given in the following Sections.

$CuO/ZnO/Al_2O_3$ (CZA) catalyst preparation

A ternary $CuO/ZnO/Al_2O_3$ (CZA) catalyst was prepared via the coprecipitation route according to the literature [199]. The Cu/Zn/Al used molar ratio was 60:30:10. Briefly, since the preparation and characterization of the catalyst is not the aim of this work, a solution of metal nitrates and a solution of sodium carbonate used as a precipitant were pumped into a stirred and heated glass beaker with a starting volume of distilled water. During the precipitation process, pH, temperature and aging time were controlled. While the metal nitrate solution was being pumped, the sodium carbonate solution was added to maintain a constant pH. After aging, the precipitates were filtered and washed with distilled water and then dried overnight.

After grinding, the dried hydroxy carbonate precursor was calcined under air, resulting in the oxide precursor. A Merlin Zeiss Field Emission – Scanning Electron Microscope (FE-SEM) operated at 3 kV equipped with an Energy Dispersive X-ray Spectroscopy System (EDS) was used to study the morphology of the samples.

Thermocatalytic CO_2 reduction tests

The thermocatalytic activity of the catalyst was tested in an 8 mm-diameter packed-bed, stainless steel reactor, arranged in a vertical position, with 1.5 g of catalyst, resulting in a bed length of approximately 40 mm. Before the catalytic measurements, the fresh catalyst was reduced in a stream of 10 % H_2/N_2 at 30 Nl/h and at 300 °C for 3 h under 2 bars. Then the tubular reactor was cooled to a given temperature and a gas mixture (H_2:CO_2:N_2 molar ratio equal to 3:1:1, with WHSV= 30 $Nm^3\ kg_{cat}^{-1}\ h^{-1}$) was introduce, raising the pressure to 25 bar., Different operatives temperatures were tested from 200 °C to 300 °C (each 20 °C). A Gas Chromatography (GC) system (7890B of Agilent technologies) was used for online gas analysis, the methanol concentration was determined by using a flame ionization detector (FID) and gaseous products were determined by using a thermal conductivity detector (TCD). The laboratory-assembly consists of four main sections: i) system for feeding and regulating the flow of reactant gases; ii) insulated and heated tubular reactor; iii) condensation and separation of water produced by hydrogenation of CO_2 and iv) system for analysing the gas leaving the reactor. The simplified TC setup of CO_2 hydrogenation to methanol process is shown in Figure 6.1

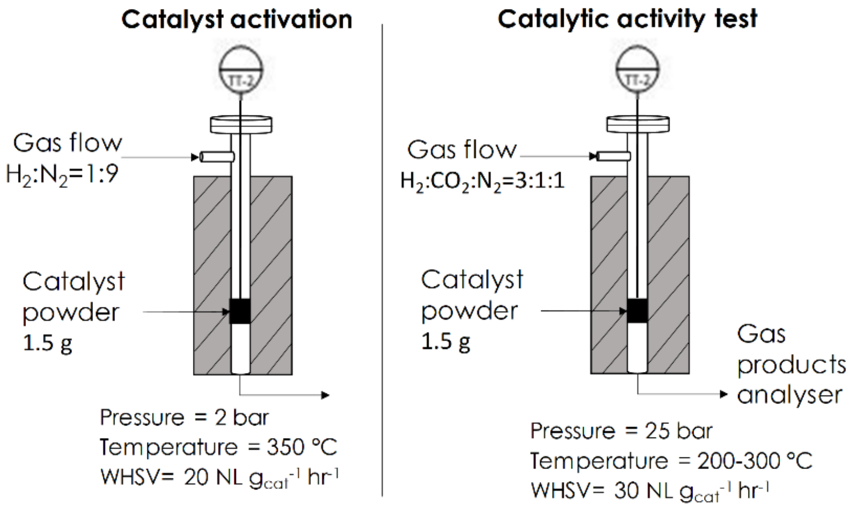

Figure 6.1. Simplified conceptual scheme of the CO_2 TC reduction setup.

CO_2 conversion (ζ_{CO_2}), CH_3OH selectivity (σ_{CH_3OH}) and CH_3OH yield (η_{CH_3OH}) values were calculated from a mass-balance in the reactor (the experimental error at the individual temperatures was evaluated on the conversion and it does not exceed 3%) according to equations (6.1), (6.2) and (6.3), respectively.

$$\zeta_{CO_2} = \frac{\dot{n}_{CO_2,in} - \dot{n}_{CO_2,out}}{\dot{n}_{CO_2,in}} \tag{6.1}$$

$$\sigma_{CH_3OH} = \frac{\dot{n}_{CH_3OH,out}}{\dot{n}_{CO_2,in} - \dot{n}_{CO_2,out}} \tag{6.2}$$

$$\eta_{CH_3OH} = \frac{\dot{n}_{CH_3OH,out}}{\dot{n}_{CO_2,in}} \tag{6.3}$$

Where $\dot{n}_{CO_2,in}$ represents the inlet CO_2 molar flow rate (mol/h), $\dot{n}_{CO_2,out}$ is the outlet molar flow rate (mol/h) and $\dot{n}_{CH_3OH,out}$ is the outlet methanol molar flow rate (mol/h).

Electrocatalytic CO_2 conversion tests

The electrocatalytic activity of the CZA-based electrode was tested at room temperature and atmospheric pressure in a Gas Diffusion Electrode (GDE) EC half-cell. As schematized in Figure 6.2, the EC cell is composed by: i) a gas chamber with a gas inlet and gas outlet connections; ii) two electrolyte chambers; iii) a platinum-iridium counter electrode (CE); iv) an Ag/AgCl reference electrode (RE) (sat. KCl); vi) a working electrode (WE), that is a catalysed GDE where the continuous reduction of CO_2 occurs. A potentiostat (Biologic VSP-300) was used to supply the necessary potential between the electrodes.

The two electrolyte chambers contain the catholyte (10 ml of solution of 0.1 M $KHCO_3$) and the anolyte (30 ml of solution of 0,1 M $KHCO_3$) compartments by a Nafion 117 proton exchange membrane (PEM). The membrane allows the selective transport of H^+ ions from the anode to the cathode chamber. The membrane was activated prior to use with hydrogen peroxide (H_2O_2) aqueous solution (5 wt.%) at 60 °C for 2 h, then immersed in a sulfuric acid (H_2SO_4) aqueous solution (1 M) at 60 °C for 2 h and, finally, rinsed with distilled water, following a standard procedure. A GC system (300 micro GC, Inficon) was used for online gas analysis of the gaseous products (CO, H_2). The MeOH concentration was determined by using a liquid chromatograph (HPLC Shimadzu, Prominence model with detector RID-10A and PDA 212 nm and Rezex ROA Organic acid 300x7.8 mm column).

The WE (geometric area, $A = 3\ cm^2$) was prepared by depositing a thin-layer of the CZA catalyst by airbrushing a suspension of the material (or ink) onto a porous Toray carbon paper (Teflon treated TGP-H-060). The catalytic ink was formed by a mixture of the CZA powder acting as electrocatalytic material, Nafion solution (5 wt. % in lower aliphatic alcohols and water, contains 15-20% water, Sigma-Aldrich) used as binder, and isopropanol (99 % purity Sigma-Aldrich) used as vehicle, with a mass ratio of 70:30 Cu/Nafion and 3 wt% of solids (Cu+Nafion).

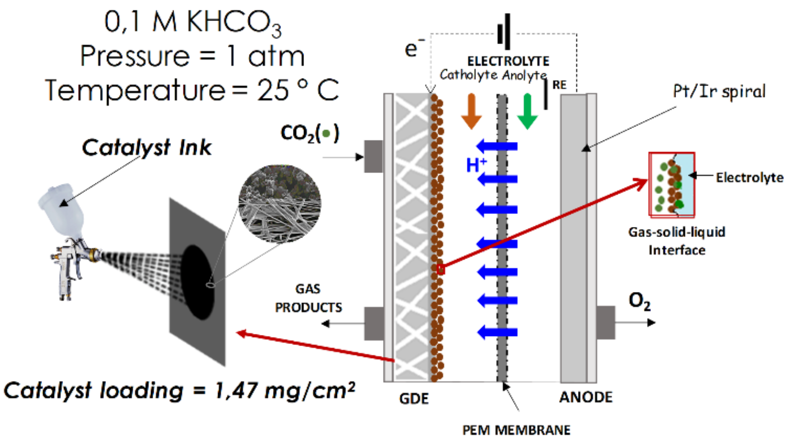

Figure 6.2. Simplified conceptual scheme of the CO_2 TC reduction setup.

The parameter used to evaluate the performance of a determinate electrocatalyst is the current density (j, A m^{-2}), that is the measured electric current per unit of surface or geometric area at a given applied potential. The reaction rate (activity) of the EC reaction is then directly proportional to the current density. The main challenge is to find a suitable electrocatalyst that produce a high current density (related to MeOH production in the present case) at a potential as close as possible to the minimum thermodynamics one (-0.81 V vs RHE) to reduce the required overpotential. The mechanism of the EC CO_2 reduction reaction is based on a series of reactions involving shuttling of electrons and the adsorption and transformation of the reactants, through intermediates, on the electrocatalyst surface[200]. According to the intermediates that are formed during the reaction, different CO_2 reduction products can be obtained. Then, the relative formation of a determinate product is calculated through of the so-called Faradaic efficiency (FE), in order to have a parameter to describe the selectivity of a catalyst. FE is defined as the ratio of the number of coulombs required to form a certain amount of product (determined by chemical analysis) to the total charge over a specific time interval[201]. The Faradaic efficiency for MeOH production can be calculated according to equation (6.4).

$$\mathrm{FE}_{\mathrm{CH_3OH}} = \frac{z \cdot \mathrm{F} \cdot \left(\dot{\mathrm{n}}_{\mathrm{CH_3OH,out}}\right)}{\mathrm{j} \cdot \mathrm{A} \cdot \mathrm{t}} \tag{6.4}$$

Where z is the number of electrons (equal to 6 for CO_2 reduction to methanol), F is the Faraday constant (96485 C mol^{-1}), j is the current density (A m^{-2}), A is the electrode area (m^2), t is the reaction time (s), $\dot{n}_{CH_3OH,in}$ is the outlet methanol molar flow rate.

6.2.2. Process scale up and simulation

The thermocatalytic and electrocatalytic processes were compared first at a laboratory scale for verifying their feasibility and obtaining raw data, which are suitable for their scale up, in order to be able to evaluate their environmental impacts and economic competitiveness. The scale-up of these processes, which is the main aim of this chapter, was simulated and the hypotheses used are described in the further paragraphs.

Thermocatalytic process

The simulated thermocatalytic process consists of four sections: a hydrogen production unit, a carbon dioxide compression chain, a reactor and a separation and purification section, as illustrated in the conceptual scheme in Figure 6.3.

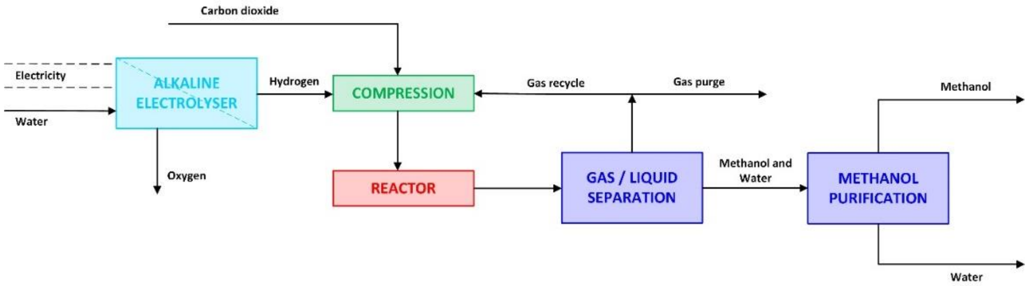

Figure 6.3. Conceptual design of the scaled-up thermocatalytic process.

Firstly, renewable hydrogen could be produced by using a low-temperature electrolyser (e.g. alkaline electrolyser)[3,9,122,202]. This strategy was exploited to render comparable the electrocatalytic and the thermocatalytic processes. Hence, water is pumped to 20 bar (suitable pressure for electrolysis) and it is fed to an alkaline electrolyser, which is powered by renewable electric energy. According to the open literature, the electrolysis has an efficiency of ~70 % (LHV basis)[3,122]; even if water splitting is an endothermic reaction, the process requires heat removal due to its low efficiency. In addition, this heat could be used for heating the inlet water stream. The cathodic outlet stream (hydrogen) is cooled down (40 °C) for condensing water vapour; and then it is mixed with fresh CO_2 and the gaseous recycle.

Secondly, CO_2 could be recovered from a process that emits large quantities of CO_2 by using carbon capture and utilization (CCU) technologies [3,15,203–207]. More specifically, the most common technologies are scrubbing with liquid solvents [160,208–210], adsorption on solids [160,206,210,211] and separation with membranes [212–214]. In order to make conservative hypotheses, a biogas-to-biomethane upgrading plant was assumed as the source of CO_2; hence, an impurity of 1.5 %mol of methane (inert) was considered. The CO_2 stream has to be compressed up to 20 bar (process pressure) by using multistage compression (a maximum discharge/inlet pressure ratio equal to 3 was assumed) for optimizing the specific energy consumption. Subsequently, CO_2 and H_2 are mixed in stoichiometric ratio (H_2/CO_2 molar ratio equal to 3) with the gas recycle stream. This gaseous stream is pre-heated through an economiser and then heated to 250 °C by using an electric heater. The reactor is kept at 250 °C by using cooling water for removing the excess of heat produced during the reaction. More in detail, the process involves three reactions: CO_2 hydrogenation to methanol and reverse water gas shift (RWGS) reaction, that are linearly independent, and CO hydrogenation to methanol (linearly dependent on the other two reactions), as reported in equations (6.5), (6.6) and (6.7), respectively [50,215].

$$CO_2 + 3\ H_2 \rightleftarrows CH_3OH + H_2O \qquad \Delta_rH°_{298K} = -49.40\ kJ\ mol^{-1} \qquad (6.5)$$

$$CO_2 + H_2 \rightleftarrows CO + H_2O \qquad \Delta_rH°_{298K} = +41.12\ kJ\ mol^{-1} \qquad (6.6)$$

$$CO + 2\ H_2 \rightleftarrows CH_3OH \qquad \Delta_rH°_{298K} = -90.55\ kJ\ mol^{-1} \qquad (6.7)$$

According to the open literature, a Langmuir-Hinshelwood-Hougen-Watson kinetic model of the CO_2 hydrogenation to methanol on a CuZnAl-based catalyst was used [50]. Finally, the gaseous products are cooled to 30 °C and separated from the condensed water and methanol. On the one hand, the gaseous stream is recycled back to the reactor, but a small portion of these gases is purged to avoid inert gas accumulation. On the other hand, the liquid stream is fed to a stripper column for removing dissolved gases (mainly CO_2) that are recirculated. Lastly, the liquid bottom stream is fed to a distillation column for purifying the methanol at 99.9 %mol in the distillate and limiting the loss of methanol in the bottom wastewater stream at 10 ppm. For the sake of clarity, all the operative conditions of the simulated thermocatalytic process are summarised in Table 6.1 and the detailed process flow diagram is illustrated in Figure 6.4

Table 6.1. Operative parameters of the simulated thermocatalytic process.

Alkaline electrolyser efficiency	% (LHV basis)	70 %
Average reactor temperature	°C	250
Weight hourly space velocity in the reactor	$Nm^3\ kg_{cat}^{-1}\ h^{-1}$	30.0
H_2/CO_2 inlet molar ratio	-	3
CO_2 molar fraction in the bottom of the stripper column	ppb	≤ 1
Methanol purity in the distillate	% mol	≥ 99.9
Methanol molar fraction in the bottom	ppm	≤ 10
Purged gas fraction	%	1.0

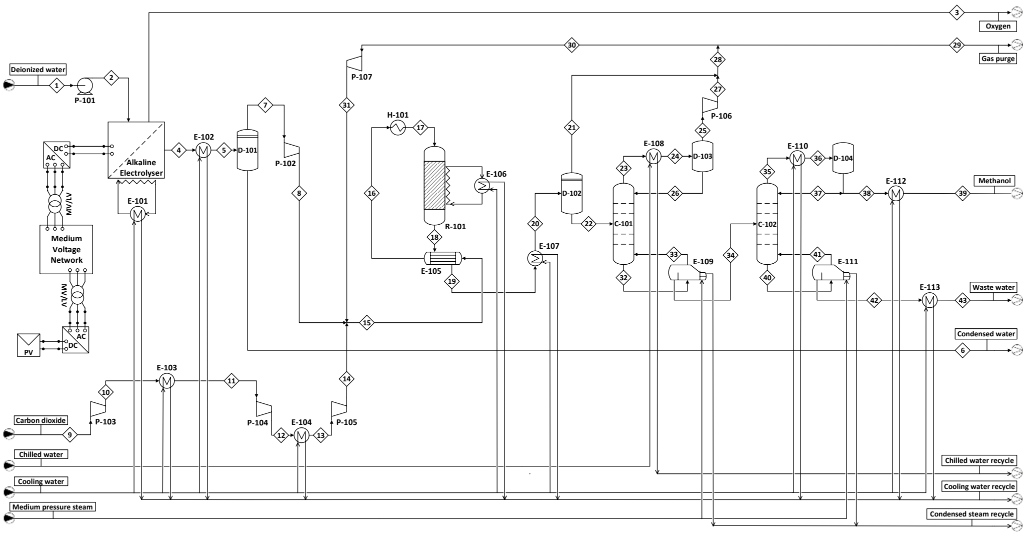

Figure 6.4. Detailed process flow diagram of the scaled-up thermocatalytic process.

Electrocatalytic process

The simulated electrocatalytic process consists of two main sections: an electrocatalytic module and a separation and purification section, as schematised in Figure 6.5.

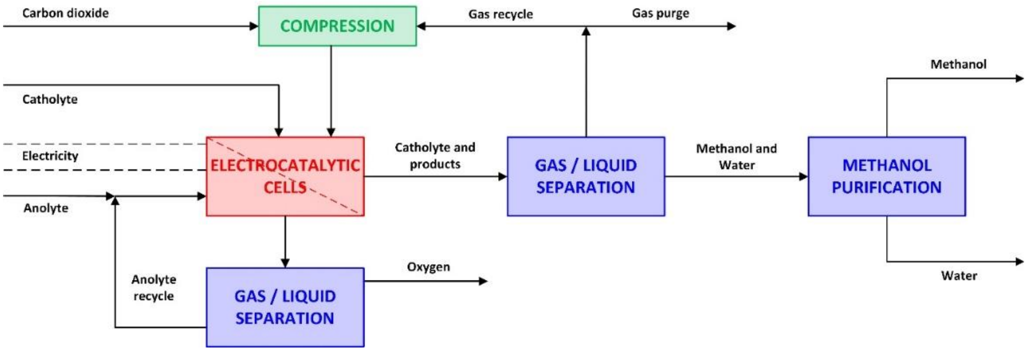

Figure 6.5. Conceptual design of the scaled-up electrocatalytic process.

First of all, the electrocatalytic module consists in several parallelised stacks of cells, that are composed by an anode, a cathode and an electrolyte. In the present work, the electrolyte is a 0.1 M aqueous solution of $KHCO_3$, while the two chambers are separated by a semi-permeable membrane that allows the permeation of OH^-. On the one side, the anode could be made of noble metals (for instance, Pt and Ir), on which the oxidation of OH^- occurs, as reported in equation (6.8). On the other side, the cathode is made of a CuZnAl-based catalyst which is deposited on a porous carbon paper. The reduction of both CO_2 and water occurs on the catalytic surface. More in detail, the cathodic reaction system is very complex; in fact, the water is reduced to H_2 and OH^-, as detailed in equation (6.9). Nevertheless, at the same time, CO_2 and water reacts to produce methanol (6.10), CO (6.11) and by-products (for instance, formate in equation (6.12)). Furthermore, CO_2 is fed to the cathode and it partially dissolves into the catholyte, producing CO_3^{2-} and HCO_3^- species that could be part of the complex reaction system. For the sake of clarity and simplicity, the reaction mechanisms were not investigated and implemented in the simulation of the EC process.

Anode:	E° (V vs. NHE) at pH=7	
$4\ OH^- \rightleftarrows O_2 + 2\ H_2O + 4\ e^-$	-0.81	(6.8)
Cathode:	E° (V vs. NHE) at pH=7	
$2\ H_2O + 2\ e^- \rightleftarrows H_2 + 2\ OH^-$	-0.41	(6.9)
$CO_2 + 5\ H_2O + 6\ e^- \rightleftarrows CH_3OH + 6\ OH^-$	-0.81	(6.10)
$CO_2 + H_2O + 2\ e^- \rightleftarrows CO + 2\ OH^-$	-0.52	(6.11)
$CO_2 + H_2O + 2\ e^- \rightleftarrows HCOO^- + OH^-$	-0.43	(6.12)

Products dilute the electrolyte solution; therefore, the residence time of the electrolyte was defined for achieving a maximum reduction of 5 % of its initial concentration and maintaining conditions similar to the laboratory-scale batch process. The anolyte is recovered and recycled in order to reduce operative costs.

The outlet catholyte stream is fed to the second section of the process for separating gases and purifying the methanol. H_2, CO and CO_2 are mainly separated from water and liquid products in a biphasic vessel. On the one side, the liquid stream is fed to a stripping column to remove dissolved gases and then it is fed to a distillation column to purify the methanol in the distillate, similarly to the TC process. On the other side, the gaseous stream is partially purged, then mixed with fresh CO_2 and recycled to the cathode of the electrocatalytic module. The operating pressure of the electrocatalytic cells is not atmospheric as the laboratory-scale cell due to dilution of the CO_2 in the recycle. For the purpose of operating in condition near the laboratory-scale test unit, a maximum operative pressure of 5 bar was assumed. The gaseous purged fraction was selected in order to guarantee a CO_2 partial pressure within the cathode equal to 1 bar, which is the operative value of the laboratory-scale cell. The main operative parameters of the electrocatalytic process are summarised in Table 6.2 and a detailed process flow diagram is illustrated in Figure 6.6

Table 6.2. Operative parameters of the simulated electrocatalytic process.

Operative total pressure of the electrocatalytic cells	bar	≤ 5
CO_2 partial pressure at the cathode inlet	bar	1
Concentration of $KHCO_3$ in the inlet electrolyte	mol dm^{-3}	0.1
CO_2 molar fraction in the bottom of of the stripper column	ppb	≤ 1
Methanol purity in the distillate	% mol	≥ 99.9
Methanol molar fraction in the bottom of the distillation column	ppm	≤ 10

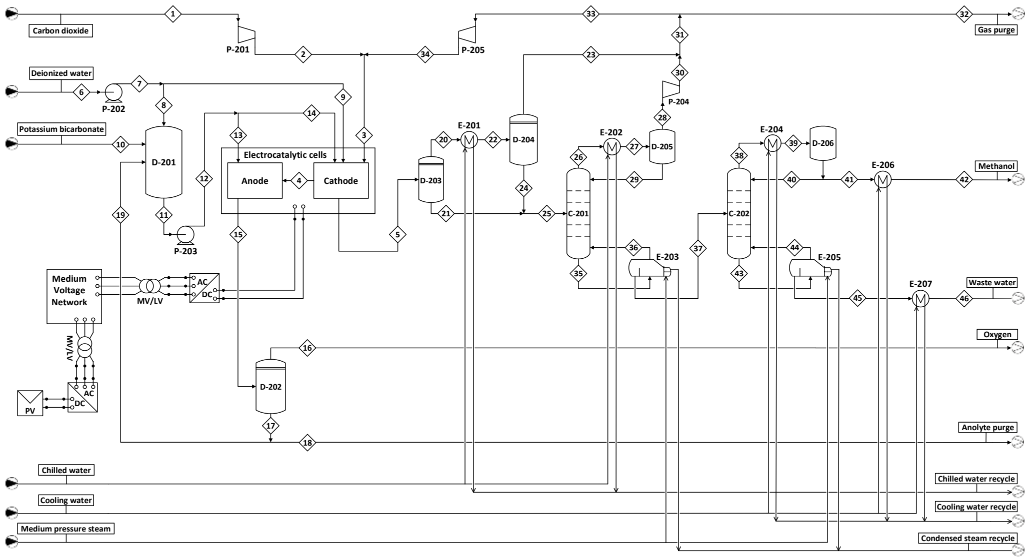

Figure 6.6. Detailed process flow diagram of the scaled-up electrocatalytic process.

Definition of the cases of study

First of all, two laboratory-scale cases were defined for the thermocatalytic and the electrocatalytic processes, namely TC-lab and EC-lab, respectively. These two cases were defined to compare the laboratory-scale processes and to obtain raw data for the Life Cycle Inventory. It is worth noting that experimental test benches do not include gas-liquid separation, product purification and heat integration. Hence, as described before, a scaled-up concept for each process was proposed in order to study the technical, economic and environmental assessment of these two different technologies, considering also the separation and purification steps required to obtain a commercial product.

Since the scale-up of an EC CO_2 reduction process has been poorly studied in literature, a step by step and more detailed study was here performed. Some electrochemical raw data are strictly related to the laboratory-scale test benches, and different operative conditions can be implemented at a higher scale. For these reasons, six EC cases were analysed: EC-1, EC-2, EC-3, EC-4, EC-5 and EC-6; whereas, only one scaled-up TC case was considered (TC-1). All the operative parameters concerning the case studies are summarised in Table 6.3.

Table 6.3. Parameters of the electrocatalytic case studies.

Parameter	Unit	EC-lab	EC-1	EC-2	EC-3	EC-4	EC-5	EC-6
Inlet gaseous molar flow rate in the cathode	mol h^{-1}	2.44	2.44	2436	2436	2436	2436	2436
Active cell area	cm^2	3	3	3	100	100	100	100
Inlet gaseous volumetric flow rate in a single cell	Nl h^{-1}	2.44	2.44	2.44	2.44	14.07	14.07	14.07
Current density	mA cm^{-2}	2.4	2.4	2.4	2.4	2.4	100	100
CO faradaic efficiency	%	14.49	14.49	14.49	14.49	14.49	14.49	2.541

CH_3OH faradaic efficiency	%	32.70	32.70	32.70	32.70	32.70	32.70	89.30
HCOOH faradaic efficiency	%	0.54	0.54	0.54	0.54	0.54	0.54	0.068
H_2 faradaic efficiency	%	52.16	52.16	52.16	52.16	52.16	52.16	8.091

The characteristics of the EC cases of study are as follows:

- **EC-1**: the process involves lab-scale EC cells and it includes a recycle of the gases. The purge fraction was optimized for keeping the CO_2 partial pressure at 1 bar at the cathode inlet. In addition, by-products (H_2 and CO) were considered as inert species (although it is known that CO electroreduction could also occur).
- **EC-2**: the overall inlet CO_2 stream was increased by 1000 times.
- **EC-3**: the active cell area was increased from 3 cm^2 to 100 cm^2, which is a state-of-the-art scale for TRL5 CO_2 electrochemical reduction demonstration technologies[80] and for fuel cells [3,122,216]. It is worth noting that this variation causes changes in the fluid-dynamic regime and in the current and potential distribution[217].
- **EC-4**: the gaseous flow rate in a single cell was increased in order to maintain the lab-scale fluid-dynamic regime. More in detail, the Reynolds number was kept constant[217] assuming a negligible thickness of the cell with respect to its sides; therefore, equation (6.13) was derived under these assumption. $A_{c,n}$ (m^2) represents the active cell area of the n-th case of study and $\dot{V}_n$ is the gaseous flow rate at the inlet of the cell of the n-th case of study.

$$\dot{V}_4 \approx \dot{V}_1 \cdot \sqrt{\frac{A_{c,4}}{A_{c,1}}} \tag{6.13}$$

- **EC-5**: the current density was increased from 2.4 mA/cm^2 to 100 mA/cm^2, which has already been achieved for some CO_2 electroreduction process [218]. The potential and current distribution undeniably depends on many characteristics of the EC cell (e.g., geometry, catalyst, electrodes, electrolyte, etc.)[217].
- **EC-6**: the electrocatalytic performances (faradaic efficiencies) were selected in order to achieve TC-1 methanol productivity.

6.2.3. Economic assessment procedure

An economic assessment of a process is crucial for establishing its feasibility and the competitiveness of a product on the market. The estimation of the capital and operating costs is described in the further paragraphs.

Levelised cost of product

The levelised cost of product (LCOP, €/kg) represents the average cost of product over the time horizon considering the inflation rate (IR), which was assumed equal to 2 %, while the time horizon (TH, y) was defined as 20 years[3,8]. The most important assumption for calculating the LCOP is the zeroing of the net present value (NPV, €) at the end of the time horizon. According to equation (6.14), the NPV is defined as the difference between the sum of the discounted cash flows over the time horizon and the total plant investment (TPI, €). The cash flow (CF_t, €/y) is defined as the difference between revenues and expenditures; while the discount rate was reasonably assumed equal to 10 % [3,8,146,153,219].

$$NPV = -TPI + \sum_{t=1}^{TH} \frac{P_{MeOH,t} \cdot LCOP - O\&M_t}{(1+DR)^t} \tag{6.14}$$

Where $P_{MeOH,t}$ (kg/y) represents the annual productivity of methanol and O&M (€/y) is the operating and maintenance cost.

Operating and maintenance cost estimation

The operating and maintenance cost (O&M, €/y) represents the overall costs related to maintenance, operating labour, replacement, raw materials, utilities, gaseous pollutant treatment, wastewater treatment and waste disposal [3,8,146,219,220].

The operating and maintenance cost estimation (O&M, €/y) represents the overall costs related to maintenance (CM, €/y), operating labour (COL, €/y), replacement (CR), raw materials (CRM, €/y), utilities (CU, €/y), gaseous pollutant treatment, waste water treatment and disposal (CWT, €/y), according to equation (6.15) [3,8,146,150,153].

$$O\&M = C_M + C_{OL} + C_R + C_{RM} + C_U + C_{WT} \tag{6.15}$$

The maintenance and insurance costs were estimated as the 3.0 % of the TPI [3,8]; these costs include equipment repairs, royalties, supervision, inspections, insurance, local taxes, overheads and unexpected costs [150]. The operating labour could be estimated as the annual wage of a single specialised operator due to highly automatization of these type of plant [3,8]. The replacement cost includes a yearly replacement of the catalyst and a replacement of the electrochemical stacks over the total plant lifetime due to degradation that affects the equipment. It is worth noting that stacks replacement is estimated as the 60 % of the total module cost (TMC, €) of the electrochemical module because only stacks, seals and enclosures are substituted [3,8]. Demineralized water, carbon dioxide and potassium bicarbonate are considered raw materials, whereas, electricity, chilled water, cooling water and medium pressure steam are utilities. Lastly, the gaseous pollutant treatment is linked to volatile organic compounds abatement and by-products oxidation, whereas, the waste treatment is related to wastewater treatment and catalyst disposal. The economic parameters related to the operative and maintenance costs are summarised in Table 6.4.

Table 6.4. Economic data for the operative cost estimation. For the sake of clarity, the economic data refers to costs in December 2019.

Parameter	**Unit**	**Value**
Maintenance and insurance cost	€/y	3.0 % TPI
Annual wage of a specialised operator[3,8]	€/y	63443
Catalyst replacement rate	times/y	1
Catalyst price	€/kg	125.00
Electrochemical stacks replacement rate	times/plant lifetime	1
Electrochemical stacks replacement cost[3,8]	€	60 % TMC
Demineralized water price[3,8]	€/t	0.85
Carbon dioxide price[3,8,203,211]	€/t	40.00
Potassium bicarbonate price	€/kg	1.50
Electricity price[3,8,116]	€/kWh	0.05
Chilled water price[221]	€/t	0.50
Cooling water price[221]	€/t	0.03
Medium pressure steam price[221]	€/kg	0.05
Gaseous pollutant treatment[221]	€/Nm^3	0.01
Waste treatment and disposal[3,8]	€/t	14.00

Capital cost estimation

The total plant investment (TPI, €) could be estimated as the sum of the total module costs (TMC, €) of all the pieces of equipment [3,8,146,219,220].

The levelized cost of product (LCOP, €/kg) depends on the capital cost estimation and the operative cost estimation. The annuity (An, €/y) that zeroes the net present value (NPV, €) at the end of the time horizon (TH, y) of the plant [8] could be calculated according to equation (6.16).

$$\mathrm{An} = TPI \cdot \frac{DR \cdot (1+DR)^{TH}}{(1+DR)^{TH}-1} \tag{6.16}$$

The annuity is directly proportional to the TPI that is the sum of the TMC of all the pieces of equipment that are installed in the plant. In addition, TPI represents the fixed capital investment without including the cost of land because of its variability. The TMC_j of each equipment in a j-th year could be estimated according to equation (6.17) [3,8,146,150,153,220].

$$TMC_j = E_R \cdot \frac{I_j}{I_i} \cdot PMC_i \cdot F_{BM} \cdot (1+\alpha_{CF}) \tag{6.17}$$

E_R (0.849 €/\$) represents the average exchange rate between Euro and US Dollar, I_j and I_i are the cost indexes in the j-th and i-th year, respectively. The chemical engineering plant cost index (CEPCI) was 114 in 1968, 394 in 2001, 444 in 2004 and 592 in December 2019 [154]. PMC_i (\$) represents the purchased module cost of the equipment in the i-th year, F_{BM} is the bare module factor that accounts for design, material and pressure, and α_{CF} is the contingency and fee factor, which was assumed equal to 0.4 [3,8]. The purchased module cost could be evaluated according to equation (6.18), where C_i (€/unit^n) is the specific price of the equipment, S is a characteristic size of the equipment and n is the scaling exponent [3,146,150,153,220].

$$PMC_i = C_i \cdot S^n \tag{6.18}$$

The purchase module cost (PMC_i) includes material and labour for construction, piping and instrumentation, taxes and indirect costs. In Table 6.5, all the economic data for the capital cost estimation are reported. It is worth mentioning that alkaline electrolyser was considered for producing hydrogen in the thermocatalytic process; whereas, the electrocatalytic process involves an electrocatalytic module, which has not a reference cost in the market. Hence, its cost was equated to a PEM electrolyser, which includes the cost of the membrane and of noble metals used in the anode [3,9].

Table 6.5. Economic data for the capital cost estimation.

Equipment	S (unit)	n	C_{1968} (\$/unit^n)	Bare module factor (F_{BM})		
				F_D	F_P	F_M
Heat exchangers	area (m^2)	0.65	21.62	$F_{BM} = 2.29 + (F_D + F_P) \cdot F_M$		
				1.0 (floating head)	0.1 (up to 20 bar)	1.0 (carbon steel) 2.7 (stainless steel)
Compressors	power (kW)	0.82	406.83	$F_{BM} = 2.11 + F_D \cdot F_M$		
				1.0 (centrifugal)	-	1.0 (stainless steel)
Reactors, vessels and columns (vertical arrangement)	diameter (m)	1.066	10.84	$F_{BM} = 2.18 + F_P \cdot F_M$		
	height (m)	0.82		-	1.0 (atmospheric) 1.35 (up to 20 bar)	1.0 (carbon steel) 3.1 (stainless steel)
Column trays	diameter (m)	1.55	0.227	$F_{BM} = F_D + F_P + F_M$		
	height (m)	1.0		1.0 (24 in tray spacing)	1.8 (bubble cap)	0.0 (carbon steel)
Pumps	volumetric flow rate (m^3/s)	0.598	4.32	$F_{BM} = 2.38 + F_P \cdot F_M$		
				-	1.0 (up to 120 °C, 10 bar)	1.0 (carbon steel)
Equipment	S (unit)	n	C_{2019} (€/unit^n)	Bare module factor (F_{BM})		
Alkaline electrolysers	power (kW)	0.91	1300	$F_{BM} = 1.0$		
Electrocatalytic modules	power (kW)	0.91	2100	$F_{BM} = 1.0$		

6.2.4. Life Cycle Assessment procedure

A comparative LCA of the previous mentioned TC and EC processes was conducted. LCA is an objective method to evaluate the environmental impacts of a product or a process and a suitable tool to assess the environmental impacts of chemical reactions[222]. LCA methodology is standardized[223,224] and this research work was carried out following the ISO standards.

The phases of an LCA are four: i. Goal and scope definition. ii. Life Cycle Inventory (LCI). iii. Impact assessment and iv. Interpretation.

Goal and scope

The comparative LCA aims to determine the environmental impacts of methanol production by means of thermocatalytic and electrocatalytic processes by using the same CO_2 conversion catalyst, which allows a more direct comparison of the influence of the different processes conditions and required downstream processing of the stream generated by these two technologies.

This LCA is based on experimental data (primary) from laboratory experiments. Insight from lab scale are interesting for research in early stage. However, there is a disparity between the productivities of these two processes, being the TC route more productive than EC. Thus, this study also explores the environmental impacts of the scaled-up versions of both technologies, considering that the EC technology theoretically reaches the TC productivity, being the latter more mature for industrialization. Hence, the here reported LCA compares first the MeOH production in lab scale. Subsequently, a comparative LCA of the cases of study: TC-1, EC-5 and EC-6 reported in the Section 6.2.2 was performed to explain the differences on environmental impacts of these scaled-up cases (at industrially relevant productions rates), including also the downstream and purification processing steps.

System boundaries of this LCA study encompass those elements necessary to carry out the CO_2 reduction into MeOH: cell materials, catalyst, gas flows (inlet and outlet) and the energy of the reaction. The results will be showed per 1g MeOH production. The approach followed in this research work covers all stages from cradle-to-gate. This is where the system boundary is drawn since it is assumed that the final product (MeOH) could be distributed to be consumed and its end-of-life is outside of the considered system, which is more focused in the production process.

Life Cycle Inventory (LCI)

Life Cycle Inventory is the phase in which all the inputs and outputs are gathered. Table 6.6 shows the LCI all case studies. In all cases, CO_2 consumption represents the net amount between CO_2 input and CO_2 output, as suggested by Pérez-Fortes 2016 et al. [77]. Hence, in terms of LCA, the CO_2 consumption is considered as a negative emission since by using it is being avoided in the atmosphere. Ecoinvent and Agrifootprint are the databases used in this study. Table 6.6 shows those datasets selected for each process.

LCI values for TC lab scale are primary data. They came from 20 h laboratory experiment in which 10.65 g CH_3OH were produced with 34.72 g CO_2 consumption. That is why in Table 6.6 shows 53.25 mg CH_3OH /h and 1736 mg CO_2/h. 0.8737 g CuO, 0.4922 g ZnO and 0.1341 g Al_2O_3 compose the catalyst. In lab scale catalyst is prepared once for each experiment. Hence catalyst lifetime in this TC lab scale experiment was 20h. Table 6.6 shows the correspondence amount per hour of experiment: 43.5 g/h, 24.5mg/h and 6.71 mg/h of CuO, ZnO and Al_2O_3, respectively. This is an assumption valid only from an LCA point of view. The electrical consumption for heating the reactor is due to the activation (560 Wh) and the methanol production test (3190 Wh) processes. Each process consists of heating the entire reactor (190 Wh) and isothermal operation (required power 150 W). Table 6.6 represents the energy consumption per hour. H_2 and N_2 are involved as gas flow fed. Energy was provided by a power supply. There are also CO, H_2 and N_2 emissions associated to this TC lab scale process presented in Table 6.6.

Table 6.6. Life Cycle Inventory. Lab scale and Scaled up case studies

		LAB SCALE			SCALE UP			
OUTPUT		EC	TC	Units	TC-1	EC-5	EC-6	Units
CH_3OH		46.58	53.25	mg/h	3009	835.1	3012	g/h
INPUTS	Dataset							
Catalyst: CuO ZnO Al_2O_3	Ecoinvent, {GLO}: Copper oxide Zinc oxide Aluminium oxide	 1.70 0.97 0.33	 43.5 24.5 6.71	 mg/h mg/h mg/h	 0.28 0.16 0.04	 $8.40\cdot10^{-4}$ $4.73\cdot10^{-4}$ $1.29\cdot10^{-4}$	 $8.87\cdot10^{-4}$ $5.00\cdot10^{-4}$ $1.36\cdot10^{-4}$	 g/h g/h g/h
Nafion 5 wt%	Modelled	26.28		mg/h		$8.61\cdot10^{-4}$	$9.10\cdot10^{-4}$	g/h
Carbon paper	Ecoinvent {GLO}: Polyethylene terephthalate	25.08		mg/h		$8.22\cdot10^{-4}$	$8.68\cdot10^{-4}$	g/h
Nafion membrane	Modelled	0.11		g/h		$3.60\cdot10^{-3}$	$3.81\cdot10^{-3}$	g/h
$KHCO_3$	Modelled	0.4		g/h		403.7	$3.49\cdot10^{2}$	g/h
H_2O deionized	Ecoinvent Water, deionised	40		mg/h	$2.72\cdot10^{4}$	$6.63\cdot10^{4}$	$6.27\cdot10^{4}$	g/h
H_2O ultrapure	Ecoinvent Water, ultrapure				8260			g/h
Ir	Modelled	2.5		mg/h		8.19·10-5	8.66·10-5	
Pt	Ecoinvent Platinum {RER}|	2.5		mg/h		8.19·10-5	8.66·10-5	
H_2	Agrifootprint: Hydrogen gas, from membrane technology, at plant/RER Mass		2.45	g/h				
N_2	Agrifootprint: Nitrogen, via cryogenic air separation, production mix, at plant, gaseous EU-27 S		16.30	g/h				
Electrolyser	Modelled				0.64			p
CH_4	Ecoinvent {GLO}| Methane, 96% from biogas				26.09	26.09	26.09	g/h
Electricity	Electricity, low voltage {Europe without Switzerland}	0.052	187.5	Wh	$3.20\cdot10^{4}$	$3.33\cdot10^{4}$	$3.52\cdot10^{4}$	Wh
Chilled water (4 ºC - 7 ºC) – refrigeration cycle	Ecoinvent {GLO}| Heat, air-water heat pump 10kW				3068	214.1	194.3	Wh
Cooling water (25 ºC -30 ºC) – cooling tower	Ecoinvent {GLO}| Cooling energy				$1.71\cdot10^{4}$	$1.26\cdot10^{4}$	$1.39\cdot10^{4}$	Wh
Medium pressure steam (150-200 ºC, 15-17 bar)	Ecoinvent {RER}| Heat, in chemical industry				6239	$1.32\cdot10^{4}$	$1.46\cdot10^{4}$	Wh
CO_2 consumption	Considered as negative emission	183	1736	mg/h	4307	3527	4511	g/h
Emissions to air								
CO	Elementary flow		0.51	g/h	106.1	1467	224.8	g/h
H_2	Elementary flow		2.33	g/h	70.68	333.5	51.12	g/h
N_2	Elementary flow		16.16	g/h				
CH_3OH	Elementary flow				3.75	7.369	3.46	g/h

CH_4	Elementary flow				26.09	26.09	26.08	g/h
H_2O	Elementary flow				0.39	11.52	1.74	g/h
O_2	Elementary flow					4794	$5.18\cdot10^{4}$	g/h
Formic acid	Elementary flow					0.0717	$1.50\cdot10^{3}$	g/h
Emissions to water								
Water	Elementary flow					$4.24\cdot10^{4}$	$3.67\cdot10^{4}$	g/h
Methanol	Elementary flow					1.41	4.89	g/h
Formic acid	Elementary flow					64.70	9.90	g/h
Potassium compounds, unspecified	Elementary flow					403.7	349.5	g/h

Table 6.6 also provides the LCI of the EC lab scale case study. In 1 hour of experiment, lab scale EC technology reported 46.58 mg MeOH production. As previously indicated, CuO, ZnO and Al_2O_3 compose the catalyst. Nafion solution 5wt% is used in the ink catalyst creation which is deposited on carbon paper. EC lab scale case study also considers the membrane, the electrolyte and the Ir-Pt wire (anode) as well as the energy involved in the reaction. Nafion (for Nafion 5% item) is not available in the LCA databases. Hence, it was modelled based on literature [225–227], being prepared based on tetrafluoroethylene polymerization. CO2 consumption is 183 mg per 46.58 mg produced MeOH. For the teflonized carbon paper the Ecoinvent item polyethylene terephthalate has been used as a proxy. Nafion membrane was modelled with the Life Cycle Inventory of [228] research study. Potassium carbonate was modelled following the reaction stoichiometry with carbon dioxide and potassium hydroxide from Ecoinvent database, which is reported in equation (6.19).

$$2\ KOH + CO_2 \rightarrow K_2CO_3 + H_2O \qquad (6.19)$$

Iridium was not neither found in common LCA databases. Hence, it was modelled based on the [229] research. In the same way as the previous study case, CO_2 consumption is the flow net between CO_2 in and CO_2 out. This net value is considered as an avoided emission to air. A potentiostat (Biologic VSP-300) was used to supply the necessary potential to the EC cell (Voltage range: -10 V to +10 V and +/-500 mA as maximum current). This device works 1h during the reaction at a constant potential of – 1.5 V vs RHE (6 V total potential of entire cell).

Battista et al. (2017) [230] indicated the importance of include the lifetime when the inputs have different replacement times. Lifetime is a determining factor in the environmental impact's reduction and in this research work, it was considered as follows. 46.58 mg of MeOH is produced by the Table 6.6 indicates amounts of $KHCO_3$, H_2O, energy and CO_2 consumption per hour. Catalyst lasts 8 h and then it should be replaced. Membrane should be replaced each week. Nevertheless, the Ir-Pt wire could be used for an entire year.

Regarding the three scaled-up case studies, the LCI was gathered according with Aspen Plus simulations. Dataset used are the same as in the lab scale cases. Energy consumption in the three scaled-up case study is composed of the next items: electricity, chilled water from a refrigeration cycle in a heat pump thermal machine; cooling water from a cooling tower and medium pressure steam as process heat in chemical industry. Table 6.6 shows the Ecoinvent dataset used for this purpose. In addition, in the TC-1 case study, an electrolyser is included. This item was modelled according with data from [231] in which electrolyser LCI was provided for 1kg H_2. Since in TC-1 the involved H_2 in the electrolyser is 642.4 g/h then it was used 0.64 parts (p) of the previously modelled electrolyser for 1kg.

Every LCA's conducted in this study considered that all impacts should be allocated to the methanol production. Assumptions like for selling oxygen and lower the impacts were also considered. However, oxygen price comparing with methanol price (as depicted in techno economical section) makes this assumption negligible.

Impact assessment

The third LCA phase is the Impact assessment. This phase involves the calculation of the potential environmental impacts of the system. In the present paper, Climate Change (CC), Water Resource Depletion (WRD) and Cumulative Energy Demand (CED) have been calculated[232–234]:

- CC is an environmental impact developed by the Intergovernmental Panel on Climate Change (IPCC)[235]. It contains the climate change factors of IPCC with a timeframe of 100 years and the results are expressed in kg CO_2 eq.
- WRD represents the freshwater scarcity [236].
- CED represents the primary energy consumption [237] of the system.

Finally, the fourth phase of an LCA is the Interpretation phase and it will be analyzed in the following section.

6.3. Results and Discussion

6.3.1. CZA characterization and tests

This study focus on the conversion of CO_2 to MeOH by using H_2 or water as source of protons (H^+) by using, as mentioned above, a CZA-based catalyst in two different reactor configurations: in a single tube, packed bed reactor and in a GDE EC half-cell, respectively.

It is important to notice that the ternary CZA catalyst presents a porous corsage of nanopyramids with a common nucleation point sample produced by co-precipitation method (see the FE-SEM micrograph in the Figure 6.7a. Information about the crystallinity of the samples was obtained by the X-ray diffraction technique in the 2θ range of 10-80, by using a Panalytical X'Pert PRO diffractometer working in Bragg-Brentano configuration and equipped with Cu Kα radiation (λ =1.54056 Å) set at 40 kV and 40 mA. The XRD spectra in the Figure 6.7b shows that the calcined catalyst is mainly composed of CuO and ZnO crystalline phases, thus most probably the Al_2O_3 remains as an amorphous phase.

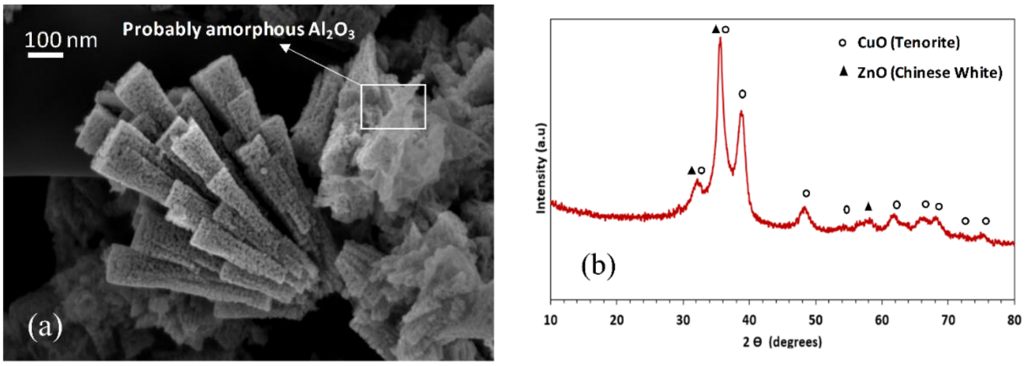

Figure 6.7. (a) FE-SEM micrograph and (b) XRD pattern of CZA synthetised catalyst.

Thermocatalytic tests

For the case of TC process, Figure 6.8a shows an increase in the overall CO_2 conversion with increasing reaction temperature (from 200 °C-300 °C), that is explained because the reaction rates increase and the reactive system is approaching the equilibrium CO_2 conversion at 300 °C. At all reaction temperatures, only MeOH and carbon monoxide were observed as products.

Methanol production via thermocatalytic hydrogenation of CO_2 is an exothermic reaction. Moreover, other reactions are involved in the process such as the hydrogenation of CO and the reverse water gas shift reaction.[238]

From the Figure 6.8b, it can be seen that methanol production is thermodynamically favoured at low temperatures while CO production (RWGS) is favoured at high temperatures. When the temperature reaches around 250 °C (25 bars with a flow rate of 45 Nl/h) the maximum yield value is reached. Nevertheless, at that temperature, the production of MeOH is slightly lower than that of CO, as well as its selectivity (48% and 52% of selectivity to MeOH and CO, respectively) (see Figure 6.8c). It is worth noting that most important amphoteric metal oxides (*i.e.* SiO_2, Al_2O_3, TiO_2, ZnO, ZrO_2) [59,239–242] and some promoters (i.e. Ga)[243] have been used as catalysts support for enhancing the catalytic activity. In agreement with the here reported results, the optimal working conditions have been observed in the 220-270°C and 2-8 MPa temperature and pressure ranges, with CO_2 conversion values lower than 20 %.

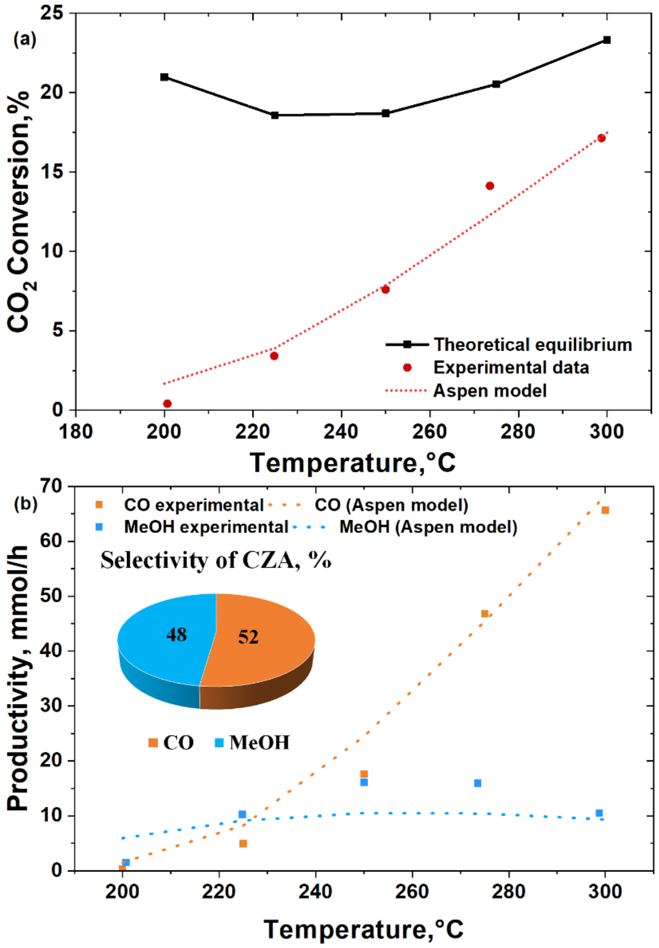

Figure 6.8. (a) CO_2 conversion, (b) productivity and (c) (inset) selectivity of CH_3OH and CO of TC process by using CZA as catalyst at WHSV= 30 Nl $g_{cat}^{-1}h^{-1}$ and 25 bar.

Electrocatalytic tests

Thermodynamically, it is possible to electrochemically reduce CO_2 to CH_3OH, but there are many issues that must be overcome. For example, the minimum energy requirement to produce MeOH from CO_2 is similar to the hydrogen evolution reaction. Besides, as mentioned before, the CO_2 molecule is very stable, and the reactions need a high amount of energy to occur. It has been widely proposed that the rate-determining step of reduction process occurs through the single electron reduction of CO_2 to the $CO_2^{\bullet-}$ radical anion intermediate from which subsequent reduction takes place[244,245]. The standard potential for the formation of this radical anion is significantly negative, *i.e.* −1.9 V vs NHE (pH=7, T=25°C)[201].

Among the materials used as electrocatalysts, copper (Cu) has been one of the only pure transition metal capable of reducing CO_2 to hydrocarbons (HC), alcohols or other chemicals in aqueous electrolytes[246]. The CO_2 transformation into fuels or chemicals at Cu, oxidized Cu and Cu-based electrodes provide the highest Faradaic efficiencies and production yields among the reported materials[73,247].

Here, we perform for the first time EC CO_2 reduction tests in a $CuO/ZnO/Al_2O_3$ based catalyst; that is the same used for the TC lab tests, but the EC tests were done under less aggressive process conditions (at room temperature and pressure conditions). The behaviour of the CZA-catalyst was first evaluated by cyclic voltammetry in a 0.1M of $KHCO_3$ aqueous solution used as catholyte (cathodic electrolyte). In order to study the performance of CZA in the working solution, a blank cyclic voltammogram (CV) was carried out at 100 mV/s, first in the electrolyte saturated with N_2 and then in the same electrolyte but saturated with CO_2 (see Figure 6.9a). A potential window between 0.5 and -1.5 V *vs* RHE was selected to study the reduction/oxidation features of the catalyst. The CVs were represented versus the RHE by using the equation (6.20), to make a reliable comparison of the results and to take into account the different pHs of the electrolyte in the different tests (*i.e.* 8.4 in the solution saturated with N_2 and 6.8 in the presence of CO_2).

$$E_{RHE} = E_{Ag/AgCl} + 0.21 + 0.059 \cdot pH \tag{6.20}$$

The CVs demonstrate two main characteristics. First, a lower on-set in the presence of CO_2 is observed as the activity (the absolute current density) increases with respect to the current potential-curve under N_2, which may be associated with the CO_2 reduction by the CZA catalyst. Second, anodic-cathodic branches (redox peaks) are present, which can be associated to oxidation (positive currents) or reduction process (negative current), respectively. The anodic peak starts at around - 0.1V vs RHE, while the cathodic one appears at -0.4V vs RHE. These peaks may be associated to CO_2 reduction reaction intermediates adsorbed on the catalyst surface and consequently to the oxidation of these adsorbed species. Nevertheless, they also may be associated to the partial formation/decomposition of the oxides on the electrode surface. To determine what of these is the prevalent phenomena, the relation by Elgrishi, N. et al. was used[248]. They stated that for an electrode-adsorbed species, the peak current (i_p) response is expected to vary linearly to scan rate (v) of the experiment, meaning that a plot of i_p *vs* v should be linear. Unlike, if there is a separation from peak to peak with the scan rate, the electrochemical process is quasi reversible, and the analyte is freely diffusing. The results in Figure 6.9b demonstrates that there are surface-adsorbed species because the current varies linearly with scan rate (coefficient of determination R^2 is 0.9943, very close to 1) and no peak to peak separation is observed. It can be concluded that, analogous to the thermocatalytic system, adding metal oxides (crystalline ZnO and amorphous Al_2O_3) to the copper catalyst contributes to enhance the CO_2 adsorption on the catalyst surface and could be useful in tuning the binding energies of *CO, *CHO (or *COH) intermediates for favouring C_1 products[249,250].

Additionally, the stability of CZA-based electrode during the EC CO_2 reduction was investigated by a continuous CO_2 electrolysis test under constant potential mode. As it can see in the Figure 6.9c, the current density profile over 1 h is very stable without any significant current changes. From online micro-GC and HPLC analysis it was determined that about 52% of the overall faradaic efficiency was due to H_2 production from the water splitting reaction (eq. 5 in the article), while the CO_2 was reduced mainly to MeOH and CO (selectivity of 68.4% and 30.5%, respectively), and in a minor amount (1.1%) to $HCOO^-$.

It is important to point out that the selectivity toward a certain product depends on the synthesis procedure, composition, morphology and chemical/physical properties of the catalyst, which influence the formation of the active phase during the reduction reaction. The catalytic activity of CZA catalyst in both reactor configurations was different, and probably the intermediates of reaction were different between the two technologies because of the settled thermodynamics conditions[42,251–253]. However, ignoring the electrons source, the reduction reaction can take place according to the same mechanism and can follow the same kinetic laws[254].

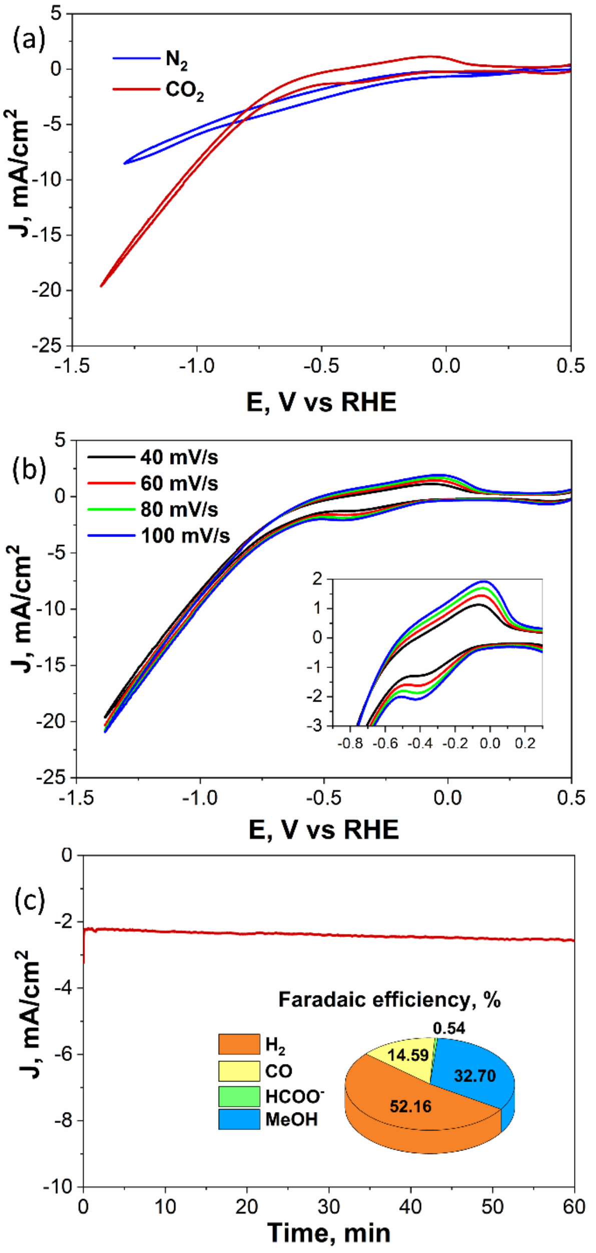

Figure 6.9. (a) Cyclic voltammetry responses for CZA-based electrodes in a CO_2 and N_2 saturated 0.1 M $KHCO_3$ aqueous solution. (b) Cyclic voltammetry responses for CZA-based electrodes in a CO_2 saturated 0.1 M $KHCO_3$ solution at different scan rates. (c) Evolution time of the current density and in the pie inset the FE for different products produced after 60 min of EC CO_2 reduction at a constant potential of -1.4 V vs. RHE.

6.3.2. Laboratory-scale methanol production

This investigation revealed that this catalyst working under high temperature and pressure conditions in a thermocatalytic process has the significant potential to produce the same product (MeOH) under milder electrochemical conditions. For a brief comparison, the best MeOH yields and productivities over the here synthesised CZA catalyst at the tested TC and EC lab-scale conditions are presented in Figure 6.10. What is striking about the result is that the electrochemical reduction of CO_2 can approach the methanol yield of a thermocatalytic process (*i.e.* ~20.5 g MeOH/kg_{cat} $gCO_{2,INLET}$). However, the best methanol productivity that was reached by means of the lab-scale EC reactor was 4-fold lower than such of the lab-scale TC reactor due to the significant difference in scale of the two test benches.

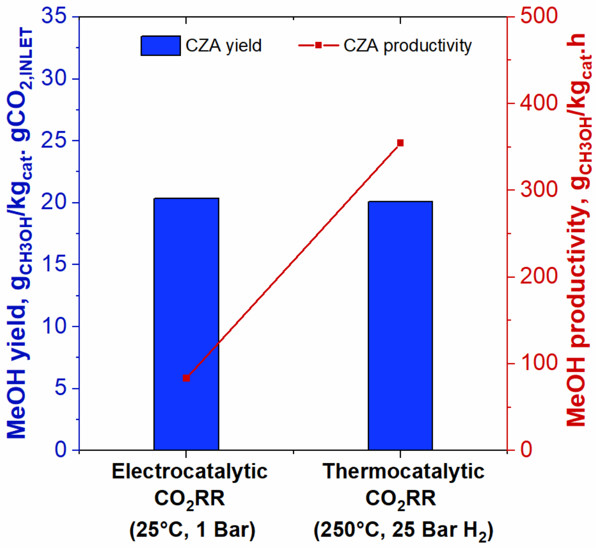

Figure 6.10. Comparison of methanol yield and productivity for TC and EC reduction CO_2 over the synthetized CZA catalyst.

Electrocatalysis would be a promising opportunity to reduce CO_2 to methanol, as long as its performance will be industrially attractive. Therefore, this work shows through simulations that, scaling up both EC and TC processes under realistic assumptions for increasing the overall CO_2 conversion and the methanol productivity, they can have an industrial appeal. Further research is needed to overcome these transition scenarios from the laboratory to the large scale, as it will be better explained in the following paragraphs.

6.3.3. Technical assessment of both TC and EC processes

All the investigated scenarios shown in Table 6.7 were modelled under realistic assumptions to simulate the transition from laboratory-scale to a large scale. Figure 6.11 sum up relevant results attained for the two technologies at the laboratory scale and in the best simulated scenarios. It can be seen from the Figure 6.11 that the difference in terms of CO_2 conversion between the two lab-scale processes is extremely significative; however, this aspect is counterbalanced by the specific electric consumption. Concerning the integrated TC case (TC-1), it achieves a CO_2 conversion of 91.4 % and the specific electric consumption of the overall process is 10.5 Wh/g_{CH3OH}. Regarding the EC process, the best industrial scenarios are EC-5 and EC-6, in which the CO_2 conversion reaches 74.9 % and 95.8 %, respectively.

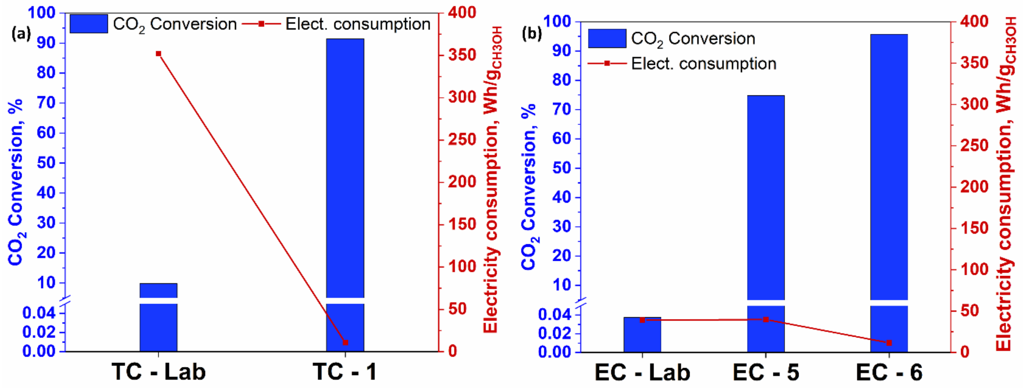

Figure 6.11. CO_2 conversion and specific electricity consumption of: (a) lab-scale (TC-Lab) and scaled-up thermocatalytic (TC-1) processes, (b) lab-scale (EC-Lab) and scaled-up electrocatalytic (EC-5 and EC-6) processes.

Nonetheless, their specific electric consumption is slightly higher than the one of the case TC-1. Figure 6.12 shows the results for all the other simulated EC cases, whose performances are far away to reach that of TC scaled-up version. These results prove how the here considered assumptions had a significant contribution to the performance of a hypothetical industrial version of the electrocatalytic process.

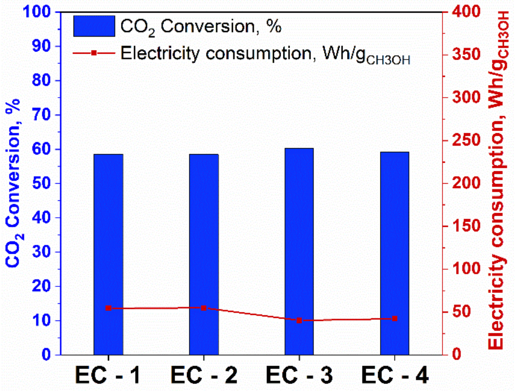

Figure 6.12. CO_2 conversion and specific electricity consumption of EC processes simulated scenario at large scale.

It is worth mentioning that considering the recycling of the unreacted CO_2 gas, among others operative conditions, the current densities that would have to be reached to get the same productivity of the TC-1 process (100 mA/cm^2) are not far from the state-of-the-art values reached up to now for the EC CO_2 reduction to methanol (see Figure 6.13) [67–75,255].

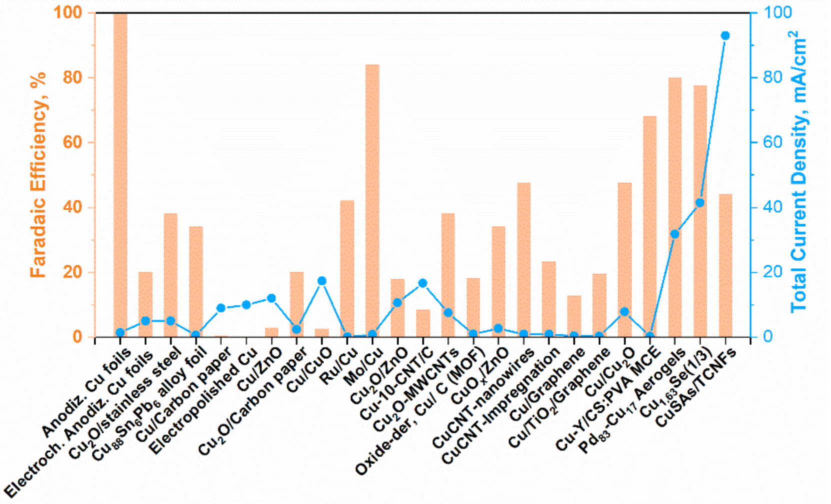

Figure 6.13. Cu-based electrocatalyst towards CH3OH production using CO2 dissolved in aqueous electrolytes. Modified from our work [255] with updated data taken from references [67–75].

On the contrary, current densities >1000 mA/cm^2 would have to be reached if the simulated scenario had not considered the recycling of the unreacted CO_2 gas. This demonstrates that by tuning the operative conditions of the process, electrocatalysis would be a promising opportunity to reduce CO_2.

As seen in the Figure 6.11, both thermocatalysis and electrocatalysis could provide promising CO_2 reducing scenarios to produce methanol. It should be noted that the TC process is a path more viable than the EC process, since the first is a well-stablished technology nowadays [64]. Nevertheless, after analysing the scientific works done so far, it is possible to realize that the actually achieved current densities in EC CO_2R reactors with methanol production (~90 mA/cm^2) [67–75,255] are only 10 % lower than the here proposed target value (i.e. 100 mA/cm^2, for EC-5 and EC-6 cases). Moreover, the transformation of CO_2 to other high-octane alcohols (C_{2+}) like ethanol has already achieved a current density of around 300 mA/cm^2.[256] Therefore, further efforts to optimize process conditions and cell designs, in order to decrease mass transfer limitation issues and pursuing high methanol production rates (high current densities) and selectivity are still envisaged. Indeed, the here reported CZA electrocatalyst is able to produce high current densities when there are no mass transfer limitations, as it can be seen in the Linear Sweep Voltammetry recorded on this electrocatalyst in a Rotating Disk Electrode (RDE) System (as shown in Figure 6.14). On the other hand, nowadays, the production of CO or/and syngas in EC CO_2R systems is valuable and have reached >100 mA/cm^2 on existing catalyst [76,201].

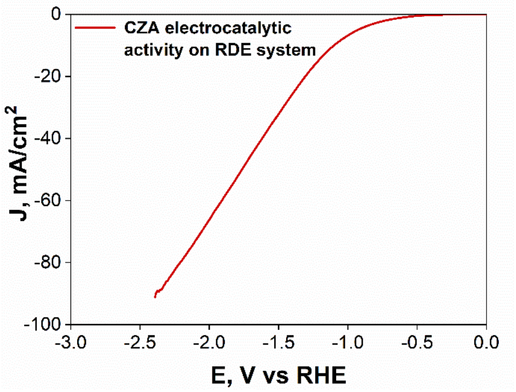

Figure 6.14. Linear Sweep Voltammetry recorded on the CZA catalyst in a Rotating Disk Electrode (RDE) System.

Therefore, a hybrid co-electrolysis of CO_2 to syngas, afterwards used for converting CO_2 to MeOH through a thermocatalytic process, could also be a promising alternative to the direct EC conversion in a one-step process[64,76–79].

In following, detailed results (see Table 6.7) and a deeper discussion on both TC and EC case studies are reported.

Table 6.7. Results on the simulated TC and EC case studies.

Parameter	Unit	TC-1	EC-1	EC-2	EC-3	EC-4	EC-5	EC-6
Number of cells	-	-	1804	$1.8\cdot10^6$	55402	54311	1651	1745
Catholyte residence time	h	-	120	120	24	10	0.5	0.5
Anolyte residence time	h	-	670	670	20	20	0.5	0.5
Pressure	bar	20	4.89	4.88	4.85	4.98	4.99	5.0
Purge fraction	%	1.00	0.11	0.11	3.61	0.64	21.1	3.89
Catalyst amount	g	3995	7.9	7939	8126	7966	242	256
CH_3OH productivity	g h^{-1}	3009	0.663	663	672	663	835	3012
Overall CO_2 conversion	%	91.43	58.54	58.44	60.30	59.14	74.86	95.76
Electric consumption	$Wh_{el}\ g^{-1}$	10.52	54.65	54.99	40.35	42.29	39.86	11.68
Chilled water consumption	$Wh_{th}\ g^{-1}$	1.02	53.55	53.31	1.66	9.28	0.26	0.07
Cooling water consumption	$Wh_{th}\ g^{-1}$	5.67	108.9	106.8	21.44	44.24	15.09	4.63
MP steam consumption	$Wh_{th}\ g^{-1}$	1.91	113.6	111.3	22.11	45.82	15.83	4.86

Regarding the thermocatalytic process (TC-1), the overall pressure in the reactor is 20 bar, the reaction temperature is 250 °C, the space velocity is 30 Nm^3 kg_{cat}^{-1} h^{-1} and the gaseous purged fraction is 1.0 % of the recycled gases. As reported in Table 6.7, the overall CO_2 conversion is greater than 91.4 %, although the CO_2 conversion per pass is 9.64 %, because a CH_3OH selectivity of around 96.1 % can be reached due to the separation of water and methanol from the gases. Moreover, the kinetic model[50] includes the CO hydrogenation to methanol and the reverse water gas shift reaction; hence, the methanol productivity is 0.878 mol_{CH3OH}/mol_{CO2} (0.639 g_{CH3OH}/g_{CO2}). As far as the specific consumptions are concerned, the electric consumption is high (10.52 Wh_{el}/g_{CH3OH}) due to the electrochemical production of renewable H_2. In detail, the electricity demand is divided as follows: 96.7 % for electrolysis, 1.7 % for CO_2 compression and water pumping and 1.6 % for heating the gases at the reactor inlet. The chilled water consumption is 1.02 Wh_{th}/g_{CH3OH} in the condenser of the stripping column, whereas, the cooling water consumption in all coolers is 5.67 Wh_{th}/g_{CH3OH}. The two reboilers require 1.91 Wh_{th}/g_{CH3OH}: 14 % for the stripper (165 °C) and 86 % for the distillation column (120 °C). In this case of study, a heat duty equal to 3.43 Wh_{th}/g_{CH3OH} was thermally integrated in the head-tail economizer.

Concerning the electrocatalytic cases of study, there are many considerations that have great importance for the scale-up of the electrocatalytic device. Firstly, EC-1 involves a separation and purification section and a gas recycle (that is of fundamental importance to enhance the CO_2 conversion and CH_3OH productivity with respect to the lab-scale, see Figure 6.11 and Figure 6.12). To keep the CO_2 partial pressure at 1 bar, the total pressure was increases up to 5 bar (arbitrary limit to have a low-pressure process and maintain the conditions close to the laboratory-scale cell, that is a CO_2 partial pressure of 1 bar). It is worth mentioning that H_2 and CO were considered as inert species within the electrocatalytic cell due to the lack of a detailed reaction pathway; therefore, these aspects should be further investigated and can be a course of improvement of the EC reactor performance. The gas recycle increases the flow rate of gaseous reactants and, for keeping constant the fluid-dynamic within a cell, the system was parallelised in 1804 cells. These features result in an increase of the overall CO_2 conversion (~58.5 %). In this case study (EC-1), the methanol productivity is 0.663 g_{CH3OH}/h, which corresponds to a specific productivity of 0.193 mol_{CH3OH}/mol_{CO2} (0.141 g_{CH3OH}/g_{CO2}). However, the specific consumptions are extremely high due to a low CH_3OH faradaic efficiency and a low concentration of the products in the liquid outlet stream (0.246 % mol methanol). The electric specific consumption is 54.65 Wh_{el}/g_{CH3OH} (71.7 % for the electrocatalytic reactions and 28.3 % for compression and pumping). The chilled water consumption is 53.55 Wh_{th}/g_{CH3OH}, the cooling water requirement is 108.9 Wh_{th}/g_{CH3OH} and MP steam consumption is 113.6 Wh_{th}/g_{CH3OH}.

In the second electrocatalytic case of study (EC-2), the variation in the CO_2 inlet flow rate drastically increases the total number of electrocatalytic cells due to the low performances of the cells and their small active area. All the other operative parameters were not affected by a change in the flow rate; hence, the specific energy consumptions are roughly the same of the previous case of study.

A realistic value of the active area (100 cm^2) was assumed in the third case of study (EC-3) for reducing the number of electrocatalytic cells. It is worth pointing out that the current and potential distribution between the electrodes changes due to a variation of the polarization, which strictly depends on the geometry of the EC cell [217]. This aspect was not modelled due to the lack of information about the distribution of the current on the surface of the electrode; nevertheless, it will have to be coped in future researches. The variation in the cell area results in an increase of the concentration of the products in the liquid stream; therefore, the specific energy consumptions are drastically reduced: 40.35 Wh_{el}/g_{CH3OH} of electricity, 1.66 Wh_{th}/g_{CH3OH} of chilled water, 21.44 Wh_{th}/g_{CH3OH} of cooling water and 22.11 Wh_{th}/g_{CH3OH} of MP steam.

Regarding the fourth case of study (EC-4), the volumetric flow rate within a cell was increased to keep constant the Reynolds number. This variation results in a decrease of the methanol concentration in the liquid stream (due to the constant faradaic efficiency) and, consequently, an increase in the specific energy consumptions. In addition, the size of the electrocatalytic stacks do not change with respect to the previous case.

In the fifth case of study (EC-5), to approach industrially relevant conditions, the current density was increased from 2.4 mA/cm^2 to 100 mA/cm^2. This parameter is affected by several features (e.g. geometry, overpotentials, polarization, etc.); however, it has to be considered as a target value, that should be achieved to obtain performances similar to other electrochemical processes that involves the electrochemical reduction of CO_2 (e.g. CO_2 reduction to CO). The variation in the current density affects all the operative parameters and the size of the electrocatalytic module. More in detail, the number of the electrocatalytic cells decreases drastically and, at the same time, both the anolyte and catholyte residence time is reduced. Moreover, an increase in the methanol specific productivity (0.244 mol_{CH3OH}/mol_{CO2}) is followed by a reduction in specific energy consumptions.

Lastly, in the sixth electrocatalytic case of study (EC-6), the methanol faradaic efficiency was increased from 26.4 % to 89.3 %, by proportionally reducing the other faradaic efficiencies. This value of the CH_3OH faradaic efficiency was selected in order to achieve a target CH_3OH productivity equal to the thermocatalytic case of study (TC-1), that is highly relevant for an industrial application. More specifically, the overall CO_2 conversion reaches 95.76 % with a specific methanol productivity equal to 0.879 mol_{CH3OH}/mol_{CO2} (0.639 g_{CH3OH}/g_{CO2}). Hence, the specific electric consumption is 11.68 Wh_{el}/g_{CH3OH} (99.23 % for electrolysis and CO_2 reduction and 0.77 % for compression and pumping); while thermal specific consumptions are: 0.07 Wh_{th}/g_{CH3OH} of chilled water, 4.63 Wh_{th}/g_{CH3OH} of cooling water and 4.86 Wh_{th}/g_{CH3OH} of MP steam. These values are comparable with the results obtained for the thermocatalytic process; more in detail, the MP steam demand in the TC-1 case is 2.5 times lower than in the EC-6 case study due to the high methanol concentration in the liquid stream which is fed to the purification section. Hence, it comes out that the EC conversion of CO_2

dissolved in the aqueous phase is one of the process conditions to improve in order to increase the product concentration and reduce the energy demand of the overall EC process.

6.3.4. Economic assessment of both TC and EC processes

Levelised cost of product

At this stage, the feasibility (technical viability and economic profitability) requires an economic assessment of the most energetically competitive cases of study. Therefore, three of them were selected for the economic assessment: TC-1, EC-5 and EC-6. Figure 6.15a illustrates the levelised cost of product at the variation of the methanol productivity of the plant. According to a market estimation, the methanol industrial price ranges between 0.2 €/kg and 0.9 €/kg[257,258], although for laboratory use it can be one order of magnitude higher. As expected, the LCOP decreases as the productivity rises for all the three cases and it exhibits a minimum. Regarding the TC-1 case of study, the LCOP of methanol decreases from 27.13 €/kg at 1 kg/h to 1.45 €/kg at $5 \cdot 10^5$ kg/h. More specifically, in the optimal economic condition, the LCOP (1.45 €/kg) is constituted by operative costs (70.2 %) and capital costs (29.8 %). In detail, the operative costs are distributed as follows: maintenance (10.9%), labour (0.6%), utilities (76.3%), replacement (3.8%), raw materials (7.2%) and waste treatment and disposal (1.2%). As expected, the most significant contribution is related to utilities and, in more detail, they are distributed as follows: electric consumption of the electrolyser (68.7 %), heating energy (24.8 %) and cooling energy (6.6 %). Considering raw materials cost, they are related to CO_2 (86.3 %) and water (13.7 %). Whereas, the capital costs are constituted by heat exchangers (41.2 %), alkaline electrolyser (10.2 %), pumps and compressors (2.5 %), columns, vessels and reactors (46.1 %). The highest investment cost of the TC-1 case is related to the heat exchangers due to the low heat transfer coefficient of gases [146,259], which increases the heat exchange area. Those findings are consistent with data reported in the literature [215,258,260–262]; however, they are strictly related to techno-economic assumptions. What stands out from Figure 6.15a is that the TC-1 process does not seem to be economically more competitive than the traditional production of methanol, but could be introduced in some specific application fields like laboratory uses.

Regarding the two electrocatalytic case studies (EC-5 and EC-6), the results of the economic assessment are completely different between them. On the one hand, the LCOP in the EC-5 case reaches a minimum (6.86 €/kg) at $2 \cdot 10^4$ kg/h, and it is divided as follows: 18 % of capital costs and 82 % of operative costs. More in detail, the LCOP is high because of the low efficiency of the electrocatalytic cells; moreover, the operative costs reflect the considerable specific energy consumptions.

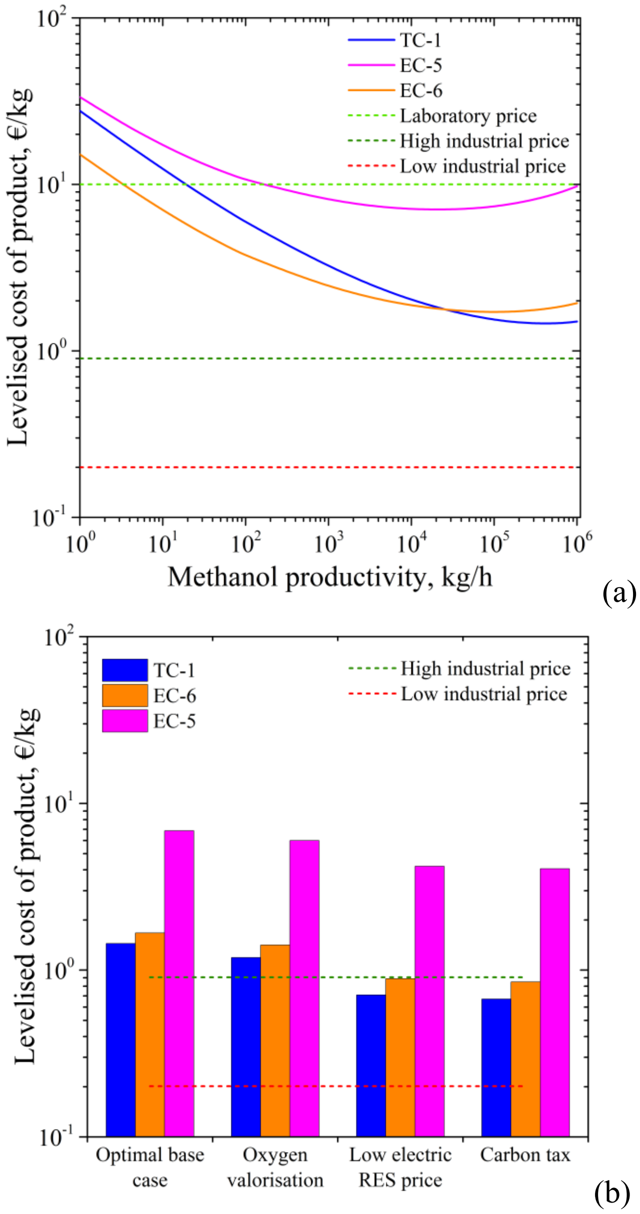

Figure 6.15. (a) Levelised cost of product (€/kg$_{MeOH}$) at the variation of the CH_3OH productivity in the three selected case studies: TC-1, EC-5 and EC-6. (b) Levelised cost of product (€/kg$_{MeOH}$) subsequently considering O_2 valorisation (0.15 €/kg$_{O2}$), a lower price of the renewable electricity (0.005 €/kWh$_{el}$) and a carbon tax (0.025 €/kg$_{CO2}$). For the sake of clarity, the economic estimation refers to the cost in December 2019 (CEPCI index equal to 592).

On the other hand, the LCOP of the EC-6 case of study ranges between 15.16 €/kg and 1.67 €/kg by varying the methanol productivity from 1 kg/h to 10^6 kg/h. In the optimal condition, operative costs (78.6 %) are greater than the capital costs (21.4 %). More specifically, capital costs are constituted by the total module costs of heat exchangers (35.8 %), electrocatalytic cells (26.0 %), columns and vessels (37.4 %) and pumps and compressors (0.8 %). The cost of heat exchangers is one of the most important items of the TPI in both cases of study (i.e. TC-1 and EC-6). In more detail, the overall heat transfer coefficient of liquids is much greater than that of gases. Hence, the size of the heat exchangers is smaller in the case of study EC-6. Consequently, if the same methanol productivity is considered, their cost in the case of study EC-6 will be 59% lower than in the case of study TC-1. Similar to the TC-1 case, operative costs are distributed as follows: labour (1.1 %), maintenance (6.9 %), utilities (79.8 %), raw materials (8.2 %), replacement (3.1 %) and waste treatment and disposal (0.9 %). These results are consistent with techno-economic analyses of other electrocatalytic processes [263]; however, the distribution of each cost depends strictly on technical and economic assumptions and on the plant size and design.

Oxygen is the main by-product of the electrochemical production of H_2 from water and it could be economically valorised. Its price ranges between 0.07 €/kg[122,264] and 0.15 €/kg[261,265] and the impact on the LCOP of the TC-1 and EC-6 cases could reach 18%, reducing it by approximately 0.25 €/kg, as reported in Figure 6.15b. Another scenario in which both TC and EC processes can become even more economically attractive is when renewable electricity prices are reduced (0.004 – 0.010 €/kWh_{el})[3,8]. Indeed, an additional reduction of about 33% could be added to the previous mentioned case (O_2 valorisation). Hence, the two optimal cases of study (TC-1 and EC-6) start to be economically competitive with the traditional methanol production. Lastly, CO_2 taxation could rise due to more severe environmental restrictions[261,265]. Therefore, if a carbon tax of 0.025 €/kg_{CO2} is considered, an additional reduction of roughly 3 % of the LCOP should be reached.

Allocation of the product on the market

The analysis of the LCOP provided the first indication of an economic viability of both processes. However, this study lack of some more precise information that could be useful for assessing a reliable economic viability. Hence, the allocation of the product on the market for NPV zeroing should add a worthwhile contribution to the economic assessment of each process.

The product of the process could be distributed on the market depending on many factors: product demand, market competition, quality, use, etc. In this work, three market categories were hypothesised: laboratory price market ($C_1 = 10$ €/kg), high industrial price market ($C_2 = 0.9$ €/kg) and low industrial price market ($C_3 = 0.2$ €/kg); besides, the fractions of methanol production allocated on each market were denoted as f_1, f_2 and f_3, respectively.

The fraction of product allocated on the low industrial price market (f_3) was sensitively analysed. Whereas, the fraction of the product allocated on the high industrial price (f_2) is calculated by using equation (6.21). Lastly, the fraction of the product allocated on the laboratory price market (f_1) is evaluated by means of equation (6.22).

$$f_2 = \frac{C_1 - LCOP}{C_1 - C_2} - \frac{C_1 - C_3}{C_1 - C_2} \cdot f_3 \tag{6.21}$$

$$f_1 = 1 - f_2 - f_3 \tag{6.22}$$

Figure 6.16 illustrates the allocation of the methanol production for NPV zeroing at the variation of the plant productivity in the three cases of study (i.e. TC-

1, EC-6 and EC-5). As a result of this assessment, if the real market scenario lay on the straight line, the NPV would be zero, the payback period (PBP) would be equal to the time horizon (i.e. 20 y) and the rate of return on investment (ROROI) would be 11.75 %. In addition, if the real market scenario lay below the straight line, the process would be economically profitable (i.e. NPV > 0, PBP < TH and ROROI > 11.75%); otherwise, it would not be cost-effective (i.e. NPV < 0, PBP > TH and ROROI < 11.75%). Moreover, cases of study TC-1, EC-6 and EC-5 start to be economically viable for methanol productivities greater than 19.1 kg/h, 3.3 kg/h and 150 kg/h, respectively.

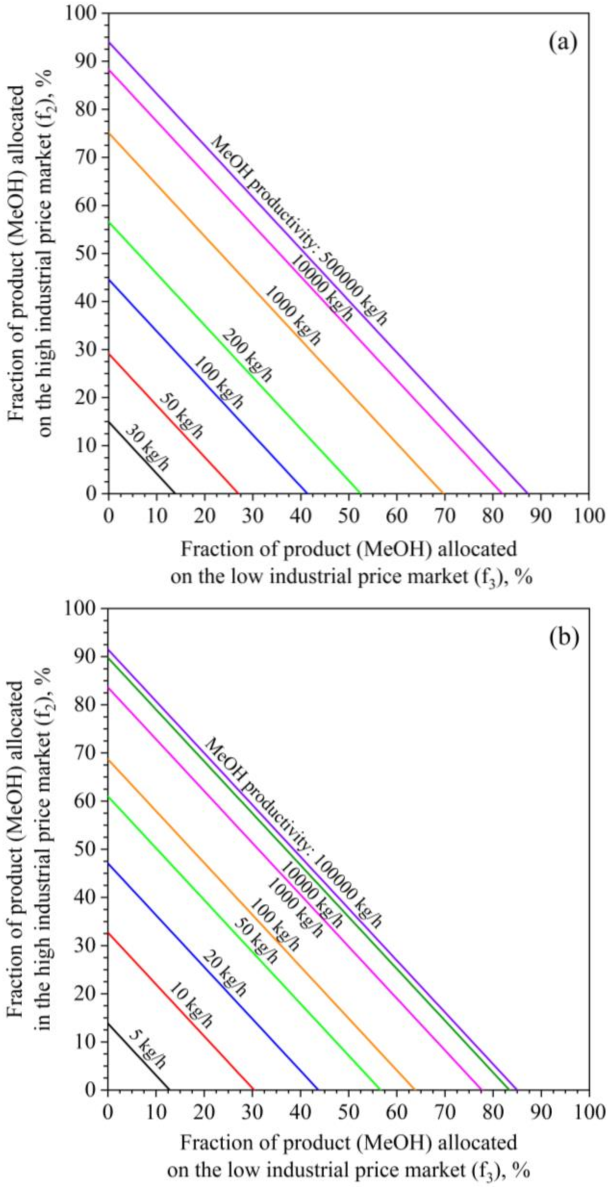

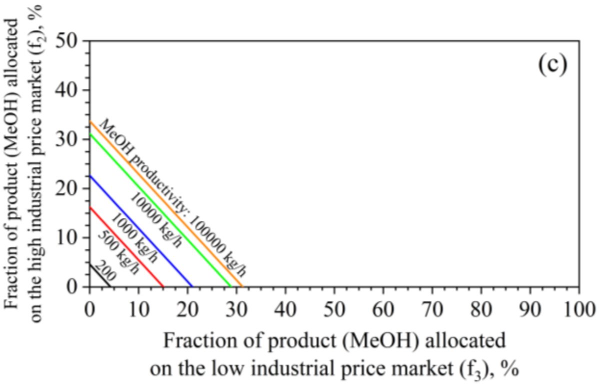

Figure 6.16. Allocation of the product on the market for zeroing the NPV at the variation of the methanol productivity in the following cases of study: (a) TC-1, (b) EC-6 and (c) EC-5. For the sake of clarity, no O_2 valorisation, low electric price or carbon tax were considered.

In conclusion, the economic assessment revealed that both small- and large-scale renewable methanol production facilities would be economically profitable if the product could be distributed successfully on the real market scenario. The EC processes requires evidently great research and development efforts to achieve the performance assumed in this work. However, even small pilot plants could be economically sustainable if the target performances are reached.

6.3.5. Life cycle assessment on the EC and TC processes

Comparative LCA on laboratory-scale EC and TC processes

A comparative LCA was conducted to investigate the environmental impacts of MeOH production by means of the two technical routes (TC and EC). LCI management was performed by using Simapro 8 software. The first set of analyses examine the impact of producing 1g MeOH by means of TC or EC technology, both using the same catalyst in the laboratory-scale (Lab).

The results for CC, WRD and CED impact categories suggest that the highest impacts are obtained when the MeOH is produced by the TC-Lab route. Regarding CC, the EC-Lab case study has the potential effect of producing $1.95 \cdot 10^{-2}$ $\mathrm{kg_{CO2\ eq}/g_{MeOH}}$ while the TC-Lab case reaches around than 10 times higher values ($1.94 \cdot 10^{-5}$ $\mathrm{kg_{CO2\ eq}/g_{MeOH}}$). Furthermore, there is a significant difference between the two assessed technologies in terms of WRD. Results revealed that WRD is 0.014 m^3 in the EC-Lab case and 0.680 m^3 in the TC-Lab one. Therefore, water saving could be 0.67 m^3 if 1g MeOH is produced by means of EC-Lab instead of the TC-Lab technology. The CED was quantified as 0.104 MJ when 1g of MeOH is produced by EC-Lab route and ~37.2 times higher (3.87 MJ/g) when is produced by the TC route.

Notwithstanding the foregoing, both lab scale cases of study were deeper analysed in order to detect the source of the effects and how they contribute to the final impact. Figure 6.17a shows the impact contributions of every material used in the EC-Lab case study. The CO_2 consumption in the gas diffusion process provokes a negative contribution in CC, which is considered as an environmental benefit.

Clearly, the catalyst components (CuO, ZnO, and Al_2O_3) and the carbon cloth, electrode substrate, have not significant contributions to the final impacts (< 1 %). It is possible to notice that the Nafion membrane gets the highest contribution (89.4%) in CC. Nevertheless, its impact was lower in WRD (36.8 %) and 41.9 % in CED. These results reflect those of Evangelisti et al (2017),[225] who also found a strong relationship between the CC impact and the membrane in a fuel cell stack. Also, the Nafion 5% solution used to prepare the electrode has some impacts, that are 4.9 % in CC, 0.5 % in WRD and in 1.1 % CED. Furthermore, the here reported results revealed that the environmental impacts of the $KHCO_3$ based electrolyte regarding CC were negligible, but $KHCO_3$ influenced by 27.2 % and 27.0 % in CED and WRD, respectively. Therefore, $KHCO_3$ is one of the main contributors to the impacts in WRD and CED and this is cannot be ignored. A recent study [266] examined the trend in capture, storage and use of CO_2 by means of a dynamic LCA for formic acid production. Despite the catholyte in that study was an aqueous solution of $KHCO_3$, it was not taken into consideration in the inventory stage. Hence, if the present research work had followed the Aldaco et al. (2019) [266] assumption about do not include the $KHCO_3$ in the inventory, the EC-Lab environmental impacts would have been lower. Nevertheless, herein, it was preferred to include all the elements that are mandatories for conducting the MeOH synthesis reaction in our experimental setup. At this respect, $KHCO_3$ is essential and cannot be excluded from the system boundaries. Considered the contribution of the Pt/Ir wire to the impacts, it is important to bear in mind the higher environmental impacts of Pt with respect to Ir. Pt can reach values up to 3.4 % of the total CED impact. The energy contribution in this EC-Lab case barely affects CC (2.6%), but in WRD it represents 15.3% and 11.4 % in CED. Similarly, the use of deionized water hardly affects the CC (4.7 %), but it gets higher values in WRD (17.2 %) and CED (13.9 %).

Figure 6.17b shows the breakdown of the environmental impacts of the TC-Lab case of study. The most striking result is that energy contributes to more than 96% in the three assessed impact categories for this case. Thus, materials and flow gases contributions are almost negligible. Due to this huge contribution of the energy, CO_2 consumption in the TC-Lab process is only able to reach 1.7 % of environmental benefits (negative value in CC).

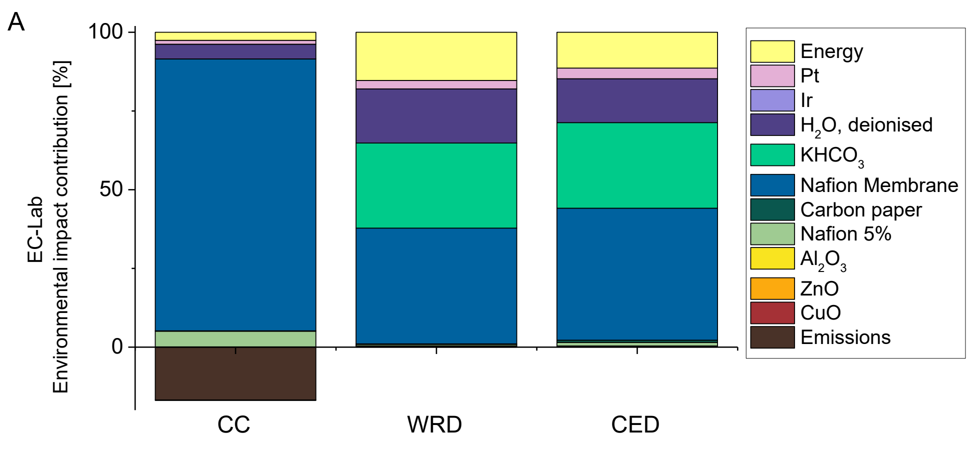

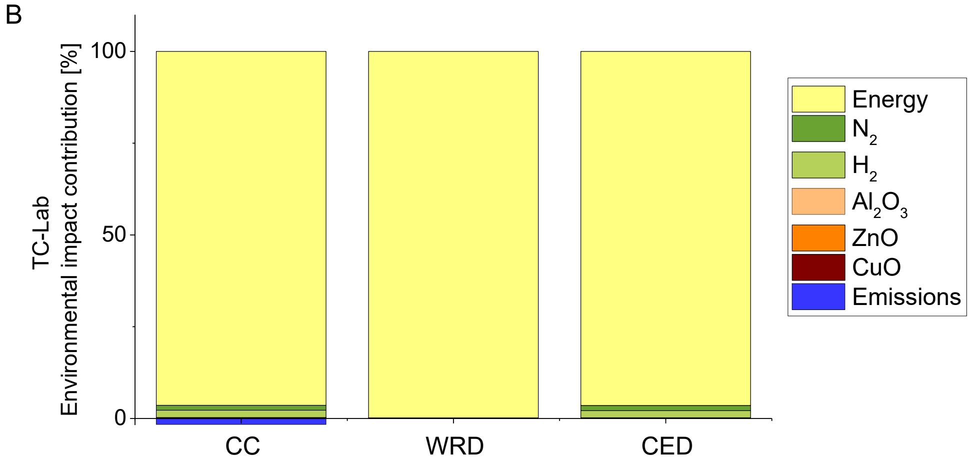

Figure 6.17. Laboratory-scale case studies Impact Contribution Results: (a) EC technology, (b) TC technology.

It is worth noting that either the energy or the H_2 did not come from a renewable source in the TC-Lab technology. There are several environmental enhances at this respect. If power supply runs with renewable energy, TC environmental impacts will be significantly decreased. In this research work, the country energy mix network powers the power supply. A sensitive assessment just changing the origin in the power supply energy item revealed a reduction in the environmental impacts. When it is assumed renewable energy origin, (i.e. open ground photovoltaic installation) reduction in the impacts was 87 % in CC, 86 % in WRD and 91 % in CED. Nevertheless, even with this assumption, impacts from the EC-Lab case are still being lower than those from TC-Lab.

Comparative LCA on scaled-up EC and TC processes

For the sake of completeness, this research work aimed to evaluate not only the environmental impacts of these two lab scale cases, but also of the scaled-up EC and TC technologies, for which the EC technology gets an industrially relevant productivity that equals that of the TC route. In this context, the EC cases of study (EC-5 and EC-6) were evaluated by varying the EC experimental conditions in the LCA inventory. In these scaled-up scenarios, CH_3OH is produced with the same catalyst as in the laboratory-scale cases, but considering the assumptions previously explained in Section 6.2.2.

Section 6.2.2 indicates that important changes should be conducted from lab-scale to the scaled-up versions of both EC and TC processes. This fact will be mirrored in their environmental impacts. The thermocatalytic process proposes recycling gas streams, pre-heat some gas streams integrating all steps in a MeOH production plant. As it will be seen, these actions will reduce the environmental burden of energy consumption that the TC technology had in the lab scale. Regarding the electrocatalytic process, it will get more productivity in its scaled-up version. Hence, the energy efficiency will be better in the scale-up than in the lab-scale. Moreover, there are recycled CO_2 gas streams, which improve the environmental behaviour with respect to a plant without this kind of recycled loops.

In the following paragraphs these changes will be explained in terms of environmental impacts.

Figure 6.18 provides the LCA results of the three environmental categories assessed in for the TC-1, EC-5 and EC-6 cases per 1 g of MeOH production. TC-1 represents the scaled-up scenario for MeOH production by means of the thermocatalytic approach, while EC-5 and EC-6 represents the electrocatalytic routes reaching a current density of 100 mA/cm^2. The main difference between EC-5 and EC-6 is an increase of selectivity. Selectivity to MeOH is 26% in EC-5, while it is around 90 % in EC-6 to reach a MeOH production of 3011.84 g/h, which is similar to the TC-1 case of 3008.76 g/h.

As shown in Figure 6.18, the MeOH production by electrocatalysis in the EC-5 scenario reported significantly more impacts than the EC-6 and TC-1 cases. The CC, WRD and CED impact categories obtained better environmental results in the TC-1 case, which is closely followed by EC-6 case of study. Hence, the lower selectivity to MeOH of the EC-5 case is a drawback also from the environmental point of view, since the energy consumption required to separate it from the water is too high, as concluded also in the economic analysis in Section 6.3.3 and better detailed in following.

Figure 6.18 depicts the contributions to the impacts of the inputs and outputs considered in the LCI, as well as, comparative LCA results between TC-1, EC-5 and EC-6. Among all the items considered in the LCI, steam, cooling energy, chilled water and electricity are the main contributors to all the assessed impact categories (i.e. CC, WD and CED). This are all items related with energy consumption. This means that energy consumption is the main responsible for the environmental impacts in the scaled-up technologies for CH_3OH production. Furthermore, in the CC results, the use of CO_2 emissions has a key role to play. Indeed, CO_2 consumption produces an environmental benefit as showed in Figure 6.18a.

Climate Change impact category represents the potential of the system to produce CO_2, which causes changes in the atmosphere and thus to contribute to climate change. In the EC-5 case study, this value is of 29.7 $kg_{CO2\ eq}$/kg CH_3OH, being the highest carbon footprint of these three scaled-up cases. Even though, EC-5 is the case study with the highest CO_2 consumption, which would be reflected as the highest environmental benefit. However, this fact is not enough to compensate the huge contributions of energy consumption that make EC-5 case as the highest in terms on CC. Instead, the carbon footprints of TC-1 and EC-6 are of 8.1 and 8.59 kg CO_2/ kg CH_3OH, respectively, being about 28% of that of the EC-5 case. For the EC-6 case the carbon footprint is only 0.480 $kg_{CO2\ eq}$/kg CH_3OH higher than for the TC-1 scenario.

However, it is important to highlight that both thermocatalysis and electrocatalysis routes (even in the here reported scaled-up versions) are far to obtain the carbon footprints of other more developed and already industrialized technologies. For instance, the carbon footprint for a generic methanol from methane process of Ecoinvent database [267] is 0.6 kg CO_2/ kg CH_3OH. Other study in China [268] by using coal to methanol (0.6 million tons/year) technology obtained 2.971 t CO_2,eq/t methanol as carbon footprint. It is evident that herein we are comparing totally different production scales but, to the best of our knowledge, there are no studies of carbon footprint for CH_3OH production via the use of $CuO/ZnO/Al_2O$ catalyst in TC or EC technologies, which makes hard to do an accurate comparison. However, these results suggest that further effort need to be conducted to lower the environmental impact from both TC and EC routes, to make them competitive and sustainable from the CC point of view. It should be noted that this research work has been conducted with transparency principles and declaring all of the items used, even if the CC results were not as encouraging as expected. As it will be shown in the next section, a reduction in CC could be get it by using as much renewable energy as possible or by using more efficient energy supplies. Also, assuming an even better performance of the EC cell can improve these results, although it could result unrealistic based on the current state-of-the-art.

With respect to the WRD question, it was found that the EC-6 case ($2.42 \cdot 10^{-2}$ m^3 H_2O/g CH_3OH) would potentially consume slightly more water than the TC-1 case ($2.29 \cdot 10^{-2}$ m^3 H_2O/g CH_3OH). However, EC-5 suggest that 1 g of CH_3OH will cause 82.4 L of water resource depletion. As shown in Figure 6.18b, the WRD category is mainly influenced by electricity contribution.

The inventory of the lab-scale cases of study suggested a higher energy consumption in the TC-Lab case than in the EC-Lab one. However, when the scale-up of these technologies is performed, energy consumption becomes optimized. In fact, a lower amount of energy is used in the TC-1 (172 kJ) case than in EC-5 (616 kJ) and EC-6 (183 kJ) per g of MeOH. This is reflected in the CED impact category, which is the indicator of the energy performance of the system, including downstream processes.

It is encouraging to compare the results for the CED with those found in literature and databases. The item in the Ecoinvent 3 database [267] describing the MeOH production from natural gas reports a CED of 33.7 kJ/g CH_3OH. This value seem to be consistent with Patel (2003) [269] which determined CED as 36.1, 40.1 and 40.8 kJ/g MeOH when it is produced from natural gas, heavy oil or brown coal, respectively. This fact means that CED in TC-1 and EC-6 routes of MeOH production are in the same order of magnitude as the conventional productions.

The comparative scaled-up LCA of the TC vs. EC technologies showed that the TC process is more environmentally friendly than the simulated EC cases under the here proposed operative conditions and electrodes scales. These means that the promising results from the experiments in the lab-scale totally changed their environmental behaviour when the scale-up was conducted. For this reason, it is important to point out that to perform more reliable LCA it is preferable to use experimental data to perform a realistic simulated scale-up, considering all the downstream separation and purification processes, which then can be then used for the environmental impacts evaluation (as it was proposed in this work).

The here reported results suggest that there is an effectively association between environmental impacts and the MeOH production scale, that is the reason of the similar environmental impacts obtained for the EC-6 and TC-1 cases, in comparison to the better impacts obtained for the EC-Lab case vs. he TC-Lab one.

The rise in energy required in EC-6 technology at the studied scale of CH_3OH production (vs. the lab scale case) provokes significant increase in the environmental impacts, mainly because the here studied EC CO_2 reduction process generates MeOH dissolved in the aqueous electrolyte, with a consequent high energy requirement due to the distillation purification process.

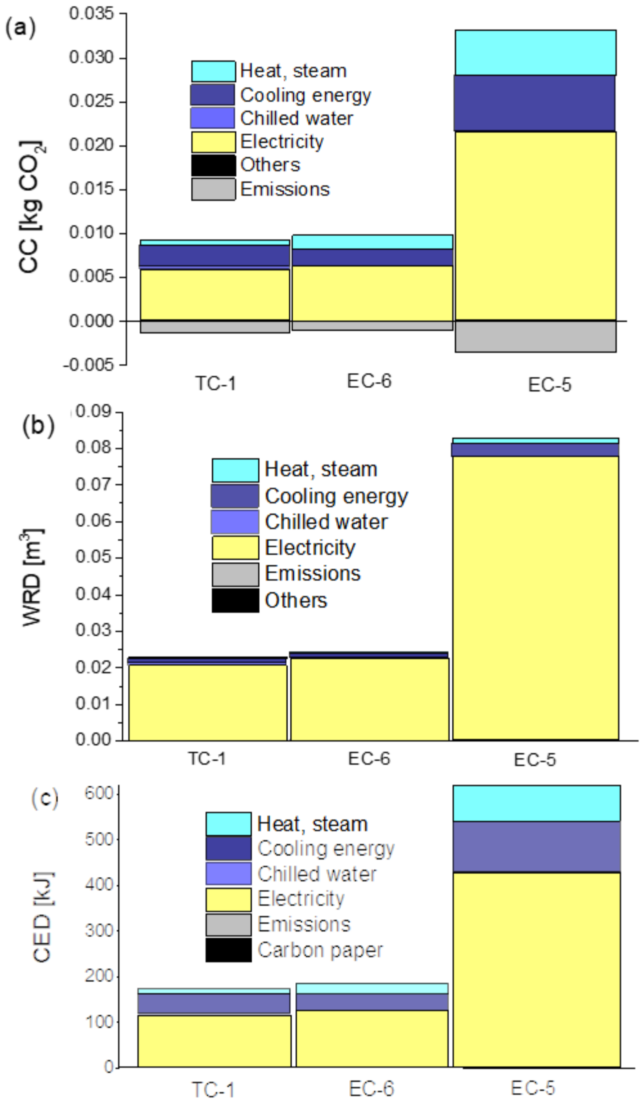

Figure 6.18. Scaled-up case studies (TC-1, EC-5, EC-6) environmental impacts and their contributions obtained per 1 g of MeOH production. (a) Climate Change impact category comparative results, (b) Water Resource Depletion impact category comparative results, (c) Cumulative Energy Demand impact category comparative results.

Future sustainability perspectives

In prospective, there are different operative and boundary conditions that can be pursued in the EC and TC technologies to render them more sustainable than the current MeOH production processes and close to be C-neutral.

To reduce the energy demand of the of the EC process, and the related MeOH purification from water by distillation, new developments should be implemented such as:

a) the gas-phase EC CO_2 conversion to MeOH that is currently at a proof-of-concept stage[270], which could allow the exploitation of less energy intensive purification technologies, like membrane processes;

b) the CO_2 partial pressure (here assumed equal to 1 bar) could be increased for improving the CO_2 conversion per passage in the EC cell, so reducing the energetic costs for the CO_2 re-compression for its recirculation;

c) the electrochemically produced CO (now considered as an inert gas) can be considered as a reagent that contribute to the MeOH production when reliable kinetic data of the CO-to-methanol electroreduction will be available[250];

d) if the produced amounts of side products like H_2 and formate are important (as in the EC-5 case) they can be exploited and considered as another valuable products of the process (after appropriate purification), so applying the green chemistry concept of atoms economy;

e) discovering of electrocatalysts with high performances (current density and methanol faradaic efficiency), lessening the formation of by-products;

f) optimization of the EC cell geometry by means of experimental data and modelling;

g) engineering of the GDE in order to favour the charge and mass transport within the cell, reducing ohmic losses and pursuing high current densities (> 100 mA/cm^2) and industrially relevant production rates.

Changing some parameters in the LCA model, it is possible to obtain encouraging results for the future of the EC technology. For instance, in both the EC-5 and EC-6 cases, 100 $mA\cdot cm^{-2}$ has been used as current density. The CH_3OH productivity could be double if this value could be increased to 200 $mA\cdot cm^{-2}$, in line with other CO_2 EC reduction results for ethanol production that already reached up to 300 mA/cm^2 [271]. Thus, doubling the current density at the same applied potential can halve the electricity used in the EC process (that is the main drawback for the environmental impacts). Consequently, the environmental impacts can be reduced of about 68% for the CC, 73% for the WRD and 67% for the CED in both EC-5 and EC-6 cases, meaning that it is independent of the MeOH FE (26% or 90%, respectively). Hence, considering for the EC-6 case, with a FE to MeOH of 90% and 200 mA/cm^2 of total current density, the new calculated impacts are 2.72 kg CO_2/kg CH_3OH, 6.45 m^3 H_2O/kg CH_3OH and 60.45 MJ/kg CH_3OH, which are about 4-times lower than in the previous conditions. In this way, the carbon footprint became comparable to that of current industrial technologies for MeOH production at much higher scales and are in-line with previous LCA analyses of other CCU process using CO_2 and H_2 for methanol production[272].

On the other hand, electricity has a major contribution in the environmental impacts of both EC and TC scaled-up technologies (see Figure 6.18); hence, its source can have a huge influence on the carbon footprint of these processes. The here considered European energy mix is composed of around 30% of renewable energy. Thus, if this electricity came 100% from renewable energy like photovoltaics (for example, by taken the Ecoinvent item: photovoltaic electricity of 570 kWp open ground in Italy), the environmental impacts will get lower values. Evaluating this possibility for the EC-6 and TC-1 processes, a reduction higher than 62% in the carbon footprint is observed in both cases. The CC passes from the initial values (8.11 $kg_{CO2\ eq}/kg_{CH3OH}$ in TC-1 and 8.59 $kg_{CO2\ eq}/kg_{CH3OH}$ in EC-6) to 3.09 $kg_{CO2\ eq}/\ kg_{CH3OH}$ in TC-1 and 3.11 $kg_{CO2\ eq}/$ kg CH_3OH in the EC-6 in this all renewable-electricity scenario. The WRD and CED are also reduced when electricity came from renewable energy instead of the generic electric mix. In the 100% renewable energy scenario, the WRD is 5.12 10^{-3} m^3_{H2O}/g_{CH3OH} in the EC-6 and 4.71 10^{-3} m^3_{H2O}/g_{CH3OH} in the TC-1, which are reductions close to 80%. Instead, the CED practically does not change because it is independent of the energy source, it is 68.37 kJ/g_{CH3OH} with the TC-1 case and changes to 69.2 kJ/g_{CH3OH} with this 100% renewable assumption.

Furthermore, a big part of the environmental impacts is also due to the cooling energy. For instance, its contribution to CC is 1.91 $kg_{CO2\ eq}/kg_{CH3OH}$ in EC-6, 2.38 $kg_{CO2\ eq}/kg_{CH3OH}$ in TC-1 and 6.34 $kg_{CO2\ eq}/kg_{CH3OH}$ in EC-5. Hence, the more we reduce the required cooling energy (used in the compressors and distillation/separation units), the lower will be the carbon footprint. This behaviour will be similar for WRD and CED environmental impacts.

6.4. Conclusion

The aim of this work was to compare the CO_2 to MeOH conversion by means of electrocatalytic and thermocatalytic technologies, starting from primary experimental data obtained with the same catalyst at laboratory-scale, and then simulating an industrial version of the both processes, including separation and purification of the final product.

It may be accepted that the electrocatalysis (heterogeneous catalysis of EC reactions) and thermocatalysis (catalytic hydrogenation) differ from each other only in the means used for the success of the conversion (molecular hydrogen, operating conditions and/or reactor capacity) and the intermediates during the reaction. But herein, we demonstrate that a Cu/Zn/Al-based catalyst working under state-of-the-art conditions in a thermocatalytic process has the potential to also produce the same product (MeOH) under milder electrochemical conditions. Hence, this work could be an attempt to provide a bridge between the fields of thermocatalysis and electrocatalysis. Further research should certainly be done to better understand the reaction mechanisms on the electrocatalyst, the current/potential distribution within the cell and the behaviour of a three-dimensional electrodes to improve EC cell performances for a future implementation of the electrocatalytic CO_2 reduction technology at a high scale.

Our primary laboratory results reveal that the EC productivity is far to reach that of TC technology, being this latter a more mature process at lab-scale and a well-stablished technology at industrial level today. Despite this, the environmental impact of EC lab-scale case (CC of 19 $kg_{CO2\ eq}$/ kg_{CH3OH}) was lower than the TC lab-scale one. Nevertheless, this tendency changes when a scale up of these technologies is performed, because it is necessary to consider not only the performance of the catalytic reactor but also of all the units of the plant, including separation and purification processes. Hence, the environmental impacts of the TC and EC processes are comparable when scaled-up to the same productivity of ~3 kg/h of methanol. The best environmental scenario was the TC-1 case, which reaches a carbon footprint of 8.11 $kg_{CO2\ eq}/kg_{CH3OH}$, and the EC-6 case reached a similar value. It is important to highlight that both these processes were highly influenced by their energy consumption. From the comparison of the lab-scale systems performances, the EC-lab technology has a 9-fold lower energy consumption than the TC-lab (352 Wh/g), but when the best scaled-up scenarios (TC-1 vs EC-6) were compared, they resulted to have similar energy consumptions due to the downstream processing units.

This study suggests that EC and TC technologies can be more sustainable if further efforts are made to reduce their energy demand, for reaching similar or lower environmental impacts than the current benchmark fossil-fuel based technologies for methanol production. For instance, doubling the current density of the EC cell to 200 mA/cm^2 results in a reduction of 68% of the carbon footprint of this process (reaching up to 2.72 $kg_{CO2\ eq}/kg_{CH3OH}$); reducing the cooling energy it is possible to get considerable savings in CC, WRD and CED. The highest contribution to the impacts in the scaled-up processes is due to the electricity. Hence, the more renewable is the electricity from the country mix, the lower environmental impacts these technologies could reach. In a scenario with a 100% renewable energy such as photovoltaic, it is possible to reach savings in the carbon footprint of up to 62%.

The techno-economic assessments here reported suggest that the EC process results to be economically advantageous over the TC one at low scales (< 10^4 kg/h MeOH). Considering an effective allocation of the methanol productivity on a real market scenario and the assumption of zeroing of the net present value in 20 years, both the TC (i.e. TC-1) and EC (i.e. EC-6) processes would start to be economically competitive at methanol productivities greater than 19.1 kg/h and 3.3 kg/h, respectively. Moreover, if O_2 valorisation, a low price of the renewable electricity and a carbon tax are considered, the economic profitability will rise. There are still high challenges for the EC CO_2-to-methanol conversion technology to reach a real industrial implementation, while the TC one is closer to this goal.

Chapter 7

CuZnZr ferrierite-based catalysts for CO_2 hydrogenation to methanol and dimethyl-ether

7.1. Introduction

The CO_2 hydrogenation to methanol and DME is the last topic addressed in this thesis. As introduced in Chapter 1, DME is a useful added-value product, it is less dangerous than methanol and it has a high power density if it is liquefied. The CO_2 hydrogenation to methanol and DME occurs on a heterogeneous catalyst that consists generally of a ternary oxide catalyst for the methanol synthesis and an acidic catalyst for the dehydration of the methanol into DME.

Therefore, the experimental activity aims to contribute to this growing area of research by exploring the catalytic performances of CuZnZr ferrierite-based catalysts for CO_2 hydrogenation to MeOH and DME, stressing the results on the activity, selectivity and stability at different on-stream reaction conditions. Synthetized CuZnZr ferrierite-based hybrid catalysts were characterized and tested in order to highlight differences between both the preparation and the composition of the catalysts. Moreover, both calcined and aged catalysts were characterized by means of several characterization techniques in order to relate their catalytic performances to their textural and chemical properties and to evaluate modifications during the operating conditions.

7.2. Methodology

7.2.1. Preparation of the catalytic systems

Preparation of the CuZnZr ternary oxide

A ternary CuZnZr (CuZnZr) catalyst for CO_2 hydrogenation to methanol was prepared by gel-oxalate co-precipitation with a Cu/Zn/Zr atomic ratio 6:3:1. In brief, the nitrates precursors of the metals were solubilized in ethanol and co-precipitated by oxalic acid under vigorous stirring at room temperature [177,178]. The precipitate was stirred for 3 h, aged overnight, filtered and dried at 110 °C for 16 h. Lastly, the solid was calcined at 350 °C for 4 h, following a stepwise procedure [177]. This catalyst was prepared by Giuseppe Bonura and Francesco Frusteri at CNR-ITAE (Messina, Italy).

A commercial CuZnAl (CZA) catalyst (copper-based methanol synthesis catalyst, Alfa Aesar®) was used as the reference material for CO_2 hydrogenation to methanol. Its nominal composition is: 63.5 %wt CuO, 25 %wt ZnO, 10 %wt Al_2O_3 and 1.5 %wt MgO.

The performances of CuZnZr and CuZnAl catalysts will be discussed in section 7.3.2. The CuZnZr catalyst resulted to be the most suitable material for CO_2 hydrogenation to methanol; hence, CuZnZr-based hybrid catalysts were synthetized for direct CO_2 hydrogenation to DME.

Preparation of the CuZnZr-based hybrid catalysts

The procedure adopted for the preparation of the CuZnZr-based hybrid systems consist of a combination of copper, zinc and zirconia, which are commonly used for methanol synthesis, and commercial ferrierite-type zeolite as described in our previous works [90,100,275]. Four different CuZnZr-based catalysts for DME synthesis were prepared by Giuseppe Bonura and Francesco Frusteri at CNR-ITAE (Messina, Italy). Two catalysts were synthesized via gel-oxalate coprecipitation following the procedure elsewhere reported [90,100]: copper, zinc and zirconia nitrates were solubilized in ethanol (Cu/Zn/Zr atomic ratio 6:3:1) and then coprecipitated by oxalic acid at ambient conditions under vigorous stirring in a solution containing finely dispersed ferrierite powder [90,100]. After filtration, drying (95 °C for 16 h) and calcination (350 °C for 4 h), the two samples were designated: CZZ/FER OX 1:2 and CZZ/FER OX 2:1; and they are respectively characterized by a CZZ/FER weight ratio of 0.5 and 2. The third catalyst was prepared by wet impregnation technique: the ferrierite powder was impregnated by the metal precursors solubilized in ethanol (Cu/Zn/Zr atomic ratio 6:3:1), dried and then calcined [90]. This sample was named CZZ/FER WI 1:2 (CZZ/FER weight ratio of 0.5). Lastly, the fourth sample denoted as CZZ-FER MIX 1:2 was obtained as a physical mixture of coprecipitated CuZnZr (gel-oxalate coprecipitation, Cu/Zn/Zr atomic ratio 6:3:1) and ferrierite powder with a CuZnZr/FER weight ratio of 0.5. Each catalyst powder was pelletized at 15 MPa, ground in an agate mortar and sieved for obtaining small particles (particle size range: 250–500 μm).

7.2.2. Catalyst characterization techniques

Catalysts were characterised by using different techniques: N_2 physisorption, X-ray diffraction (XRD), field emission scanning electron microscopy (FE-SEM), transmission electron microscopy (TEM), temperature programmed reduction (H_2-TPR), ammonia pulse chemisorption, X-ray photoelectron spectroscopy (XPS) and ICP-MS. More in detail, calcined, fresh reduced and aged catalysts were characterised to relate their catalytic performances to their characteristics.

Total surface area and porosimetry measurements

Textural properties of both calcined and aged catalysts were determined by N_2 physisorption at -196 °C using a Micromeritics Tristar II ASAP 3020 analyser. The samples (~80 mg) were previously outgassed at 200 °C in inert (N_2) gas for 2 h using a Micromeritics Flow-Prep 060, in order to remove water and other atmospheric contaminants from the surface. The total surface area of ternary oxides catalysts was calculated according to the Brunauer-Emmett-Teller theory [179]. Whereas, the total surface area of hybrid catalysts was calculated by means of equation (7.1), using the relative pressure points of the adsorption isotherm between 0.05 and 0.35 according to the Langmuir theory (7.2) [276], because the Brunauer-Emmett-Teller (BET) method [179] could not be applied due to the negative value of the BET constant for the ferrierite-based catalysts.

$$S_{LANG} = \frac{10^{-6} \cdot q_m \cdot N_A \cdot \sigma_{N_2}}{\tilde{v}} \tag{7.1}$$

$$\frac{p}{q} = \frac{1}{\tau \cdot q_m} + \frac{1}{q_m} \cdot p \tag{7.2}$$

In equations (7.1) and (7.2), S_{LANG} (m^2/g_{cat}) represents the specific surface area, N_A ($6.022 \cdot 10^{23}$ mol^{-1}) is the Avogadro's number, σ_{N_2} ($1.62 \cdot 10^{-19}$ m^2) is the N_2 molecular cross-sectional area, $\tilde{v}$ ($2.2414 \cdot 10^{-2}$ Nm^3/mol) is the molar volume of an ideal gas at normal conditions (i.e. 273.15 K and 101325 Pa), p (mmHg) represents the absolute pressure, q (cm^3_{STP}/g_{cat}) is the amount of N_2 adsorbed, q_m (cm^3_{STP}/g_{cat}) is the amount of N_2 adsorbed in a monolayer and τ ($mmHg^{-1}$) is the average life of an adsorbed molecule of N_2.

The micropore surface area and volume were evaluated via the t-plot method by using the Harkins and Jura equation (7.3) for the estimation of the statistical thickness (t, Å) [180–182]; p/p^s represents the relative pressure.

$$t = \sqrt{\frac{13.99}{0.034 - \log_{10}\left(\frac{p}{p^s}\right)}} \tag{7.3}$$

The porosimetry analysis was performed by applying the Barrett-Joyner-Halenda (BJH) algorithm to the desorption branch of the isotherm [183,184].

X-ray diffraction (XRD) measurements

Powders of both fresh and aged catalysts were investigated in a Philips X'Pert PW3040 diffractometer operating at 40 kV and 40 mA, using a Ni β-filtered Cu-Kα radiation characterized by a wavelength (λ) equal to $1.5406 \cdot 10^{-10}$ m. X-ray diffraction (XRD) patterns were collected at room temperature over the 2θ angle range of 5°–90°, with a scan step size of 0.013° 2θ and a time per step equal to 0.3 s. The average crystallite size (d_c, nm) was estimated according to Scherrer's equation (7.4) [185], where F_s is a shape factor equal to 0.9, θ (rad) is the Bragg's angle, β (rad) and β_0 (rad) represent respectively the full-width at half maximum (FWHM) of the most intense peak of the phase and the nearest peak of the lanthanum hexaboride (LaB_6) standard.

$$d_c = \frac{F_s \cdot \lambda}{(\beta - \beta_0) \cdot \cos\theta} \tag{7.4}$$

Chemical and morphological analyses

Both calcined and aged catalysts were observed with a field emission scanning electron microscope (FE-SEM) Zeiss Merlin equipped with a Gemini-II column, for the purpose of analysing their morphology. Moreover, energy dispersive X-ray spectroscopy (EDS) was employed to determine the elemental composition of portions of the catalysts. For the sake of clarity, in this case the samples were not coated with a thin and conductive layer of metal for observing the extremely low dimensions of the nanoparticles.

Furthermore, both morphology and crystalline structure of the samples were investigated by a transmission electron microscopy (TEM) with FEI Tecnai F20 ST microscope operating at 200 kV acceleration voltage. Concerning sample preparation, each sample powder was dispersed in ethanol (purity > 99.8 %) through sonication for 2 min and subsequently drop-casted on a Cu holey-carbon TEM grid.

Furthermore, for determining the real elemental composition of the catalysts, an inductively coupled plasma mass spectrometer (iCAP Q ICP-MS, Thermo Fisher Scientific) was employed. Each calcined catalyst (~100 mg) was digested in 10 ml of acid solution (6 ml of HCl 37 % vol, 2 ml of HNO_3 65 % vol and 2 ml of HF 48 % vol) by using a Milestone ETHOS EASY SK15. Each solution was heated at 10 °C/min from room temperature to 220 °C and hold for 15 min at the maximum temperature, then it was cooled at room temperature in about 30 min. After that, each concentrated solution was diluted using deionised water to achieve the concentration of each element within the calibration range (i.e. 100 – 2000 ppb), then these samples were analysed by using ICP-MS.

Temperature programmed reduction (H_2-TPR) measurements

Temperature-programmed analyses were performed in a Thermoquest TPD/R/O 1100 analyser, equipped with a thermal conductivity detector (TCD). For performing temperature-programmed reduction (H_2-TPR) experiments, each calcined catalyst (~20 mg) was placed in a quartz tube reactor between two layers of quartz wool. Each sample was pre-treated in pure O_2 flow (40 ml/min) to ensure the complete oxidation of metals, heating the oven from room temperature to 350 °C [90] with a constant heating rate of 10 °C/min and holding it for 30 min. Subsequently the sample was cleaned in He flow (40 ml/min) at 350 °C for 30 min and then it was cooled to 50 °C. The H_2-TPR was carried out under a constant flow (20 ml/min) of 5.000 %vol H_2/Ar, heating the sample from 50 °C to 900 °C with a heating rate of 10 °C/min.

Ammonia pulse chemisorption measurements

Surface concentration of acid sites was evaluated by means of ammonia (NH_3) pulse chemisorption in the Thermoquest TPD/R/O 1100 analyser. The analyses were performed placing the catalyst powder (~90 mg) in a quartz tube reactor. Each sample was pre-treated flowing He (25 ml/min) from room temperature to 120 °C, then it was reduced using 5 %vol H_2/Ar (25 ml/min), heating the sample up to 350 °C with a heating rate of 10 °C/min and holding it for 1 h at the maximum temperature. After that the sample was cleaned in He flow (25 ml/min) for 30 min at 350 °C and then cooled down to 100 °C in inert flow. The NH_3 pulse chemisorption analysis was carried out in isothermal conditions (100 °C) using 9.99 %vol NH_3/He and He as carrier gas (25 ml/min).

X-ray photoelectron spectroscopy (XPS) measurements

The surface of the catalysts was investigated via X-ray photoelectron spectroscopy (XPS) employing a PHI 5000 Versa Probe equipment, using a band-pass energy of 187.85 eV, a take-off angle of 45° and an X-ray spot diameter of 100 μm; high resolution spectra were collected using a band-pass energy of 23.50 eV.

7.2.3. Catalytic tests

The catalytic activity of each sample (catalyst load: 1.5 g) was investigated in a fixed bed stainless steel reactor. The catalytic bed had an annular section (i.d. 3 mm, o.d. 8 mm) due to the presence of a little tube, in which was inserted a thermocouple for the measurement of the reaction temperature within the catalytic bed. The height of the catalytic bed varies because catalysts have different apparent densities (as shown in Table 7.1), which were evaluated as the ratio between the mass and the total volume of the catalysts, thus including both bed void fraction and internal porosity. In order to compare the results, all the catalytic tests were carried out keeping constant the weight hourly space velocity (WHSV, $Nl \cdot g_{cat}^{-1} \cdot h^{-1}$). For the sake of clarity, normal conditions were defined at 0 °C (273.15 K) and 101325 Pa.

Table 7.1. Apparent densities of small particles of calcined catalysts.

	Bare ferrierite	CuZnZr-based hybrid catalysts (CZZ/FER)			
Catalyst	FER	OX 1:2	OX 2:1	WI 1:2	MIX 1:2
Apparent density, $kg \cdot m^{-3}$	463 ± 20	639 ± 23	902 ± 45	795 ± 50	579 ± 24

Concerning the CuZnZr and CuZnAl catalysts, each sample was reduced in situ at the calcination temperature (350 °C) for 1 h using 10 %vol H_2/N_2 (30 Nl/h) at 0.2 MPa prior to undertaking the experimental campaign. Subsequently, each sample was tested continuatively (stability test) for 20 h at 275 °C, 2.5 MPa and 20 $Nl \cdot g_{cat}^{-1} \cdot h^{-1}$ (inlet composition: 60 %vol H_2, 20 %vol CO_2 and 20 %vol N_2). After the stabilization, activity tests were performed on each catalyst at 2.5 MPa (inlet composition: 60 %vol H_2, 20 %vol CO_2 and 20 %vol N_2) both varying the reaction temperature between 200 °C and 300 °C and ranging the WHSV between 20 $Nl \cdot g_{cat}^{-1} \cdot h^{-1}$ and 40 $Nl \cdot g_{cat}^{-1} \cdot h^{-1}$.

Regarding the CuZnZr-based hybrid catalysts, each sample was pre-treated similarly to the ternary oxides by using 30 Nl/h (10 %vol H_2/N_2) at 0.2 MPa and 350 °C for 1 h. Afterwards, the stability test was performed on each sample (20 h at 275 °C, 2.5 MPa and 13.3 $Nl \cdot g_{cat}^{-1} \cdot h^{-1}$ (inlet composition: 60 %vol H_2, 20 %vol CO_2 and 20 %vol N_2)). Eventually, activity tests were carried out on the hybrid catalysts at 2.5 MPa (inlet composition: 60 %vol H_2, 20 %vol CO_2 and 20 %vol N_2) both varying the reaction temperature between 200 °C and 300 °C and ranging the WHSV between 6.67 $Nl \cdot g_{cat}^{-1} \cdot h^{-1}$ and 20 $Nl \cdot g_{cat}^{-1} \cdot h^{-1}$.

The gases at the outlet of the reactor were split in two streams. On the one side, a portion of the gases was directly analysed using a gas chromatograph (7890B GC System, Agilent Technologies) equipped with a heated transfer line (120 °C, atmospheric pressure), a two-columns separation system (HP-PLOT/Q and HP-PLOT Molesieve) connected to a thermal conductivity detector (TCD) and a flame ionization detector (FID). On the other side, water and methanol were condensed in a tank (room temperature and 2.5 MPa), then the gaseous stream was completely dehydrated using a silica gel trap (room temperature and atmospheric pressure), and was eventually analysed with an in-line X-STREAM EMERSON gas analyser equipped with two nondispersive infrared (NDIR) sensors and a thermal conductivity detector (TCD) for monitoring CO, CO_2 and H_2 concentrations, respectively.

7.3. Results and Discussion

7.3.1. Physic-chemical properties of the catalysts

In this section the results on the characterisation of the catalysts are discussed focusing mainly on the CuZnZr-ferrierite hybrid catalysts.

Surface area and porosimetry

In our work, textural properties were investigated on both calcined and aged catalysts for the purpose of examining variations in terms of surface area, porosimetry and catalytic performances. First of all, textural properties of both calcined and aged CuZnAl and CuZnZr catalysts are compared. As reported in Table 7.2, the specific surface area of the calcined samples is comparable and it roughly halves for the aged ones. The mesoporous structure changes during the pre-treatment and during the tests because the overall pore volume decreases and the small amount of micropores tends to disappear, in fact, the average pore size increases. It is worth noting that the commercial CuZnAl catalyst seems to be structurally more stable than the CuZnZr; this is certainly linked to the synthesis conditions.

Table 7.2. Textural properties of calcined and aged CuZnAl and CuZnZr catalysts estimated by means of N_2 physisorption.

Catalysts	Catalyst type	S_{BET}[(a)]	S_{LANG}[(b)]	S_{mp}[(c)]	V_{BJH}[(d)]	V_{mp}[(c)]	d_p[(e)]
		m^2/g_{cat}	m^2/g_{cat}	m^2/g_{cat}	cm^3_{STP}/g_{cat}	cm^3_{STP}/g_{cat}	nm
CuZnZr	Calcined	83.5	137.5	8.2	0.288	0.0036	13.8
	Aged	35.7	63.2	0	0.140	0	15.7
CuZnAl	Calcined	80.6	145.5	5.5	0.163	0.0030	8.1
	Aged	42.0	73.2	4.2	0.135	0.0025	12.9

(a) The specific surface area (S_{BET}) was calculated according to the Brunauer-Emmett-Teller theory.

(b) The specific surface area (S_{LANG}) was calculated according to the Langmuir theory.

(c) The micropore specific surface area (S_{mp}) and the micropore volume (V_{mp}) were estimated using the t-plot method.

(d) The pore volume between 1.7 nm and 300 nm (V_{BJH}) was determined by applying the BJH algorithm to the desorption branch of the isotherm.

(e) The average pore diameter was calculated considering cylindrical pores: $d_p = 4 \cdot \frac{V_{BJH}}{S_{BET}}$

As presented in Table 7.3, the bare ferrierite exhibits a high specific surface area which matches the nominal value (400 m^2/g_{cat}), while the porosimetry analysis confirms the presence of a microporous structure and a broadened distribution of macropores [103,277].

Concerning CuZnZr-based hybrid catalysts, their textural properties appear to be directly linked to the metallic load/ferrierite weight ratio, as illustrated in Figure 7.1. Nevertheless, the specific surface areas of both calcined CZZ/FER OX 1:2 (311 m^2/g_{cat}) and CZZ/FER WI 1:2 (302.1 m^2/g_{cat}) are lower than CZZ-FER MIX 1:2 (337 m^2/g_{cat}) specific surface area; this is certainly caused by the synthesis techniques. In fact, the metallic load, which is deposited on the surface of the bare ferrierite (coprecipitation or impregnation), reduces its microporosity. This loss in specific surface area is however partially balanced by the mesoporosity of the oxides. More specifically, the coprecipitated catalysts show a sharpened mesopore size distribution at around 15 nm. Whereas, the aged catalysts exhibit a decrease both of the total specific surface area and of the total pore volume. Textural modifications during experimental tests which affect the CuZnZr-based hybrid catalysts are certainly connected to the sintering of the metallic load [102,278,279]. In addition, as illustrated in Figure 7.1, there is a direct correlation between the specific surface area and the micropore volume [90]. More in detail, the slope of the straight line of the aged catalysts is greater than the one of the calcined samples. This means that the sintering of the metallic load obstructs the micropores of the ferrierite reducing both the volume and the surface of micropores, occludes the microporosity of the metallic load and reduces strongly its surface area and mesoporosity.

Table 7.3. Textural properties of calcined and aged CuZnZr-based hybrid catalysts estimated by means of N_2 physisorption.

Catalysts	Catalyst type	S_{LANG}[(a)]	S_{mp}[(b)]	V_{BJH}[(c)]	V_{mp}[(b)]	d_p[(d)]
		m^2/g_{cat}	m^2/g_{cat}	cm^3_{STP}/g_{cat}	cm^3_{STP}/g_{cat}	nm
	Calcined	456.8	414.7	0.084	0.140	0.7

Bare ferrierite (FER)	Aged	-	-	-	-	-
CZZ/FER OX 1:2	Calcined	311.1	253.5	0.217	0.079	2.7
	Aged	218.5	173.7	0.170	0.054	3.1
CZZ/FER WI 1:2	Calcined	302.1	254.4	0.143	0.081	1.9
	Aged	233.7	204.2	0.115	0.066	2.0
CZZ-FER MIX 1:2	Calcined	337.0	288.2	0.145	0.093	1.7
	Aged	264.1	228.1	0.106	0.073	1.6
CZZ/FER OX 2:1	Calcined	211.6	148.8	0.207	0.037	3.9
	Aged	145.8	94.4	0.196	0.021	5.4
(a) The specific surface area (S_{LANG}) was calculated according to the Langmuir theory.						
(b) The micropore specific surface area (S_{mp}) and the micropore volume (V_{mp}) were estimated using the t-plot method.						
(c) The pore volume between 1.7 nm and 300 nm (V_{BJH}) was determined by applying the BJH algorithm to the desorption branch of the isotherm.						
(d) The average pore diameter was calculated considering cylindrical pores: $d_p = 4 \cdot \frac{V_{BJH}}{S_{LANG}}$						

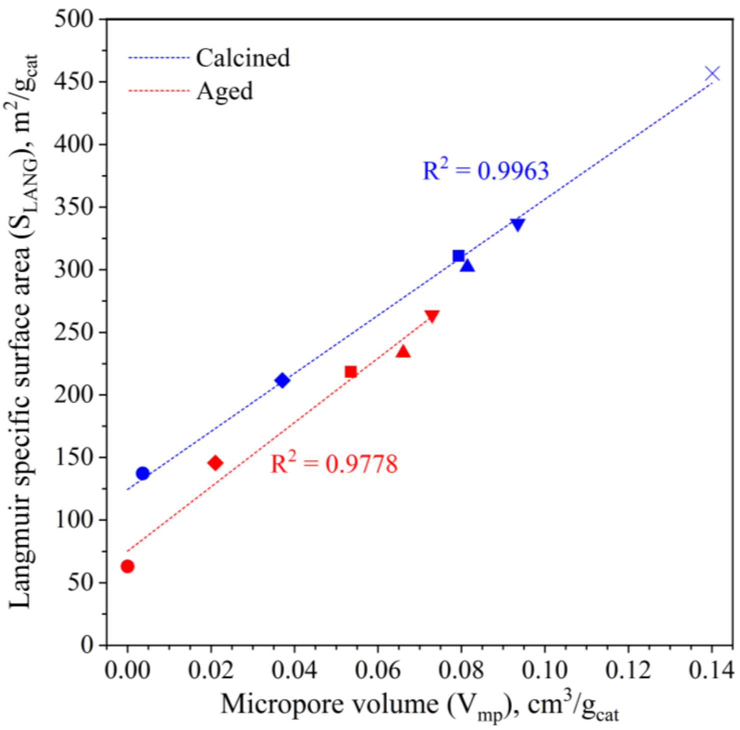

Figure 7.1. Relationship between the micropore volume and the specific surface area for calcined and aged catalysts. For the sake of clarity, the symbols represent: ● CuZnZr, ♦ CZZ/FER OX 2:1, ■ CZZ/FER OX 1:2, ▲ CZZ/FER WI 1:2, ▼ CZZ-FER MIX 1:2 and × FER.

X-ray diffraction

X-ray diffraction patterns of calcined and aged ternary oxides (CuZnZr and CuZnAl catalysts) are shown in Figure 7.2. Regarding calcined samples, their patterns exhibit three wide halos between 30° and 40°, which correspond to at least convoluted peaks. These signals are indeed the main reflections of the monoclinic CuO phase at (PDF 00-045-0937) at 32.5°, 35.5°, 38.7° and 38.9°, and of the hexagonal structure of ZnO (PDF 00-036-1451) at 31.8°, 34.4° and 36.3°. The broadening of these peaks is principally caused by the small crystallite size of CuO and ZnO. On the contrary, Al_2O_3 and ZrO_2 were not detected in the diffractograms; thus, they are probably amorphous. Moreover, the pattern of the calcined CuZnAl revealed a small peak at 24.2° corresponding to the reflection of malachite (PDF 00-001-0959), which may be attributed to a residue of the synthesis that did not decompose during calcination [280,281]. Lastly, the narrow peak at 26.4° has been assigned to graphite (PDF 00-041-1487), which was clearly detected by means of FESEM-EDS analysis. As shown in Figure 7.3, graphite grains are included in the particles of the catalyst; they may have been used as lubricant during the extrusion of the commercial pellets.

Concerning aged ternary oxide catalysts, their x-ray diffractograms show three peaks at 43.3°, 50.4° and 74.1°, corresponding to the reflection of the cubic structure of metallic Cu. However, CuO did not reduce completely to Cu during the pre-treatment and the experimental tests; characteristic peaks of CuO were indeed detected in aged catalysts. As shown in Table 7.4, it is worth noting that the Cu crystallite size of the aged CuZnAl is roughly 3 times wider than in the aged CuZnZr catalyst, and this aspect has a great importance in the activity of the catalysts as detailed in further sections.

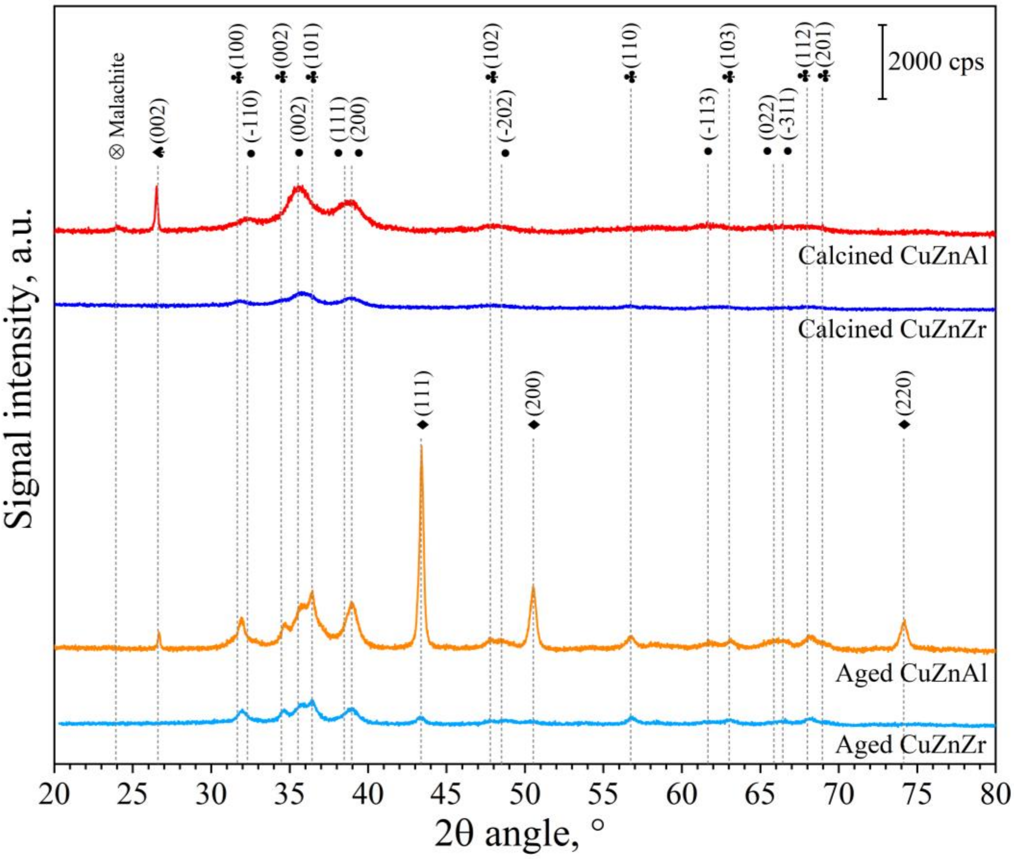

Figure 7.2. XRD patterns of calcined and aged catalysts; different phases were indexed: ● CuO, ♦ Cu, ♣ ZnO, ♠ graphite and ⊗ malachite. For the sake of clarity, XRD data are not manipulated, but they are only vertically offset.

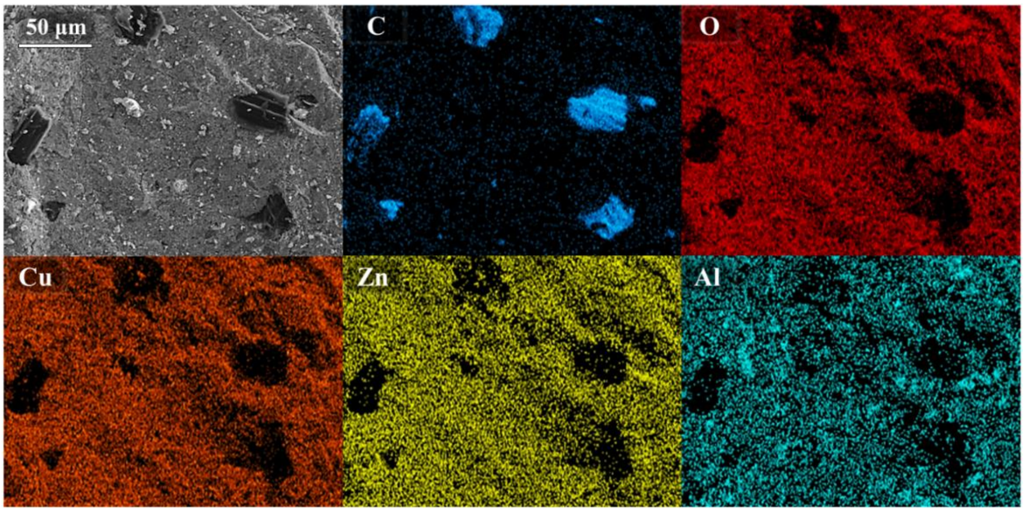

Figure 7.3. FESEM image and EDS maps of the calcined commercial CuZnAl catalyst.

Table 7.4. Average crystallite size of CuO, Cu and ZnO of CuZnAl and CuZnZr catalysts estimated by means of Scherrer's equation.

Catalysts	d_{CuO} (calcined)	d_{CuO} (aged)	d_{Cu} (aged)	d_{ZnO} (calcined)	d_{ZnO} (aged)
	nm	nm	nm	nm	nm
CuZnZr	8.9	10.5	16.4	7.1	11.9
CuZnAl	5.8	17.9	44.3	3.6	8.6

X-ray patterns were collected for both calcined and aged catalysts in order to evidence the influence of the experimental activity on the samples, as displayed in Figure 7.4a and Figure 7.4b. The XRD pattern of calcined bare ferrierite (FER) is characterized by several intense and narrow peaks between 7° and 30° (PDF 00-044-0104 and PDF 01-088-1796), as also reported in literature [90,280,282,283]. Its crystalline structure could not be observed by means of TEM due to its instability under the beam and its instantaneous transformation from crystalline to amorphous structure [284].

X-ray diffractograms of CuZnZr-based hybrid catalysts show three wide halos between 30° and 40°, which correspond to at least seven convoluted peaks: the monoclinic phase of CuO (PDF 00-045-0937) at 32.5°, 35.5°, 38.7° and 38.9°; and the hexagonal structure of ZnO (PDF 00-036-1451) at 31.8°, 34.4° and 36.3°. The broadening of these peaks is principally caused by the small crystallite size of those phases, as reported in Table 7.5. Zirconia (ZrO_2) was not detected due to its small amount; in addition, it is probably present as an amorphous phase. As shown in Table 7.5, CuO crystallite size is lower than 10 nm; the only exception is related to CZZ/FER WI 1:2, in which CuO crystallite size is around 18 nm. This fact could be linked to the synthesis technique in which the precursors form large clusters of precipitate during the evaporation of the solvent.

Figure 7.4b illustrates XRD patterns of aged catalysts; the three main reflection peaks of the cubic structure of metallic copper are clearly visible at 43.3°, 50.4° and 74.1° (PDF 00-004-0836). Those patterns reveal that CuO is not completely reduced to metallic Cu in some samples (CuZnZr, CZZ/FER OX 1:2 and CZZ-FER MIX 1:2). Regarding the formation of Cu_2O, its main characteristic peak at 36.4° overlaps with the most intense peak of ZnO located at 36.3°. In fact, the metallic load is deposited on the surface of the ferrierite; thus, oxides were more accessible to the gas. These observations agree with both H_2-TPR and morphological analyses as detailed in further sections. Furthermore, ZnO was not reduced during tests due to the low activation temperature (350 °C) with respect to the ZnO reduction temperature (around 600 °C) [285]. It is noteworthy that the Cu crystallite size is larger than the CuO crystallite size for all the aged catalysts. Coprecipitated hybrid catalysts have revealed a smaller increase in Cu crystallite size compared with the other aged catalysts. Zinc oxide has a more stable structure and its crystallite size did not expand dramatically.

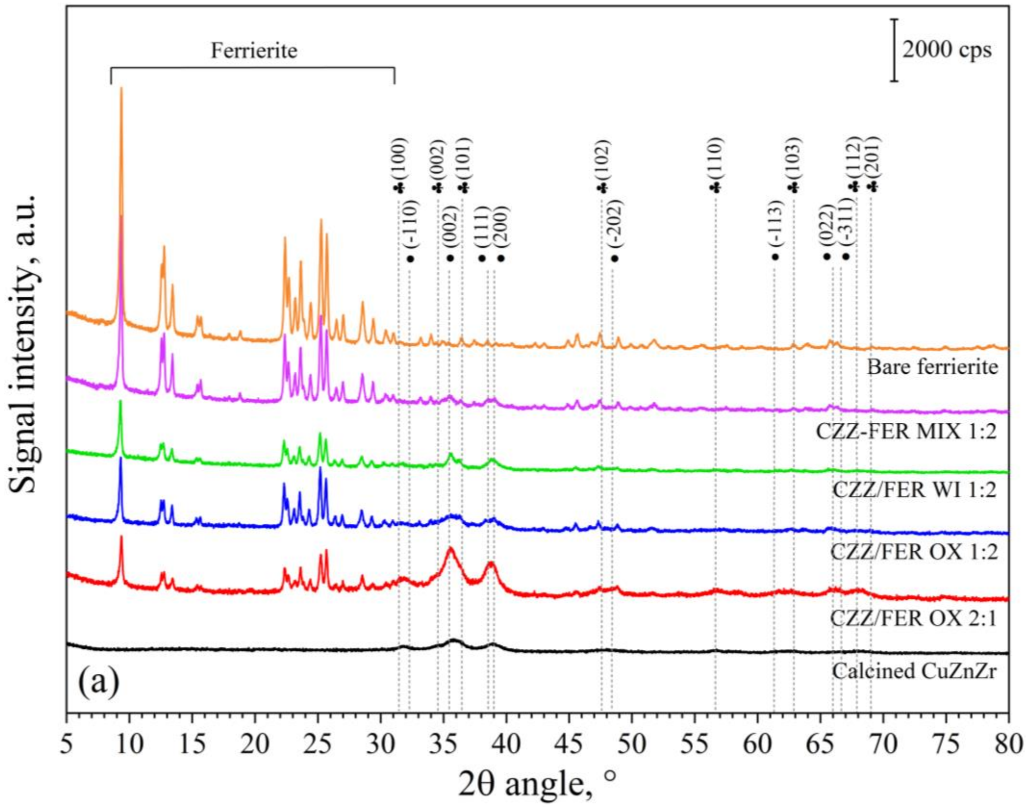

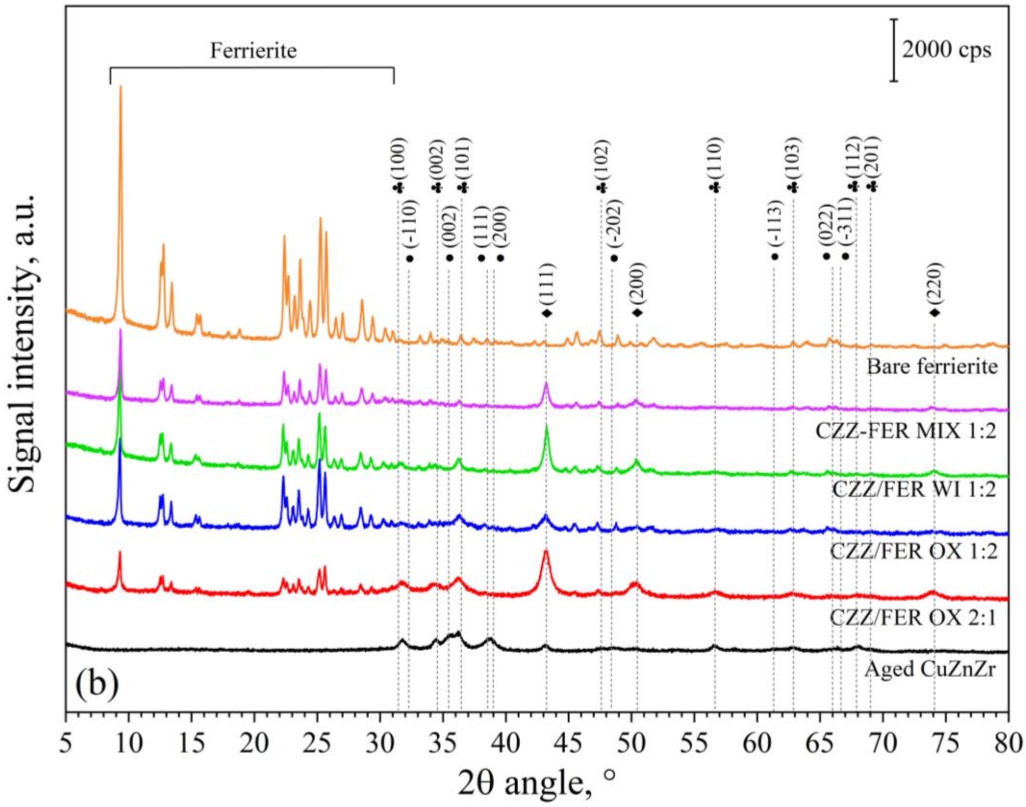

Figure 7.4. XRD patterns of calcined (a) and aged (b) catalysts; different phases were indexed: ● CuO, ♦ Cu and ♣ ZnO. For the sake of clarity, XRD data are not manipulated, but they are only vertically offset.

Table 7.5. Average crystallite size of CuO, Cu and ZnO of CuZnZr-ferrierite hybrid catalysts estimated by means of Scherrer's equation.

Catalysts	d_{CuO} (calcined)	d_{CuO} (aged)	d_{Cu} (aged)	d_{ZnO} (calcined)	d_{ZnO} (aged)
	nm	nm	nm	nm	nm
CuZnZr	8.9	10.5	16.4	7.1	11.9
CZZ/FER OX 2:1	8.2	-	11.6	4.7	8.0
CZZ/FER OX 1:2	5.2	11.2	11.4	5.7	7.0
CZZ/FER WI 1:2	18.5	-	24.9	14.9	16.4
CZZ-FER MIX 1:2	8.8	15.6	24.3	6.2	9.8

Temperature programmed reduction (H_2-TPR)

Concerning the ternary oxides, it is worth noting that the CuZnAl catalyst is extremely more reducible than the CuZnZr. As shown in Figure 7.5 and Table 7.6, the H_2/CuO molar ratio for the CuZnAl sample is 1.32, while it is 0.13 for CuZnZr at $T \leq 350$ °C. This means that CuZnAl adsorbs H_2 within ZnO structure during the reduction of CuO, in fact there is a large negative peak at 810 °C linked to the H_2 desorption and ZnO reduction to metallic Zn. A low reduction of the CuZnZr samples is also confirmed by its XRD pattern, in fact, the Cu diffraction peaks have a small intensity.

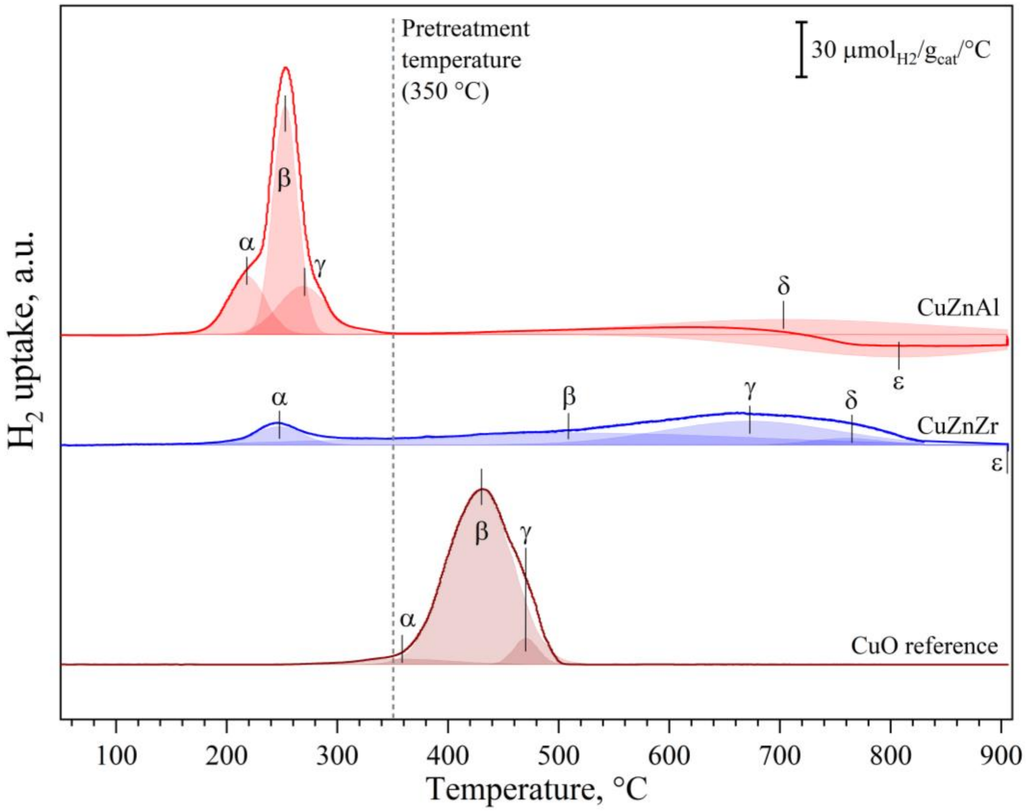

Figure 7.5. H_2-TPR profiles of calcined ternary oxides and reference (CuO).

Table 7.6. Quantitative analyses of the H_2-TPR measurements of CuZnAl and CuZnZr ternary oxide catalysts.

Catalysts	H_2 consumption at T ≤ 350°C	H_2 consumption of δ peak	H_2 desorption of ε peak	H_2 / CuO ratio at T ≤ 350°C$^{(a)}$	Reduced CuO$^{(b)}$	Reduced ZnO$^{(c)}$
	mmol$_{H2}$/g$_{cat}$	mmol$_{H2}$/g$_{cat}$	mmol$_{H2}$/g$_{cat}$	-	%	%
CuZnZr	0.94	0.28	0.36	0.13	13	8
CuZnAl	10.58	3.07	3.91	1.32	84	~100

Catalysts	CuO to Cu reduction peaks$^{(d)}$			Peak temperature				
	α	β	γ	α	β	γ	δ	ε
	%	%	%	°C	°C	°C	°C	°C
CuZnZr	10	46	44	247	515	672	761	906
CuZnAl	21	56	23	218	253	268	705	810

(a) The H_2/CuO molar ratio was evaluated considering the area of the reduction peaks at T ≤ 350 °C and the nominal composition of the catalyst.

(b) The fraction of reduced CuO to metallic Cu at T ≤ 350 °C was evaluated subtracting the desorbed amount of H_2 at T > 350 °C to the area of the reduction peak at T ≤ 350 °C considering the nominal composition of the catalyst.

(c) The fraction of reduced ZnO to metallic Zn at T > 350 °C was evaluated using the nominal composition of the catalysts.

(d) The fractions of α, β and γ peaks were evaluated as the ratio between the area of a deconvoluted peak and their total area.

The analysis of the reducibility is a crucial aspect for Cu-based catalysts. Previous studies have been reported that CuO and ZnO shows a synergistic effect on the reducibility of both phases [286–288]. CuO is indeed reduced by H_2 to metallic Cu between 380 °C and 500 °C, as shown in Figure 7.6 [286]. However, a high dispersion of CuO and the presence of ZnO favour the reducibility of CuO at lower temperatures [288]. More specifically, the reduction peak of CuO has been usually deconvoluted in three peaks at increasing reduction temperature corresponding respectively to highly dispersed CuO particles, CuO particles in contact with ZnO and bulky CuO species without ZnO contact [99,289]. Nevertheless, other authors have related them to subsequent reduction steps of CuO to metallic Cu [99]. H_2-TPR characterization was performed on each sample for the purpose of evaluating the reducibility, and the H_2-TPR profiles are illustrated in Figure 7.6. It is worth noting that the amount of H_2 consumed during the reduction of the hybrid catalysts is proportional to the metallic load; furthermore, the main reduction peak of CuO of each catalyst is located between 180 °C and 300 °C, thus a beneficial effect of ZnO on the reducibility of CuO is evident with respect to the reference CuO. Moreover, two low and broad peaks could be qualitatively identified: the first one is positive and located between 500 °C and 750 °C; while, the second is negative with respect to the baseline of the profile and located at higher temperatures (~800 °C).

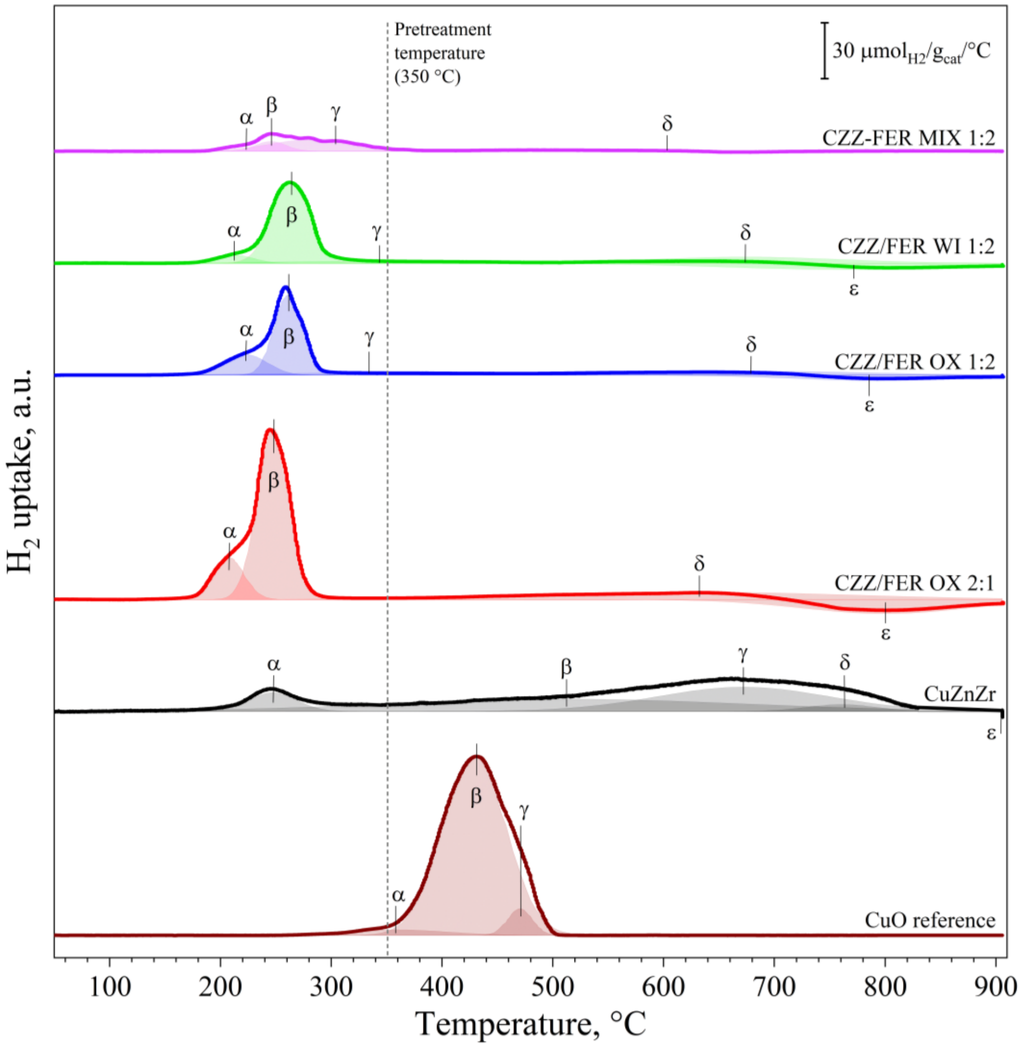

Figure 7.6. H_2-TPR profiles of calcined CuZnZr-based catalysts and reference (CuO).

A quantitative analysis of each H_2-TPR profiles was performed in order to better clarify some key aspects on the behaviour of these catalysts. More in detail, reduction peaks were deconvoluted as gaussian curves and the results of the investigation are provided in Table 7.7. Firstly, as previously mentioned, the specific H_2 uptake of the main reduction peak (T < 350 °C) is directly proportional to the oxides/zeolite weight ratio. However, what stands out in the table is the extremely high experimental H_2/CuO molar ratio (between 1.42 and 1.60) with respect to the theoretical stoichiometric H_2/CuO ratio equal to 1. As mentioned in the literature, some authors have reported that a synergistic effect between CuO and ZnO results in a reduction of CuO and a partial reduction of ZnO at low temperature [286,288,290]. More specifically, the H_2 uptake is comparable to the complete reduction of both CuO and ZnO; nevertheless, this interpretation is in contrast with XRD and XPS results. In fact, these characterization techniques show that ZnO does not reduce at T < 350 °C (maximum temperature during the pre-treatment procedure). Interestingly, other researchers have stated that nanoparticles of ZnO are capable of storing huge amount of hydrogen within their crystalline structure [291–294]. More in detail, atomic hydrogen could occupy interstitial position on the surface and in the subsurface regions (~10 atomic layers) [291,292]. In addition, H_2 adsorbs and dissociates on the surface of metallic Cu, and then atomic H migrates towards the oxide structure of ZnO [291]. Therefore, an intimate contact of Cu and ZnO particles emphasizes this phenomenon [292]. As shown in Figure 7.7a, the fraction of the β-peak increases as the H_2/CuO molar ratio rises, which probably means that atomic H is interstitially absorbed in the ZnO structure according to the stoichiometric ratio, which is reported in equation (7.5) [291].

$$ZnO + H_2 \rightleftarrows ZnH + OH \tag{7.5}$$

Table 7.7. Quantitative analyses of the H_2-TPR measurements of CuZnAl and CuZnZr ternary oxide catalysts.

Catalysts	H_2 consumption at T ≤ 350°C	H_2 consumption of δ peak	H_2 desorption of ε peak	H_2 / CuO ratio at T ≤ 350°C$^{(a)}$	Reduced CuO$^{(b)}$	Reduced ZnO$^{(c)}$
	$mmol_{H2}/g_{cat}$	$mmol_{H2}/g_{cat}$	$mmol_{H2}/g_{cat}$	-	%	%
CuZnZr	0.94	0.28	0.36	0.13	13	8
CZZ/FER OX 2:1	6.83	2.32	2.34	1.44	95	98
CZZ/FER OX 1:2	3.67	1.18	1.09	1.42	~100	~100
CZZ/FER WI 1:2	3.80	1.18	1.58	1.60	94	~100
CZZ-FER MIX 1:2	1.95	0.51	-	0.82	82	7

Catalysts	CuO to Cu reduction peaks$^{(d)}$			Peak temperature				
	α	β	γ	α	β	γ	δ	ε
	%	%	%	°C	°C	°C	°C	°C
CuZnZr	10	46	44	247	515	672	761	906
CZZ/FER OX 2:1	19	81	-	207	248	-	630	800
CZZ/FER OX 1:2	24	62	14	224	261	336	675	795
CZZ/FER WI 1:2	8	81	11	214	263	341	674	768

CZZ-FER MIX 1:2	12	13	57	223	253	302	603	-
(a) The H_2/CuO molar ratio was evaluated considering the area of the reduction peaks at $T \leq 350$ °C and the nominal composition of the catalyst.								
(b) The fraction of reduced CuO to metallic Cu at $T \leq 350$ °C was evaluated subtracting the desorbed amount of H_2 at $T > 350$ °C to the area of the reduction peak at $T \leq 350$ °C considering the nominal composition of the catalyst.								
(c) The fraction of reduced ZnO to metallic Zn at $T > 350$ °C was evaluated using the nominal composition of the catalysts.								
(d) The fractions of α, β and γ peaks were evaluated as the ratio between the area of a deconvoluted peak and their total area.								

The fraction of CuO reduced by H_2 to metallic Cu was evaluated considering the H_2 absorbed within the structure of ZnO. More in detail, H_2-TPR profiles were fitted considering three peaks at low temperature (180 °C – 300 °C), a positive peak at high temperature (500 °C – 800 °C), which corresponds to the reduction of ZnO to metallic Zn, and a negative peak at extremely high temperature (600 °C – 900 °C), which corresponds to the desorption of hydrogen from ZnO. The presence of the negative peak at high temperatures is confirmed by further analysis, which are reported in Figure 7.8. In fact, it is not caused by the copper or by the ferrierite; moreover, it seems to be directly proportional to the amount of oxides in the catalyst, as displayed in Figure 7.7b. Hence, a H_2-TPD on the commercial CuZnAl was performed for evaluating the strength of H_2 adsorption and the profile is illustrated in Figure 7.8. According to the literature, a H_2 desorption peak is located between 120 °C and 280 °C, which correspond to three desorption peaks at 147 °C, 193 °C and 275 °C [291]; however, an intense H_2 desorption peak is located at 420 °C, which probably involves the desorption of the hydrogen from the structure of the ZnO. Secondly, as displayed in Figure 7.8, a H_2-TPR was carried out on pure ZnO powder, and the profile confirms a shift of the two H_2 desorption peaks from 190 °C and 420 °C to 440 °C and 820 °C, respectively, which could probably due to the change of the atmosphere. What stands out from Figure 7.6 and Table 7.7 is that hybrid catalysts are more reducible than the ternary oxides and the physical mixed catalyst. Gel-oxalate coprecipitation seems to be the best technique for producing high reducible copper particles with intimate contact with ZnO. In fact, these results are in accordance with both XRD and XPS characterizations. Furthermore, the area of the α-peak of the H_2-TPR profile decreases, while the peak temperature of the γ-peak rises as the average crystallite size of CuO increases; hence α-peak could be related to the highly dispersed CuO particles, whereas the γ-peak could be linked to bulky CuO species.

As far as ZnO is concerned, it was completely reduced by H_2 to metallic Zn at high temperatures (around 670 °C), as reported in Table 7.7. Contrary to expectations, the peak temperature of ZnO reduction (δ-peak) decreases as both the ZnO and CuO average crystallite sizes increase. Whereas, the H_2 desorption peak (ε-peak) could be related to the release of interstitial hydrogen from ZnO structure, that could not be stored within the material after the reduction of ZnO to metallic Zn. Furthermore, the calculated amount of H_2 desorbed is directly proportional to the amount of ZnO in the catalysts, as illustrated in Figure 7.7.

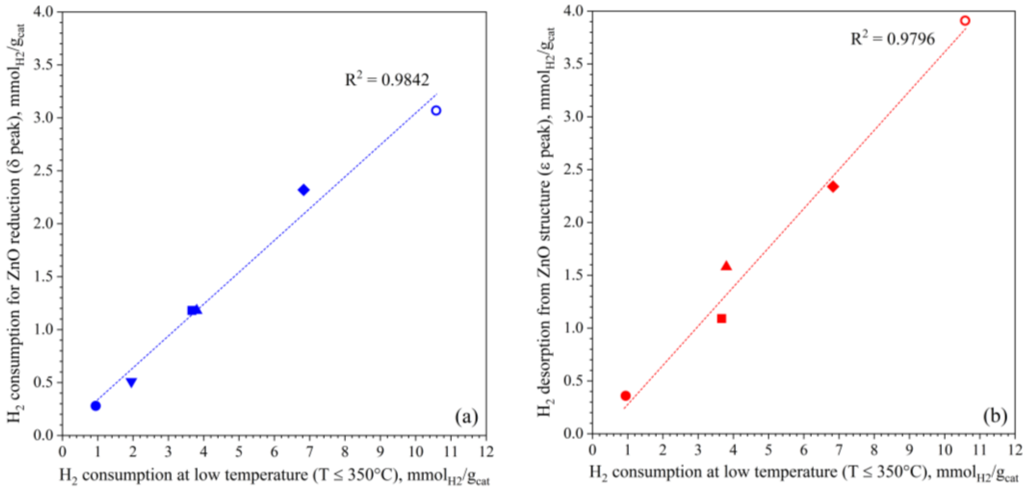

Figure 7.7. Correlation between the H_2 consumption at low temperature (T ≤ 350 °C) and the H_2 consumption for ZnO reduction (a); and correlation between the H_2 consumption at low temperature (T ≤ 350 °C) and the interstitial H_2 desorption (ε-peak) (b). For the sake of clarity, the symbols represent: ● CuZnZr, ○ CuZnAl, ♦ CZZ/FER OX 2:1, ■ CZZ/FER OX 1:2, ▲ CZZ/FER WI 1:2 and ▼ CZZ-FER MIX 1:2.

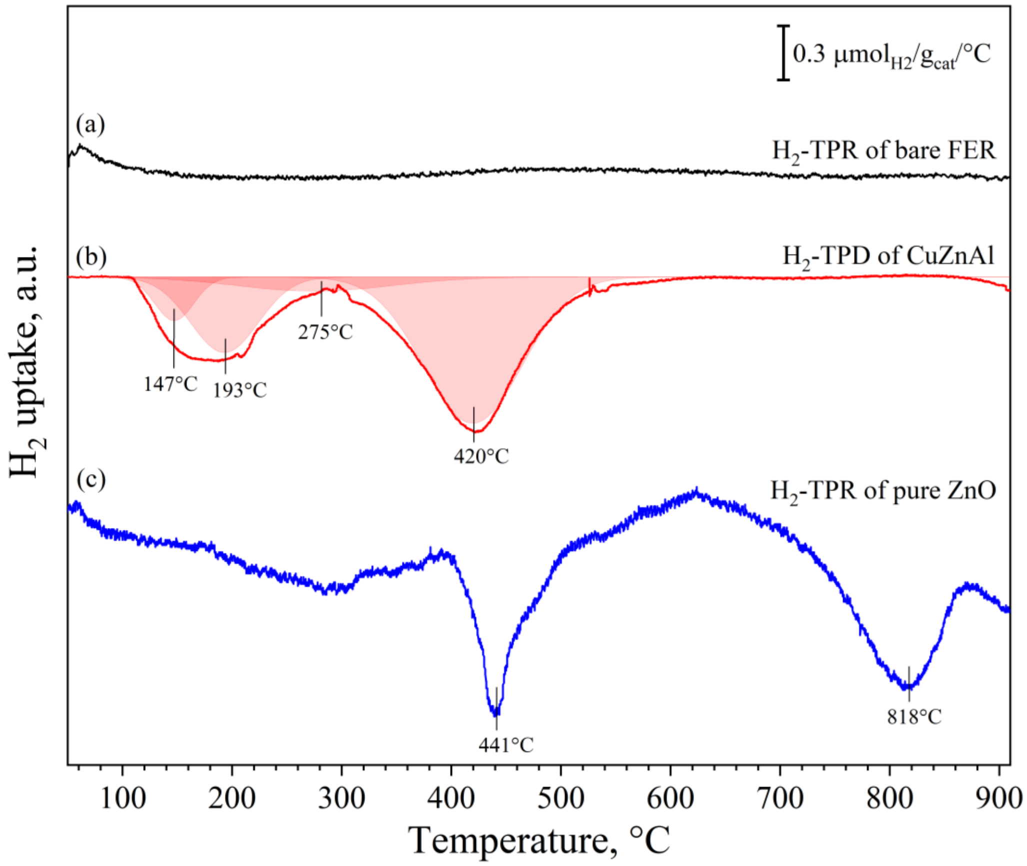

Figure 7.8. H_2-TPR profile of bare ferrierite (a), H_2-TPD profile of commercial CuZnAl (b) and H_2-TPR profile of pure ZnO (c). Considering H_2-TPD, the CuZnAl sample was previously reduced with 5 % vol H_2/Ar (20 ml/min) at 350 °C for 1 h and subsequently cooled down in the same reducing atmosphere. After that, the sample was cleaned with N_2 (20 ml/min) for 1 h, and eventually the H_2-TPD was carried out with N_2 (20 ml/min) between 50 °C and 900 °C (heating rate: 10 °C/min). For clearness, negative peaks correspond to H_2 desorption.

Considering CuZnZr and physically mixed catalyst (CZZ-FER MIX 1:2), they exhibited a completely different reducing behaviour during H_2-TPR characterization. In fact, ~84% of CuO of CuZnZr was reduced between 200 °C and 700 °C (α, β and γ peaks), while ~8% of ZnO was reduced at ~760 °C and a small negative peak was identified in the isothermal holding at 906 °C. The incomplete reduction of CuZnZr could be seen in its XRD pattern (see Figure 7.4), in fact, it exhibited a low intensity of the metallic Cu diffraction peaks. The physically mixed catalyst exhibited an analogous behaviour; however, the positive peaks are small, and the negative peak was not detected due to the low amount of metallic load.

NH_3 pulse chemisorption

Quantitative results of NH_3-pulse chemisorption are summarized in Table 7.8, a small variation in total number of acidic sites was revealed between fresh and aged catalysts. According to the literature, commercial bare FER is characterized by a concentration of acidic sites of about 494 $\mu mol_{NH3}/g_{cat}$ [90,101]. Fresh reduced hybrid catalysts obtained by gel oxalate coprecipitation and wet impregnation exhibit a greater concentration of acidic sites ($\mu mol_{NH3}/g_{FER}$) with respect to the bare ferrierite; this feature may be probably linked to the dispersion of the metallic load on the surface of the zeolite. In the literature, some more specific analyses on the acidity of hybrid catalysts have been reported [90,280,288,295–297]. Some authors have stated that the deposition of a metallic load on the surface of the zeolite masks acidic sites; notwithstanding, the metallic load adds weak acidic hydroxyl groups on the surface of the catalyst [280,295]. The blockage or the exchange of acidic sites caused by metal ions could not be excluded during activity tests; hence, aged CZZ/FER OX 1:2 and CZZ/FER WI 1:2 catalysts reveal a loss of acidity [90,288]. Furthermore, the CZZ/FER MIX 1:2 sample (~400 $\mu mol_{NH3}/g_{FER}$) exhibit an acidity comparable to the bare FER and it may be linked to the preparation technique. In fact, CuZnZr and FER powders were physically mixed to obtain the bifunctional catalyst and the FER was not present during the synthesis of the oxides. Eventually, it is worth mentioning that a large inaccuracy sensibly affects the results and their interpretation.

Table 7.8. Quantitative data of NH_3 pulse chemisorption.

Catalysts	Catalyst type	NH_3 uptake	NH_3 uptake
		$\mu mol_{NH3}/g_{cat}$	$\mu mol_{NH3}/g_{FER}$
Commercial FER	Fresh reduced	494 ± 50	494 ± 50
	Aged	-	-
CZZ/FER OX 1:2	Fresh reduced	540 ± 37	810 ± 56
	Aged	465 ± 12	698 ± 18
CZZ/FER WI 1:2	Fresh reduced	511 ± 24	767 ± 36
	Aged	466 ± 17	699 ± 26
CZZ-FER MIX 1:2	Fresh reduced	270 ± 31	405 ± 47

	Aged	248 ± 25	372 ± 38
CZZ/FER OX 2:1	Fresh reduced	271 ± 15	813 ± 45
	Aged	269 ± 34	807 ± 102

Morphological characterization

FE-SEM and EDS measurements were carried out on the samples in order to better understand their morphology and the metallic distribution on the zeolite. Figure 7.9 clearly highlights the differences and inhomogeneities of all the hybrid systems. First of all, commercial FER (see Figure 7.9k), CZZ/FER OX 1:2 (see Figure 7.9a and Figure 7.9b)) and CZZ/FER WI 1:2 (see Figure 7.9g and Figure 7.9h) are characterized by particles of ferrierite ranging approximately from 30 nm to 500 nm with different shapes. Moreover, CZZ/FER OX 2:1 (see Figure 7.9d and Figure 7.9e) revealed a completely different structure of the ferrierite-type zeolite in some portion of the catalyst; in fact, it has exposed a lamellar structure on which metals are deposited. This feature could not be clearly explained because there were no differences in XRD patterns or previous characterization [90,100]. Secondly, with respect to the metallic load, CZZ/FER OX 1:2 has a low amount of metals dispersed on the surface of the zeolite. They do not completely cover the surface, but form some sponge-like structures, which are characterized by small nanometric monocrystalline grains. However, the backscattered image and the EDS mapping of this catalyst (see Figure 7.10a) illustrate a macroscopic uniformity of the metal load on the surface without evident inhomogeneities. As far as CZZ/FER OX 2:1 is concerned, the metallic load was deposited on the surface by means of gel oxalate coprecipitation as for the CZZ/FER OX 1:2; nevertheless, a completely different disposition of the metals can be observed in FESEM images. During the synthesis metals could form small aggregates of nanoparticles or a uniform coating on the surface of the zeolite. In addition, the backscattered FESEM image and the EDS maps (see Figure 7.10b) highlight the lack of structural and compositional homogeneity. Similarly, CZZ/FER WI 1:2 exhibited an inhomogeneous deposition of the metallic load on the external surface of the ferrierite despite the lower amount of metallic precursors. This fact may be due to an uncomplete wettability of the bare zeolite with respect to the ethanol solution. Hence, core-shell structures could be observed in Figure 7.9g and Figure 7.9h [90]; besides, the backscattered FE-SEM image and the EDS map (see Figure 7.10c) of the surface of this catalyst evidence these aspects. A completely different macrostructure was observed for CZZ-FER MIX 1:2 catalyst, some portions of the sample are indeed constituted by ferrierite and other parts by metals, as shown both in the backscattered FE-SEM image and in Figure 7.10d. In general, all the samples exhibited a small size of metallic nanoparticles, and this aspect means that the contact between copper and zinc favours a synergistic effect between the two phases: the metallic dispersion is high, and thus the specific surface area of the active species for MeOH synthesis is large [99,100]. FE-SEM images do not have high resolution due to the low conductivity of the samples; hence, no macroscopic changes were observed between calcined and aged catalysts. However, further investigations were carried out by means of a transmission electron microscope.

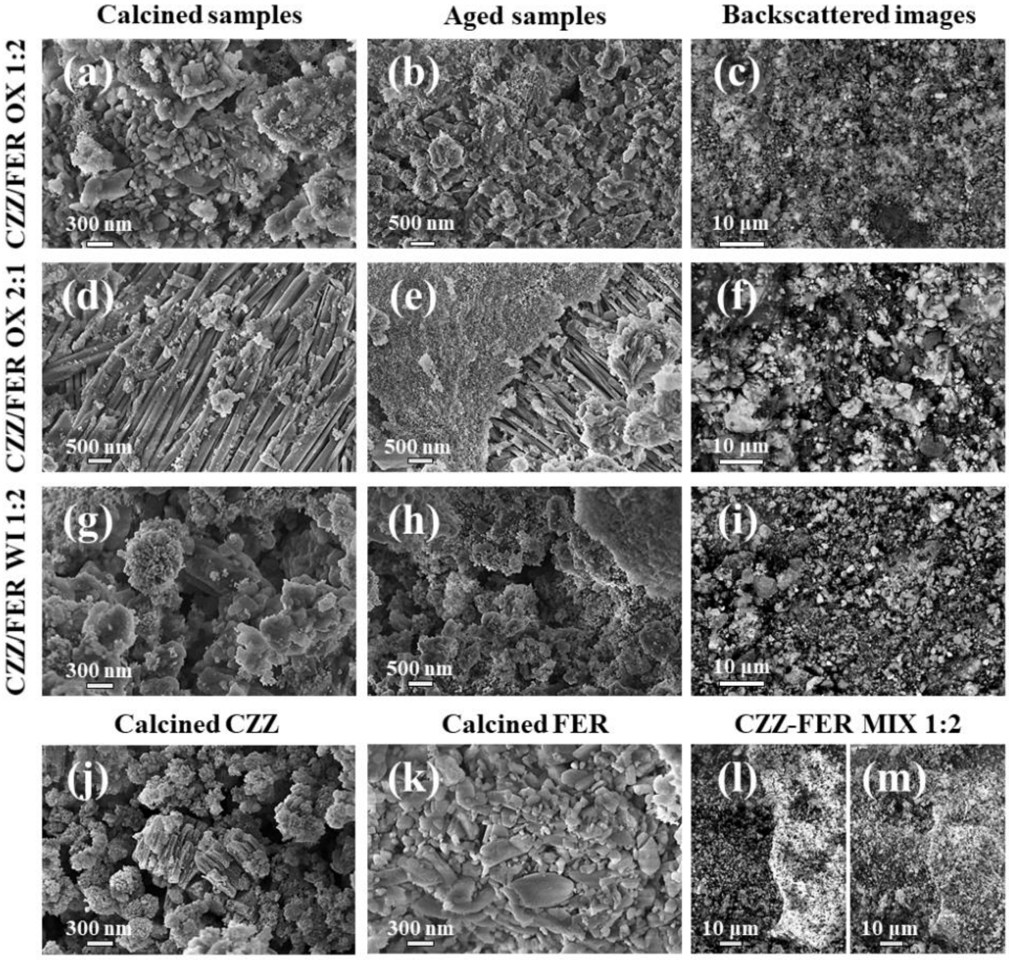

Figure 7.9. FE-SEM images of calcined samples: (a) CZZ/FER OX 1:2, (d) CZZ/FER OX 2:1, (g) CZZ/FER WI 1:2, (j) CuZnZr, (k) commercial bare ferrierite and (m) CZZ-FER MIX 1:2. FE-SEM images of aged catalysts: (b) CZZ/FER OX 1:2, (e) CZZ/FER OX 2:1 and (h) CZZ/FER WI 1:2. Backscattered FE-SEM images of calcined samples: (c) CZZ/FER OX 1:2, (f) CZZ/FER OX 2:1, (i) CZZ/FER WI 1:2 and (l) CZZ-FER MIX 1:2.

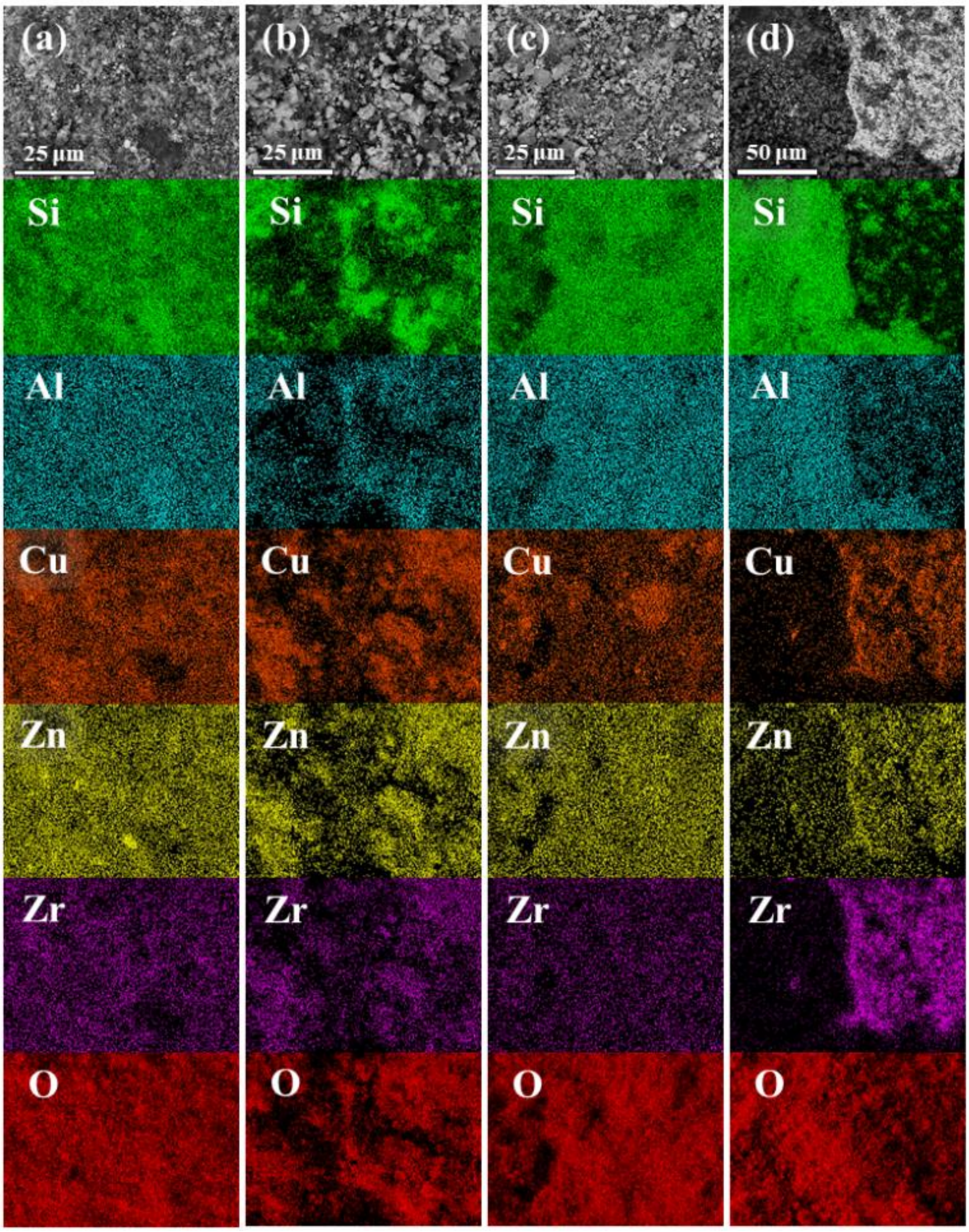

Figure 7.10. Backscattered FE-SEM images and EDS maps of fresh CZZ/FER OX 1:2 (a), CZZ/FER OX 2:1 (b), CZZ/FER WI 1:2 (c) and CZZ/FER MIX 1:2 (d).

Bright-field TEM imaging provides an efficient way to visualize the distribution of the metal oxide nanoparticles with respect to the ferrierite structures due to difference in morphology and average atomic number. Figure 7.11 shows a comparison between representative low-magnification images of CuZnZr-based samples obtained with different preparation methods (gel-oxalate co-precipitation, wet impregnation, physical mixing). CZZ/FER samples do not show a homogeneous coverage of the ferrierite over the whole external surface area with metal-oxide nanoparticles, in fact, they create agglomerates on the edges. It is interesting to notice that the higher loading (sample CZZ/FER OX 2:1) leads to a more homogenous distribution of the metal oxide nanoparticles on ferrierite. It must be stressed that, regardless of the loading, the co-precipitation approach leads to better interdispersion of metal oxide nanoparticles and ferrierite structures also when compared to wet impregnation (CZZ/FER WI) and physical mixing (CZZ/FER MIX) approaches.

In summary, based on TEM characterization, CZZ/FER samples obtained by co-precipitation show the most promising structure of the catalyst in terms of interdispersion of the different phases (especially for the 2:1 loading): these findings are in accordance with results obtained from the characterization of the catalytic performance, as discussed in the other sections.

CZZ/FER OX 2:1

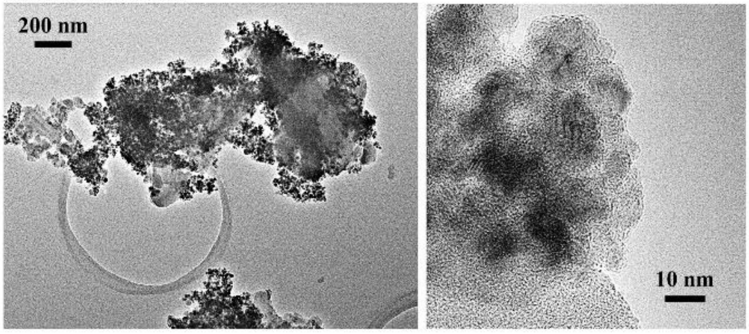

(a)

CZZ/FER OX 1:2

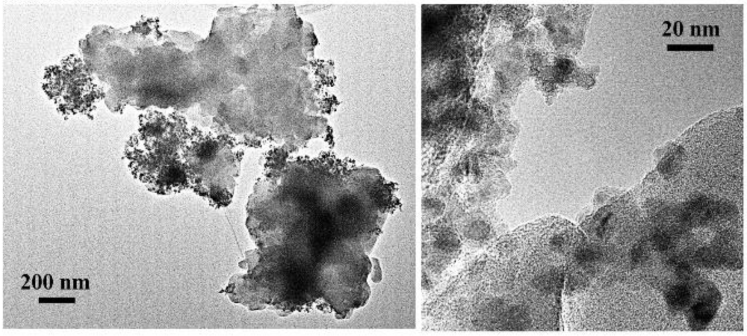

(b)

CZZ/FER WI 1:2

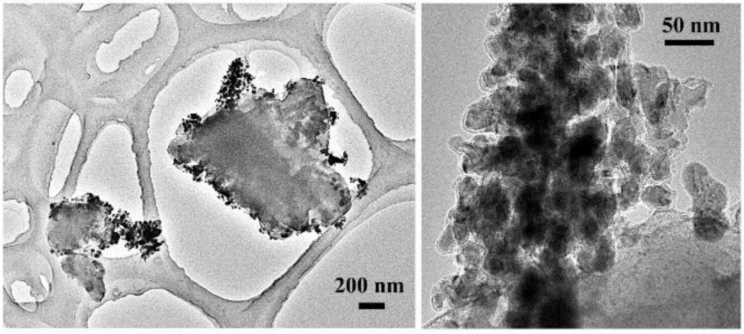

(c)

CZZ-FER MIX 1:2

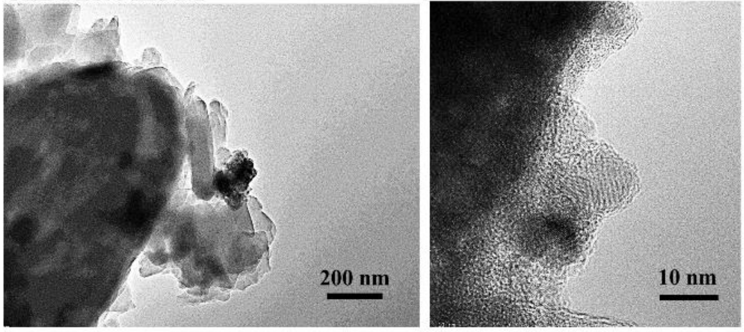

(d)

Figure 7.11. Bright-field TEM images of aged hybrid catalysts: (a) CZZ/FER OX 2:1, (b) CZZ/FER OX 1:2, (c) CZZ/FER WI 1:2 and (d) CZZ/FER MIX 1:2.

XPS measurements

XPS analyses was performed on calcined and aged samples in order to obtain information regarding the oxidation state of all the elements present in the rear hardly or never detected by XPS, due to a probable migration or coverage phenomenon, which have prevented their photoelectron signal to come out from the first 10 nm of the exposed surface. Survey scans were acquired to highlight the presence of all the chemical elements involved (not reported) and high-resolution spectra were selected in order to obtain further information regarding chemical shifts due to bonds formation between elements. To be much more precise, the relative atomic concentration (at. %) for all the calcined samples was calculated using high-resolution spectra and reported in Table 7.9.

Table 7.9. Relative atomic concentration (at. %), calculated from high-resolution spectra, for calcined and aged samples measured by XPS.

		Relative atomic concentration (%at)									
		$Cu_{2p3/2}$		$Zn_{2p3/2}$		Zr_{3d}	Si_{2p}		Al_{2s}	O_{1s}	
Samples		CuO	Cu_2O and Cu	ZnO	$Zn(OH)_2$	ZrO_2	SiO_2	Si_2O	Al_2O_3	Oxide	C-O bonds
Ferrierite	calcined	-	-	-	-	-	25.1	-	2.5	59.4	3.9
CuZnZr	calcined										
	aged										
CZZ/FER OX 1:2	calcined	4.9	1.2	3.4	0.9	2.0	15.5	-	-	52.3	7.6
	aged	1.1	3.0	1.8	0.8	1.4	7.3	6.9	-	40.2	11.4
CZZ/FER OX 2:1	calcined	6.6	1.5	5.6	0.7	3.2	8.0	-	-	41.8	12.8
	aged	2.3	2.7	2.4	1.1	1.9	4.6	5.9	-	36.2	14.5
CZZ/FER WI 1:2	calcined	4.8	1.0	4.2	0.8	5.5	8.1	1.1	-	42.3	8.7
	aged	2.0	3.2	2.7	0.3	3.6	5.6	3.0	-	35.1	13.3

The main goal of this analysis, according to literature [298] was the proof of the Cu reduction from (+2) to (0), since it is considered the main element which plays a fundamental role in this catalytic process. As reported in Figure 7.12, the Cu2p doublet has been acquired for all the samples together with a metal reference, which has been previously Ar+ sputtered to remove oxide surface layer. A clear feature due to Cu(+2) oxidation state is the presence of a shake-up satellite, located between Cu2p$_{3/2}$ and Cu2p$_{1/2}$ peaks (and another paired satellite at higher binding energy after Cu2p$_{1/2}$). This satellite peak, due to outgoing photoelectrons that interact with a valence electron and excite it to a higher-energy level, is not present in Cu(0) (see metallic Cu reference curve in Figure 7.12) and also in Cu(+1). An intensity reduction of this secondary signal is a clear evidence that the reduction process has been occurred [299]. More in details, as can be seen in Figure 7.12, a complete reduction was not achieved in all the aged samples and this result is in accordance with the XRD patterns (see Figure 7.4). Moreover, for the aforementioned samples, we can also account for a reduction in the $Cu2p_{3/2}$ peak FWHM and a shift towards lower binding energy, where the Cu(0) contribution is located (932.7 eV).

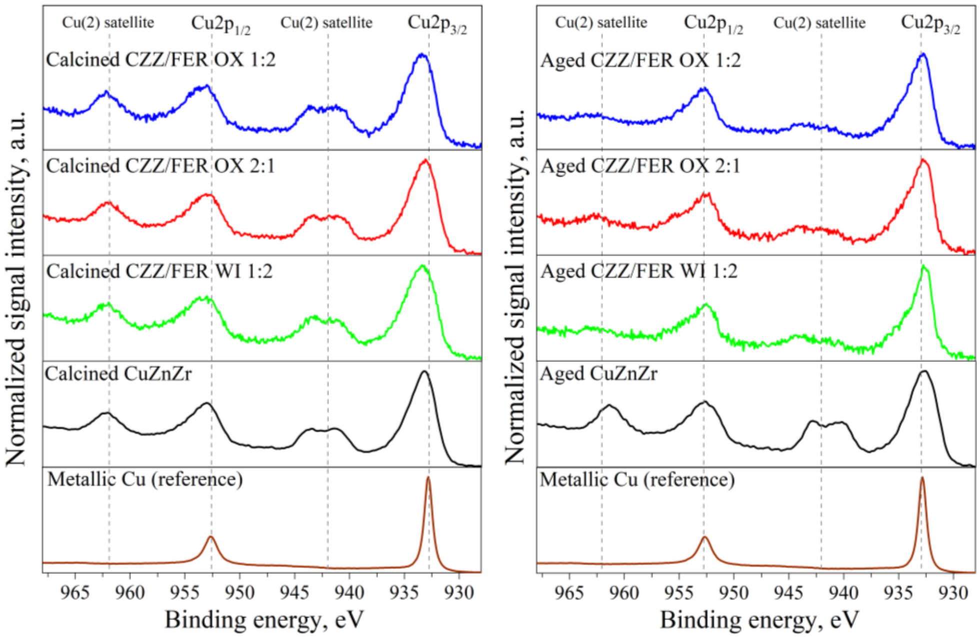

Figure 7.12. Cu2p high-resolution spectra for all XPS tested samples and metallic Cu reference for comparison. For clearness, each spectrum was normalized with respect to the maximum height of the $Cu2p_{3/2}$ peak.

Furthermore, as illustrated in Figure 7.13, Zn2p, Zr3d, Si2p and O1s HR spectra were also compared, in order to check for other clear changes in the oxidation state of the selected elements. All the Zn containing samples showed a main peak located at ~1022 eV, which is due to ZnO species [300]. Zr3d doublet also appear to be mostly identical for all the samples, and the peaks position has been ascribed to stoichiometric zirconia [301,302] without any contribution due to sub-oxide states. Also, Si2p peak has shown a main peak centred at 103.7 eV due to SiO_2 chemical shift. Nevertheless, in some of the samples, a small shift towards lower binding energy was registered. At 101.6 eV the SiO contribution could be recognized, while at 100.7 eV the Si_2O signal could affect the Si2p peak position shifting it at lower binding energy. In addition, it seems a feature of the CuZnZr-ferrierite based catalysts probably strictly linked to the synthesis environment [303]. For the O1s peak all samples show three main peaks (denoted as A, B, and C), which are attributed to the lattice oxygen (metal oxide), surface-adsorbed oxygen (organic compound), and surface hydroxyl species (metal carbonate or hydroxide), respectively [302]. It is not easy to separate the contribution due to each species, since there is an overlap between all of them. However, exhaust powders exhibited a decrease in the signal intensity of the O1s contribution located at ~529.5 eV (named peak A), which should correspond to the loss of lattice oxygen (oxides) caused by the Cu reduction from (+2) to (0) during the catalyst activation.

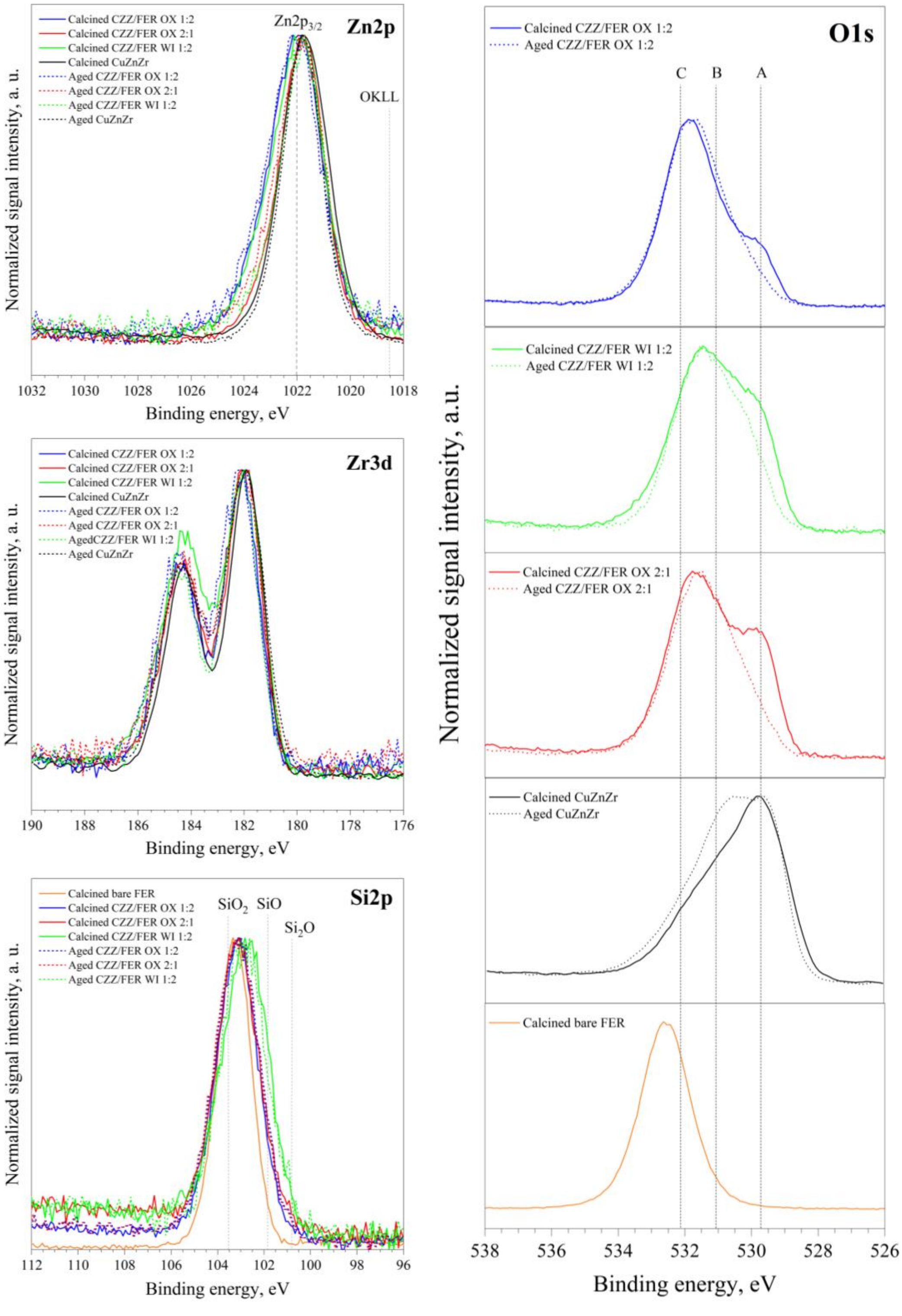

Figure 7.13. XPS HR spectra for Zn2p$_{3/2}$, Zr3d, Si2p and O1s peaks of CZZ/FER hybrid samples.

ICP measurements

The main goal of the ICP-MS characterization is to evaluate the actual elemental composition of the catalysts for ensuring that the theoretical composition was achieved during the synthesis. As summarized in Table 7.10, the actual composition of all the samples is coherent with both the nominal atomic concentration of all elements and the XPS results. It is worth noting that the bulk composition is similar to the nominal one; whereas, as expected, the XPS analyses have confirmed a greater amount of metals on the surface of the CuZnZr-based samples due to the synthesis techniques. In addition, oxygen was not measured, but it was calculated in order to have an idea of the effect of all the deviations of the other elements on the composition of the catalysts. Lastly, the CZZ/FER OX 2:1 catalyst exhibits a lower content of metals with respect to the nominal atomic composition.

Table 7.10. Relative atomic concentration (at. %), calculated from ICP measurements, for all the calcined samples.

Calcined catalysts		Relative atomic concentration (%at)					
		Cu	Zn	Al	Zr	Si	O(a)
Commercial FER	Nominal	-	-	3.1	-	30.8	66.2
	Actual	-	-	3.7 ± 0.3	-	30.3 ± 4.9	66.1 ± 4.7
Calcined CuZnZr	Nominal						
	Actual						
CZZ/FER OX 1:2	Nominal	5.7	2.9	2.5	1.0	24.6	63.4
	Actual	4.9 ± 0.3	2.9 ± 0.2	2.6 ± 0.1	0.83 ± 0.02	25.1 ± 0.5	63.6 ± 0.5
CZZ/FER OX 2:1	Nominal	14.3	7.1	1.5	2.4	15.4	53.9
	Actual	10.6 ± 0.4	5.8 ± 0.3	2.09 ± 0.01	1.55 ± 0.03	19.1 ± 0.4	60.8 ± 0.5
CZZ/FER WI 1:2	Nominal	5.7	2.9	2.5	1.0	24.6	63.4
	Actual	4.8 ± 0.2	2.5 ± 0.1	2.5 ± 0.1	0.71 ± 0.02	25.6 ± 0.3	63.8 ± 0.4
CZZ-FER MIX 1:2	Nominal	5.7	2.9	2.5	1.0	24.6	63.4
	Actual	4.5 ± 0.6	1.7 ± 0.2	3.1 ± 0.2	2.6 ± 0.1	24.0 ± 1.2	64.1 ± 1.2

(a) The oxygen atomic concentration was calculated considering CuO, ZnO, Al_2O_3, ZrO_2 and SiO_2.

7.3.2. Activity tests

For the purpose of investigating the performance of the catalysts, they were tested at different conditions in order to highlight different behaviours of the catalytic samples and to find relations between morphological, textural and compositional features and activity results.

CuZnZr and CuZnAl catalysts for MeOH synthesis

The performances of the CuZnAl and CuZnZr catalysts for methanol synthesis were compared by conducting activity tests at the variation of the temperature and of the space velocity. What stands out in Figure 7.14 is that the CuZnZr catalyst exhibited higher performance than the CuZnAl catalyst under all conditions. This could be ascribed to a smaller size of the copper crystallites in the CuZnZr catalyst and to a greater total pore volume of the material. The specific surface area of the two samples is similar; however, the lower reducibility of CuZnZr and the smaller crystallite size in the exhausted sample could indicate that the number of active sites is greater and that therefore the CO_2 conversion and the yield to methanol are greater than the reference sample. In particular, the CuZnZr catalyst approached to the thermodynamic equilibrium CO_2 conversion at 275 ° C while the CuZnAl catalyst approached to the thermodynamic equilibrium at 300 ° C and low space velocity, but the yield to methanol was drastically reduced. As mentioned in previous chapters, the operating temperature range is generally 240-260 ° C, where the CuZnZr catalyst exhibited a methanol yield approximately double with respect to the CuZnAl catalyst.

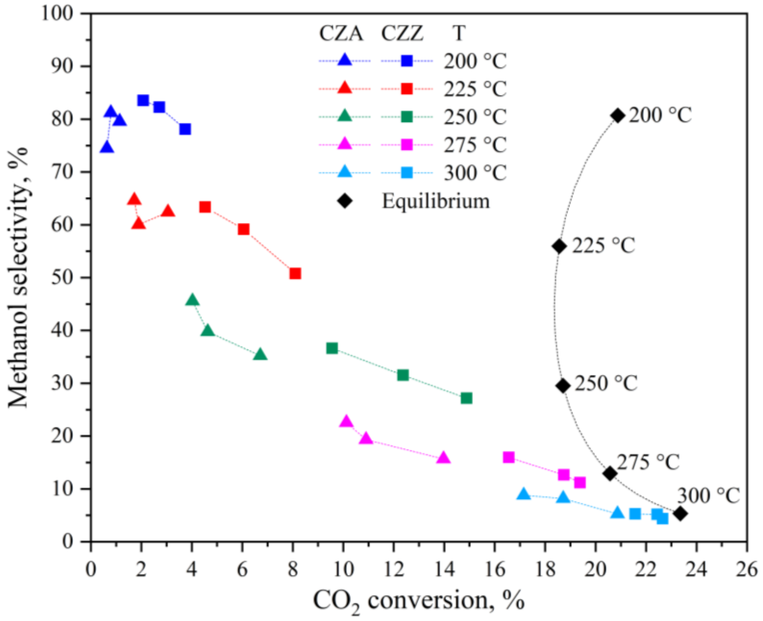

Figure 7.14. Conversion-selectivity map of CuZnZr and commercial CuZnAl catalysts. Reaction conditions: 2.5 MPa and inlet $H_2/CO_2/N_2$ molar ratios equal to 3:1:1, varying the reaction temperature (200 °C – 300 °C) and the space velocity (20 $Nl{\cdot}g_{cat}^{-1}{\cdot}h^{-1}$, 30 $Nl{\cdot}g_{cat}^{-1}{\cdot}h^{-1}$ and 40 $Nl{\cdot}g_{cat}^{-1}{\cdot}h^{-1}$).

CuZnZr ferrierite-based hybrid catalysts for DME and MeOH synthesis

In this section the results of the activity tests on the CuZnZr ferrierite-based catalysts are reported. These experiments were conducted at 2.5 MPa, inlet $H_2/CO_2/N_2$ molar ratio equal to 3:1:1, varying the reaction temperature in the range of 200 – 300 °C and the WHSV between 6.67 $Nl{\cdot}g_{cat}^{-1}{\cdot}h^{-1}$ and 20 $Nl{\cdot}g_{cat}^{-1}{\cdot}h^{-1}$.

With respect to the synthesized CuZnZr ferrierite-based catalysts with a CZZ/FER weight ratio equal to 0.5, as illustrated in Figure 7.15 (a, d and g), irrespective of the preparation method the activity of these catalysts follows the same trend increasing with the reaction temperature rises. Firstly, CZZ/FER OX 1:2 appears to be the less active synthesized catalyst at these operating conditions because its CO_2 conversion ranges between ~1 % at 200 °C and ~14 % at 300 °C. Moreover, its performances are very sensible to the WHSV, in fact, the CO_2 conversion at 275 °C doubles by tripling the residence time. On the contrary, the CZZ/FER WI 1:2 catalyst is less affected by a change in the WHSV, also attaining the same performances of the CZZ/FER OX 1:2 at high temperature. In our previous work, a completely different result was obtained at 5.0 MPa and 8.8 $Nl{\cdot}g_{cat}^{-1}{\cdot}h^{-1}$: in fact, CZZ/FER WI 1:2 revealed an extremely poor activity (from ~5 % at

200 °C to ~14 % at 260 °C) compared to CZZ/FER OX 1:2 (from ~9 % at 200 °C to ~21 % at 260 °C) [90]. Hence, a reduction in partial pressure of the reactants mainly affects the activity of the CZZ/FER OX 1:2. The CO_2 conversion of the CZZ-FER MIX 1:2 catalyst is extremely low at 200 °C; while it rapidly increases rising the temperature achieving ~18.5 % at 300 °C and 6.67 $Nl \cdot g_{cat}^{-1} \cdot h^{-1}$.

What stands out in Figure 7.15 are the different DME yields between CZZ-FER MIX 1:2 and the other two samples: in fact, CZZ/FER OX 1:2 and CZZ/FER WI 1:2 are less active than the other one, but their DME yield is extremely higher due to a lower activity in CO_2 hydrogenation to CO through RWGS. More in detail, the DME yield peaks at 275 °C in the case of 6.67 $Nl \cdot g_{cat}^{-1} \cdot h^{-1}$, reaching 2.1 % (26.7 $mg_{DME} \cdot g_{cat}^{-1} \cdot h^{-1}$), 2.06 % (26.4 $mg_{DME} \cdot g_{cat}^{-1} \cdot h^{-1}$) and 1.18 % (15.3 $mg_{DME} \cdot g_{cat}^{-1} \cdot h^{-1}$) for CZZ/FER OX 1:2, CZZ/FER WI 1:2 and CZZ-FER MIX 1:2, respectively. As expected, the DME yield decreases at higher WHSV, but the specific productivity of DME ($mg_{DME} \cdot g_{cat}^{-1} \cdot h^{-1}$) approximately doubles. Furthermore, as expected, the DME selectivity trend decreases as the reaction temperature rises, for instance at ~225 °C and 13.3 $Nl \cdot g_{cat}^{-1} \cdot h^{-1}$ it achieves 53 %, 47 % and 33 % for the CZZ/FER WI 1:2, CZZ/FER OX 1:2 and CZZ-FER MIX 1:2, respectively. Besides, it is worth noting that the DME selectivity does not change sensibly varying the residence time. As far as the CO yield is concerned, RWGS reaction starts to prevail at 250 °C since it is a thermodynamically unfavoured process at low temperatures. More specifically, CZZ-FER MIX 1:2 is the most selective towards CO, while CZZ/FER WI 1:2 exhibits the lowest CO selectivity in any experimental conditions. Lastly, MeOH is dehydrated to DME during the reaction; thus, MeOH yield is extremely low. However, it slightly increases as the temperature rises because the process approaches to the thermodynamic equilibrium and the DME yield rapidly decreases at 300 °C. In conclusion, CZZ/FER OX 1:2 and CZZ/FER WI 1:2 exhibited comparable performances at high residence time achieving a DME yield of ~2.1 % (26.7 $mg_{DME} \cdot g_{cat}^{-1} \cdot h^{-1}$). Notwithstanding, CZZ/FER WI 1:2 is less affected by an increase in WHSV resulting in a higher DME yield at 13.3 $Nl \cdot g_{cat}^{-1} \cdot h^{-1}$ compared to CZZ/FER OX 1:2. Whereas, CZZ-FER MIX 1:2 revealed a high activity in CO_2 hydrogenation and an extremely low MeOH and DME selectivity, which may be caused by the macroscopic segregation of CuZnZr and ferrierite within the catalytic particles during their preparation, as shown in FESEM images and EDS maps.

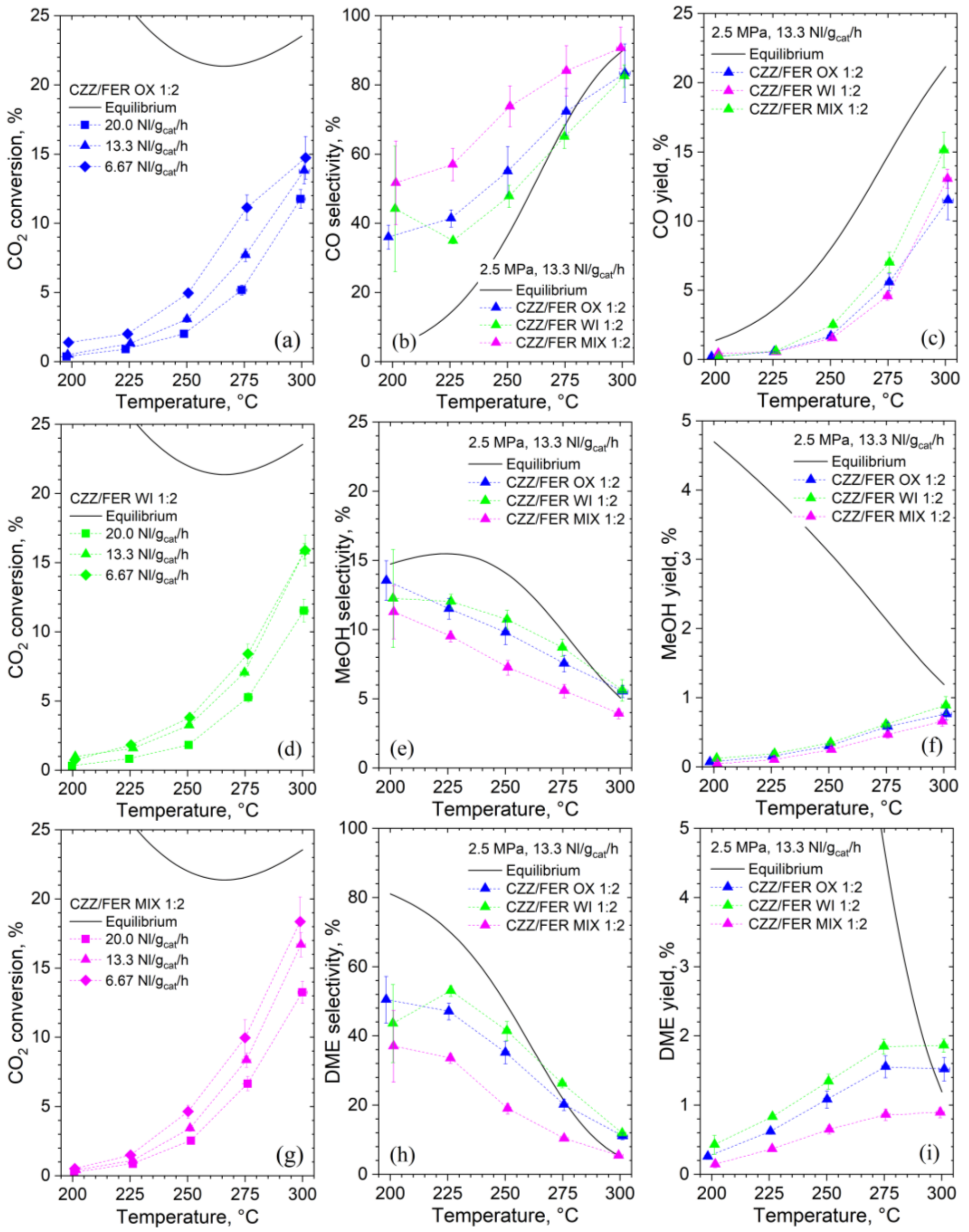

Figure 7.15. CO_2 conversion of CZZ/FER OX 1:2 (a), CZZ/FER WI 1:2 (d) and CZZ/FER MIX 1:2 (g). CO, MeOH and DME selectivities at 13.3 $Nl \cdot g_{cat}^{-1} \cdot h^{-1}$ (b, e and h) and CO, MeOH and DME yields at 13.3 $Nl \cdot g_{cat}^{-1} \cdot h^{-1}$ (c, f and i). Reaction conditions: 2.5 MPa, inlet $H_2/CO_2/N_2$ molar ratio equal to 3:1:1.

Focusing now on the experimental evidences of coprecipitated CZZ/FER OX 2:1, Figure 7.16 illustrates its activity and selectivity pattern. What is striking about the graphs is the completely different activity between the catalysts with an oxides/ferrierite weight ratio of 0.5 and 2. CZZ/FER OX 2:1 is indeed extremely more active in CO_2 hydrogenation due to a double amount of metals. More specifically, the CO_2 conversion of this sample is affected by the variation in WHSV at low temperatures, but it approaches to the thermodynamic equilibrium at 275 °C. This aspect could be explained by the reaction pathways; in fact, CO_2 is converted to CO and MeOH on the metallic sites of the CuZnZr, and then MeOH is dehydrated on the acidic sites of the ferrierite [90,100,304,305]. Furthermore, the overall specific surface area of CZZ/FER OX 2:1 is roughly halved with respect to the bare ferrierite because oxides are characterized by a lower specific surface area. For these reasons, a high amount of metals with a good dispersion increases the area for converting CO_2 to MeOH or CO, and at the same time, the exposed surface of the ferrierite is adequate to dehydrate MeOH to DME.

The DME yield of CZZ/FER OX 2:1 is extremely higher with respect to the catalysts examined previously, and it approaches to the equilibrium value at 275 °C. More in detail, coprecipitated CZZ/FER OX 2:1 exhibited a DME yield that peaks at 4.54 % (58.9 $mg_{DME} \cdot g_{cat}^{-1} \cdot h^{-1}$) at 250 °C and 6.67 $Nl \cdot g_{cat}^{-1} \cdot h^{-1}$ and at 3.45 % (138.3 $mg_{DME} \cdot g_{cat}^{-1} \cdot h^{-1}$) at 275 °C and 20.0 $Nl \cdot g_{cat}^{-1} \cdot h^{-1}$. The CO yield follows the thermodynamic profile because CO_2 is hydrogenated to CO via RWGS reaction on the surface of the metallic load. CZZ/FER OX 2:1 is sensible to a variation in WHSV and it does not reach the equilibrium at 13.3 $Nl \cdot g_{cat}^{-1} \cdot h^{-1}$. Finally, a high oxides/ferrierite ratio (equal to 2) favours the production of MeOH: in fact, the MeOH yield peaks at 275 °C roughly achieving ~1.4 %. In conclusion, CZZ/FER OX 2:1 have exhibited good performances than all the other samples with an oxides/ferrierite weight ratio equal to 0.5.

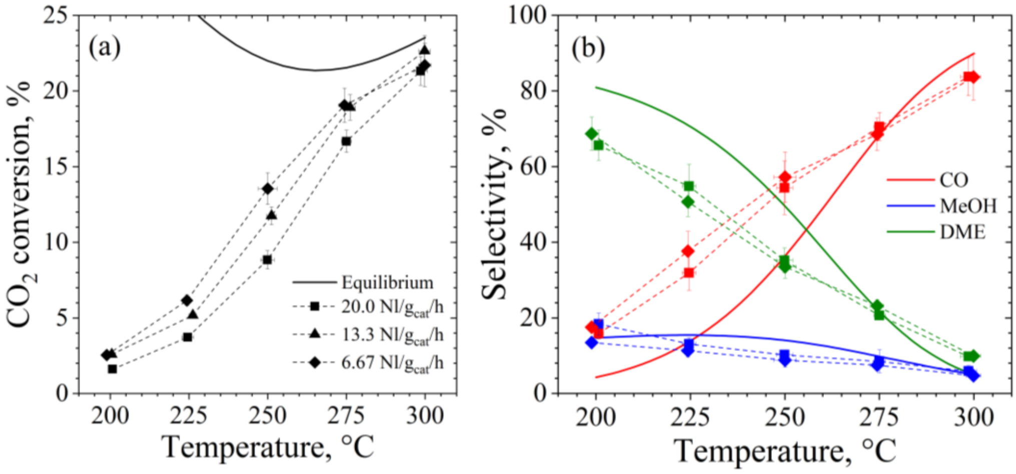

Figure 7.16. (a) CO_2 conversion and (b) selectivities of CZZ/FER OX 2:1. Reaction conditions: 2.5 MPa, inlet $H_2/CO_2/N_2$ molar ratio equal to 3:1:1.

The results obtained from the experimental tests of catalytic activity could be related to the textural and physicochemical properties of the catalytic materials. It is worth pointing out that the samples are not homogeneous: the behaviour and characteristics of the metal oxides and of the zeolite are completely different from each other; therefore, catalytic performances are the result of the set of distinctive characteristics of each material, which may produce similar or opposite effects. For these reasons, the decoupling of the causes could be often very challenging for identifying clear and unambiguous correlations.

As previously stated, the total specific surface area and the specific micropores area decrease as the metallic load in the catalyst increases, while the average pore diameter increases. However, as shown in Figure 7.17a, the specific CO_2 conversion rate decreases as the total specific surface area rises because it is hydrogenated to CO and methanol only on the CuZnZr metal catalyst, while the zeolite dehydrates the methanol to DME. The zeolite is required for producing

DME and to shift the equilibrium favouring the products, therefore the total specific production of methanol on the surface of the metal catalyst tends to be higher. More in detail, the production of DME is favoured by a high oxide/zeolite ratio because the specific surface area of the metal load is much smaller than that of the zeolite.

Furthermore, as shown in Figure 7.17b, the specific CO_2 conversion rate ($mmol_{CO2}/g_{cat}/h$) appears to exhibit a maximum for intermediate sizes of metallic Cu crystallites (i.e. ~17 nm). This behaviour was also observed considering the specific CO_2 conversion rate with respect to the metallic load ($mmol_{CO2}/g_{CuZnZr}/h$). On the one hand, the dispersion of the metals probably decreases as the size of the Cu crystallites increases and consequently also the number of active sites for the conversion of CO_2 to CO and methanol diminishes. On the other hand, a smaller size of the metallic Cu crystallites should favour the dispersion of the metals and the number of active sites, as reported in the literature[10]. However, the crystallites of CZZ/FER OX 1:2 catalyst could be aggregated to form nanoparticles of a size comparable to those of the catalysts CZZ/FER WI 1:2 and CZZ-FER MIX 1:2 and therefore the number of active sites is comparable. Furthermore, it is worth noting that the coprecipitated catalysts are much more sensitive to an increase in temperature. The activity also depends on the dispersion of ZnO, which is thermally more stable with smaller crystallite sizes (~8 nm) and is also active in the conversion of CO_2 [54].

Compared to the other characteristics of the catalysts, a higher average initial crystallite size of CuO causes a reduction of the α peak of the H_2-TPR profile and an increase in the area of the γ peak of the H_2-TPR because the bulk CuO of the crystallites and of nanoparticles is more difficult to reduce. Similarly, the H_2 consumption of the low temperature peak (i.e. $\alpha+\beta+\gamma$) decreases as the size of the ZnO crystallites increases since the crystallites are larger and the atomic H penetrates partially the ZnO structure. Consequently, the H_2 uptake of the δ and ε peaks of the H_2-TPR profile decreases. Furthermore, at the same time, the fraction of copper and zinc on the surface of the material measured by using XPS increases as the average size of the copper and ZnO crystallites increases. According to [54], a greater quantity of ZnO exposed on the surface of the catalyst seems to improve the methanol selectivity and therefore the CO selectivity decreases slightly. The increase in the exposed metal load is also confirmed by the increase in the atomic concentration of Zr as well as the atomic concentration of copper and zinc. This trend is accompanied by a decrease in the surface atomic concentration of Si_2O, while that of SiO_2 remains practically constant. These two aspects probably lead to a decrease in the total specific surface acidity of the samples and, consequently, an increase in CO selectivity and a decrease in methanol and DME selectivity.

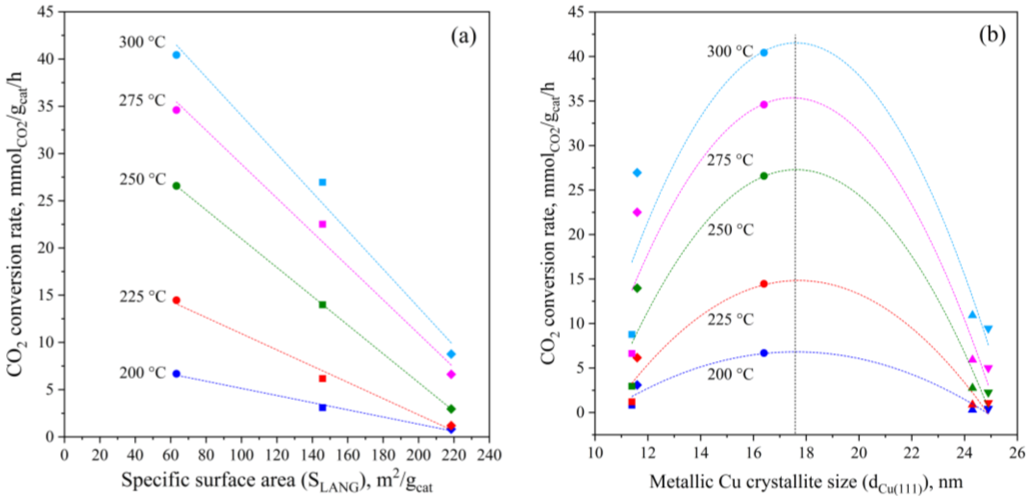

Figure 7.17. Relationships between the CO_2 conversion rate and (a) the specific surface area and (b) the average crystallite size of the metallic Cu of the aged samples. Reaction conditions: 2.5 MPa, inlet $H_2/CO_2/N_2$ molar ratio equal to 3:1:1 and WHSV equal to 20 $Nl/g_{CuZnZr}/h$. For the sake of clarity, symbols represent: ● CuZnZr, ♦ CZZ/FER OX 2:1, ■ CZZ/FER OX 1:2, ▲ CZZ/FER WI 1:2 and ▼ CZZ-FER MIX 1:2.

7.3.3. Stability tests

The stability of a catalyst is an important issue, which must be investigated. Therefore, in this section the results of the stability tests on the CuZnZr ferrierite-based hybrid catalysts are reported. They were carried out at 13.3 $Nl \cdot g_{cat}^{-1} \cdot h^{-1}$ and 275 °C for ~20 h in order to stress the catalysts in a comparable range of performances. As shown in Figure 7.18, the CO_2 conversion profile is comparable for the synthesized catalysts with an oxides/ferrierite weight ratio of 0.5, whereas CZZ/FER OX 2:1 exhibits a greater activity in CO_2 hydrogenation.

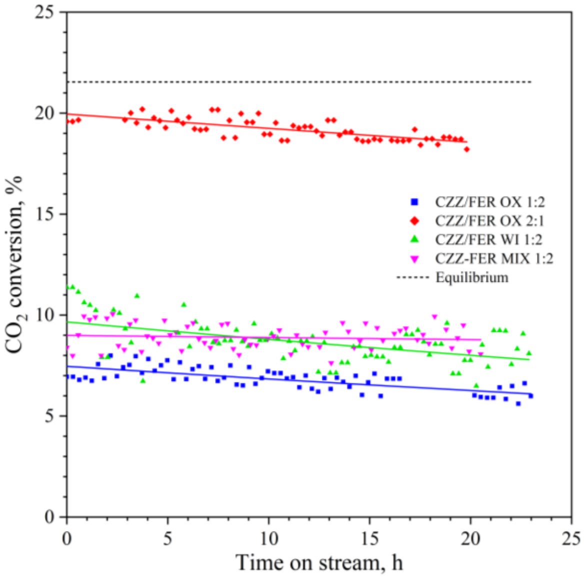

Figure 7.18. CO_2 conversion during stability tests (~20 h). Reaction conditions: 2.5 MPa, 275 °C, 13.3 $Nl \cdot g_{cat}^{-1} \cdot h^{-1}$ and inlet $H_2/CO_2/N_2$ molar ratio equal to 3:1:1. For the sake of clarity, solid lines represent the interpolated exponential function of the catalyst deactivation.

The DME yield of the CZZ/FER WI 1:2 (~2.2 %) is greater than the one of CZZ/FER OX 1:2 (~1.3 %) and CZZ/FER MIX 1:2 (~0.9 %), even if the CZZ-FER MIX 1:2 catalyst resulted to be the most active in CO_2 hydrogenation and the CZZ/FER OX 1:2 the less active. In fact, according to the activity tests, the DME selectivity of the CZZ/FER WI 1:2 is higher than the one of the other two synthesized catalysts (see Figure 7.19). As previously discussed, the low DME yield of the CZZ/FER MIX 1:2 could be linked to the macroscopic segregation of the oxides with respect to the ferrierite during the mixing of the two catalytic powders and, therefore, the mass transfer limitation between neighbouring sites could be the cause of the lower performance in DME production of this mixed catalyst [26]. Whereas, the difference between CZZ/FER OX 1:2 and CZZ/FER WI 1:2 may be linked to the distribution of the oxides on the surface of the bare ferrierite during the synthesis process. In fact, there is an inhomogeneous distribution of the oxides on the surface of the ferrierite, as highlighted by microscope investigations. In the present case, this feature seems to affect positively the CO_2 hydrogenation to DME

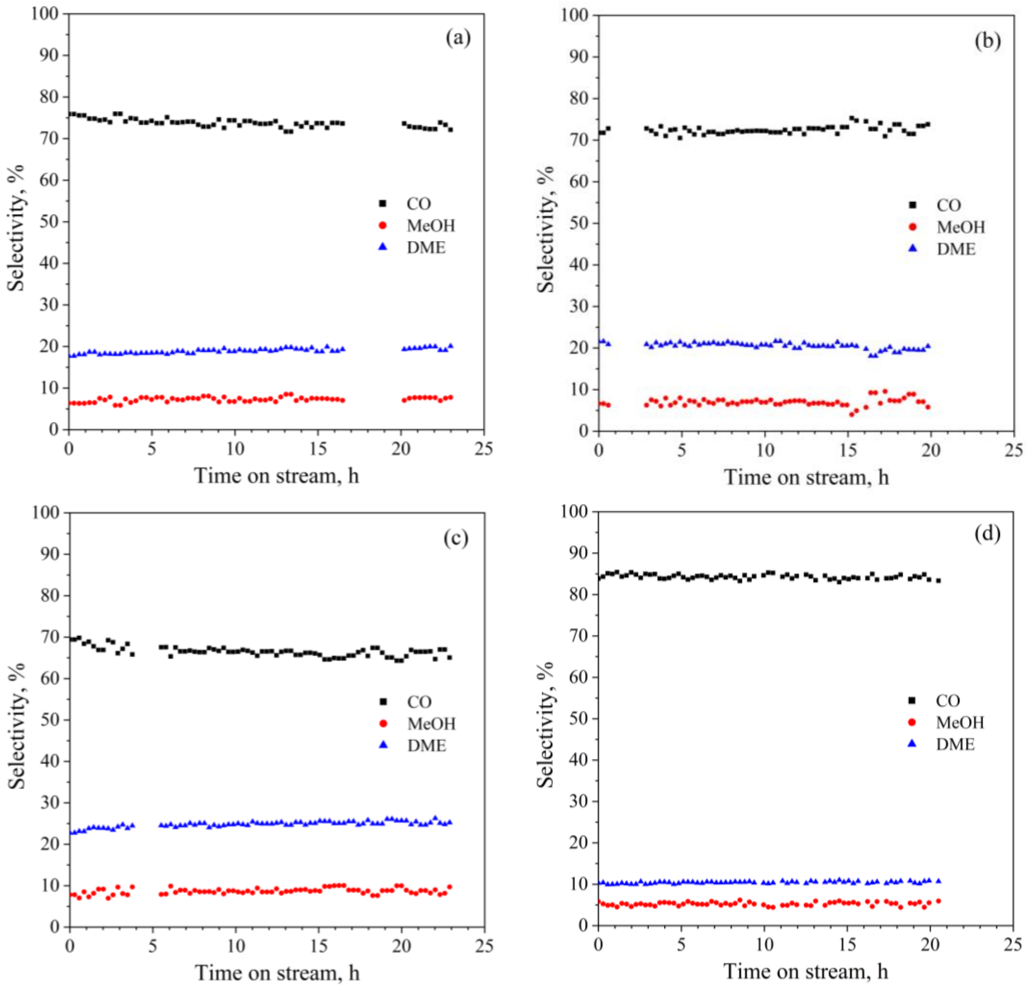

Figure 7.19. CO, methanol and DME selectivity profiles of the hybrid catalysts during the stability test: (a) CZZ/FER OX 1:2, (b) CZZ/FER OX 2:1, (c) CZZ/FER WI 1:2 and (d) CZZ-FER MIX 1:2.. Reaction conditions: 2.5 MPa, 275 °C, 13.3 $Nl \cdot g_{cat}^{-1} \cdot h^{-1}$ and inlet $H_2/CO_2/N_2$ molar ratio equal to 3:1:1.

The activity of the catalysts is related to the CO_2 conversion; therefore, the CO_2 conversion profile of each durability test could be fitted by using an exponential function according to equation (7.6) [26]. Equation (7.6) was linearised for obtaining a first-order deactivation rate (see equation (7.7)) and interpolating the experimental data. In equations (7.6) and (7.7), $\zeta_{CO_2}(t)$ represents the CO_2 conversion at time t (h), $\zeta_{CO_2,0}$ is the initial CO_2 conversion and k_d (h^{-1}) is the deactivation constant.

$$\zeta_{CO_2}(t) = \zeta_{CO_2,0} \cdot e^{-k_d \cdot t} \tag{7.6}$$

$$\ln\left[\zeta_{CO_2}(t)\right] = \ln\left(\zeta_{CO_2,0}\right) - k_d \cdot t \tag{7.7}$$

Table 7.11 summarises the deactivation parameters of the exponential deactivation function of all hybrid catalysts; more in detail, CZZ/FER WI 1:2 exhibited the highest loss in activity ($9.36 \cdot 10^{-3}$ h^{-1}), whereas, the physically mixed catalyst was the most stable ($1.17 \cdot 10^{-3}$ h^{-1}).

Table 7.11. Deactivation parameters of the CuZnZr ferrierite-based hybrid catalysts.

Catalyst	Deactivation constant (k_d)	Initial CO_2 conversion ($\zeta_{CO2,0}$)
CZZ/FER OX 1:2	$8.75 \cdot 10^{-3}$ h^{-1}	7.47 %
CZZ/FER OX 2:1	$3.63 \cdot 10^{-3}$ h^{-1}	19.96 %
CZZ/FER WI 1:2	$9.36 \cdot 10^{-3}$ h^{-1}	9.67 %
CZZ-FER MIX 1:2	$1.17 \cdot 10^{-3}$ h^{-1}	9.00 %

The loss in activity and the change in selectivity could be caused by several phenomena. According to the open literature, the water produced during the process could inhibit active sites of the catalyst and mainly affect the acidic sites of the zeolite [25], [26], [69]. The catalytic performances during a duration test are indeed sensible to the variation of the spatial velocity due to catalyst modifications [26]. As reported in Figure 7.19, the transitional behaviour of the selectivity profiles of CO, methanol and DME lasts ~3 h at 13.3 $Nl \cdot g_{cat}^{-1} \cdot h^{-1}$ as reported by Bonura et al. [26]; after the initial modifications, the selectivity profiles of each catalysts are roughly constant. More in detail, the initial loss in activity was ascribed to the sintering of the metallic load favoured by water adsorption and acidic sites availability [26]. More specifically, as illustrated in Figure 7.20, the deactivation rate increases as the acidity of the samples rises; in addition, the intimate contact between the metallic load and the zeolite seems to affect negatively the stability of the hybrid catalysts [26]. Furthermore, according to the literature, the intimate contact between oxides and the surface of the ferrierite in the synthesized hybrid catalysts could also cause a deactivation of both copper nanoparticles and acidic sites of the ferrierite by a progressive migration of ZnO [49], [53]. Some recent studies have reported a progressive deactivation of hybrid catalysts, which has been confirmed by a significant loss in CO_2 conversion, DME selectivity and an increase in CO selectivity during stability tests at high residence time [25], [26]. Notwithstanding, as illustrated in Figure 7.18**Errore. L'origine riferimento non è**

stata trovata. and Figure 7.19, the stability tests conducted on the examined catalysts highlighted a progressive loss in activity, but slightly changes were registered in the selectivity patterns.

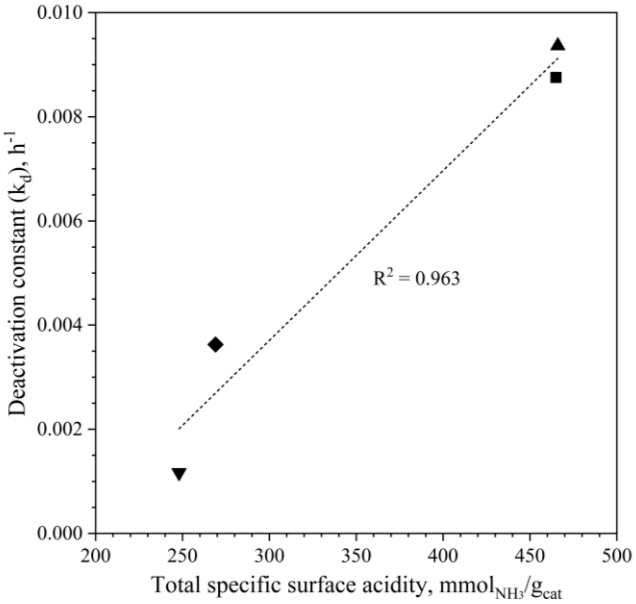

Figure 7.20. Relationship between the deactivation constant and the total specific surface acidity of the CuZnZr ferrierite-based hybrid catalysts. For the sake of clarity, symbols represent: ♦ CZZ/FER OX 2:1, ■ CZZ/FER OX 1:2, ▲ CZZ/FER WI 1:2 and ▼ CZZ-FER MIX 1:2

7.4. Conclusion

In this research work the behaviour of CuZnZr ferrierite-based hybrid catalysts was investigated. The CuZnZr-based samples were synthesized by means of gel-oxalate coprecipitation, wet impregnation and physical mixtures. Moreover, two different oxides/zeolite weight ratio were tested. The N2 physisorption and the porosimetry analyses highlighted a reduction in the specific surface area and a broadening of the mesopore size distribution, which could be mainly related to the sintering of the metallic load on the surface of the ferrierite. In addition, these phenomena may be enhanced by a blockage of the active sites caused by wetting. Furthermore, XRD analyses revealed a widening of the metallic crystallites, whereas Al and Zr are present in an amorphous phase. XRD, XPS and H2-TPR characterizations confirmed an incomplete reduction of the CuO at 350 °C. Morphological and textural analyses (FESEM, EDS and TEM) evidenced an inhomogeneous distribution of the metallic load on the surface of the zeolite, which affects the mass-transfer phenomena among neighbouring sites during the catalytic process.

Performances of the hybrid catalysts were investigated at 2.5 MPa and an inlet H2/CO2/N2 molar ratio equal to 3:1:1, varying both the reaction temperature (200 °C – 300 °C) and the WHSV (6.67 Nl·gcat-1·h-1 – 20 Nl·gcat-1·h-1). Regarding the activity tests, CZZ/FER OX 2:1 reached ~4.54 % (58.9 mgDME·gcat-1·h-1) at 250 °C and 6.67 Nl·gcat-1·h-1. Concerning the samples with an oxides/zeolite weight ratio of 0.5, the highest activity was obtained with the CZZ/FER WI 1:2 and the

CZZ/FER OX 1:2 hybrid catalysts reaching a DME yield of ~2.1 % (26.7 mgDME·gcat-1·h-1) at 275 °C and 6.67 Nl·gcat-1·h-1. Furthermore, their activity decreased as the WHSV increased and the CZZ/FER OX 1:2 seemed to be more sensible to a variation in the residence time. The CZZ/FER MIX 1:2 resulted the worst catalyst for CO2 hydrogenation to DME owing to the low selectivity towards DME, even if it exhibited a more stable CO2 conversion profile due to a lower intimate contact between metallic and acidic sites. Finally, stability tests showed a decrease in the CO2 conversion, which is probably related to a progressive sintering of the metallic load evidenced by a reduction in the specific surface area, a broadening of the mesopore size distribution and a widening of the crystallites. Further research should be carried out to establish the structural difference in the synthesized catalysts. Moreover, a kinetic and a deactivation model should be evaluated to model the behaviour of these hybrid catalysts.

Conclusion

The research work carried out in this thesis ranges from the development of catalysts for CO_2 hydrogenation to renewable fuels and value-added products up to the techno-economic and environmental assessments of PtF processes also considering the impacts on the electric grid. More in detail, the PtG process has been widely investigated in the literature and its TRL level is high; therefore, the coupling of a PtG plant with the intermittent electric production profile was examined in Chapter 2, providing a complete techno-economic assessment of the coupling between PtG systems and the intermittent electric production profile, in which both electrochemical and chemical storage were examined. Furthermore, the natural progression of this first work was presented in Chapter 3, and it is the assessment of the connection of this PtG model with the electric grid model that could provide further explanation on the coupling of the PtG technology with the electric grid.

The main result obtained analysing the coupling of the SOEC-based PtG plant with the intermittent RES-based electric profile is that electrolyser and the methanation unit could be decoupled by using a H_2 storage tank, which allows the reactors to work continuously even if the SOEC electrolyser is kept in hot standby configuration. Thus, the number of PtG plant stops could be reduced to improve and facilitate the management of the PtG plant. This fact was reflected on the LCOP, which exhibited a minimum at ~7 MW of PtG plant capacity. However, as explained in Chapter 3, PtG plant capacity greater than 2.5 – 3 MW could not solve the electrical problems generated by a high penetration of RES in the MV electric network. Therefore, the PtG plants must be placed in strategic nodes of the electric grid. Results seem to be promising because reductions of 70-100% of the reverse power flow were achieved. Furthermore, the installation of PtG systems reduced grid losses and no undervoltage problems were detected during the annual simulation. In conclusion, it can be stated that PtG systems can stabilize the network even for high RES penetrations; thus, rising the capacity of a network to counterbalance the intermittent RES power generation. The deployment of the plants has to be taken in account for both electric network and gas injection points of the NG distribution grid. Those promising results unlocks new perspectives for decarbonising the entire energy system.

The economic assessment presented in Chapter 2 showed that the LCOP varied from 60.2 €/MWh to 224.9 €/MWh (LHV basis), which means that in the future scenario (i.e. 2050) the PtG process could be economically competitive when compared to the current NG price. However, strong efforts must be made to reduce the economic impact of the electrolytic technology and therefore to reduce costs.

Furthermore, the overall efficiency was ~77% (LHV basis), and the number of plant shutdowns of the PtG plant is extremely high. The investigation of the long-term storage of the SNG revealed that the gas produced could be stored in the natural gas distribution grid and used for repowering the electricity network. However, the amount of SNG was not enough due to the low repowering efficiency. In fact, the overall power-to-power efficiency corresponds to 34.6%.

Concerning the comparison of thermocatalytic and electrocatalytic Power-to-Methanol technologies presented in Chapter 6, the techno-economic assessments suggested that the electrocatalytic process results to be economically advantageous over the thermocatalytic process at low scales (i.e. $< 10^4$ kg/h MeOH). Considering an effective allocation of the methanol productivity on a real market scenario and the assumption of zeroing of the net present value in 20 years, both the TC (i.e. TC-1) and EC (i.e. EC-6) processes would start to be economically competitive at methanol productivities greater than 19.1 kg/h and 3.3 kg/h, respectively. Moreover, if O_2 valorisation, a low price of the renewable electricity and a carbon tax are considered, the economic profitability will rise. There are still high challenges for the EC CO_2-to-methanol conversion technology to achieve a real industrial implementation, while the TC one is closer to this goal.

In conclusion, PtG technology seems to be more suitable for producing a product that could be distributed and stored in the large NG distribution grid coupling it to different electrolysis technologies. However, the current scenario seems to not be economically viable compared to the traditional natural gas. Conversely, the TC production of methanol seems to be economically feasible in the current scenario. This fact is strictly related to the H_2 consumption to produce the products. In fact, the capital and operative costs of the electrolyser are the most relevant cost items of the LCOP. Methanol has the advantage of being a liquid product with a higher volumetric energy density than methane and it is widely used on an industrial level. The latest CO_2 hydrogenation product presented in this thesis is DME, which has a more limited use than methanol, but is less toxic and dangerous. However, studying the synthesis of DME from CO_2 may be extremely useful for other processes involving the production of hydrocarbons from CO_2 because it could be used as a reaction intermediate in those processes.

Regarding the PtF plants for the production of methanol and DME via CO_2 hydrogenation, the development areas involve not only the techno-economic analysis, but also the development of innovative catalysts to improve the catalytic performance and the overall efficiency of the plants. Considering the development of mixed copper-ceria catalysts presented in Chapter 4, it is worth noting that WI catalysts have significantly lower performance than SCS and OX catalysts. More in detail, the Cu crystallites are coarser in the WI samples than in the SCS and OX samples. In addition, the activity (at 250 °C) of the catalysts decreases linearly as the crystallite size rises because of the lower dispersion of the active phase. The SCS and OX techniques produced much smaller crystallites, the interface areas increase creating a more intimate contact between the phases and a more marked synergistic effect which translates into an enhanced methanol yield. Among SCS and OX samples $Cu_{40}Ce_{60}$ samples exhibited the lowest methanol yield due to large Cu crystallite size and a lower intimate contact between Cu and CeO_2. Finally, the synergistic effect between Cu and CeO_2 enhance the catalytic performances of mixed CuCe catalysts; however, the performances of commercial CuZnAl catalyst are extremely higher at lower temperature. Therefore, the synergistic effect between Cu and Zn is extremely important. Hence, ternary catalysts such as CuZnCe might be further investigated.

Another important aspect that has been analysed in this thesis concerns the development of the methanol reactor model that was presented in Chapter 5. Three types of reactors (i.e. isothermal, adiabatic and refrigerated) were modelled and validated; in addition, a simplified model of the plant was developed. The simulation of the scheme was performed for estimating the start-up time of the plant. Furthermore, this simulation allowed the pseudo-temporal evolution of variables to be studied. Five different plant configurations were compared by defining key performance indicators and the configuration that exhibited the best performances consists of two refrigerated reactors in series. Sensitivity analyses ware performed varying the operating condition of the plant between 25% and 100% of the nominal productivity and the split fraction of the recirculated gases between the two reactors. However, the configuration with two refrigerated reactors did not show any critical issues in this regard. A natural progression of this work should be oriented towards the development of a heterogeneous model, that is more suitable for identifying hotspots within the reactor.

Lastly, concerning the direct CO_2 hydrogenation to dimethyl-ether, the behaviour of CuZnZr ferrierite-based hybrid catalysts was investigated. They were synthesized by using three different techniques (i.e. gel-oxalate coprecipitation, wet impregnation and physical mixtures). The N_2 physisorption and the porosimetry analyses highlighted a reduction in the specific surface area and a broadening of the mesopore size distribution, which could be mainly related to the sintering of the metallic load on the surface of the ferrierite. Furthermore, XRD analyses revealed a widening of the metallic crystallites. Besides, XRD, XPS and H_2-TPR characterizations confirmed an incomplete reduction of the CuO at 350 °C, which correspond to ~15 % mol for the CuZnAl catalyst and to ~5 % mol for the other samples. Morphological and textural analyses (FESEM, EDS and TEM) evidenced an inhomogeneous distribution of the metallic load on the surface of the zeolite, which affects the mass-transfer phenomena during the catalytic process.

CZZ/FER OX 2:1 sample exhibited the best performance reaching a DME yield of 4.54 % (58.9 $mg_{DME} \cdot g_{cat}^{-1} \cdot h^{-1}$); whereas, concerning the samples with an oxides/zeolite weight ratio of 0.5, a comparable activity was obtained with the CZZ/FER WI 1:2 and the CZZ/FER OX 1:2 reaching a DME yield of 2.1 % (26.7 $mg_{DME} \cdot g_{cat}^{-1} \cdot h^{-1}$) at 275 °C and 6.67 $Nl \cdot g_{cat}^{-1} \cdot h^{-1}$; in addition, their activity decreased as the WHSV increased. The CZZ-FER MIX 1:2 resulted the worst catalyst for CO_2 hydrogenation to DME owing to the lowest selectivity towards DME, even if it exhibited a high activity in CO_2 conversion. This fact could be caused by a macroscopic segregation of the CuZnZr with respect to the ferrierite within the particle. Lastly, stability tests showed a decrease in the CO_2 conversion, which is probably related to a progressive sintering of the metallic load evidenced by a reduction in the specific surface area, a broadening of the mesopore size distribution and a widening of the crystallites.

References

1. International Energy Agency (IEA) *Key World Energy Statistics*; 2017;
2. *Statistics : Key electricity trends 2016*; 2017;
3. Salomone, F.; Giglio, E.; Ferrero, D.; Santarelli, M.; Pirone, R.; Bensaid, S. Techno-economic modelling of a Power-to-Gas system based on SOEC electrolysis and CO2 methanation in a RES-based electric grid. *Chem. Eng. J.* **2019**, *377*, 120233, doi:10.1016/j.cej.2018.10.170.
4. Guzmán, H.; Salomone, F.; Batuecas, E.; Tommasi, T.; Russo, N.; Bensaid, S.; Hernández, S. How to make sustainable CO2 conversion to Methanol: Thermocatalytic versus electrocatalytic technology. *Chem. Eng. J.* **2020**, 127973, doi:10.1016/j.cej.2020.127973.
5. Mazza, A.; Salomone, F.; Arrigo, F.; Bensaid, S.; Bompard, E.; Chicco, G. Impact of Power-to-Gas on distribution systems with large renewable energy penetration. *Energy Convers. Manag. X* **2020**, *7*, 100053, doi:10.1016/j.ecmx.2020.100053.
6. Specht, M.; Baumgart, F.; Feigl, B.; Frick, V.; Stürmer, B.; Zuberbühler, U.; Sterner, M.; Waldstein, G. Storing bioenergy and renewable electricity in the natural gas grid. In Proceedings of the FVEE AEE Topics 2009; 2009; pp. 69–78.
7. Nikolaidis, P.; Poullikkas, A. A comparative overview of hydrogen production processes. *Renew. Sustain. Energy Rev.* **2017**, *67*, 597–611, doi:10.1016/j.rser.2016.09.044.
8. Giglio, E.; Lanzini, A.; Santarelli, M.; Leone, P. Synthetic natural gas via integrated high-temperature electrolysis and methanation: Part II—Economic Analysis. *J. Energy Storage* **2015**, *1*, 22–37, doi:10.1016/j.est.2015.04.002.
9. Schmidt, O.; Gambhir, A.; Staffell, I.; Hawkes, A.; Nelson, J.; Few, S. Future cost and performance of water electrolysis: An expert elicitation study. *Int. J. Hydrogen Energy* **2017**, *42*, 30470–30492, doi:10.1016/j.ijhydene.2017.10.045.
10. Laguna-Bercero, M.A. Recent advances in high temperature electrolysis using solid oxide fuel cells: A review. *J. Power Sources* **2012**, *203*, 4–16, doi:10.1016/j.jpowsour.2011.12.019.
11. Buttler, A.; Spliethoff, H. Current status of water electrolysis for energy storage, grid balancing and sector coupling via power-to-gas and power-to-liquids: A review. *Renew. Sustain. Energy Rev.* **2017**, *82*, 2440–2454, doi:10.1016/j.rser.2017.09.003.
12. Götz, M.; Lefebvre, J.; Mörs, F.; McDaniel Koch, A.; Graf, F.; Bajohr, S.; Reimert, R.; Kolb, T. Renewable Power-to-Gas: A technological and economic review. *Renew. Energy* **2016**, *85*, 1371–1390, doi:10.1016/j.renene.2015.07.066.
13. GAS, S.R. *Codice di rete*; 2016;
14. O'Shea, R.; Wall, D.M.; McDonagh, S.; Murphy, J.D. The potential of power to gas to provide green gas utilising existing CO2sources from industries, distilleries and wastewater treatment facilities. *Renew. Energy* **2017**, *114*, 1090–1100, doi:10.1016/j.renene.2017.07.097.
15. Aminu, M.D.; Ali Nabavi, S.; Rochelle, C.A.; Manovic, V. A review of

developments in carbon dioxide storage Carbon capture and storage Geologic CO 2 storage CO 2 storage reservoir CO 2 storage projects. *Appl. Energy* **2017**, *208*, 1389–1419, doi:10.1016/j.apenergy.2017.09.015.

16. Gahleitner, G. Hydrogen from renewable electricity: An international review of power-to-gas pilot plants for stationary applications. *Int. J. Hydrogen Energy* **2013**, *38*, 2039–2061, doi:10.1016/j.ijhydene.2012.12.010.
17. Ghaib, K.; Ben-Fares, F.-Z.Z. Power-to-Methane: A state-of-the-art review. *Renew. Sustain. Energy Rev.* **2018**, *81*, 433–446, doi:10.1016/j.rser.2017.08.004.
18. Schiebahn, S.; Grube, T.; Robinius, M.; Tietze, V.; Kumar, B.; Stolten, D. Power to gas: Technological overview, systems analysis and economic assessment for a case study in Germany. *Int. J. Hydrogen Energy* **2015**, *40*, 4285–4294, doi:10.1016/j.ijhydene.2015.01.123.
19. Bailera, M.; Lisbona, P.; Romeo, L.M.; Espatolero, S. Power to Gas projects review: Lab, pilot and demo plants for storing renewable energy and CO2. *Renew. Sustain. Energy Rev.* **2017**, *69*, 292–312, doi:10.1016/j.rser.2016.11.130.
20. Blanco, H.; Faaij, A. A review at the role of storage in energy systems with a focus on Power to Gas and long-term storage. *Renew. Sustain. Energy Rev.* **2018**, *81*, 1049–1086, doi:10.1016/j.rser.2017.07.062.
21. Rönsch, S.; Schneider, J.; Matthischke, S.; Schlüter, M.; Götz, M.; Lefebvre, J.; Prabhakaran, P.; Bajohr, S. Review on methanation - From fundamentals to current projects. *Fuel* **2016**, *166*, 276–296, doi:10.1016/j.fuel.2015.10.111.
22. Brynolf, S.; Taljegard, M.; Grahn, M.; Hansson, J. Electrofuels for the transport sector: A review of production costs. *Renew. Sustain. Energy Rev.* **2018**, *81*, 1887–1905, doi:10.1016/j.rser.2017.05.288.
23. Martinez Molina, M.; Kern, C.; Jess, A. Catalytic Hydrogenation of Carbon Dioxide to Methane in Wall-Cooled Fixed-Bed Reactors ‡. *Chem. Eng. Technol.* **2016**, *39*, 2404–2415, doi:10.1002/ceat.201500614.
24. Marocco, P.; Morosanu, E.A.; Giglio, E.; Ferrero, D.; Mebrahtu, C.; Lanzini, A.; Abate, S.; Bensaid, S.; Perathoner, S.; Santarelli, M.; et al. CO2 methanation over Ni/Al hydrotalcite-derived catalyst: Experimental characterization and kinetic study. *Fuel* **2018**, *225*, 230–242, doi:10.1016/j.fuel.2018.03.137.
25. Giglio, E.; Deorsola, F.A.; Gruber, M.; Harth, S.R.; Morosanu, E.A.; Trimis, D.; Bensaid, S.; Pirone, R. Power-to-Gas through High Temperature Electrolysis and Carbon Dioxide Methanation: Reactor Design and Process Modeling. *Ind. Eng. Chem. Res.* **2018**, *57*, 4007–4018, doi:10.1021/acs.iecr.8b00477.
26. Wang, W.; Gong, J. Methanation of carbon dioxide: An overview. *Front. Chem. Eng. China* **2011**, *5*, 2–10, doi:10.1007/s11705-010-0528-3.
27. Katoufa, M.; Giglio, E.; Katsourinis, D.; Vourliotakis, G.; Bensaid, S.; Deorsola, F.; Pirone, R.; Saracco, G.; Founti, M. CO 2 Methanation Under Atmospheric Pressure Conditions on a Ni catalyst : Experiments and Kinetic Modelling. In Proceedings of the 5th European PEFC & H2 Forum; Lucerne, 2015; pp. 1–10.
28. Abate, S.; Mebrahtu, C.; Giglio, E.; Deorsola, F.; Bensaid, S.; Perathoner, S.; Pirone, R.; Centi, G. Catalytic Performance of γ-Al 2 O 3 −ZrO 2 −TiO 2 −CeO 2 Composite Oxide Supported Ni-Based Catalysts for CO 2 Methanation., doi:10.1021/acs.iecr.6b00134.

29. Morosanu, E.A.; Salomone, F.; Pirone, R.; Bensaid, S.; Bensaid, and S. Insights on a Methanation Catalyst Aging Process: Aging Characterization and Kinetic Study. *Catalysts* **2020**, *10*, 283, doi:10.3390/catal10030283.
30. Robinius, M.; Raje, T.; Nykamp, S.; Rott, T.; Müller, M.; Grube, T.; Katzenbach, B.; Küppers, S.; Stolten, D. Power-to-Gas: Electrolyzers as an alternative to network expansion – An example from a distribution system operator. *Appl. Energy* **2018**, *210*, 182–197, doi:10.1016/J.APENERGY.2017.10.117.
31. Estermann, T.; Newborough, M.; Sterner, M. Power-to-gas systems for absorbing excess solar power in electricity distribution networks. *Int. J. Hydrogen Energy* **2016**, *41*, 13950–13959, doi:10.1016/j.ijhydene.2016.05.278.
32. Park, C.; Bigler, F.; Korba, P. Power-to-Gas Concept for Integration of Increased Photovoltaic Generation into the Distribution. *Energy Procedia* **2016**, *99*, 411–417, doi:10.1016/J.EGYPRO.2016.10.131.
33. Simonis, B.; Newborough, M. Sizing and operating power-to-gas systems to absorb excess renewable electricity. *Int. J. Hydrogen Energy* **2017**, *42*, 21635–21647, doi:10.1016/j.ijhydene.2017.07.121.
34. El-Taweel, N.A.; Khani, H.; Farag, H.E.Z. Voltage regulation in active power distribution systems integrated with natural gas grids using distributed electric and gas energy resources. *Int. J. Electr. Power Energy Syst.* **2019**, *106*, 561–571, doi:10.1016/J.IJEPES.2018.10.037.
35. Dalmau, A.R.; Perez, D.M.; Diaz de Cerio Mendaza, I.; Pillai, J.R. Decentralized voltage control coordination of on-load tap changer transformers, distributed generation units and flexible loads. In Proceedings of the 2015 IEEE Innovative Smart Grid Technologies - Asia (ISGT ASIA); IEEE, 2015; pp. 1–6.
36. de Cerio Mendaza, I.D.; Bak-Jensen, B.; Chen, Z. Alkaline electrolyzer and V2G system DIgSILENT models for demand response analysis in future distribution networks. In Proceedings of the 2013 IEEE Grenoble Conference; IEEE, 2013; pp. 1–8.
37. Diaz de Cerio Mendaza, I.; Bhattarai, B.P.; Kouzelis, K.; Pillai, J.R.; Bak-Jensen, B.; Jensen, A. Optimal sizing and placement of power-to-gas systems in future active distribution networks. In Proceedings of the 2015 IEEE Innovative Smart Grid Technologies - Asia (ISGT ASIA); IEEE, 2015; pp. 1–6.
38. Khani, H.; El-Taweel, N.; Farag, H.E.Z. Real-time optimal management of reverse power flow in integrated power and gas distribution grids under large renewable power penetration. *IET Gener. Transm. Distrib.* **2018**, *12*, 2325–2331, doi:10.1049/iet-gtd.2017.1513.
39. Khani, H.; El-Taweel, N.; Farag, H.E.Z. Power Congestion Management in Integrated Electricity and Gas Distribution Grids. *IEEE Syst. J.* **2019**, *13*, 1883–1894, doi:10.1109/JSYST.2018.2850882.
40. Khani, H.; El-Taweel, N.; Farag, H.E.Z. Power Loss Alleviation in Integrated Power and Natural Gas Distribution Grids. *IEEE Trans. Ind. Informatics* **2019**, *3203*, 1–1, doi:10.1109/tii.2019.2890824.
41. Project STORE&GO.
42. Álvarez, A.; Bansode, A.; Urakawa, A.; Bavykina, A. V.; Wezendonk, T.A.; Makkee, M.; Gascon, J.; Kapteijn, F. Challenges in the Greener Production of Formates/Formic Acid, Methanol, and DME by Heterogeneously Catalyzed CO 2 Hydrogenation Processes. *Chem. Rev.* **2017**, *117*, 9804–

9838, doi:10.1021/acs.chemrev.6b00816.

43. Catizzone, E.; Bonura, G.; Migliori, M.; Frusteri, F.; Giordano, G. CO2 Recycling to Dimethyl Ether: State-of-the-Art and Perspectives. *Molecules* **2017**, *23*, 31, doi:10.3390/molecules23010031.
44. Leonzio, G.; Foscolo, P.U. Analysis of a 2-D model of a packed bed reactor for methanol production by means of CO2 hydrogenation. *Int. J. Hydrogen Energy* **2020**, *45*, 10648–10663, doi:10.1016/j.ijhydene.2020.01.248.
45. Leonzio, G.; Zondervan, E.; Foscolo, P.U. Methanol production by CO2 hydrogenation: Analysis and simulation of reactor performance. *Int. J. Hydrogen Energy* **2019**, *44*, 7915–7933, doi:10.1016/j.ijhydene.2019.02.056.
46. Eggemann, L.; Escobar, N.; Peters, R.; Burauel, P.; Stolten, D. Life cycle assessment of a small-scale methanol production system: A power-to-fuel strategy for biogas plants. *J. Clean. Prod.* **2020**, *271*, 122476, doi:10.1016/j.jclepro.2020.122476.
47. Huang, C.; Chen, S.; Fei, X.; Liu, D.; Zhang, Y. Catalytic Hydrogenation of CO2 to Methanol: Study of Synergistic Effect on Adsorption Properties of CO2 and H2 in CuO/ZnO/ZrO2 System. *Catalysts* **2015**, *5*, 1846–1861, doi:10.3390/catal5041846.
48. Graciani, J.; Mudiyanselage, K.; Xu, F.; Baber, A.E.; Evans, J.; Senanayake, S.D.; Stacchiola, D.J.; Liu, P.; Hrbek, J.; Sanz, J.F.; et al. Highly active copper-ceria and copper-ceria-titania catalysts for methanol synthesis from CO2. *Science (80-.).* **2014**, *345*, 546–550, doi:10.1126/science.1253057.
49. PROGETTO - BIO-RAFFINERIA SATURNO Available online: https://saturnobioeconomia.it/progetto/ (accessed on Jan 5, 2021).
50. Kiss, A.A.; Pragt, J.J.; Vos, H.J.; Bargeman, G.; de Groot, M.T. Novel efficient process for methanol synthesis by CO 2 hydrogenation. *Chem. Eng. J.* **2016**, *284*, 260–269, doi:10.1016/j.cej.2015.08.101.
51. Graaf, G.H.; Stamhuis, E.J.; Beenackers, A.A.C.M. Kinetics of low-pressure methanol synthesis. *Chem. Eng. Sci.* **1988**, *43*, 3185–3195, doi:10.1016/0009-2509(88)85127-3.
52. Bozzano, G.; Manenti, F. Efficient methanol synthesis: Perspectives, technologies and optimization strategies. *Prog. Energy Combust. Sci.* **2016**, *56*, 71–105, doi:10.1016/j.pecs.2016.06.001.
53. Chen, W.-H.; Lin, B.-J.; Lee, H.-M.; Huang, M.-H. One-step synthesis of dimethyl ether from the gas mixture containing CO2 with high space velocity. *Appl. Energy* **2012**, *98*, 92–101, doi:10.1016/j.apenergy.2012.02.082.
54. Chen, H.-B.; Liao, D.-W.; Yu, L.-J.; Lin, Y.-J.; Yi, J.; Zhang, H.-B.; Tsai, K.-R. Influence of trivalent metal ions on the surface structure of a copper-based catalyst for methanol synthesis. *Appl. Surf. Sci.* **1999**, *147*, 85–93, doi:10.1016/S0169-4332(99)00081-1.
55. Hirano, M.; Akano, T.; Imai, T.; Kuroda, K. Methanol synthesis from carbon dioxide on CuO-ZnO-Al2O3. *Energy Convers. Manag.* **1995**, *36*, 585–588.
56. Liu, X.-M.; Lu, G.Q.; Yan, Z.-F.; Beltramini, J. Recent Advances in Catalysts for Methanol Synthesis via Hydrogenation of CO and CO 2. *Ind. Eng. Chem. Res.* **2003**, *42*, 6518–6530, doi:10.1021/ie020979s.
57. Wu, J.; Saito, M.; Takeuchi, M.; Watanabe, T. The stability of Cu/ZnO-based catalysts in methanol synthesis from a CO2-rich feed and from a CO-rich feed. *Appl. Catal. A Gen.* **2001**, *218*, 235–240, doi:10.1016/S0926-860X(01)00650-0.

58. Studt, F.; Sharafutdinov, I.; Abild-Pedersen, F.; Elkjær, C.F.; Hummelshøj, J.S.; Dahl, S.; Chorkendorff, I.; Nørskov, J.K. Discovery of a Ni-Ga catalyst for carbon dioxide reduction to methanol. *Nat. Chem.* **2014**, *6*, 320–324, doi:10.1038/nchem.1873.
59. Xiao, J.; Mao, D.; Guo, X.; Yu, J. Effect of TiO 2 , ZrO 2 , and TiO 2 -ZrO 2 on the performance of CuO-ZnO catalyst for CO 2 hydrogenation to methanol. *Appl. Surf. Sci.* **2015**, *338*, 146–153, doi:10.1016/j.apsusc.2015.02.122.
60. Olah, G.A.; Goeppert, A.; Prakash, G.K.S. Chemical Recycling of Carbon Dioxide to Methanol and Dimethyl Ether: From Greenhouse Gas to Renewable, Environmentally Carbon Neutral Fuels and Synthetic Hydrocarbons. *J. Org. Chem.* **2009**, *74*, 487–498, doi:10.1021/jo801260f.
61. Ausfelder, F.; Bazzanella, A.; VanBracki, H.; Wilde, R.; Beckmann, C.; Mills, R.; Rightor, E.; Tam, C.; Trudeau, N.; Botschek, P. Technology Roadmap Energy and GHG Reductions in the. **2013**, 1–60.
62. Alper, E.; Yuksel Orhan, O. CO2 utilization: Developments in conversion processes 2017, *3*, 109–126.
63. Zachopoulos, A.; Heracleous, E. Overcoming the equilibrium barriers of CO2 hydrogenation to methanol via water sorption: A thermodynamic analysis. *J. CO2 Util.* **2017**, *21*, 360–367, doi:10.1016/j.jcou.2017.06.007.
64. Tackett, B.M.; Gomez, E.; Chen, J.G. Net reduction of CO2 via its thermocatalytic and electrocatalytic transformation reactions in standard and hybrid processes. *Nat. Catal.* **2019**, *2*, 381–386, doi:10.1038/s41929-019-0266-y.
65. Pérez-Fortes, M.; Tzimas, E. *Techno-economic and environmental evaluation of CO2 utilisation for fuel production. Synthesis of methanol and formic acid*; 2016; ISBN 9789279591334.
66. Jarvis, S.M.; Samsatli, S. Technologies and infrastructures underpinning future CO2 value chains: A comprehensive review and comparative analysis. *Renew. Sustain. Energy Rev.* **2018**, *85*, 46–68, doi:10.1016/j.rser.2018.01.007.
67. Albo, J.; Alvarez-Guerra, M.; Castaño, P.; Irabien, A. Towards the electrochemical conversion of carbon dioxide into methanol. *Green Chem.* **2015**, *17*, 2304–2324, doi:10.1039/c4gc02453b.
68. Lv, J.J.; Jouny, M.; Luc, W.; Zhu, W.; Zhu, J.J.; Jiao, F. A Highly Porous Copper Electrocatalyst for Carbon Dioxide Reduction. *Adv. Mater.* **2018**, *30*, 1–8, doi:10.1002/adma.201803111.
69. Le, M.; Ren, M.; Zhang, Z.; Sprunger, P.T.; Kurtz, R.L.; Flake, J.C. Electrochemical Reduction of CO2 to CH3OH at Copper Oxide Surfaces. *J. Electrochem. Soc.* **2011**, *158*, E45, doi:10.1149/1.3561636.
70. Genovese, C.; Ampelli, C.; Perathoner, S.; Centi, G. Mechanism of C-C bond formation in the electrocatalytic reduction of CO2 to acetic acid. A challenging reaction to use renewable energy with chemistry. *Green Chem.* **2017**, *19*, 2406–2415, doi:10.1039/c6gc03422e.
71. Lu, L.; Sun, X.; Ma, J.; Yang, D.; Wu, H.; Zhang, B.; Zhang, J.; Han, B. Highly Efficient Electroreduction of CO2 to Methanol on Palladium–Copper Bimetallic Aerogels. *Angew. Chemie - Int. Ed.* **2018**, *57*, 14149–14153, doi:10.1002/anie.201808964.
72. Yuan, J.; Yang, M.P.; Hu, Q.L.; Li, S.M.; Wang, H.; Lu, J.X. Cu/TiO2 nanoparticles modified nitrogen-doped graphene as a highly efficient catalyst for the selective electroreduction of CO2 to different alcohols. *J.*

CO2 Util. **2018**, *24*, 334–340, doi:10.1016/j.jcou.2018.01.021.

73. Zhao, K.; Liu, Y.; Quan, X.; Chen, S.; Yu, H. CO2 Electroreduction at Low Overpotential on Oxide-Derived Cu/Carbons Fabricated from Metal Organic Framework. *ACS Appl. Mater. Interfaces* **2017**, *9*, 5302–5311, doi:10.1021/acsami.6b15402.
74. Albo, J.; Irabien, A. Cu2O-loaded gas diffusion electrodes for the continuous electrochemical reduction of CO2 to methanol. *J. Catal.* **2016**, *343*, 232–239, doi:10.1016/j.jcat.2015.11.014.
75. Marepally, B.C.; Ampelli, C.; Genovese, C.; Tavella, F.; Veyre, L.; Quadrelli, E.A.; Perathoner, S.; Centi, G. Role of small Cu nanoparticles in the behaviour of nanocarbon-based electrodes for the electrocatalytic reduction of CO2. *J. CO2 Util.* **2017**, *21*, 534–542, doi:10.1016/j.jcou.2017.08.008.
76. Vennekoetter, J.B.; Sengpiel, R.; Wessling, M. Beyond the catalyst: How electrode and reactor design determine the product spectrum during electrochemical CO2 reduction. *Chem. Eng. J.* **2019**, *364*, 89–101, doi:10.1016/j.cej.2019.01.045.
77. Pérez-Fortes, M.; Schöneberger, J.C.; Boulamanti, A.; Tzimas, E. Methanol synthesis using captured CO2 as raw material: Techno-economic and environmental assessment. *Appl. Energy* **2016**, *161*, 718–732, doi:10.1016/j.apenergy.2015.07.067.
78. Haitham Al-Kalbani, Jin Xuan, Susana García, H.W. Comparative energetic assessment of methanol production from CO2: Chemical versus electrochemical process Haitham. **1395**, 1–37.
79. Matzen, M.; Alhajji, M.; Demirel, Y. Technoeconomics and Sustainability of Renewable Methanol and Ammonia Productions Using Wind Power-based Hydrogen. *Adv. Chem. Eng.* **2015**, *5*.
80. CELBICON Project Available online: https://www.celbicon.org/ (accessed on Mar 28, 2020).
81. RECODE project.
82. OCEAN project.
83. Gutiérrez-Guerra, N.; Moreno-López, L.; Serrano-Ruiz, J.C.; Valverde, J.L.; de Lucas-Consuegra, A. Gas phase electrocatalytic conversion of CO2 to syn-fuels on Cu based catalysts-electrodes. *Appl. Catal. B Environ.* **2016**, *188*, 272–282, doi:10.1016/j.apcatb.2016.02.010.
84. S. Michailos, P. Sanderson, A. Villa Zaragoza, S. McCord, K. Armstrong, P. Styring, F. Mason, G. Stokes, E. Williams, A.Z. Methanol Worked Examples for the TEA and LCA Guidelines for CO2 Utilization.
85. Fang, X.; Men, Y.; Wu, F.; Zhao, Q.; Singh, R.; Xiao, P.; Du, T.; Webley, P.A. Improved methanol yield and selectivity from CO2 hydrogenation using a novel Cu-ZnO-ZrO2 catalyst supported on Mg-Al layered double hydroxide (LDH). *J. CO2 Util.* **2019**, *29*, 57–64, doi:10.1016/j.jcou.2018.11.006.
86. Hu, B.; Guild, C.; Suib, S.L. Erratum: Thermal, electrochemical, and photochemical conversion of CO 2 to fuels and value-added products (Journal of CO2 Utilization (2013) 18-27). *J. CO2 Util.* **2013**, *2*, 64, doi:10.1016/j.jcou.2013.07.006.
87. Mattia, D.; Jones, M.D.; O’Byrne, J.P.; Griffiths, O.G.; Owen, R.E.; Sackville, E.; McManus, M.; Plucinski, P. Towards Carbon-Neutral CO2 Conversion to Hydrocarbons. *ChemSusChem* **2015**, *8*, 4064–4072, doi:10.1002/cssc.201500739.

88. Bareiß, K.; de la Rua, C.; Möckl, M.; Hamacher, T. Life cycle assessment of hydrogen from proton exchange membrane water electrolysis in future energy systems. *Appl. Energy* **2019**, *237*, 862–872, doi:10.1016/j.apenergy.2019.01.001.
89. Artz, J.; Müller, T.E.; Thenert, K.; Kleinekorte, J.; Meys, R.; Sternberg, A.; Bardow, A.; Leitner, W. Sustainable Conversion of Carbon Dioxide: An Integrated Review of Catalysis and Life Cycle Assessment. *Chem. Rev.* **2018**, *118*, 434–504, doi:10.1021/acs.chemrev.7b00435.
90. Bonura, G.; Cannilla, C.; Frusteri, L.; Mezzapica, A.; Frusteri, F. DME production by CO2 hydrogenation: Key factors affecting the behaviour of CuZnZr/ferrierite catalysts. *Catal. Today* **2017**, *281*, 337–344, doi:10.1016/j.cattod.2016.05.057.
91. Azizi, Z.; Rezaeimanesh, M.; Tohidian, T.; Rahimpour, M.R. Dimethyl ether: A review of technologies and production challenges. *Chem. Eng. Process. Process Intensif.* **2014**, *82*, 150–172, doi:10.1016/j.cep.2014.06.007.
92. Saeidi, S.; Amin, N.A.S.; Rahimpour, M.R. Hydrogenation of CO2 to value-added products—A review and potential future developments. *J. CO2 Util.* **2014**, *5*, 66–81, doi:10.1016/j.jcou.2013.12.005.
93. Bonura, G.; Cordaro, M.; Cannilla, C.; Mezzapica, A.; Spadaro, L.; Arena, F.; Frusteri, F. Catalytic behaviour of a bifunctional system for the one step synthesis of DME by CO2 hydrogenation. *Catal. Today* **2014**, *228*, 51–57, doi:10.1016/j.cattod.2013.11.017.
94. Ali, K.A.; Abdullah, A.Z.; Mohamed, A.R. Recent development in catalytic technologies for methanol synthesis from renewable sources: A critical review. *Renew. Sustain. Energy Rev.* **2015**, *44*, 508–518, doi:10.1016/j.rser.2015.01.010.
95. Chen, W.-H.; Hsu, C.-L.; Wang, X.-D. Thermodynamic approach and comparison of two-step and single step DME (dimethyl ether) syntheses with carbon dioxide utilization. *Energy* **2016**, *109*, 326–340, doi:10.1016/j.energy.2016.04.097.
96. Jadhav, S.G.; Vaidya, P.D.; Bhanage, B.M.; Joshi, J.B. Catalytic carbon dioxide hydrogenation to methanol: A review of recent studies. *Chem. Eng. Res. Des.* **2014**, *92*, 2557–2567, doi:10.1016/j.cherd.2014.03.005.
97. Studt, F.; Behrens, M.; Kunkes, E.L.; Thomas, N.; Zander, S.; Tarasov, A.; Schumann, J.; Frei, E.; Varley, J.B.; Abild-Pedersen, F.; et al. The Mechanism of CO and CO 2 Hydrogenation to Methanol over Cu-Based Catalysts. *ChemCatChem* **2015**, *7*, 1105–1111, doi:10.1002/cctc.201500123.
98. Kunkes, E.L.; Studt, F.; Abild-Pedersen, F.; Schlögl, R.; Behrens, M. Hydrogenation of CO2 to methanol and CO on Cu/ZnO/Al2O3: Is there a common intermediate or not? *J. Catal.* **2015**, *328*, 43–48, doi:10.1016/j.jcat.2014.12.016.
99. Bahmani, M.; Vasheghani Farahani, B.; Sahebdelfar, S. Preparation of high performance nano-sized Cu/ZnO/Al2O3 methanol synthesis catalyst via aluminum hydrous oxide sol. *Appl. Catal. A Gen.* **2016**, *520*, 178–187, doi:10.1016/j.apcata.2016.04.018.
100. Frusteri, F.; Migliori, M.; Cannilla, C.; Frusteri, L.; Catizzone, E.; Aloise, A.; Giordano, G.; Bonura, G. Direct CO 2 -to-DME hydrogenation reaction: New evidences of a superior behaviour of FER-based hybrid systems to obtain high DME yield. *J. CO2 Util.* **2017**, *18*, 353–361,

doi:10.1016/j.jcou.2017.01.030.

101. Bonura, G.; Migliori, M.; Frusteri, L.; Cannilla, C.; Catizzone, E.; Giordano, G.; Frusteri, F. Acidity control of zeolite functionality on activity and stability of hybrid catalysts during DME production via CO2 hydrogenation. *J. CO2 Util.* **2018**, *24*, 398–406, doi:10.1016/j.jcou.2018.01.028.
102. García-Trenco, A.; Martínez, A. The influence of zeolite surface-aluminum species on the deactivation of CuZnAl/zeolite hybrid catalysts for the direct DME synthesis. *Catal. Today* **2014**, *227*, 144–153, doi:10.1016/j.cattod.2013.09.051.
103. Flores, J.H.; Pais da Silva, M.I. Acid properties of the hybrid catalyst CuO–ZnO or CuO–ZnO–Al2O3/H-ferrierite: An infrared study. *Colloids Surfaces A Physicochem. Eng. Asp.* **2008**, *322*, 113–123, doi:10.1016/j.colsurfa.2008.02.033.
104. Saravanan, K.; Ham, H.; Tsubaki, N.; Bae, J.W. Recent progress for direct synthesis of dimethyl ether from syngas on the heterogeneous bifunctional hybrid catalysts. *Appl. Catal. B Environ.* **2017**, *217*, 494–522, doi:10.1016/j.apcatb.2017.05.085.
105. Adelung, S.; Maier, S.; Dietrich, R. Impact of the reverse water-gas shift operating conditions on the Power-to-Liquid process efficiency. *Sustain. Energy Technol. Assessments* **2021**, *43*, 100897, doi:10.1016/j.seta.2020.100897.
106. Vidal, F.; Koponen, J.; Ruuskanen, V.; Bajamundi, C.; Kosonen, A.; Simell, P.; Ahola, J.; Frilund, C.; Elfving, J.; Reinikainen, M.; et al. Power-to-X technology using renewable electricity and carbon dioxide from ambient air : SOLETAIR proof-of-concept and improved process concept. *J. CO2 Util.* **2018**, *28*, 235–246, doi:10.1016/j.jcou.2018.09.026.
107. König, D.H.; Baucks, N.; Dietrich, R.U.; Wörner, A. Simulation and evaluation of a process concept for the generation of synthetic fuel from CO2 and H2. *Energy* **2015**, *91*, 833–841, doi:10.1016/j.energy.2015.08.099.
108. Wang, G.; Zeng, L.; Cao, J.; Liu, F.; Lin, Q.; Yi, Y.; Pan, H. Microporous and Mesoporous Materials Highly selective conversion of CO 2 to hydrocarbons over composite catalysts. *Microporous Mesoporous Mater.* **2019**, *284*, 133–140, doi:10.1016/j.micromeso.2019.04.023.
109. Ramirez, A.; Chowdhury, A.D.; Dokania, A.; Cnudde, P.; Caglayan, M.; Yarulina, I.; Abou-hamad, E.; Gevers, L.; Ould-chikh, S.; Wispelaere, K. De; et al. Effect of Zeolite Topology and Reactor Configuration on the Direct Conversion of CO 2 to Light Olefins and Aromatics. **2019**, doi:10.1021/acscatal.9b01466.
110. Visconti, C.G.; Martinelli, M.; Falbo, L.; Fratalocchi, L.; Lietti, L. CO 2 hydrogenation to hydrocarbons over Co and Fe-based Fischer-Tropsch catalysts. *Catal. Today* **2016**, *277*, 161–170, doi:10.1016/j.cattod.2016.04.010.
111. Panzone, C.; Philippe, R.; Chappaz, A.; Fongarland, P.; Bengaouer, A. Power-to-Liquid catalytic CO 2 valorization into fuels and chemicals : focus on the Fischer-Tropsch route. *J. CO2 Util.* **2020**, *38*, 314–347, doi:10.1016/j.jcou.2020.02.009.
112. Stöcker, M. Methanol-to-hydrocarbons: Catalytic materials and their behavior. *Microporous Mesoporous Mater.* **1999**, *29*, 3–48, doi:10.1016/S1387-1811(98)00319-9.
113. Wang, Y.; Chen, S.; Gao, Y.; Cao, Y.; Zhang, Q.; Chang, W. Enhanced Methanol to Olefin Catalysis by Physical Mixtures of SAPO- 34 Molecular

Sieve and MgO. **2017**, doi:10.1021/acscatal.7b01285.

114. Wei, J.; Yao, R.; Wen, Z.; Fang, C.; Guo, L.; Xu, H.; Ge, Q.; Sun, J. Directly converting CO 2 into a gasoline fuel. *Nat. Commun.* **2017**, *8*, 1–8, doi:10.1038/ncomms15174.
115. Mazza, A.; Bompard, E.; Chicco, G. Applications of power to gas technologies in emerging electrical systems. *Renew. Sustain. Energy Rev.* **2018**, *92*, 794–806.
116. Spiecker, S.; Weber, C. The future of the European electricity system and the impact of fluctuating renewable energy – A scenario analysis. *Energy Policy* **2013**, *65*, 185–197, doi:10.1016/j.enpol.2013.10.032.
117. Klaus, T.; Vollmer, C.; Werner, K.; Lehmann, H.; Müschen, K. *Energy target 2050: 100% renewable electricity supply*; Dessau-Roßlau, 2010;
118. Wang, J.; Zong, Y.; You, S.; Traeholt, C. A review of Danish integrated multi-energy system flexibility options for high wind power penetration. *Clean Energy* **2018**, *1*, 23–35, doi:10.1093/ce/zkx002.
119. McKenna, R.C.; Bchini, Q.; Weinand, J.M.; Michaelis, J.; König, S.; Köppel, W.; Fichtner, W. The future role of Power-to-Gas in the energy transition: Regional and local techno-economic analyses in Baden-Württemberg. *Appl. Energy* **2018**, *212*, 386–400, doi:10.1016/j.apenergy.2017.12.017.
120. Kopp, M.; Coleman, D.; Stiller, C.; Scheffer, K.; Aichinger, J.; Scheppat, B. Energiepark Mainz: Technical and economic analysis of the worldwide largest Power-to-Gas plant with PEM electrolysis. *Int. J. Hydrogen Energy* **2017**, *42*, 13311–13320, doi:10.1016/j.ijhydene.2016.12.145.
121. König, S.; Bchini, Q.; McKenna, R.; Köppel, W.; Bachseitz, M.; Entress, J.; Ryba, M.; Michaelis, J.; Roser, A.; Schakib-Ekbatan, K. Analysing the regional potential and social acceptance of power-to-gas in the context of decentralized co-generation in Baden-Württemberg. *J. Energy Storage* **2018**, *16*, 93–107, doi:10.1016/j.est.2017.12.011.
122. McDonagh, S.; O'Shea, R.; Wall, D.M.; Deane, J.P.; Murphy, J.D. Modelling of a power-to-gas system to predict the levelised cost of energy of an advanced renewable gaseous transport fuel. *Appl. Energy* **2018**, *215*, 444–456, doi:10.1016/j.apenergy.2018.02.019.
123. Colbertaldo, P.; Guandalini, G.; Campanari, S. Modelling the integrated power and transport energy system: The role of power-to-gas and hydrogen in long-term scenarios for Italy. *Energy* **2018**, *154*, 592–601, doi:10.1016/j.energy.2018.04.089.
124. Lorenzi, G.; Baptista, P. Promotion of renewable energy sources in the Portuguese transport sector: A scenario analysis. *J. Clean. Prod.* **2018**, *186*, 918–932, doi:10.1016/j.jclepro.2018.03.057.
125. Balan, O.M.; Buga, M.-R.; Brunot, A.; Badea, A.; Froelich, D. Technical and economic evaluation of Power-to-Gas in link with a 50MW wind park. *J. Energy Storage* **2016**, *8*, 111–118, doi:10.1016/j.est.2016.10.002.
126. Gutiérrez-Martín, F.; Rodríguez-Antón, L.M.M. Power-to-SNG technology for energy storage at large scales. *Int. J. Hydrogen Energy* **2016**, *41*, 19290–19303, doi:10.1016/j.ijhydene.2016.07.097.
127. Lisbona, P.; Frate, G.F.; Bailera, M.; Desideri, U. Power-to-Gas: Analysis of potential decarbonization of Spanish electrical system in long-term prospective. *Energy* **2018**, *159*, 656–668, doi:10.1016/j.energy.2018.06.115.
128. Ancona, M.A.; Antonioni, G.; Branchini, L.; De Pascale, A.; Melino, F.; Orlandini, V.; Antonucci, V.; Ferraro, M. Renewable Energy Storage System Based on a Power-to-Gas Conversion Process. *Energy Procedia* **2016**, *101*,

854–861, doi:10.1016/j.egypro.2016.11.108.

129. Ferrero, D.; Lanzini, A.; Santarelli, M.; Leone, P. A comparative assessment on hydrogen production from low- and high-temperature electrolysis. *Int. J. Hydrogen Energy* **2013**, *38*, 3523–3536, doi:10.1016/j.ijhydene.2013.01.065.
130. Lanzini, A.; Leone, P.; Asinari, P. Microstructural characterization of solid oxide fuel cell electrodes by image analysis technique. *J. Power Sources* **2009**, *194*, 408–422, doi:10.1016/j.jpowsour.2009.04.062.
131. Dalgaard, S.; Højgaard, S.; Bjerg, M.; Hauch, A.; Ebbesen, S.D.; Jensen, S.H.; Mogensen, M. Solid Oxide Electrolysis Cells: Microstructure and Degradation of the Ni/Yttria- Stabilized Zirconia Electrode Solid Oxide Electrolysis Cells: Microstructure and Degradation of the Ni/Yttria-Stabilized Zirconia Electrode. *J. Electrochem. Soc.* **2008**, *155*, doi:10.1149/1.2967331.
132. Muroyama, H.; Tsuda, Y.; Asakoshi, T.; Masitah, H.; Okanishi, T.; Matsui, T.; Eguchi, K. Carbon dioxide methanation over Ni catalysts supported on various metal oxides. *J. Catal.* **2016**, *343*, 178–184, doi:10.1016/j.jcat.2016.07.018.
133. Deutsche Energie-Agentur (dena) *Biogaspartner – Gemeinsam Einspeisen*; 2011;
134. NAWARO BioEnergie AG Gustrow BioEnergie Park Available online: http://www.nawaro.ag/en/company/guestrow-bioenergy-park/ (accessed on May 25, 2018).
135. Ha, S.; Gallagher, K.G. Estimating the system price of redox flow batteries for grid storage. *J. Power Sources* **2015**, *296*, 122–132, doi:10.1016/j.jpowsour.2015.07.004.
136. Joerissen, L.; Garche, J.; Fabjan, C.; Tomazic, G. Possible use of vanadium redox-flow batteries for energy storage in small grids and stand-alone photovoltaic systems. *J. Power Sources* **2004**, *127*, 98–104, doi:10.1016/j.jpowsour.2003.09.066.
137. European Environment Agency's home page — European Environment Agency Available online: https://www.eea.europa.eu/ (accessed on Mar 15, 2021).
138. ENTSO-E Transparency Platform Available online: https://transparency.entsoe.eu/dashboard/show (accessed on Mar 16, 2018).
139. Schefold, J.; Brisse, A. Long-term Steam Electrolysis with Solid Oxide Cells with up to 23 000 h Operation Steam Electrolysis with Solid Oxide Cells. **2017**, 9–12.
140. Petipas, F.; Brisse, A.; Bouallou, C. Model-based behaviour of a high temperature electrolyser system operated at various loads. *J. Power Sources* **2013**, *239*, 584–595, doi:10.1016/j.jpowsour.2013.03.027.
141. Newby, R.; Keairns, D. *Analysis of Natural Gas Fuel Cell Plant Configurations*; 2011;
142. Schwarze, K.; Posdziech, O.; Kroop, S.; Lapeña-Rey, N.; Mermelstein, J. Green Industrial Hydrogen via Reversible High-Temperature Electrolysis. *ECS Trans.* **2017**, *78*, 2943–2952, doi:10.1149/07801.2943ecst.
143. Singer, D.V. Reversible solid oxide cells for bidirectional energy conversion in spot electricity and fuel markets, Columbia University, 2017.
144. *STEELFLEX ® Isolamento per alte temperature con pannelli in microporoso*;
145. San Gvozdenac, D.; Gvozdenac, B.; Sevi C, U.; Menke, C.; Uro Sevi C C,

D.; Bangviwat, A. High efficiency cogeneration: CHP and non-CHP energy. *Energy* **2017**, *135*, 269–278, doi:10.1016/j.energy.2017.06.143.

146. Sinnott, R.K. *Coulson & Richardson's Chemical Engineering Design*; 4th ed.; Oxford, 2005; Vol. 6; ISBN 008049255X.
147. Fan, F.Y.; Woodford, W.H.; Li, Z.; Baram, N.; Smith, K.C.; Helal, A.; McKinley, G.H.; Carter, W.C.; Chiang, Y.M. Polysulfide flow batteries enabled by percolating nanoscale conductor networks. *Nano Lett.* **2014**, *14*, 2210–2218, doi:10.1021/nl500740t.
148. Perry, R.H.; Green, D.W.; Maloney, J.O. *Perry's Chemical Engineers' Handbook 7th edition*; Perry, R.H., Green, D.W., Maloney, J.O., Eds.; 7th ed.; The McGraw-Hill Companies, 1999; ISBN 0070498415.
149. Becker, W.L.; Braun, R.J.; Penev, M.; Melaina, M. Production of Fischer–Tropsch liquid fuels from high temperature solid oxide co-electrolysis units. *Energy* **2012**, *47*, 99–115, doi:10.1016/J.ENERGY.2012.08.047.
150. Richard Turton, Richard C. Bailie, Wallace B. Whiting, J.A.S. *Analysis, Synthesis and Design of Chemical Processes*; 3rd ed.; Pearson Education International, 2009; ISBN 9788578110796.
151. ECB euro reference exchange rate: US dollar (USD) Available online: https://www.ecb.europa.eu/stats/policy_and_exchange_rates/euro_reference_exchange_rates/html/eurofxref-graph-usd.en.html (accessed on May 28, 2018).
152. Data about the energy system | Energinet Available online: https://en.energinet.dk/Electricity/Energy-data (accessed on May 30, 2018).
153. Ulrich, G.D.; Vasudevan, P.T. Economic Analysis. In *Chemical Engineering Process Design and Economics. A Practical Guide*; Process Publishing: Durham, 2004; pp. 324–483.
154. The Chemical Engineering Plant Cost Index - Chemical Engineering Available online: http://www.chemengonline.com/pci-home (accessed on Feb 24, 2020).
155. Zhang, M.; Moore, M.; Watson, J.S.; Zawodzinski, T.A.; Counce, R.M. Capital Cost Sensitivity Analysis of an All-Vanadium Redox-Flow Battery. *J. Electrochem. Soc.* **2012**, *159*, A1183–A1188, doi:10.1149/2.041208jes.
156. Mazza, A.; Cavana, M.; Mercado Medina, E.L.; Chicco, G.; Leone, P. Creation of Representative Gas Distribution Networks for Multi-vector Energy System Studies. **2019**, 1–6, doi:10.1109/eeeic.2019.8783701.
157. Yang, Z.; Gao, C.; Zhao, M. Coordination of integrated natural gas and electrical systems in day-ahead scheduling considering a novel flexible energy-use mechanism. *Energy Convers. Manag.* **2019**, *196*, 117–126, doi:10.1016/j.enconman.2019.05.109.
158. Samavati, M.; Santarelli, M.; Martin, A.; Nemanova, V. Thermodynamic and economy analysis of solid oxide electrolyser system for syngas production. *Energy* **2017**, *122*, 37–49, doi:10.1016/j.energy.2017.01.067.
159. Ulleberg, Ø.; Nakken, T.; Eté, A. The wind/hydrogen demonstration system at Utsira in Norway: Evaluation of system performance using operational data and updated hydrogen energy system modeling tools. *Int. J. Hydrogen Energy* **2010**, *35*, 1841–1852, doi:10.1016/j.ijhydene.2009.10.077.
160. Morosanu, E.A.; Saldivia, A.; Antonini, M.; Bensaid, S. Process Modeling of an Innovative Power to LNG Demonstration Plant. *Energy & Fuels* **2018**, *32*, 8868–8879, doi:10.1021/acs.energyfuels.8b01078.
161. Seborg, D.E.; Edgar, T.F.; Mellichamp, D.A. *Process Dynamics and Control*; 2nd editio.; John Wiley & Sons, 2003;

162. Ogunnaike, B.A.; Ray, W.H. *Process Dynamics, Modeling and Control*; Oxford University Press, 1994; ISBN 0195091191.

163. Sundaresan, K.R.; Krishnaswamy, P.R. Estimation of Time Delay Time Constant Parameters in Time, Frequency, and Laplace Domains. *Can. J. Chem. Eng.* **1978**, *56*, 257–262, doi:http://dx.doi.org/10.1002/cjce.5450560215.

164. Jeckins, N.; Ekanayake, J.B.; Strbac, G. *Distributed Generation*; IER Renewable Energy Series: London, 2010;

165. Enel-Energia Enel Energia a tutto storage.

166. Fink, L.H.; Carlsen, K. Operating Under Stress and Strain. *IEEE Spectr.* **1978**, *15*, 48–53, doi:10.1109/MSPEC.1978.6369445.

167. Mazza, A.; Carpaneto, E.; Chicco, G.; Ciocia, A. Creation of Network Case Studies with High Penetration of Distributed Energy Resources. In Proceedings of the Proceedings - 2018 53rd International Universities Power Engineering Conference, UPEC 2018; IEEE, 2018.

168. Carpaneto, E.; Chicco, G.; Sumaili Akilimali, J. Characterization of the loss allocation techniques for radial systems with distributed generation. *Electr. Power Syst. Res.* **2008**, doi:10.1016/j.epsr.2008.01.001.

169. Mazza, A.; Chicco, G. Losses Allocated to the Nodes of a Radial Distribution System with Distributed Energy Resources — A Simple and Effective Indicator.; IEEE, 2019; pp. 1–6.

170. JRC *Distribution System Operators Observatory 2018*; 2018;

171. Bompard, E.; Chicco, G.; Mazza, A.; Bensaid, S. *Deliverable 6.4 Report on the model of the power system with PtG*; 2019;

172. Bracale, A.; Caldon, R.; Celli, G.; Coppo, M.; Dal Canto, D.; Langella, R.; Petretto, G.; Pilo, F.; Pisano, G.; Proto, D.; et al. Analysis of the Italian distribution system evolution through reference networks. In Proceedings of the IEEE PES Innovative Smart Grid Technologies Conference Europe; IEEE, 2012; pp. 1–8.

173. Shirmoharmnadi, D.; Hong, H.W.; Semlyen, A.; Luo, G.X. A compensation-based power flow method for weakly meshed distribution and transmission networks. *IEEE Trans. Power Syst.* **1988**, *3*, 753–762.

174. van Laarhoven, P.J.M.; Aarts, E.H.L. *Simulated Annealing: Theory and Applications*; D.Reidel Publ. Company: Dordrecht, Holland, 1987;

175. Piumetti, M.; Bensaid, S.; Andana, T.; Russo, N.; Pirone, R.; Fino, D. Cerium-copper oxides prepared by solution combustion synthesis for total oxidation reactions: From powder catalysts to structured reactors. *Appl. Catal. B Environ.* **2017**, *205*, 455–468, doi:10.1016/j.apcatb.2016.12.054.

176. Palmisano, P.; Russo, N.; Fino, P.; Fino, D.; Badini, C. High catalytic activity of SCS-synthesized ceria towards diesel soot combustion. *Appl. Catal. B Environ.* **2006**, *69*, 85–92, doi:10.1016/j.apcatb.2006.06.002.

177. Zno, /; Zno, C./; Al, /; Sun, Q.; Zhang, Y.-L.; Chen, H.-Y.; Deng, J.-F.; Wu, D.; Chen, S.-Y. *A Novel Process for the Preparation of Cu/ZnO and Cu/ZnO/Al2O3 Ultrafine Catalyst: Structure, Surface Properties, and Activity for Methanol Synthesis from CO2 + H2*; 1997; Vol. 167;.

178. Bonura, G.; Cordaro, M.; Cannilla, C.; Arena, F.; Frusteri, F. The changing nature of the active site of Cu-Zn-Zr catalysts for the CO2 hydrogenation reaction to methanol. *Appl. Catal. B Environ.* **2014**, *152–153*, 152–161, doi:10.1016/j.apcatb.2014.01.035.

179. Brunauer, S.; Emmett, P.H.; Teller, E. Adsorption of Gases in Multimolecular Layers. *J. Am. Chem. Soc.* **1938**, *60*, 309–319,

doi:10.1021/ja01269a023.

180. de Boer, J.H.; Lippens, B.C.; Linsen, B.G.; Broekhoff, J.C.P.; van den Heuvel, A.; Osinga, T.J. Thet-curve of multimolecular N2-adsorption. *J. Colloid Interface Sci.* **1966**, *21*, 405–414, doi:10.1016/0095-8522(66)90006-7.

181. Buttersack, C.; Möllmer, J.; Hofmann, J.; Gläser, R. Determination of micropore volume and external surface of zeolites. *Microporous Mesoporous Mater.* **2016**, *236*, 63–70, doi:10.1016/j.micromeso.2016.08.018.

182. Harkins, W.D.; Jura, G. Surfaces of Solids. XIII. A Vapor Adsorption of a Monolayer Area, and the Areas Occupied be Nitrogen and other Molecules on the Surfase of a Solid. *J. Am. Chem. Soc.* **1944**, *66*, 1366–1373.

183. Storck, S.; Bretinger, H.; Maier, W.F. Characterization of micro- and mesoporous solids by physisorption methods and pore-size analysis. *Appl. Catal. A Gen.* **1998**, *174*, 137–146.

184. Condon, J.B. *Surface Area and Porosity Determinations by Physisorption Measurements and Theory*; 1st editio.; Elsevier, 2006; ISBN 9780444519641.

185. Patterson, A.L. The Scherrer Formula for X-Ray Particle Size Determination. *Phys. Rev.* **1939**, *56*, 978–982, doi:10.1103/PhysRev.56.978.

186. Beaudoux, X.; Virot, M.; Chave, T.; Durand, G.; Leturcq, G.; Nikitenko, S.I. Vitamin C boosts ceria-based catalyst recycling. *Green Chem.* **2016**, *18*, 3656–3668, doi:10.1039/C6GC00434B.

187. Zabilskiy, M.; Djinović, P.; Erjavec, B.; Dražić, G.; Pintar, A. Small CuO clusters on CeO2 nanospheres as active species for catalytic N2O decomposition. *Appl. Catal. B Environ.* **2015**, *163*, 113–122, doi:10.1016/j.apcatb.2014.07.057.

188. Tschöpe, A.; Trudeau, M.L.; Ying, J.Y. Redox Properties of Nanocrystalline Cu-Doped Cerium Oxide Studied by Isothermal Gravimetric Analysis and X-ray Photoelectron Spectroscopy. *J. Phys. Chem. B* **1999**, *103*, 8858–8863, doi:10.1021/jp9915681.

189. Caputo, T.; Lisi, L.; Pirone, R.; Russo, G. On the role of redox properties of CuO/CeO2 catalysts in the preferential oxidation of CO in H2-rich gases. *Appl. Catal. A Gen.* **2008**, *348*, 42–53, doi:10.1016/j.apcata.2008.06.025.

190. Guo, X.; Mao, D.; Wang, S.; Wu, G.; Lu, G. Combustion synthesis of CuO-ZnO-ZrO2 catalysts for the hydrogenation of carbon dioxide to methanol. *Catal. Commun.* **2009**, *10*, 1661–1664, doi:10.1016/j.catcom.2009.05.004.

191. Hubbard, C.R.; Snyder, R.L. RIR — Measurement and Use in Quantitative XRD. *Powder Diffr.* **1988**, *3*, 74–77, doi:10.1017/S0885715600013257.

192. Piumetti, M.; Bensaid, S.; Russo, N.; Fino, D. Nanostructured ceria-based catalysts for soot combustion: Investigations on the surface sensitivity. *Appl. Catal. B Environ.* **2015**, *165*, 742–751, doi:10.1016/j.apcatb.2014.10.062.

193. Kim, J.Y.; Rodriguez, J.A.; Hanson, J.C.; Frenkel, A.I.; Lee, P.L. Reduction of CuO and Cu2O with H2: H embedding and kinetic effects in the formation of suboxides. *J. Am. Chem. Soc.* **2003**, *125*, 10684–10692, doi:10.1021/ja0301673.

194. Gao, P.; Li, F.; Zhao, N.; Xiao, F.; Wei, W.; Zhong, L.; Sun, Y. Influence of modifier (Mn, La, Ce, Zr and Y) on the performance of Cu/Zn/Al catalysts via hydrotalcite-like precursors for CO2 hydrogenation to methanol. *Appl. Catal. A Gen.* **2013**, *468*, 442–452, doi:10.1016/j.apcata.2013.09.026.

195. Wang, W.; Qu, Z.; Song, L.; Fu, Q. CO2 hydrogenation to methanol over

Cu/CeO2 and Cu/ZrO2 catalysts: Tuning methanol selectivity via metal-support interaction. *J. Energy Chem.* **2020**, *40*, 22–30, doi:10.1016/j.jechem.2019.03.001.

196. Gao, P.; Li, F.; Zhan, H.; Zhao, N.; Xiao, F.; Wei, W.; Zhong, L.; Wang, H.; Sun, Y. Influence of Zr on the performance of Cu/Zn/Al/Zr catalysts via hydrotalcite-like precursors for CO2 hydrogenation to methanol. *J. Catal.* **2013**, *298*, 51–60, doi:10.1016/j.jcat.2012.10.030.
197. Parvasi, P.; Rahimpour, M.R.; Jahanmiri, A. Incorporation of dynamic flexibility in the design of a methanol synthesis loop in the presence of catalyst deactivation. *Chem. Eng. Technol.* **2008**, *31*, 116–132, doi:10.1002/ceat.200700209.
198. Baltes, C.; Vukojević, S.; Schüth, F.; VUKOJEVIC, S.; SCHUTH, F.; Vukojević, S.; Schüth, F. Correlations between synthesis, precursor, and catalyst structure and activity of a large set of CuO/ZnO/Al2O3 catalysts for methanol synthesis. *J. Catal.* **2008**, *258*, 334–344, doi:10.1016/j.jcat.2008.07.004.
199. Baltes, C.; Vukojević, S.; Schüth, F. Correlations between synthesis, precursor, and catalyst structure and activity of a large set of CuO/ZnO/Al2O3 catalysts for methanol synthesis. *J. Catal.* **2008**, *258*, 334–344, doi:10.1016/j.jcat.2008.07.004.
200. Zoski; Cynthia G *Handbook of Electrochemistry*; ISBN 9780444519580.
201. Hernández, S.; Farkhondehfal, M.A.; Francesc, S.; Makkee, M.; Saracco, G.; Russo, N. Syngas production from electrochemical reduction of CO2: Current status and prospective implementation. *Green Chem.* **2017**, *19*, 2326–2346, doi:10.1039/c7gc00398f.
202. Parra, D.; Zhang, X.; Bauer, C.; Patel, M.K. An integrated techno-economic and life cycle environmental assessment of power-to-gas systems. *Appl. Energy* **2017**, *193*, 440–454, doi:10.1016/j.apenergy.2017.02.063.
203. Hägg, M.B.; Lindbråthen, A.; He, X.; Nodeland, S.G.; Cantero, T. Pilot Demonstration-reporting on CO2 Capture from a Cement Plant Using Hollow Fiber Process. *Energy Procedia* **2017**, *114*, 6150–6165, doi:10.1016/j.egypro.2017.03.1752.
204. Sepehri, A.; Sarrafzadeh, M.-H.; Avateffazeli, M. Interaction between Chlorella vulgaris and nitrifying-enriched activated sludge in the treatment of wastewater with low C/N ratio. *J. Clean. Prod.* **2020**, *247*, 119164, doi:10.1016/j.jclepro.2019.119164.
205. Voloshin, R.A.; Rodionova, M. V.; Zharmukhamedov, S.K.; Nejat Veziroglu, T.; Allakhverdiev, S.I. Review: Biofuel production from plant and algal biomass. *Int. J. Hydrogen Energy* **2016**, *41*, 17257–17273, doi:10.1016/j.ijhydene.2016.07.084.
206. Ntiamoah, A.; Ling, J.; Xiao, P.; Webley, P.A.; Zhai, Y. CO2 Capture by Temperature Swing Adsorption: Use of Hot CO2-Rich Gas for Regeneration. *Ind. Eng. Chem. Res.* **2016**, *55*, 703–713, doi:10.1021/acs.iecr.5b01384.
207. Akinola, T.E.; Oko, E.; Wang, M. Study of CO 2 removal in natural gas process using mixture of ionic liquid and MEA through process simulation. *Fuel* **2019**, *236*, 135–146, doi:10.1016/j.fuel.2018.08.152.
208. Boot-Handford, M.E.; Abanades, J.C.; Anthony, E.J.; Blunt, M.J.; Brandani, S.; Mac Dowell, N.; Fernández, J.R.; Ferrari, M.C.; Gross, R.; Hallett, J.P.; et al. Carbon capture and storage update. *Energy Environ. Sci.* **2014**, *7*, 130–189, doi:10.1039/c3ee42350f.

209. Yang, J.; Yu, X.; Yan, J.; Tu, S. CO 2 Capture Using Amine Solution Mixed with Ionic Liquid. **2014**, doi:10.1021/ie4040658.
210. MacDowell, N.; Florin, N.; Buchard, A.; Hallett, J.; Galindo, A.; Jackson, G.; Adjiman, C.S.; Williams, C.K.; Shah, N.; Fennell, P. An overview of CO2 capture technologies. *Energy Environ. Sci.* **2010**, *3*, 1645, doi:10.1039/c004106h.
211. Nelson, T.O.; Coleman, L.J.I.; Mobley, P.; Kataria, A.; Tanthana, J.; Lesemann, M.; Bjerge, L.-M. Solid Sorbent CO2 Capture Technology Evaluation and Demonstration at Norcem's Cement Plant in Brevik, Norway. *Energy Procedia* **2014**, *63*, 6504–6516, doi:10.1016/j.egypro.2014.11.686.
212. Stanovsky, P.; Karaszova, M.; Petrusova, Z.; Monteleone, M.; Jansen, J.C.; Comesaña-Gándara, B.; McKeown, N.B.; Izak, P. Upgrading of raw biogas using membranes based on the ultrapermeable polymer of intrinsic microporosity PIM-TMN-Trip. *J. Memb. Sci.* **2021**, *618*, 118694, doi:10.1016/j.memsci.2020.118694.
213. Jeon, Y.W.; Lee, D.H. Gas membranes for CO2/CH4 (biogas) separation: A review. *Environ. Eng. Sci.* **2015**, *32*, 71–85, doi:10.1089/ees.2014.0413.
214. Kárászová, M.; Sedláková, Z.; Izák, P. Review: Gas permeation processes in biogas upgrading: A short review. *Chem. Pap.* **2015**, *69*, 1277–1283, doi:10.1515/chempap-2015-0141.
215. Matzen, M.; Alhajji, M.; Demirel, Y. Chemical storage of wind energy by renewable methanol production: Feasibility analysis using a multi-criteria decision matrix. *Energy* **2015**, *93*, 343–353, doi:10.1016/j.energy.2015.09.043.
216. Newby, R.; Keairns, D. *Analysis of Integrated Gasification Fuel Cell Plant Configurations*; 2011;
217. Sulaymon, A.H.; Abbar, A.H. Scale-Up of Electrochemical Reactors. In *Electrolysis*; InTech, 2012; pp. 189–202.
218. Dinh, C.T.; García De Arquer, F.P.; Sinton, D.; Sargent, E.H. High rate, selective, and stable electroreduction of co2 to co in basic and neutral media. *ACS Energy Lett.* **2018**, *3*, 2835–2840, doi:10.1021/acsenergylett.8b01734.
219. Richard Turton, Richard C. Bailie, Wallace B. Whiting, J.A.S.; Turton, R.; Bailie, R.C.; Whiting, W.B.; Shaeiwitz, J.A.; Bhattacharyya, D.; Richard Turton, Richard C. Bailie, Wallace B. Whiting, J.A.S. *Analysis, Synthesis and Design of Chemical Processes*; 3rd ed.; Pearson Education International, 2009; ISBN 9788578110796.
220. Douglas, J.M. *Conceptual Design Of Chemical Processes*; McGraw-Hill, Inc., 1988;
221. Ulrich, G.D.; Vasudevan, P.T. *How to Estimate Utility Costs*; 2006;
222. Domènech, X.; Ayllón, J.A.; Peral, J.; Rieradevall, J. How green is a chemical reaction? Application of LCA to green chemistry. *Environ. Sci. Technol.* **2002**, *36*, 5517–5520, doi:10.1021/es020001m.
223. Technical Committe 207/SC5 *ISO 14040:2006 Environmental management -- Life cycle assessment -- Principles and framework*; 2006;
224. Technical Committe 207/SC5 *ISO 14044:2006 Environmental management -- Life cycle assessment -- Requirements and guidelines*; 2006;
225. Evangelisti, S.; Tagliaferri, C.; Brett, D.J.L.; Lettieri, P. Life cycle assessment of a polymer electrolyte membrane fuel cell system for passenger vehicles. *J. Clean. Prod.* **2017**, *142*, 4339–4355, doi:10.1016/j.jclepro.2016.11.159.

226. Hickner, M.A.; Ghassemi, H.; Kim, Y.S.; Einsla, B.R.; McGrath, J.E. Alternative polymer systems for proton exchange membranes (PEMs). *Chem. Rev.* **2004**, *104*, 4587–4611, doi:10.1021/cr020711a.
227. Carlson, E.J.; Kopf, P.; Sinha, J.; Sriramulu, S.; Yang, Y. Cost Analysis of PEM Fuel Cell Systems for Transportation. *Natl. Renew. Energy Lab.* **2005**, NREL/SR-560-39104.
228. Weber, S.; Peters, J.F.; Baumann, M.; Weil, M. Life cycle assessment of a vanadium redox flow battery. *Environ. Sci. Technol.* **2018**, *52*, 10864–10873.
229. Nuss, P.; Eckelman, M.J. Life cycle assessment of metals: a scientific synthesis. *PLoS One* **2014**, *9*.
230. Battista, F.; Montenegro Camacho, Y.S.; Hernández, S.; Bensaid, S.; Herrmann, A.; Krause, H.; Trimis, D.; Fino, D. LCA evaluation for the hydrogen production from biogas through the innovative BioRobur project concept. *Int. J. Hydrogen Energy* **2017**, *42*, 14030–14043, doi:10.1016/j.ijhydene.2016.12.065.
231. Maack, M. Deliverable n° 8-5 RS1a Life cycle approaches to assess emerging energy technologies. *Proj. no 502687 NEEDS New Energy Externalities Dev. Sustain.* **2008**.
232. Encinas-Sánchez, V.; Batuecas, E.; Macías-García, A.; Mayo, C.; Díaz, R.; Pérez, F.J. Corrosion resistance of protective coatings against molten nitrate salts for thermal energy storage and their environmental impact in CSP technology. *Sol. Energy* **2018**, *176*, 688–697, doi:10.1016/j.solener.2018.10.083.
233. Batuecas, E.; Tommasi, T.; Battista, F.; Negro, V.; Sonetti, G.; Viotti, P.; Fino, D.; Mancini, G. Life Cycle Assessment of waste disposal from olive oil production: Anaerobic digestion and conventional disposal on soil. *J. Environ. Manage.* **2019**, *237*, 94–102, doi:10.1016/j.jenvman.2019.02.021.
234. Page, G.; Ridoutt, B.; Bellotti, B. Carbon and water footprint tradeoffs in fresh tomato production. *J. Clean. Prod.* **2012**, *32*, 219–226, doi:10.1016/j.jclepro.2012.03.036.
235. Stocker, T.F.; Qin, D.; Plattner, G.K.; Tignor, M.M.B.; Allen, S.K.; Boschung, J.; Nauels, A.; Xia, Y.; Bex, V.; Midgley, P.M. *Climate change 2013 the physical science basis: Working Group I contribution to the fifth assessment report of the intergovernmental panel on climate change*; New York, 2013;
236. Frischknecht, R.; Steiner, R.; Jungbluth, N. Ökobilanzen: Methode der ökologischen Knappheit–Ökofaktoren 2006. *Zürich öbu* **2008**.
237. Frischknecht, R.; Wyss, F.; Büsser Knöpfel, S.; Lützkendorf, T.; Balouktsi, M. Cumulative energy demand in LCA: the energy harvested approach. *Int. J. Life Cycle Assess.* **2015**, *20*, 957–969, doi:10.1007/s11367-015-0897-4.
238. Ganesh, I. Conversion of carbon dioxide into methanol - A potential liquid fuel: Fundamental challenges and opportunities (a review). *Renew. Sustain. Energy Rev.* **2014**, *31*, 221–257, doi:10.1016/j.rser.2013.11.045.
239. Witoon, T.; Kachaban, N.; Donphai, W.; Kidkhunthod, P.; Faungnawakij, K.; Chareonpanich, M.; Limtrakul, J. Tuning of catalytic CO2 hydrogenation by changing composition of CuO-ZnO-ZrO2 catalysts. *Energy Convers. Manag.* **2016**, *118*, 21–31, doi:10.1016/j.enconman.2016.03.075.
240. Phongamwong, T.; Chantaprasertporn, U.; Witoon, T.; Numpilai, T.; Poo-arporn, Y.; Limphirat, W.; Donphai, W.; Dittanet, P.; Chareonpanich, M.; Limtrakul, J. CO2 hydrogenation to methanol over CuO–ZnO–ZrO2–SiO2

catalysts: Effects of SiO2 contents. *Chem. Eng. J.* **2017**, *316*, 692–703, doi:10.1016/j.cej.2017.02.010.

241. Saeidi, S.; Amin, N.A.S.; Rahimpour, M.R. Hydrogenation of CO2 to value-added products - A review and potential future developments. *J. CO2 Util.* **2014**, *5*, 66–81, doi:10.1016/j.jcou.2013.12.005.
242. Toyir, J.; Miloua, R.; Elkadri, N.E.; Nawdali, M.; Toufik, H.; Miloua, F.; Saito, M. Sustainable process for the production of methanol from CO2 and H2 using Cu/ZnO-based multicomponent catalyst. *Phys. Procedia* **2009**, *2*, 1075–1079, doi:10.1016/j.phpro.2009.11.065.
243. Studt, F.; Sharafutdinov, I.; Abild-Pedersen, F.; Elkjær, C.F.; Hummelshøj, J.S.; Dahl, S.; Chorkendorff, I.; Nørskov, J.K. Discovery of a Ni-Ga catalyst for carbon dioxide reduction to methanol. *Nat. Chem.* **2014**, *6*, 320–324, doi:10.1038/nchem.1873.
244. Akhter, P.; Farkhondehfal, M.A.; Hernández, S.; Hussain, M.; Fina, A.; Saracco, G.; Khan, A.U.; Russo, N. Environmental issues regarding CO2 and recent strategies for alternative fuels through photocatalytic reduction with titania-based materials. *J. Environ. Chem. Eng.* **2016**, *4*, 3934–3953, doi:10.1016/j.jece.2016.09.004.
245. Whipple, D.T.; Kenis, P.J.A. Prospects of CO2 utilization via direct heterogeneous electrochemical reduction. *J. Phys. Chem. Lett.* **2010**, *1*, 3451–3458, doi:10.1021/jz1012627.
246. Liu, X.; Xiao, J.; Peng, H.; Hong, X.; Chan, K.; Nørskov, J.K. Understanding trends in electrochemical carbon dioxide reduction rates. *Nat. Commun.* **2017**, *8*, 1–7, doi:10.1038/ncomms15438.
247. Goodpaster, J.D.; Bell, A.T.; Head-Gordon, M. Identification of Possible Pathways for C-C Bond Formation during Electrochemical Reduction of CO2: New Theoretical Insights from an Improved Electrochemical Model. *J. Phys. Chem. Lett.* **2016**, *7*, 1471–1477, doi:10.1021/acs.jpclett.6b00358.
248. Elgrishi, N.; Rountree, K.J.; McCarthy, B.D.; Rountree, E.S.; Eisenhart, T.T.; Dempsey, J.L. A Practical Beginner's Guide to Cyclic Voltammetry. *J. Chem. Educ.* **2018**, *95*, 197–206, doi:10.1021/acs.jchemed.7b00361.
249. Back, S.; Kim, H.; Jung, Y. Selective heterogeneous CO2 electroreduction to methanol. *ACS Catal.* **2015**, *5*, 965–971, doi:10.1021/cs501600x.
250. Liu, X.; Schlexer, P.; Xiao, J.; Ji, Y.; Wang, L.; Sandberg, R.B.; Tang, M.; Brown, K.S.; Peng, H.; Ringe, S.; et al. pH effects on the electrochemical reduction of CO (2) towards C 2 products on stepped copper. *Nat. Commun.* **2019**, *10*, 1–10, doi:10.1038/s41467-018-07970-9.
251. Xiao, H.; Goddard, W.A.; Cheng, T.; Liu, Y. Cu metal embedded in oxidized matrix catalyst to promote CO2 activation and CO dimerization for electrochemical reduction of CO2. *Proc. Natl. Acad. Sci. U. S. A.* **2017**, *114*, 6685–6688, doi:10.1073/pnas.1702405114.
252. Qin, T.; Qian, Y.; Zhang, F.; Lin, B.L. Cloride-derived copper electrode for efficient electrochemical reduction of CO2 to ethylene. *Chinese Chem. Lett.* **2019**, *30*, 314–318, doi:10.1016/j.cclet.2018.07.003.
253. Fan, Q.; Zhang, M.; Jia, M.; Liu, S.; Qiu, J.; Sun, Z. Electrochemical CO2 reduction to C2+ species: Heterogeneous electrocatalysts, reaction pathways, and optimization strategies. *Mater. Today Energy* **2018**, *10*, 280–301, doi:10.1016/j.mtener.2018.10.003.
254. Horányi, G. Heterogeneous catalysis and electrocatalysis. *Catal. Today* **1994**, *19*, 285–311, doi:10.1016/0920-5861(94)80188-6.
255. Guzmán, H.; Farkhondehfal, M.A.; Rodulfo Tolod, K.; Russo, N.;

Hernández, S. Photo/electrocatalytic hydrogen exploitation for CO2 reduction toward solar fuels production. In *Solar Hydrogen Production Processes, Systems and Technologies*; Elsevier Inc., 2019; p. 560 ISBN 978-0-12-814853-2.

256. Wang, X.; Wang, Z.; Arquer, F.P.G. De; Dinh, C.; Ozden, A.; Li, Y.C.; Nam, D.; Li, J.; Liu, Y.; Wicks, J.; et al. Efficient electrically powered CO2 -to-ethanol via suppression of deoxygenation. *Nat. Energy* **2020**, doi:10.1038/s41560-020-0607-8.
257. Pricing | Methanex Corporation Available online: https://www.methanex.com/our-business/pricing (accessed on Mar 28, 2020).
258. Rivarolo, M.; Bellotti, D.; Magistri, L.; Massardo, A.F. Feasibility study of methanol production from different renewable sources and thermo-economic analysis. *Int. J. Hydrogen Energy* **2016**, *41*, 2105–2116, doi:10.1016/j.ijhydene.2015.12.128.
259. Kern, D.Q. *Process Heat Transfer*; McGraw-Hill Book Company, 1965;
260. Lee, B.; Lee, H.; Lim, D.; Brigljević, B.; Cho, W.; Cho, H.S.; Kim, C.H.; Lim, H. Renewable methanol synthesis from renewable H2 and captured CO2: How can power-to-liquid technology be economically feasible? *Appl. Energy* **2020**, *279*, doi:10.1016/j.apenergy.2020.115827.
261. Bellotti, D.; Rivarolo, M.; Magistri, L. Economic feasibility of methanol synthesis as a method for CO2 reduction and energy storage. *Energy Procedia* **2019**, *158*, 4721–4728, doi:10.1016/j.egypro.2019.01.730.
262. Li, J.; Ma, X.; Liu, H.; Zhang, X. Life cycle assessment and economic analysis of methanol production from coke oven gas compared with coal and natural gas routes. *J. Clean. Prod.* **2018**, *185*, 299–308, doi:10.1016/j.jclepro.2018.02.100.
263. Orella, M.J.; Brown, S.M.; Leonard, M.E.; Román-Leshkov, Y.; Brushett, F.R. A General Technoeconomic Model for Evaluating Emerging Electrolytic Processes. *Energy Technol.* **2019**, *1900994*, 1–12, doi:10.1002/ente.201900994.
264. Asif, M.; Gao, X.; Lv, H.; Xi, X.; Dong, P. Catalytic hydrogenation of CO2 from 600 MW supercritical coal power plant to produce methanol: A techno-economic analysis. *Int. J. Hydrogen Energy* **2018**, *43*, 2726–2741, doi:10.1016/j.ijhydene.2017.12.086.
265. Szima, S.; Cormos, C.C. Improving methanol synthesis from carbon-free H2 and captured CO2: A techno-economic and environmental evaluation. *J. CO2 Util.* **2018**, *24*, 555–563, doi:10.1016/j.jcou.2018.02.007.
266. Aldaco, R.; Butnar, I.; Margallo, M.; Laso, J.; Rumayor, M.; Dominguez-Ramos, A.; Irabien, A.; Dodds, P.E. Bringing value to the chemical industry from capture, storage and use of CO 2 : A dynamic LCA of formic acid production. *Sci. Total Environ.* **2019**, *663*, 738–753, doi:10.1016/j.scitotenv.2019.01.395.
267. Wernet, G.; Bauer, C.; Steubing, B.; Reinhard, J.; Moreno-Ruiz, E.; Weidema, B. The ecoinvent database version 3 (part I): overview and methodology. *Int. J. Life Cycle Assess.* **2016**, *21*, 1218–1230, doi:10.1007/s11367-016-1087-8.
268. Qin, Z.; Zhai, G.; Wu, X.; Yu, Y.; Zhang, Z. Carbon footprint evaluation of coal-to-methanol chain with the hierarchical attribution management and life cycle assessment. *Energy Convers. Manag.* **2016**, *124*, 168–179.
269. Patel, M. Cumulative energy demand (CED) and cumulative CO2 emissions

for products of the organic chemical industry. *Energy* **2003**, *28*, 721–740, doi:10.1016/S0360-5442(02)00166-4.

270. Gabardo, C.M.; Colin, P.; Brien, O.; Jonathan, P.; Li, J.; Edward, H.; Sinton, D.; Gabardo, C.M.; Brien, C.P.O.; Edwards, J.P.; et al. Continuous Carbon Dioxide Electroreduction to Concentrated Multi-carbon Products Using a Membrane Electrode Assembly Continuous Carbon Dioxide Electroreduction to Concentrated Multi-carbon Products Using a Membrane Electrode Assembly. **2019**, 2777–2791, doi:10.1016/j.joule.2019.07.021.
271. De Luna, P.; Hahn, C.; Higgins, D.; Jaffer, S.A.; Jaramillo, T.F.; Sargent, E.H. What would it take for renewably powered electrosynthesis to displace petrochemical processes? *Science (80-.).* **2019**, *364*, 1–9, doi:10.1126/science.aav3506.
272. Von Der Assen, N.; Jung, J.; Bardow, A. Life-cycle assessment of carbon dioxide capture and utilization: Avoiding the pitfalls. *Energy Environ. Sci.* **2013**, *6*, 2721–2734, doi:10.1039/c3ee41151f.
273. Aneke, M.; Wang, M. Energy storage technologies and real life applications – A state of the art review. *Appl. Energy* **2016**, *179*, 350–377, doi:10.1016/j.apenergy.2016.06.097.
274. Kar, S.; Kothandaraman, J.; Goeppert, A.; Prakash, G.K.S. Advances in catalytic homogeneous hydrogenation of carbon dioxide to methanol. *J. CO2 Util.* **2018**, *23*, 212–218, doi:10.1016/j.jcou.2017.10.023.
275. Bonura, G.; Frusteri, F.; Cannilla, C.; Drago Ferrante, G.; Aloise, A.; Catizzone, E.; Migliori, M.; Giordano, G. Catalytic features of CuZnZr–zeolite hybrid systems for the direct CO2-to-DME hydrogenation reaction. *Catal. Today* **2016**, *277*, 48–54, doi:10.1016/j.cattod.2016.02.013.
276. Langmuir, I. THE ADSORPTION OF GASES ON PLANE SURFACES OF GLASS, MICA AND PLATINUM. *J. Am. Chem. Soc.* **1918**, *40*, 1361–1403, doi:10.1021/ja02242a004.
277. Ortega, C.; Rezaei, M.; Hessel, V.; Kolb, G. Methanol to dimethyl ether conversion over a ZSM-5 catalyst: Intrinsic kinetic study on an external recycle reactor. *Chem. Eng. J.* **2018**, *347*, 741–753, doi:10.1016/j.cej.2018.04.160.
278. Sun, J.T.; Metcalfe, I.S.; Sahibzada, M. Deactivation of Cu/ZnO/Al 2 O 3 Methanol Synthesis Catalyst by Sintering. *Ind. Eng. Chem. Res.* **1999**, *38*, 3868–3872, doi:10.1021/ie990078s.
279. Miletto, I.; Catizzone, E.; Bonura, G.; Ivaldi, C.; Migliori, M.; Gianotti, E.; Marchese, L.; Frusteri, F.; Giordano, G. In Situ FT-IR Characterization of CuZnZr/Ferrierite Hybrid Catalysts for One-Pot CO2-to-DME Conversion. *Materials (Basel).* **2018**, *11*, 2275, doi:10.3390/ma11112275.
280. Flores, J.H.; da Silva, M.I.P. Influence of the Preparation Method on Hybrid Catalysts CuO–ZnO–Al2O3 and H-Ferrierite for Syngas Transformation to Hydrocarbons via Methanol. *Catal. Letters* **2016**, *146*, 1505–1516, doi:10.1007/s10562-016-1771-0.
281. Koga, N.; Criado, J.M.; Tanaka, H. Apparent kinetic behavior of the thermal decomposition of synthetic malachite. *Thermochim. Acta* **1999**, *340–341*, 387–394, doi:10.1016/S0040-6031(99)00289-0.
282. Bae, J.W.; Kang, S.-H.; Lee, Y.-J.; Jun, K.-W. Synthesis of DME from syngas on the bifunctional Cu–ZnO–Al2O3/Zr-modified ferrierite: Effect of Zr content. *Appl. Catal. B Environ.* **2009**, *90*, 426–435, doi:10.1016/j.apcatb.2009.04.002.
283. Wei, P.; Zhu, X.; Wang, Y.; Chu, W.; Xie, S.; Yang, Z.; Liu, X.; Li, X.; Xu,

L. Rapid synthesis of ferrierite zeolite through microwave assisted organic template free route. *Microporous Mesoporous Mater.* **2019**, *279*, 220–227, doi:10.1016/J.MICROMESO.2018.12.036.

284. Mayoral, A.; Anderson, P.A.; Diaz, I. Zeolites are no longer a challenge: Atomic resolution data by Aberration-corrected STEM. *Micron* **2015**, *68*, 146–151, doi:10.1016/j.micron.2014.05.009.
285. Arena, F.; Italiano, G.; Barbera, K.; Bordiga, S.; Bonura, G.; Spadaro, L.; Frusteri, F. Solid-state interactions, adsorption sites and functionality of Cu-ZnO/ZrO2 catalysts in the CO2 hydrogenation to CH3OH. *Appl. Catal. A Gen.* **2008**, *350*, 16–23, doi:10.1016/j.apcata.2008.07.028.
286. Tisseraud, C.; Comminges, C.; Belin, T.; Ahouari, H.; Soualah, A.; Pouilloux, Y.; Le Valant, A. The Cu–ZnO synergy in methanol synthesis from CO 2 , Part 2: Origin of the methanol and CO selectivities explained by experimental studies and a sphere contact quantification model in randomly packed binary mixtures on Cu–ZnO coprecipitate catalysts. *J. Catal.* **2015**, *330*, 533–544, doi:10.1016/j.jcat.2015.04.035.
287. Bonura, G.; Cannilla, C.; Frusteri, L.; Frusteri, F. The influence of different promoter oxides on the functionality of hybrid CuZn-ferrierite systems for the production of DME from CO 2 -H 2 mixtures. *Appl. Catal. A Gen.* **2017**, *544*, 21–29, doi:10.1016/j.apcata.2017.07.010.
288. García-Trenco, A.; Vidal-Moya, A.; Martínez, A. Study of the interaction between components in hybrid CuZnAl/HZSM-5 catalysts and its impact in the syngas-to-DME reaction. *Catal. Today* **2012**, *179*, 43–51, doi:10.1016/j.cattod.2011.06.034.
289. Dow, W.-P.; Wang, Y.-P.; Huang, T.-J. Yttria-Stabilized Zirconia Supported Copper Oxide Catalyst. *J. Catal.* **1996**, *160*, 155–170, doi:10.1006/jcat.1996.0135.
290. Grunwaldt, J.-D.; Molenbroek, A..; Topsøe, N.-Y.; Topsøe, H.; Clausen, B.. In Situ Investigations of Structural Changes in Cu/ZnO Catalysts. *J. Catal.* **2000**, *194*, 452–460, doi:10.1006/jcat.2000.2930.
291. Waugh, K.C. Methanol Synthesis. *Catal. Today* **1992**, *15*, 51–75, doi:10.1016/0920-5861(92)80122-4.
292. Meliàn-Cabrera, I.; Granados, M.L.; Fierro, J.L.G. Pd-Modified Cu?Zn Catalysts for Methanol Synthesis from CO2/H2 Mixtures: Catalytic Structures and Performance. *J. Catal.* **2002**, *210*, 285–294, doi:10.1006/jcat.2002.3677.
293. Bailey, S.; Waugh, K.C. Comment on the use of temperature-programmed desorption of H2 as a tool to determine metal surface area of Cu catalysts. *Catal. Letters* **1993**, *17*, 371–374, doi:10.1007/BF00766160.
294. Muhler, M.; Nielsen, L.P.; Törnqvist, E.; Clausen, B.S.; Topsøe, H. Reply to the comment by Bailey and Waugh on the use of temperature programmed desorption of H2 to determine metal surface area of Cu catalysts. *Catal. Letters* **1993**, *17*, 375–376, doi:10.1007/BF00766161.
295. MAO, D.; YANG, W.; XIA, J.; ZHANG, B.; SONG, Q.; CHEN, Q. Highly effective hybrid catalyst for the direct synthesis of dimethyl ether from syngas with magnesium oxide-modified HZSM-5 as a dehydration component. *J. Catal.* **2005**, *230*, 140–149, doi:10.1016/j.jcat.2004.12.007.
296. Jung, J.W.; Lee, Y.J.; Um, S.H.; Yoo, P.J.; Lee, D.H.; Jun, K.-W.; Bae, J.W. Effect of copper surface area and acidic sites to intrinsic catalytic activity for dimethyl ether synthesis from biomass-derived syngas. *Appl. Catal. B Environ.* **2012**, *126*, 1–8, doi:10.1016/j.apcatb.2012.06.026.

297. Huertas Flores, J.; Isabel Pais da Silva, M. Acid properties of the hybrid catalyst CuO-ZnO or CuO-ZnO-Al2O3/H-ferrierite: An infrared study. *Physicochem. Eng. Asp.* **2008**, *322*, 113–123, doi:10.1016/j.colsurfa.2008.02.033.
298. Natesakhawat, S.; Lekse, J.W.; Baltrus, J.P.; Ohodnicki, P.R.; Howard, B.H.; Deng, X.; Matranga, C. Active Sites and Structure–Activity Relationships of Copper-Based Catalysts for Carbon Dioxide Hydrogenation to Methanol. *ACS Catal.* **2012**, *2*, 1667–1676, doi:10.1021/cs300008g.
299. Ju, W.; Zeng, J.; Bejtka, K.; Ma, H.; Rentsch, D.; Castellino, M.; Sacco, A.; Pirri, C.F.; Battaglia, C. Sn-Decorated Cu for Selective Electrochemical CO 2 to CO Conversion: Precision Architecture beyond Composition Design. *ACS Appl. Energy Mater.* **2019**, *2*, 867–872, doi:10.1021/acsaem.8b01944.
300. Laurenti, M.; Canavese, G.; Stassi, S.; Fontana, M.; Castellino, M.; Pirri, C.F.; Cauda, V. A porous nanobranched structure: an effective way to improve piezoelectricity in sputtered ZnO thin films. *RSC Adv.* **2016**, *6*, 76996–77004, doi:10.1039/C6RA17319E.
301. Gionco, C.; Hernández, S.; Castellino, M.; Gadhi, T.A.; Muñoz-Tabares, J.A.; Cerrato, E.; Tagliaferro, A.; Russo, N.; Paganini, M.C. Synthesis and characterization of Ce and Er doped ZrO2 nanoparticles as solar light driven photocatalysts. *J. Alloys Compd.* **2019**, *775*, 896–904, doi:10.1016/j.jallcom.2018.10.046.
302. Hernández, S.; Gionco, C.; Husak, T.; Castellino, M.; Muñoz-Tabares, J.A.; Tolod, K.R.; Giamello, E.; Paganini, M.C.; Russo, N. Insights Into the Sunlight-Driven Water Oxidation by Ce and Er-Doped ZrO2. *Front. Chem.* **2018**, *6*, doi:10.3389/fchem.2018.00368.
303. Cotirlan, C.; Galca, A.C.; Ciobanu, C.S.; Logofatu, C. The study of the silicon oxide thickness on crystalline Si by X-ray photoelectron spectroscopy and spectroscopic ellipsometry. *J. Optoelectron. Adv. Mater.* **2010**, *12*, 1092–1097.
304. Kobl, K.; Thomas, S.; Zimmermann, Y.; Parkhomenko, K.; Roger, A.-C. Power-law kinetics of methanol synthesis from carbon dioxide and hydrogen on copper–zinc oxide catalysts with alumina or zirconia supports. *Catal. Today* **2016**, *270*, 31–42, doi:10.1016/j.cattod.2015.11.020.
305. Bonura, G.; Cordaro, M.; Spadaro, L.; Cannilla, C.; Arena, F.; Frusteri, F. Hybrid Cu–ZnO–ZrO2/H-ZSM5 system for the direct synthesis of DME by CO2 hydrogenation. *Appl. Catal. B Environ.* **2013**, *140–141*, 16–24, doi:10.1016/j.apcatb.2013.03.048.
306. Ateka, A.; Ereña, J.; Bilbao, J.; Aguayo, A.T. Kinetic modeling of the direct synthesis of dimethyl ether over a CuO-ZnO-MnO/SAPO-18 catalyst and assessment of the CO2 conversion. *Fuel Process. Technol.* **2018**, *181*, 233–243, doi:10.1016/j.fuproc.2018.09.024.